



HAL
open science

Multi-scale modeling of thermo-mechanical dynamic damage in quasi-brittle materials

Kokouvi Gbetchi

► **To cite this version:**

Kokouvi Gbetchi. Multi-scale modeling of thermo-mechanical dynamic damage in quasi-brittle materials. Mechanics of materials [physics.class-ph]. Université de Lorraine, 2020. English. NNT : 2020LORR0049 . tel-02940741

HAL Id: tel-02940741

<https://hal.univ-lorraine.fr/tel-02940741>

Submitted on 16 Sep 2020

HAL is a multi-disciplinary open access archive for the deposit and dissemination of scientific research documents, whether they are published or not. The documents may come from teaching and research institutions in France or abroad, or from public or private research centers.

L'archive ouverte pluridisciplinaire **HAL**, est destinée au dépôt et à la diffusion de documents scientifiques de niveau recherche, publiés ou non, émanant des établissements d'enseignement et de recherche français ou étrangers, des laboratoires publics ou privés.



AVERTISSEMENT

Ce document est le fruit d'un long travail approuvé par le jury de soutenance et mis à disposition de l'ensemble de la communauté universitaire élargie.

Il est soumis à la propriété intellectuelle de l'auteur. Ceci implique une obligation de citation et de référencement lors de l'utilisation de ce document.

D'autre part, toute contrefaçon, plagiat, reproduction illicite encourt une poursuite pénale.

Contact : ddoc-theses-contact@univ-lorraine.fr

LIENS

Code de la Propriété Intellectuelle. articles L 122. 4

Code de la Propriété Intellectuelle. articles L 335.2- L 335.10

http://www.cfcopies.com/V2/leg/leg_droi.php

<http://www.culture.gouv.fr/culture/infos-pratiques/droits/protection.htm>

THÈSE

Pour l'obtention du titre :

DOCTEUR de L'UNIVERSITÉ DE LORRAINE

(Mention : Mécanique des Matériaux)

Par :

Kokouvi GBETCHI

Multi-scale modeling of thermo-mechanical dynamic damage in quasi-brittle materials

Soutenue publiquement le 24 Juin 2020 à Metz

Composition du Jury

Président : Albert Giraud Professeur, Université de Lorraine

Rapporteurs : Jia Li Professeur, Institut Galilée Université Paris XIII

Ralf Müller Professeur, Technische Universität Kaiserslautern

Examineurs : Hubert Maigre Chargé de recherche CNRS, INSA-Lyon

Anna Pandolfi Professeur, Politecnico di Milano

Directeur : Cristian Dascalu Professeur, Université de Lorraine

Mis en page avec la classe thesul.

Acknowledgments

The research investigations of this PhD thesis were carried out at the laboratory LEM3 in Metz, under the supervision of Prof. Cristian Dascalu to whom I would like to express my great acknowledgements. I thank him for his availability, his scientific advices, his contributions, his patience and for giving me opportunity to discover the academic research. I consider myself fortunate to have had him as supervisor. It would have been more difficult without his full involvement.

On the other hand, I would like to extend my sincere gratitude to Prof. Albert Giraud who granted me the honor of chairing the doctoral committee, but also to Prof. Ralf Müller and Prof. Jia Li who accepted to review the dissertation, for their kind attention to my work and careful reading of the text. I also express my gratitude to Prof. Anna Pandolfi and Dr. Hubert Maigne for their participation to the defense committee.

This is also an opportunity for me to thank all the members of the LEM3 laboratory especially Julien Oury, the PhD students and all the researchers for their conviviality and their support during the thesis period.

I particularly thank the members of ITN OUTCOME project, Prof. Sébastien Mercier, Prof. Marion Martiny, Prof. Christophe Czarnota and the ESRs with whom I shared these moments. Many thanks need to be expressed to Prof. Daniel Rittel, Prof. Shmuel Osovski (Technion, Israel), Prof. José A. Rodríguez-Martínez (UC3M, Madrid) for hosting my research stays in their laboratories and for having guided me. Special acknowledgements to Alicia Ayuso, Eugenio Grande with whom I had fruitful discussions and learned a lot during my stay at Airbus Defense and Space (Madrid).

I would also like to thank my friends and colleagues Komi Espoir Nsouglo, Essossinam Simlissi, Megbeme Komla Atiezo and Irfan Habeeb who have been a source of support during all these years of research work.

Finally, I would like to express my heartfelt thanks to my family for the love and daily moral support that allowed me to go through with this work.

Thanks to those I did not mention!

This PhD thesis has received funding from the European Union's Horizon 2020 Programme (Excellent Science, Marie Skłodowska-Curie Actions) under REA grant agreement 675602, ITN project OUTCOME.

*Dedicated to
My mum and dad,
My brother and sisters.*

Abstract

Under impact mechanical loadings, structural components made of brittle materials may be exposed to dynamic failure. The appropriate modeling of the failure mechanisms at different scales of observation and the prediction of the corresponding thermo-mechanical damage evolution in such materials is essential for structural reliability predictions. Experimental observations on dynamic failure in brittle materials report important cooling and heating effects in the vicinity of the crack tip. Theoretical modeling of the thermo-mechanical coupling during fracture have been generally undertaken without accounting for microstructural aspects. The objective of the present thesis is to develop a procedure to obtain macroscopic thermo-mechanical damage laws in which the damage evolution is deduced from the propagation of microcracks and the associated small-scale thermal effects in the material. We use the asymptotic homogenization method to obtain the macroscopic thermo-mechanical and damage response of the solid. A Griffith type criterion is assumed for microcracks propagating in modes I or II. Heat sources at the tips of microcracks are considered as a consequence of the energy dissipated during propagation. Frictional heating effects are also considered on the lips of microcracks evolving in the shear mode. An energy approach is developed in combination with the homogenization procedure to obtain macroscopic damage laws. The resulting thermoelastic and damage system involves strong couplings between mechanical and thermal fields. Computation of the effective coefficients allowed us to study the local response predicted by the new models. The macroscopic response exhibits strain-rate sensitivity, microstructural size effects, degradation of thermoelastic properties and specific thermal evolutions due to microcracking and frictional effects at the small scale. Distributed heat sources are present in the macroscopic temperature equation linked to damage and frictional dissipations. The implementation of the proposed damage models in a FEM software allowed us to perform numerical simulations at the structural level. We reproduced numerically experimental tests reported in the literature concerning the rapid failure of PMMA samples under impact. The results obtained in the simulations are in good agreement with the experimental observations.

Keywords: Dynamic brittle failure, thermo-mechanical coupling, micro-cracks, crack-tip and frictional heating, asymptotic homogenization, damage laws, finite-element simulations, impact tests.

Résumé

Sous l'effet des impacts mécaniques, les structures constituées de matériaux fragiles peuvent être exposés à la rupture dynamique. La modélisation appropriée des mécanismes de rupture à différentes échelles d'observation et la prédiction de l'endommagement thermo-mécanique dans ces matériaux sont essentielles pour la conception de structures fiables. Des observations expérimentales sur la rupture dynamique des matériaux fragiles montrent des effets de refroidissement et d'échauffement importants à proximité d'une pointe de fissure. La modélisation du couplage thermo-mécanique lors de la rupture fragile a été entreprise, en général, sans tenir compte des aspects microstructuraux. L'objectif de cette thèse est de développer une procédure pour obtenir des lois d'endommagement thermo-mécaniques dans lesquelles l'évolution de l'endommagement est déduite à partir de la propagation des microfissures et des effets thermiques associés à l'échelle petite du matériau. Nous utilisons la méthode d'homogénéisation asymptotique pour obtenir la réponse macroscopique thermo-mécanique et d'endommagement du solide. Pour la propagation des microfissures, en mode I ou II, un critère de type Griffith est adopté. Des sources de chaleur sont considérées aux pointes des microfissures en mouvement, en lien avec l'énergie dissipée pendant la propagation. Nous considérons aussi des sources de chaleur représentant la dissipation par frottement sur les lèvres des microfissures qui se propagent en mode de cisaillement. Grâce à une analyse énergétique combinée avec la méthode d'homogénéisation nous obtenons des lois d'endommagement macroscopiques. Dans le système thermoélastique et d'endommagement ainsi obtenu, on identifie de forts couplages entre les champs mécaniques et thermiques. Le calcul des coefficients effectifs nous a permis d'étudier la réponse locale prédite par les nouveaux modèles. Cette réponse montre des effets de vitesse de déformation, de taille de la microstructure, de dégradation des propriétés thermo-élastiques et des évolutions thermiques spécifiques engendrées par la microfissuration et le frottement à l'échelle petite du matériau. Dans l'équation macroscopique de la température, on retrouve des termes sources de chaleur distribuées en lien avec les dissipations d'endommagement et de frottement. L'implémentation de modèles d'endommagement dans un logiciel d'éléments finis nous a permis d'effectuer des simulations numériques à l'échelle des structures. Nous avons reproduit numériquement certains tests expérimentaux publiés dans la littérature concernant la rupture rapide d'échantillons de PMMA sous sollicitation d'impact. Les résultats des simulations obtenus sont en bon accord avec les observations expérimentales.

Mots-clés: Rupture fragile dynamique, couplage thermo-mécanique, microfissures, échauffement par propagation et frottement, homogénéisation asymptotique, lois d'endommagement, simulations éléments finis, test d'impact.

Contents

General introduction	1
Chapter 1 Background and literature review	5
1.1 Introduction	5
1.2 Dynamic fracture mechanics	6
1.2.1 Asymptotic analysis and fields singularity	7
1.2.2 Dynamic stress intensity factors	9
1.2.3 Dynamic energy release rate	10
1.2.4 Thermoelastic dynamic fracture	12
1.3 Damage mechanics	16
1.3.1 Effective stress	16
1.3.2 Damage evolution laws	17
1.3.3 Thermodynamics of damage	19
1.4 Asymptotic homogenization	20
1.5 Thermal effects in dynamic failure experiments	22
Chapter 2 Two-scale dynamic damage model for mode I microcracking with heat dissipation	25
2.1 Introduction	25
2.2 Two-scale thermoelastic fracture problem	27
2.3 Asymptotic developments and homogenization analysis	30
2.4 Dynamic damage evolution	36
2.5 Local macroscopic response	40
2.5.1 Homogenized coefficients	40
2.5.2 Local response analysis	42
2.6 Numerical Simulation of the CCS Impact Test	48

2.7	Heat conduction versus adiabatic conditions	51
2.7.1	Single element test	51
2.7.2	Numerical simulations of an impact test	52
2.8	Conclusions	56
Chapter 3 Dynamic damage evolution for mode II microcracks with frictional contact		59
3.1	Introduction	59
3.2	Formulation of the initial fracture problem	61
3.3	Homogenized elastodynamic equations	63
3.4	Dynamic damage law with friction effects	65
3.5	Local macroscopic behavior	67
3.5.1	Homogenized coefficients C_{mnpq} and I_{mnpq}	67
3.5.2	Local response analysis	69
3.6	Numerical simulations of mode II failure of PMMA samples under impact .	72
Chapter 4 Thermo-mechanical couplings in dynamic shear failure		79
4.1	Introduction	79
4.2	Thermoelastic fracture problem formulation	81
4.3	Asymptotic homogenization analysis	83
4.4	Dynamic damage law	90
4.5	Local macroscopic response	94
4.5.1	Homogenized coefficients	94
4.5.2	Macroscopic response	97
4.6	Numerical simulations of heating in mode II failure under impact	102
4.7	Conclusions	105
General conclusions		107
Appendix A Asymptotic expansion of the energy release-rate		109
Appendix B Computation of the effective coefficients C_{ijkl} and I_{mnpq}		111
Appendix C Thermoelastic effective coefficients and damage law		115
Bibliography		125

List of Figures

1.1	Three modes of crack propagation	6
1.2	Universal function $k_I(\dot{l})$	10
1.3	Solid with a moving crack	11
1.4	Universal functions $g_I(\dot{l})$ and $g_{II}(\dot{l})$	12
1.5	One dimensional thermoelastic fracture problem [132].	15
1.6	Damaged solid	17
1.7	Micro-fissured medium with locally periodic distributed microcracks	21
1.8	Compact compression specimen test [115]. Crack-tip temperature measurement with thermocouple.	22
1.9	Multi-point temperature measurement in opening mode dynamic fracture experiment [17, 18].	23
1.10	Multi-point temperature measurement in shear mode dynamic fracture experiment [17, 19].	24
2.1	a) Micro-fissured medium with locally periodic microstructure with l_c the size of a period, l the local micro-crack length and L_c the characteristic length of the macro-structure. b) Reference cell of size L_c with rescaled crack length $d.L_c$	28
2.2	Scaling of the microscopic period of the material to the reference cell.	31
2.3	Homogenized coefficients C_{ijkl}^{eff} versus the damage variable d : computed values and interpolation curves.	41
2.4	Effective stress-temperature moduli β_{11}^{eff} and β_{22}^{eff} versus damage.	42
2.5	Effective thermal modulus $S^*(d)$ and conductivity coefficient $k_{22}^{eff}(d)$	42
2.6	Temperature $T^{(0)}$ versus the applied strain $e_{x22}(u^{(0)})(t)$, for three sizes of the microstructure: a) $l_c = 10^{-4} m$; b) $l_c = 10^{-5} m$; c) $l_c = 10^{-6} m$. Evolutions with (continuous line) or without (dotted line) crack tip heating.	44
2.7	Influence of size of the microstructure on the effective stress, damage and temperature for: $l_c = 5 \times 10^{-4} m$; $l_c = 5 \times 10^{-5} m$; $l_c = 5 \times 10^{-6} m$	45
2.8	Final value of the temperature (at $d = 1$) and its minimal value (at the end of the cooling phase) versus the size of the microstructure l_c	45
2.9	Effective stress, damage and temperature for different strain rates: $\dot{e}_{x22} = 100 s^{-1}$, $\dot{e}_{x22} = 1000 s^{-1}$ and $\dot{e}_{x22} = 10000 s^{-1}$	46
2.10	Macroscopic fields for initial values of damage: $d_0 = 0.1$, $d_0 = 0.2$ and $d_0 = 0.3$	47

2.11	Geometry of the specimen, with dimensions in mm . The impact velocity V is applied over a region of $16.5 mm$	48
2.12	Local geometry near the notch tip and finite element mesh with refinement in the failure initiation zone.	49
2.13	Left: damage variable represented with element deletion at complete failure. Right: temperature field with cooling and heating zones near the moving tip.	50
2.14	Temperature variation at $1 mm$ from the tip of the notch: measured values (left) from [115] and computed values (right) in 4 neighbor elements in the area of the thermocouple location.	50
2.15	One-element test : a) boundary conditions and b) displacement u_1	51
2.16	Stress Σ_{11} , damage variable d and macroscopic temperature $T^{(0)}$ obtained with and without adiabatic assumption	52
2.17	Rectangular PMMA specimen with initial notch subjected to impact loading	53
2.18	FE mesh with refinement near the initial notch tip.	53
2.19	Temperature contours during the crack initiation regime: simulations with (a) and without (b) heat conduction.	54
2.20	Temperature contours during the crack propagation regime: simulations with (a) and without (b) heat conduction.	54
2.21	Evolutions of temperature in a point situated at a distance of $0.6 mm$ from the initial notch tip.	55
2.22	Crack-tip velocity during propagation: (a) experimental results [17] vs (b) numerical results	55
2.23	Crack length evolution with time: (a) experimental results [17] vs (b) numerical results.	55
2.24	Temperature evolution with time : (a) experimental results [17] vs (b) numerical results.	56
3.1	a) Micro-fissured medium with locally periodic microstructure with l_c the size of a period, l the local micro-crack length and L_c the characteristic length of the macro-structure. b) Reference cell of size L_c with rescaled crack length $d.L_c$	62
3.2	Scaling of the microscopic period of the material to the reference cell.	63
3.3	The function $g_2(v)$ and its approximations $g_2^\alpha(v)$ for $\alpha = 1$ and $\alpha = 0.9$	66
3.4	Effective moduli $C_{1222}(d)$ and $C_{1212}(d)$ for three values of the friction coefficient: $\mu_f = 0$, $\mu_f = 0.25$ and $\mu_f = 0.5$	68
3.5	I_{2222} vs d for three values of the friction coefficient: $\mu_f = 0$, $\mu_f = 0.25$ and $\mu_f = 0.5$	69
3.6	Stress $-\Sigma_{12}$ and damage d vs strain $-e_{x12}$ for three values of the friction coefficient: $\mu_f = 0$, $\mu_f = 0.25$ and $\mu_f = 0.5$	70
3.7	Stress $-\Sigma_{12}$ and damage d responses for three values of the compressive strain.	70
3.8	Stress $-\Sigma_{12}$ and damage d response for three values of the strain rate: $\dot{e}_{x12} = -100 /s$, $\dot{e}_{x12} = -1000 /s$, $\dot{e}_{x12} = -10000 /s$	71

3.9	Stress $-\Sigma_{12}$ and damage d vs strain $-e_{x12}$ for micro-structural lengths: $l_c = 5 \times 10^{-3} m$, $l_c = 5 \times 10^{-4} m$ and $l_c = 5 \times 10^{-5} m$	71
3.10	Stress $-\Sigma_{12}$ and damage d vs strain $-e_{x12}$, for constant and crack-velocity dependent fracture energy.	72
3.11	Geometry of the specimen and applied loadings: a) impact, b) impact and normal compression.	72
3.12	Details of the mesh used in the FE simulations.	73
3.13	Damage band propagation inside the groove.	74
3.14	Lines of constant shear stress Σ_{12} at: a) $40 \mu s$ and b) $60 \mu s$. The absolute values of Σ_{12} are increasing when approaching the tip of the damage band.	74
3.15	Variation of the crack-tip position with time for constant values of \mathcal{G}_c	75
3.16	Crack-tip position vs time for different values of a and variable fracture energy $\mathcal{G}_c = 2100 \times (1 + a.v)$	76
3.17	Crack-tip position vs time for $\mathcal{G}_c = 2100 \times (1 + 0.0075.v)$	76
3.18	Crack-tip position vs time for $\mu_f = 0$ and $\mu_f = 0.5$	77
3.19	Crack-tip position vs time for different values of the applied normal displacement u_c at the top of the specimen.	78
4.1	a) Solid body with locally periodic microstructure with l_c the size of a period, l the micro-crack length and L_c the characteristic length of the macro-structure. b) Reference cell of size L_c with rescaled crack length $d.L_c$	82
4.2	Scaling of the microscopic period B_ϵ with a crack C into the reference cell Y with the crack CY . The unit vectors \mathbf{n} and \mathbf{e} indicate the normal to the crack-tip contours Γ_r and ΓY_r and, respectively, the propagation direction.	84
4.3	Effective elastic coefficients C_{1212} (a) and C_{1222} (b) vs damage variable d computed for the friction coefficients $\mu_f = 0, 0.25, 0.5$	94
4.4	Homogenized coefficients I_{1212} (a), $I_{1222} + I_{2212}$ (b) and I_{2222} (c) vs damage variable d , for $\mu_f = 0, 0.25, 0.5$	95
4.5	Coefficients \mathcal{Z}_{1212}^1 (a), \mathcal{Z}_{2212}^1 (b) vs damage variable d , for $\mu_f = 0, 0.25, 0.5$	96
4.6	Components I_{1212}^2 (a), $I_{1222}^2 + I_{2212}^2$ (b), I_{2222}^2 (c) of I_{mnpq}^2 vs damage variable d , for $\mu_f = 0, 0.25, 0.5$	96
4.7	Effective stress Σ_{12} , damage variable d and temperature variation ΔT vs. the strain e_{x12} , for different values of the microstructural length: $l_c = 5 \times 10^{-5} m$, $l_c = 5 \times 10^{-4} m$, $l_c = 5 \times 10^{-3} m$	98
4.8	Effective stress Σ_{12} , damage variable d and temperature variation ΔT vs. the strain e_{x12} , for different values of strain rate: $\dot{e}_{x12} = -100 s^{-1}$, $\dot{e}_{x12} = -1000 s^{-1}$, $\dot{e}_{x12} = -10000 s^{-1}$	99
4.9	Effective stress Σ_{12} , damage variable d and temperature variation ΔT vs. the strain e_{x12} , for initial values of damage $d_0 = 0.05$, $d_0 = 0.25$, $d_0 = 0.5$	99
4.10	Effective stress Σ_{12} , damage variable d and temperature variation ΔT vs. the strain e_{x12} , for different compressive strains: $e_{x22} = -5 \times 10^{-3}$, $e_{x22} = -2 \times 10^{-2}$, $e_{x22} = -3.5 \times 10^{-2}$	100
4.11	Effective stress Σ_{12} , damage variable d and temperature variation ΔT for different values of the friction coefficient μ_f	101

4.12	Temperature variations for different expressions of the heat source \mathcal{R} in the temperature equation (4.94), with \mathcal{R}_d and \mathcal{R}_f respectively the damage and frictional heating terms. Results are presented for a) $d_0 = 0.3$, b) $d_0 = 0.5$ and c) $d_0 = 0.7$	101
4.13	Geometry of the specimen and loading for mode II impact test.	103
4.14	Details of the mesh used in the FE computations.	103
4.15	Damage band in the groove at $70 \mu s$	104
4.16	Temperature variation induced by damage at $20 mm$ of the initial notch tip.	104
4.17	Temperature variation: measured values (a) from [19] and (b) computed values in 3 neighbor elements located in the region of IR detectors.	105
B.1	Displacements \mathbf{v}^{11} (a), \mathbf{v}^{12} (b) and \mathbf{v}^{22} (c) obtained from FE unit cell computations.	112
C.1	Components $\bar{\phi}_1$ and $\bar{\phi}_2$ of the solution $\bar{\phi}$ computed with FEM	117
1	Géométrie de l'échantillon, avec des dimensions in mm . La vitesse d'impact V est appliquée sur une zone de $16.5 mm$	138
2	Variation de température à $1 mm$ de la pointe de l'entaille initiale: valeurs expérimentales (gauche) [115] et calculées (droite) dans 4 éléments voisins dans la région du thermocouple.	139
3	Echantillon avec rainure sous sollicitation d'impact non-symétrique et détecteurs IR pour mesure de température [17, 19].	140
4	Bande d'endommagement à l'intérieur de la rainure.	141
5	Position de la pointe de fissure en fonction du temps : valeurs expérimentales [109] et numériques.	141
6	Variation de la température dans la région des détecteurs IR : (a) valeurs mesurées [19] et (b) valeurs numériques dans 3 éléments voisins correspondant aux trois détecteurs les plus proches de la fissure.	142

List of Tables

3.1	Parameters used in the simulations of the asymmetric impact test.	73
4.1	Generic material parameters for PMMA used in the local macroscopic analysis.	94
4.2	Normal strain, shear strain rate, internal length and initial damage and temperature used in the study of the macroscopic response.	97
4.3	Material parameters used in the FEM simulations.	102

General introduction

Brittle materials (polymers, rocks, ceramics...) are widely used for many engineering applications. Due to its excellent optical properties and lightweight, a glassy polymer like Polymethylmethacrylate (PMMA) is highly employed in aerospace industry, like aircraft windows, helicopter cockpits, ... Depending on the different applications, these industrial components can be subjected to dynamic impact loadings leading to their failure. Prediction of the failure of solids made of brittle materials is therefore crucial for the efficient design of structures. For this purpose, experimental methods and predictions using numerical tools need to be used. Efficient numerical prediction of the failure of brittle materials under dynamic loadings requires accounting of microstructural aspects and multi-physical couplings.

The first theories of fracture mechanics were developed by considering fracture mechanism as an isothermal process independent of the effects of thermomechanical coupling [68], [75]. Nevertheless, research investigations published in [25], [18], [19], [115], [116], [62], [135], [123], [138] showed the necessity to account for thermal effects in dynamic failure of materials. Fracture energy is dissipated to heat during dynamic crack propagation while temperature variation can influence the strength of the material. Brittle materials may contain heterogeneities such as microcracks, porosities, grains... Microcracks evolution is a typical damage mechanism of brittle materials [36], [111]. This process occurring at the level of the microstructure induces changes at the macroscopic level such as degradation of material properties and initiation of fracture.

Appropriate scales of modeling may depend on the technologies available for observations and measurements of physical phenomena. Considerable progress has been made in the last period in the field of material sciences using methods to study physical phenomena by taking into account different scales of observation. As the failure of materials is generally a multi-scale phenomenon, it is therefore appropriate to use modeling at multiple scales. The models developed in this thesis will take into account the microscopic scale of microcracks and the macroscopic scale of solid structures.

Over the last decades, several investigations have been made in order to model material damage. Models based on the propagation of microcracks have been proposed. These include, among many others, contributions like: [97], [100], [113], [73], [72], [86], [87], [16], [101], [43], [106], [107]. One of the proposed multi-scale failure modeling techniques is that developed in [37], [39], [47], [61], [140] in which damage evolution laws are obtained from the microscopic description of microcrack evolution using the asymptotic homogenization method. This procedure has been used in the case of rapid propagation of micro-cracks in mode I in [82], [41]. The dynamic damage model obtained by this method

is derived completely from the evolving microstructure without additional assumptions at the macroscopic scale and shows dependency on the size of the microstructure.

In this thesis, we extend the previous two-scale damage model in order to account for thermo-mechanical couplings during failure of brittle materials. First we develop a new homogenized thermomechanical damage model from microstructures with dynamically propagating microcracks in mode I assuming crack-tip heating. Then, we use a similar procedure to obtain a dynamic damage model in case of mode II microcracks propagation with frictional contact. Finally, we develop the model in the framework of dynamic thermo-elasticity, by assuming both crack-tip and crack lips sources of heat dissipated during propagation and, respectively, frictional sliding of shear microcracks. A fully coupled thermoelastic dynamic shear damage model is obtained in this way. The constructed damage laws are implemented in a Finite Elements code and numerical simulations are performed in order to predict the macroscopic behaviour of structures during rapid failure.

The manuscript is organized into four main chapters. In the first chapter, we give some preliminary notions and literature review on dynamic fracture and damage models, thermo-mechanical couplings and the asymptotic homogenization technique. It essentially introduces basic elements necessary for the developments in other parts of the manuscript.

In the second chapter, the development of the two-scale thermomechanical dynamic damage model for mode I propagation is given. We perform first the homogenization analysis based on asymptotic developments to obtain the effective behavior of microcracked thermoelastic solid. After this the thermomechanical damage law is obtained by an energetic approach combined with the homogenization method, with special emphasis on heat dissipation at propagating tips of microcracks. We then conduct a parametric study of the local response predicted by the new damage model while highlighting the effects of microstructural size and heat dissipation. Using this model, we reproduce numerically the experimental results of Rittel [115] concerning the impact test of PMMA samples. We finish the second chapter with verification of the assumptions of adiabatic heating made for rapid failure problem, by comparison with the full heat conduction solutions.

The third chapter presents a dynamic shear damage model with frictional contact. The model is obtained using similar procedure as in the the second chapter without considerations of the thermomechanical coupling. Among the boundary conditions, unilateral contact with friction is assumed on crack faces. In this particular case of mode II damage evolution, specific methods of resolution presented in the Appendix B are used for the computation of the effective coefficients. An energetic approach giving the energy dissipation due to friction is used to obtain the damage law. A study of the local macroscopic response predicted by the model is carried out with highlights on the influence of the strain rate, the initial damage, the size of the microstructure and the friction coefficient on the evolution of the damage. Macroscopic simulations have been carried out with the objective to reproduce numerically the experimental results of Ravi-Chandar et al. [109] on shear failure under impact loadings.

The last chapter concerns the formulation of the dynamic shear damage model with thermo-mechanical coupling. In addition to the unilateral contact conditions and the crack-tip heating, it is assumed that friction sliding between microcracks lips generates heat. As in the case of opening microcracks, homogenization leads to macroscopic temperature equations containing volumetric heat sources representing the microscopic dissipa-

tions. The obtained damage model account for microstructural size effects and strain-rate sensitivity. The analysis of the local macroscopic response with emphasis on the effects of the friction coefficient, the microstructural size, the shear and compression loadings is presented.

Chapter 1

Background and literature review

Contents

1.1	Introduction	5
1.2	Dynamic fracture mechanics	6
1.2.1	Asymptotic analysis and fields singularity	7
1.2.2	Dynamic stress intensity factors	9
1.2.3	Dynamic energy release rate	10
1.2.4	Thermoelastic dynamic fracture	12
1.3	Damage mechanics	16
1.3.1	Effective stress	16
1.3.2	Damage evolution laws	17
1.3.3	Thermodynamics of damage	19
1.4	Asymptotic homogenization	20
1.5	Thermal effects in dynamic failure experiments	22

1.1 Introduction

The phenomenon of damage is a process of progressive deterioration that can lead to the failure of a material. It is caused by the presence of surface discontinuities in the form of cavities, microcracks... These defects are often invisible since they only exist in the microstructure. For efficient damage modeling the concepts of Damage mechanics but also Homogenization theories are necessary. Indeed, the homogenization procedures allow us to obtain a homogeneous equivalent material with properties depending on the physical details of the microstructure. Thus for a microcracked material, for example, a homogeneous medium without cracks is obtained by homogenization which properties take into account the presence of microcracks in the material. Damage mechanics makes possible the modeling of the evolution of multiple pre-existing small defects at a macroscopic level. The state of damage is represented by a damage variable which will evolve in time up to a

threshold. The material failure is defined by this threshold value. The fracture mechanics concepts provide useful information about the propagation of cracks which size is not very small as compared with that of the whole structure. For the accurate modeling of failure, the concepts of fracture and damage mechanics can be incorporated in a multi-scale scheme in which their link is assured by the homogenization procedure.

This chapter introduces the basic concepts damage and fracture mechanics, in framework of dynamics and thermo-mechanical couplings, as well as the asymptotic homogenization procedure. These formulations will be used in the next chapters for the construction of multi-scale models damage.

1.2 Dynamic fracture mechanics

Three modes are usually distinguished in crack propagation. The Mode I or the opening mode (Figure 1.1.a) is achieved with tensile loading in the x_2 direction, while shear loading leading to displacements of cracks faces along the x_1 -axis is called the in-plane shear or Mode II propagation (Figure 1.1.b). The Mode III is obtained by applying an out-of-plane loading provoking displacements along the x_3 -axis as in Figure 1.1.c. We will not consider the Mode III in the present document.

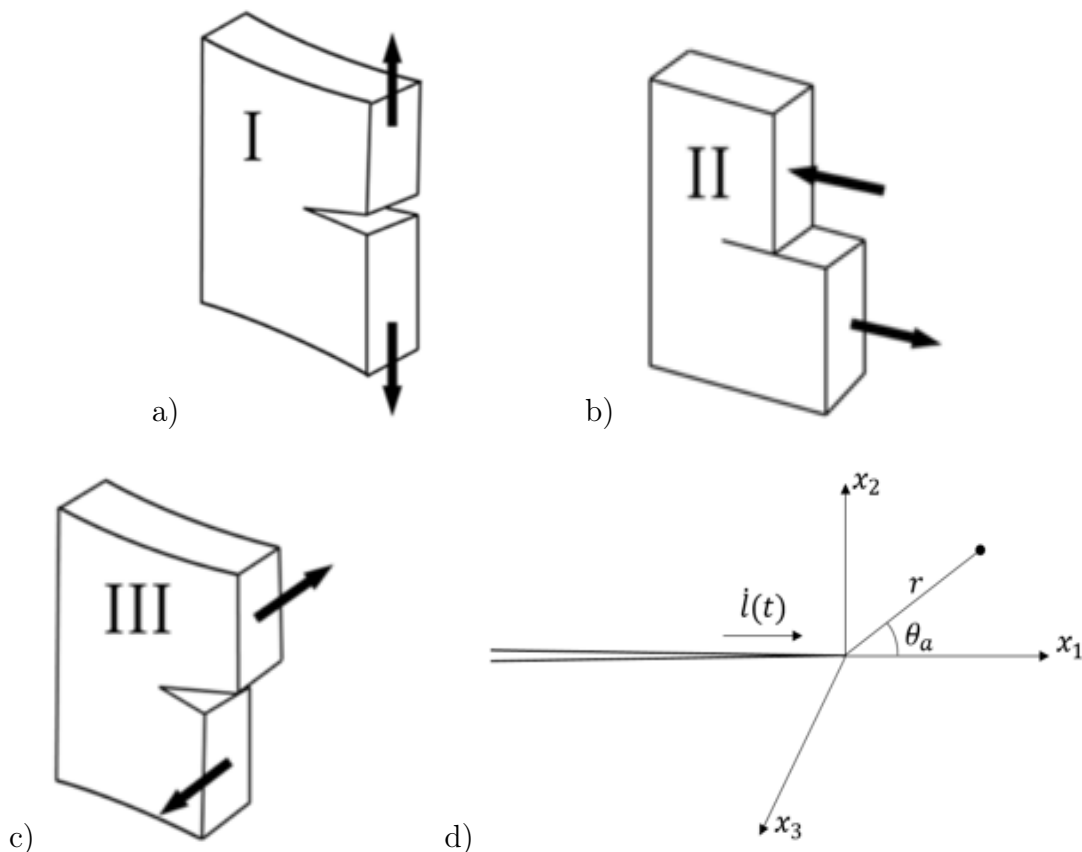


Figure 1.1: Three modes of crack propagation

Fracture mechanics problems are often investigated by assuming simple cases of two-

dimensional problems where either a 2-D plane stress or plane strain state is considered. We consider an isotropic elastic solid and denote by E and ν the Young's modulus and the Poisson's ratio, respectively.

$$e_{ij} = \frac{1+\nu}{E}\sigma_{ij} - \frac{\nu}{E}\sigma_{kk}\delta_{ij} \quad (1.1)$$

- In a case of plane stress state in $x_1 - x_2$, we have:

$$\sigma_{ij} = \begin{pmatrix} \sigma_{11} & \sigma_{12} & 0 \\ \sigma_{12} & \sigma_{22} & 0 \\ 0 & 0 & 0 \end{pmatrix} \quad \text{and} \quad e_{ij} = \begin{pmatrix} e_{11} & e_{12} & 0 \\ e_{12} & e_{22} & 0 \\ 0 & 0 & e_{33} \end{pmatrix} \quad (1.2)$$

Using Equation (1.1) we can easily write the components of e_{ij} as follows:

$$\begin{aligned} e_{11} &= \frac{1+\nu}{E}\sigma_{11} - \frac{\nu}{E}(\sigma_{11} + \sigma_{22}) \\ e_{22} &= \frac{1+\nu}{E}\sigma_{22} - \frac{\nu}{E}(\sigma_{11} + \sigma_{22}) \\ e_{33} &= -\frac{\nu}{E}(\sigma_{11} + \sigma_{22}) \\ e_{12} &= \frac{1+\nu}{E}\sigma_{12} \end{aligned}$$

- For a plane strain state in $x_1 - x_2$, we have:

$$\sigma_{ij} = \begin{pmatrix} \sigma_{11} & \sigma_{12} & 0 \\ \sigma_{12} & \sigma_{22} & 0 \\ 0 & 0 & \sigma_{33} \end{pmatrix} \quad \text{and} \quad e_{ij} = \begin{pmatrix} e_{11} & e_{12} & 0 \\ e_{12} & e_{22} & 0 \\ 0 & 0 & 0 \end{pmatrix} \quad (1.3)$$

where the components of e_{ij} are:

$$\begin{aligned} e_{11} &= \frac{1+\nu}{E}\sigma_{11} - \frac{\nu}{E}(\sigma_{11} + \sigma_{22} + \sigma_{33}) \\ e_{22} &= \frac{1+\nu}{E}\sigma_{22} - \frac{\nu}{E}(\sigma_{11} + \sigma_{22} + \sigma_{33}) \\ e_{12} &= \frac{1+\nu}{E}\sigma_{12} \end{aligned}$$

1.2.1 Asymptotic analysis and fields singularity

Consider a two-dimensional solid containing a straight crack of length l and a polar coordinate system $(r; \theta^a)$ at the crack-tip as depicted on Figure 1.1.d, $\theta^a = 0$ corresponds to the crack propagation direction. We suppose dynamic propagation of the crack with the speed $\dot{l}(t)$ and stress free conditions on crack faces. The momentum balance equation of the solid is written as:

$$\frac{\partial \sigma_{ij}}{\partial x_j} = \rho \frac{\partial^2 u_i}{\partial t^2} \quad (1.4)$$

where u_i denote the displacement fields. In a framework of isothermal behaviour the stress field is $\sigma_{ij} = \lambda e_{kk} \delta_{ij} + 2\mu e_{ij}$ with λ and μ the Lamé's coefficients: $\lambda = \frac{E\nu}{(1+\nu)(1-2\nu)}$; $\mu = \frac{E}{2(1+\nu)}$ with the strain tensor : $e_{ij} = \frac{1}{2} \left(\frac{\partial u_i}{\partial x_j} + \frac{\partial u_j}{\partial x_i} \right)$. For this elasto-dynamic fracture problem, the stress and displacement fields in the vicinity of the crack-tip depends on the propagation speed (Freund [59]).

In the polar coordinates system with the crack-tip as origin we have the relation: $re^{i\theta^a} = x_1 + ix_2$. We introduce the modified polar coordinates $(r_d; \theta_d^a)$, $(r_s; \theta_s^a)$ as:

$$r_d e^{i\theta_d^a} = x_1 + i\alpha_d x_2 \quad (1.5)$$

$$r_s e^{i\theta_s^a} = x_1 + i\alpha_s x_2 \quad (1.6)$$

where α_d and α_s are velocity dependent parameters defined as:

$$\alpha_d = \sqrt{1 - \left(\frac{\dot{l}}{c_d}\right)^2} \quad ; \quad \alpha_s = \sqrt{1 - \left(\frac{\dot{l}}{c_s}\right)^2}$$

with c_d and c_s the dilatational and shear wave velocities

$$c_d = \sqrt{\frac{E(1-\nu)}{\rho(1+\nu)(1-2\nu)}} \quad ; \quad c_s = \sqrt{\frac{E}{2\rho(1+\nu)}}$$

The asymptotic stress field near the tip of an opening crack are:

$$\begin{aligned} \sigma_{11} &= \frac{K_I}{D\sqrt{2\pi}} \left((1 + \alpha_s^2)(1 + 2\alpha_d^2 - \alpha_s^2) \frac{\cos \frac{\theta_d^a}{2}}{\sqrt{r_d}} - 4\alpha_d \alpha_s \frac{\cos \frac{\theta_s^a}{2}}{\sqrt{r_s}} \right) \\ \sigma_{22} &= -\frac{K_I}{D\sqrt{2\pi}} \left((1 + \alpha_s^2)^2 \frac{\cos \frac{\theta_d^a}{2}}{\sqrt{r_d}} - 4\alpha_d \alpha_s \frac{\cos \frac{\theta_s^a}{2}}{\sqrt{r_s}} \right) \\ \sigma_{12} &= \frac{2K_I \alpha_d (1 + \alpha_s^2)}{D\sqrt{2\pi}} \left(\frac{\sin \frac{\theta_d^a}{2}}{\sqrt{r_d}} - \frac{\sin \frac{\theta_s^a}{2}}{\sqrt{r_s}} \right) \end{aligned} \quad (1.7)$$

The corresponding displacement field is:

$$\begin{aligned} u_1 &= \frac{2K_I}{\mu D\sqrt{2\pi}} \left((1 + \alpha_s^2) \sqrt{r_d} \cos \frac{\theta_d^a}{2} - 2\alpha_d \alpha_s \sqrt{r_s} \cos \frac{\theta_s^a}{2} \right) \\ u_2 &= \frac{2K_I}{\mu D\sqrt{2\pi}} \left(2\alpha_d \sqrt{r_s} \sin \frac{\theta_s^a}{2} - \alpha_d (1 + \alpha_s^2) \sqrt{r_d} \sin \frac{\theta_d^a}{2} \right) \end{aligned} \quad (1.8)$$

where K_I is the mode I dynamic stress intensity factor, with D depending on α_d and α_s : $D = 4\alpha_d \alpha_s - (1 + \alpha_s)^2$.

Similarly, the asymptotic stress and displacement fields in mode II are obtained as functions of the stress intensity factor K_{II} as:

$$\begin{aligned}\sigma_{11} &= -\frac{K_{II}}{D\sqrt{2\pi}} \left(2\alpha_s(1 + 2\alpha_d^2 - \alpha_s^2) \frac{\sin \frac{\theta_d^a}{2}}{\sqrt{r_d}} - (1 + \alpha_s^2) \frac{\sin \frac{\theta_s^a}{2}}{\sqrt{r_s}} \right) \\ \sigma_{22} &= \frac{2K_{II}\alpha_s(1 + \alpha_s^2)}{D\sqrt{2\pi}} \left(\frac{\sin \frac{\theta_d^a}{2}}{\sqrt{r_d}} - \frac{\sin \frac{\theta_s^a}{2}}{\sqrt{r_s}} \right)\end{aligned}\quad (1.9)$$

$$\begin{aligned}\sigma_{12} &= \frac{K_{II}}{D\sqrt{2\pi}} \left(4\alpha_d\alpha_s \frac{\cos \frac{\theta_d^a}{2}}{\sqrt{r_d}} - (1 + \alpha_s^2) \frac{\cos \frac{\theta_s^a}{2}}{\sqrt{r_s}} \right) \\ u_1 &= \frac{2K_{II}}{\mu D\sqrt{2\pi}} \left(2\alpha_s^2\sqrt{r_d} \sin \frac{\theta_d^a}{2} - \alpha_s(\alpha_s^2 + 1)\sqrt{r_s} \sin \frac{\theta_s^a}{2} \right) \\ u_2 &= \frac{2K_{II}}{\mu D\sqrt{2\pi}} \left(2\alpha_d\alpha_s\sqrt{r_d} \sin \frac{\theta_d^a}{2} - (1 + \alpha_s^2)\sqrt{r_s} \cos \frac{\theta_s^a}{2} \right)\end{aligned}\quad (1.10)$$

Remark the $r^{-1/2}$ singularity of the stresses and the $r^{1/2}$ dominant terms of the displacements near the crack tip.

1.2.2 Dynamic stress intensity factors

Dynamic and quasi-static stress intensity factors are linked [59]. If we denote by K_p^s ($p = I, II$ corresponding to the fracture mode) the instantaneous quasi-static stress intensity factor, the expression of the dynamic stress intensity factor is:

$$K_p = k_p(\dot{l})K_p^s \quad (1.11)$$

The dynamic effects in K_I and K_{II} are given correspondingly by the universal functions k_I and k_{II} depending on the crack propagation speed and the material's elastic properties through the waves velocities. For the Mode I, the expression of k_I is [59]:

$$k_I(\dot{l}) \simeq \frac{1 - \frac{\dot{l}}{C_R}}{\sqrt{1 - \frac{\dot{l}}{c_d}}} \quad (1.12)$$

with the Rayleigh wave speed $C_R \simeq \frac{0.862 + 1.14\nu}{1 + \nu}c_s$. As represented on Figure 1.2, k_I is a decreasing function of the crack-tip speed. It is easy to notice that $k_I = 1$ when $\dot{l} = 0$ showing that K_I corresponds to K_I^s for a stationary crack. The function k_I vanishes when $\frac{\dot{l}}{C_R} = 1$, the speed of a growing crack in mode I can not exceed the Rayleigh wave speed.

The universal function $k_{II}(\dot{l})$ corresponding to mode II is:

$$k_{II}(\dot{l}) \simeq \frac{1 - \frac{\dot{l}}{C_R}}{\sqrt{1 - \frac{\dot{l}}{c_s}}} \quad (1.13)$$

Similarly to k_I , k_{II} also decreases from 1 to 0 for values of the crack-tip speed \dot{l} running from 0 to c_R .

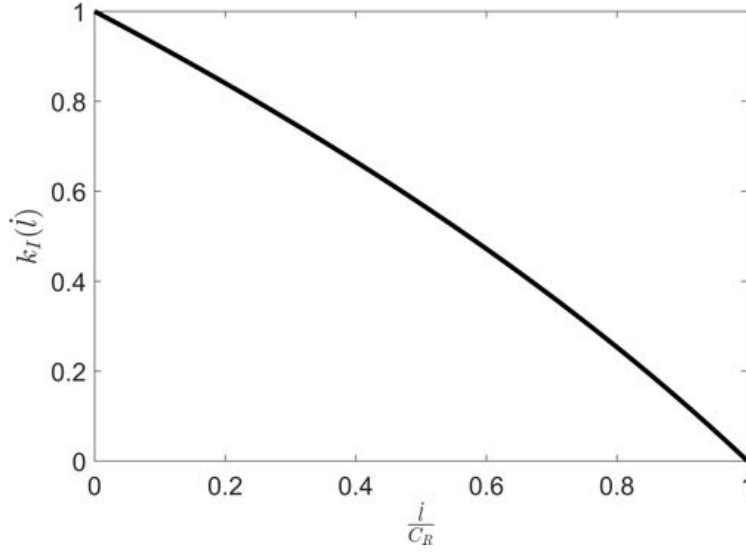


Figure 1.2: Universal function $k_I(i)$

1.2.3 Dynamic energy release rate

We consider an elastic solid Ω containing a crack of length $l(t)$. Assuming that the crack faces are free of stresses, the energy balance during the dynamic propagation can be written as [59, 112]:

$$\frac{d}{dt} \int_{\Omega} \left(e + \frac{1}{2} \rho \frac{\partial u_i}{\partial t} \frac{\partial u_i}{\partial t} \right) d\Omega + \mathcal{G}^d j - \int_{\partial\Omega} \sigma_{ij} n_j \frac{\partial u_i}{\partial t} ds = 0 \quad (1.14)$$

where \mathcal{G}^d is the dynamic energy release rate calculated as the limit at the crack tip:

$$\mathcal{G}^d = \lim_{r \rightarrow 0} \int_{\Gamma_r} \left(\left(e + \frac{1}{2} \rho \frac{\partial u_i}{\partial t} \frac{\partial u_i}{\partial t} \right) n_1 + \sigma_{ij} n_j \frac{\partial u_i}{\partial t} \right) ds \quad (1.15)$$

with Γ_r a closed circular contour surrounding and moving with the crack tip and with \mathbf{n} the external normal unit vector, as shown in Figure 1.3.

The internal energy e is defined as:

$$e = \frac{1}{2} \lambda e_{ii} e_{jj} + 2\mu e_{ij} e_{ij} \quad (1.16)$$

Following [59, 112, 129], the use of the asymptotic fields in the previous expression gives the dynamic energy release rate as a function of the stress intensity factors K_I , K_{II} :

$$\mathcal{G}^d = \frac{1}{E'} \left(A_I(i) K_I^2 + A_{II}(i) K_{II}^2 \right) \quad (1.17)$$

with $E' = E$ in plane stress and $E' = \frac{E}{1-\nu^2}$ in plane strain. Here A_I and A_{II} are universal functions depending on the crack-tip and material properties:

$$A_I(i) = \frac{i^2 \alpha_d}{(1-\nu) c_s^2 D} \quad ; \quad A_{II}(i) = \frac{i^2 \alpha_s}{(1-\nu) c_s^2 D} \quad (1.18)$$

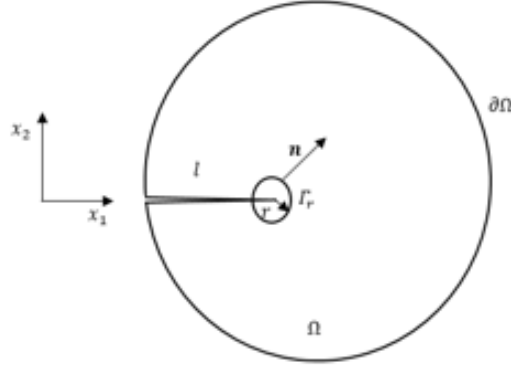


Figure 1.3: Solid with a moving crack

If we denote by \mathcal{G}_I , \mathcal{G}_{II} the quasi-static energy release rate corresponding to mode I, II and introduce the functions g_I and g_{II} [59], [112], [129]:

$$g_I(\dot{l}) = k_I^2(\dot{l})A_I(\dot{l}) \quad ; \quad g_{II}(\dot{l}) = k_{II}^2(\dot{l})A_{II}(\dot{l}) \quad (1.19)$$

we obtain the dynamic energy release rate:

$$\mathcal{G}^d = g_I(\dot{l})\mathcal{G}_I + g_{II}(\dot{l})\mathcal{G}_{II} \quad (1.20)$$

In this expression, the quasi-static energy-release rates are:

$$\mathcal{G}_I = \frac{(K_I^s)^2}{E'} \quad ; \quad \mathcal{G}_{II} = \frac{(K_{II}^s)^2}{E'} \quad (1.21)$$

The functions g_I and g_{II} are decreasing with the crack propagation speed as illustrated on Figure 1.4. For a stationary crack or slow propagation ($\frac{\dot{l}}{C_R} \rightarrow 0$) the universal functions g_I and g_{II} are equal to 1 and we retrieve the quasi-static fracture energy. Remark that $g_I(\dot{l})$ can be approximated by $g_I \simeq 1 - \frac{\dot{l}}{C_R}$ [59].

Fracture criterion

Following the energy approach of Griffith [68], a crack starts to propagate as soon as the energy dissipated at the tip \mathcal{G}^d becomes equal with a critical energy \mathcal{G}_c , necessary for breaking the bonds of the specific constitutive material of the solid. This criterion can be expressed in mathematical form by the conditions:

$$\mathcal{G}^d \leq \mathcal{G}_c, \quad \dot{l}(t) \geq 0, \quad \dot{l}(\mathcal{G}^d - \mathcal{G}_c) = 0 \quad (1.22)$$

When the value of energy available for the fracture is less than \mathcal{G}_c the crack does not propagate and remains stationary. The length of the crack $l(t)$ can only increase, without healing.

Similar criteria can be defined using the stress intensity factor of the material which are related to the stress field at the crack-tip and depend on the applied loadings. Therefore a threshold value of the intensity factor K_c called fracture toughness is defined. Crack propagation is not achieved for values of stress intensity factors $K < K_c$, but for $K = K_c$. \mathcal{G}_c and K_c are material properties that can be determined experimentally.

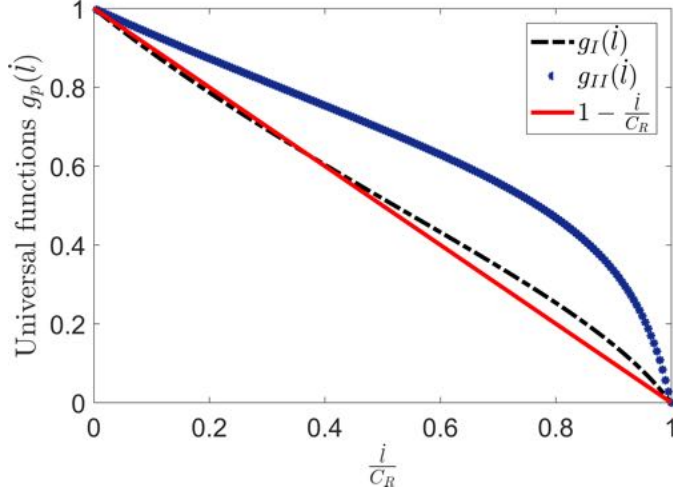


Figure 1.4: Universal functions $g_I(\dot{l})$ and $g_{II}(\dot{l})$.

1.2.4 Thermoelastic dynamic fracture

Let us consider a thermoelastic body with a crack and denote by \mathbf{u} and T the displacement and temperature fields. The length of the evolving crack is $l(t)$. The two principles of thermodynamics allow us to write:

$$\begin{aligned} \dot{e} + \dot{E}_{kin} &= P_{ex} + P_{cr} \\ \dot{S} + \int_{\partial\Omega} \frac{q_j n_j}{T} ds &\geq 0 \end{aligned} \quad (1.23)$$

where e , E_{kin} , P_{ex} , P_{cr} , S , q_j denote correspondingly the internal energy, kinetic energy, power of external forces, received heating, entropy and heat flux.

We consider a thermally isolated system and stress free conditions are assumed on the crack faces. The presence of the crack introduces a singularity of the thermomechanical fields at the tip. This singularity will play an essential role in the thermomechanical modeling of dynamic fracture process. The energy balance can be written as :

$$\int_{\Omega_r} \frac{d}{dt} \left(e + \frac{1}{2} \rho \frac{\partial u_i}{\partial t} \frac{\partial u_i}{\partial t} \right) d\Omega - \int_{\partial\Omega_r} \left(\sigma_{ij} \frac{\partial u_i}{\partial t} - q_j \right) n_j ds = 0 \quad (1.24)$$

$$(1.25)$$

on the domain Ω_r which is defined such that $\lim_{r \rightarrow 0} \Omega_r = \Omega$, as in Figure 1.3.

As for the purely mechanical analysis, we define around the crack tip a closed contour Γ_r moving with it. For integrals on such moving domains a the transport theorem [137] can be used to permute the time derivative with the integral sign:

$$\int_{\Omega_r} \frac{d}{dt} \left(e + \frac{1}{2} \rho \frac{\partial u_i}{\partial t} \frac{\partial u_i}{\partial t} \right) d\Omega = \frac{d}{dt} \int_{\Omega_r} \left(e + \frac{1}{2} \rho \frac{\partial u_i}{\partial t} \frac{\partial u_i}{\partial t} \right) d\Omega + \int_{\Gamma_r} \left(e + \frac{1}{2} \rho \frac{\partial u_i}{\partial t} \frac{\partial u_i}{\partial t} \right) \dot{l} n_1 d\mathbf{a} \quad (1.26)$$

Using an integration by parts of the second integral, we obtain the energy balance in the form:

$$\begin{aligned} \frac{d}{dt} \int_{\Omega_r} \left(e + \frac{1}{2} \rho \frac{\partial u_i}{\partial t} \frac{\partial u_i}{\partial t} \right) d\Omega + \int_{\Gamma_r} \left(e + \frac{1}{2} \rho \frac{\partial u_i}{\partial t} \frac{\partial u_i}{\partial t} \right) l n_1 ds - \\ \int_{\partial\Omega} \left(\sigma_{ij} n_j \frac{\partial u_i}{\partial t} - q_j n_j \right) ds + \int_{\Gamma_r} \left(\sigma_{ij} n_j \frac{\partial u_i}{\partial t} - q_j n_j \right) ds = 0 \end{aligned} \quad (1.27)$$

And for $r \rightarrow 0$ we get:

$$\frac{d}{dt} \int_{\Omega} \left(e + \frac{1}{2} \rho \frac{\partial u_i}{\partial t} \frac{\partial u_i}{\partial t} \right) d\Omega + \mathcal{G}^d \dot{l} - \lim_{r \rightarrow 0} \int_{\Gamma_r} q_j n_j ds - \int_{\partial\Omega} \left(\sigma_{ij} n_j \frac{\partial u_i}{\partial t} - q_j n_j \right) ds = 0 \quad (1.28)$$

The internal energy e is defined as:

$$e = \frac{1}{2} \left(\lambda e_{ii} e_{jj} + 2\mu e_{ij} e_{ij} \right) + \alpha(3\lambda + 2\mu) T_0 e_{ij} \delta_{ij} + cT \quad (1.29)$$

and the dynamic energy release rate \mathcal{G}^d :

$$\mathcal{G}^d = \lim_{r \rightarrow 0} \int_{\Gamma_r} \left(\left(e + \frac{1}{2} \rho \frac{\partial u_i}{\partial t} \frac{\partial u_i}{\partial t} \right) n_1 + \sigma_{ij} n_j \frac{\partial u_i}{\partial t} \right) ds \quad (1.30)$$

Following [25, 26] we link the two terms defined at the the crack-tip by the relation

$$D = \lim_{r \rightarrow 0} \int_{\Gamma_r} q_j n_j ds = \mathcal{G}^d \dot{l} \quad (1.31)$$

This condition express the fact that the energy dissipated for fracture is converted into heat and acts like a heat source placed at the tip of the crack (Dirac-type distribution δ).

With this energetic condition, the thermo-mechanical equations are written as follows:

$$c \frac{\partial T}{\partial t} + \alpha(3\lambda + 2\mu) \frac{\partial}{\partial t} (e_{11} + e_{22}) + \frac{\partial q_j}{\partial x_j} = \mathcal{G}^d \dot{l} \delta(F) \quad (1.32)$$

$$\frac{\partial \sigma_{ij}}{\partial x_j} = \rho \frac{\partial^2 u_i}{\partial t^2} \quad (1.33)$$

In the dynamic momentum balance equation (1.33) σ_{ij} , ρ are correspondingly the stress tensor, mass density. The stress tensor σ_{ij} is defined as function of the strain tensor e_{ij} , the material's Lamé coefficients (λ , μ) and the thermal expansion coefficient α :

$$\sigma_{ij} = \lambda e_{kk} \delta_{ij} + 2\mu e_{ij} - \alpha(3\lambda + 2\mu)(T - T_0) \delta_{ij} \quad (1.34)$$

with T_0 the initial temperature. In the thermal equation (1.32), q_j and c are correspondingly the heat flux and the specific heat. The heat flux is given by the Fourier law:

$$q_j = -k \frac{\partial T}{\partial x_j} \quad (1.35)$$

with k the heat conduction coefficient.

$\mathcal{G}^{d\dot{l}}\delta(F)$ is the energy dissipated to heat at the crack-tip, denoted by F , during the fracture process ($\dot{l} \neq 0$). The formulated problem reveals double couplings between thermal and mechanical fields: the classical dynamic thermoelasticity coupling in any point of the solid, and the new thermomechanical coupling between the heat source in the temperature equation and the dynamic energy-release rate.

The asymptotic expressions of the thermomechanical fields at the crack tip, for this non-classical problem, have been obtained in [25, 26] for the displacement \mathbf{u} and the temperature T :

$$\begin{aligned}\mathbf{u} &\simeq \mathbf{u}^{(1)} + k\mathbf{u}^{(2)} \\ T &\simeq T^{(1)} + T^{(2)}\end{aligned}$$

where $\mathbf{u}^{(n)}$ et $T^{(n)}$ are functions of the form: $r^\beta (\text{Log} r)^{\beta_1} \dots (\text{Log}_m r)^{\beta_m} f(\theta, t)$, with $\beta, \beta_1, \dots, \beta_m$ real numbers and $\text{Log}_m r = \text{Log}(\text{Log}_{m-1} r)$ and $f(\theta, t)$ giving the angular variations over $]-\pi, \pi[$. The time derivative can be calculated according to the singularity transport as: $\dot{a} = -\dot{l}a_{,1} + \text{regular terms}$.

With appropriate boundary conditions on the crack faces and the condition $D \neq 0$, Bui et al. [25] found the first order asymptotic solution of the thermal field in the form:

$$T^{(1)} = -\frac{\mathcal{G}^{d\dot{l}}}{2\kappa\pi} \text{Log} r \quad (1.36)$$

To satisfy the condition $D \neq 0$, $T^{(1)}$ should have less dominant singularity than $e^{(1)}$; $\mathbf{u}^{(1)}$ verify the classical isothermal elastodynamic problem of Yoffé [144]:

$$\begin{aligned}(\lambda + \mu) \frac{\partial}{\partial x_1} (e_{11}^{(1)} + e_{22}^{(1)}) + \mu \left(\frac{\partial^2 u_1^{(1)}}{\partial x_1^2} + \frac{\partial^2 u_1^{(1)}}{\partial x_2^2} \right) - \rho \dot{l} \frac{\partial^2 u_1^{(1)}}{\partial x_1^2} &= 0 \\ (\lambda + \mu) \frac{\partial}{\partial x_2} (e_{11}^{(1)} + e_{22}^{(1)}) + \mu \left(\frac{\partial^2 u_2^{(1)}}{\partial x_1^2} + \frac{\partial^2 u_2^{(1)}}{\partial x_2^2} \right) - \rho \dot{l} \frac{\partial^2 u_2^{(1)}}{\partial x_1^2} &= 0\end{aligned}$$

The expression of $\mathbf{u}^{(1)}$ is similar to the one obtained in isothermal dynamic fracture.

At the order 2, the term $T^{(2)}$ is obtained solving the following equation:

$$k \left(\frac{\partial T^{(2)}}{\partial x_1^2} + \frac{\partial T^{(2)}}{\partial x_2^2} \right) + \alpha(3\lambda + 2\mu) T^{(1)} \dot{l} \frac{\partial}{\partial x_1} (e_{11}^{(1)} + e_{22}^{(1)}) = 0 \quad (1.37)$$

The solution $T^{(2)}$ is obtained with a constant $\bar{T}(t)$ in the form:

$$T^{(2)} = \bar{T}(t) + r^{1/2} \text{Log} r f(\theta, \dot{l}) \quad (1.38)$$

where $f(\theta, \dot{l})$ is a function depending on crack faces boundary conditions and mode of propagation ([25], [26], [131]).

It is known that this solution of \mathbf{u} gives a singularity $e_{ij} \sim r^{-1/2}$ to the strain at the crack tip. As the thermal field $T \sim \text{Log} r$ is less dominant than the strain in the vicinity of the crack-tip, the singularity of the thermoelastic stress is then: $\sigma_{ij} \sim r^{-1/2}$.

One-dimensional example [132]

Based on the theory of Bui et al. [25] [26], Soumahoro & Maigre [131] analysed the temperature field at the tip of a moving crack considering a one-dimensional problem and obtained limit value for the temperature. The thermomechanical fracture problem is solved for the double cantilever beam (DCB) depicted on Figure 1.5.

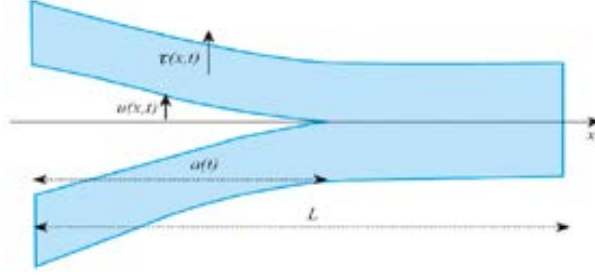


Figure 1.5: One dimensional thermoelastic fracture problem [132].

The mechanical and thermal equations are uncoupled in the absence of volume variation ($e_{ii} = 0$). The motion equation is written as:

$$\frac{\partial \tau}{\partial x} = \rho S \frac{\partial^2 u}{\partial t^2} u(x, t) \quad (1.39)$$

where τ denotes the shear effort given by the elastic constitutive law as function of the spatial derivative of the transverse displacement:

$$\tau(x, t) = \mu S \frac{\partial u}{\partial x}(x, t) \quad (1.40)$$

where μ is the shear modulus and S is the sectional area of the beam. As initial conditions the displacement $u(x, 0) = 0$ and the velocity $\dot{u}(x, 0) = 0$ while the initial length of the crack is $a(0) = a_0$. The boundary conditions are given with the applied force F at $x = 0$ such that $\tau(0, t) = -F(x, t)$ and the transverse displacement at the crack tip $u(a(t), t) = 0$.

The motion equation can be obtained as the wave equation:

$$\frac{\partial u}{\partial x^2} - \frac{1}{c^2} \frac{\partial^2 u}{\partial t^2} = 0 \quad (1.41)$$

where $c = \sqrt{\frac{\mu}{\rho}}$ is the wave velocity. The general solution of this wave equation has the form: $u(x, t) = f(x - ct) + g(x + ct)$.

The first principle of thermodynamics for this problem is written as:

$$\frac{d}{dt} \int_0^L \frac{1}{2} \frac{\tau^2}{\mu S} dx + \frac{d}{dt} \int_0^L \frac{1}{2} \rho S \dot{u}^2 dx + D = F(t) \cdot \dot{u}(x = 0, t) \quad (1.42)$$

From this the energy balance it can be proved that [131, 132]: $D = \frac{1}{2} \dot{a} \frac{\tau^2(a(t), t)}{\mu S} \left(1 - \frac{a^2}{c^2}\right)$.

This allows to obtain the energy-release rate in the form:

$$\mathcal{G}^d = \frac{1}{2} \frac{\tau^2(a(t), t)}{\mu S} \left(1 - \frac{a^2}{c^2}\right) \quad (1.43)$$

The positiveness of the energy-release rate imposes the limit value $\dot{a} \leq c$ for the crack tip speed.

The thermal equation corresponding to this problem is:

$$kS \frac{\partial^2 T}{\partial x^2} - C \frac{\partial T}{\partial t} = \mathcal{G}^d \delta(a(t)) \quad (1.44)$$

where C is the specific heat. The temperature field at the crack-tip field is ([32]):

$$T(x, t) = \int_0^t \frac{1}{2S \sqrt{\rho C k \pi (t - \zeta)}} e^{-\frac{\rho C (x - a(\zeta))^2}{4k(t - \zeta)}} \mathcal{G}^d \dot{a}(\zeta) d\zeta \quad (1.45)$$

The analysis his solution [132] shows that it is not singular at crack-tip and admits, for propagation at constant velocity and a constant value of $\mathcal{G}^d = \mathcal{G}_c$, a limit value:

$$T_{lim} = \frac{\mathcal{G}_c}{\rho C S} \quad (1.46)$$

which is reached in a time $t_{car} = \frac{0.91k}{\rho C \dot{a}^2}$. As expected, the limit temperature is proportional to the amount of energy dissipated at the crack tip.

1.3 Damage mechanics

Damage is a progressive deterioration leading to the failure of a material. It reflects the presence of defects (cracks, voids...) in the microstructure. Figure 1.6 shows a representative elementary volume, characteristic of the microstructure of a damaged solid. The state of deterioration is defined by a damage variable : $d = \frac{S_d}{S}$, with S_d the area of the defects and S the total surface of the element. Many theories (e.g., [78], [108]) represent the state of damage with a variable evolving with the propagation of microdefects. In this manuscript we will adopt this representation of damage and introduce a variable d that takes its values $0 \leq d \leq 1$. The case $d = 0$ corresponds to a material without defects, while $d = 1$ characterizes the complete failure of the representative element.

1.3.1 Effective stress

In order to characterize the loading effect on the resisting area of a damaged solid the effective stress concept (e.g., [108], [92]) is introduced. The stress obtained by applying a force F is $\sigma = \frac{F}{S}$ with S the area on which F is applied. When defects are present, the resisting area is $S - S_d$, with S_d the total surface of the defects. The effective stress is then introduced:

$$\sigma_{eff} = \frac{F}{S - S_d} \quad (1.47)$$

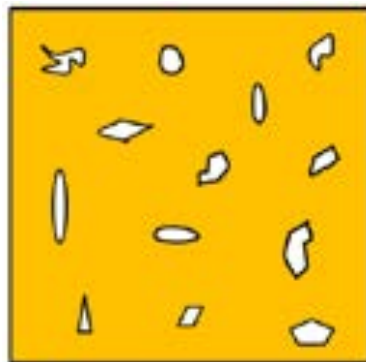


Figure 1.6: Damaged solid

As $\frac{S_d}{S}$ represents the damage variable, we can write the effective stress in the form:

$$\sigma_{eff} = \frac{\sigma}{1-d} \quad (1.48)$$

Since the thermo-elastic response is valid for the effective stress in the points of the resisting area, we obtain in the uniaxial case:

$$\sigma = (1-d)E(e_1 - \alpha\Delta T) \quad (1.49)$$

where e_1 is the uniaxial strain, α the thermal expansion coefficient and ΔT the variation of temperature. With $E^d = (1-d)E$ and $\beta^d = (1-d)E\alpha$, we have the stress in the form $\sigma = E^d - \beta^d\Delta T$. E^d represents the effective elastic modulus and β^d is the effective thermoelastic coefficient. When the value of the damage variable d is increasing, the material loses its strength since E^d decreases with d . In the same way, the thermoelastic coupling property is also affected by an increasing of d . The previous relations can be directly extended to three dimensions using the effective stress $\sigma_{ij}^{eff} = \frac{\sigma_{ij}}{1-d}$.

1.3.2 Damage evolution laws

The material response is affected by the damage variable. The formulation of a damage model requires an equation describing the way in which damage evolves: a damage evolution law. We present in the followings paragraphs two examples of damage laws proposed in [50], [51], [76], [77].

Damage model of Dubé, Pijaudier-Cabot and La Borderie

The loading rate effects on the response of concrete material like the increase of the strength and the decrease of the softening modulus with increasing strain rate can be predicted by the rate dependent damage model proposed by Dubé et al [50], [51].

With d the damage variable, the Gibbs free energy for a damaged material can be written as:

$$\rho\chi = \frac{1}{2} \frac{D_{ijkl}^0}{1-d} \sigma_{kl} \sigma_{ij} \quad (1.50)$$

where D_{ijkl}^0 is the compliance of the undamaged material defined as:

$$D_{ijkl}^0 = \frac{1 + \nu_0}{2E_0}(\delta_{ik}\delta_{jl} + \delta_{jk}\delta_{il}) - \frac{\nu_0}{E_0}\delta_{ij}\delta_{kl}$$

where E_0 and ν_0 are the Young's modulus and the Poisson's ratio of the undamaged material. With $\rho\chi$ defined as the state potential; the damage energy release rate Y and the strain e_{ij} defined as the state variables associated to damage and stress the following relations are obtained as:

$$Y = \rho \frac{\partial \chi}{\partial d} = \frac{1}{2} \frac{D_{ijkl}^0}{(1-d)^2} \sigma_{kl} \sigma_{ij} \quad (1.51)$$

$$e_{ij} = \rho \frac{\partial \chi}{\partial \sigma_{ij}} = \frac{1}{2} \frac{D_{ijkl}^0}{(1-d)} \sigma_{kl} \quad (1.52)$$

In order to obtain a damage evolution law a loading function f is introducing:

$$f(Y, Z) = Y - Y_0 - Z \quad (1.53)$$

where Y_0 is the damage threshold and Z is a variable controlling the hardening-softening. Similarly to the viscoplasticity model of Perzyna [104], the damage law obtained in [51] has the form:

$$\dot{d} = \dot{\lambda} \frac{\partial f}{\partial Y} \quad ; \quad \dot{\lambda} = \frac{1}{m} \left(\frac{\langle f(Y, Z) \rangle}{Y_0} \right)^n \quad (1.54)$$

where $m > 0$ and $n > 0$ are parameters to be identified by comparison with experimental data.

Gatuingt [63] proposed a modified expression of the model of Dubé et al [51] in the form:

$$\dot{d} = \left(\frac{\langle F_d(\bar{\epsilon}) \rangle}{m_d} \right)^{n_d} \quad (1.55)$$

where m_d and n_d are material parameters and F_d represents the damage threshold function. The threshold function is calculated with the equivalent elastic strain $\bar{\epsilon} = \sqrt{\Sigma \langle \varepsilon_i \rangle^2}$ as function of positive principal strains. The expression of F_d is:

$$F_d(\bar{\epsilon}) = \bar{\epsilon} - \bar{\epsilon}_{d0} - \frac{1}{a} \left(\frac{1}{1-d} \right)^{1/b} \quad (1.56)$$

with a and b material parameters and $\bar{\epsilon}_{d0}$ the initial damage threshold.

In order to account for damage propagation under compressive and tensile loadings, the damage variable is defined as $d = \alpha_c d_c + \alpha_t d_t$, where d_c and d_t are respectively damage variables in compression and tension. The loading cases are defined through the parameters α_c and α_t : $\alpha_c = 0$ in tensile loading, $\alpha_t = 0$ in compressive loading and $\alpha_t + \alpha_c = 1$ for combined compressive and tensile loadings. The damage variables d_c and d_t are solutions of equations of the form (1.55) with distinct sets of material parameters.

Damage model of Johnson-Cook

Several years ago, a coupled thermomechanical dynamic damage model for ductile materials was developed by Johnson & Cook [76]. In the formulation of this model widely used to study the failure of metal structures under impact loadings, d represents the damage accumulated in the material element during plastic straining. d is calculated as :

$$\dot{d} = \frac{\dot{\epsilon}_{pl}}{e_f} \quad (1.57)$$

with $\dot{\epsilon}_{pl}$ the equivalent plastic strain rate. The failure strain e_f which depends on the equivalent plastic strain rate and is given by the expression:

$$e_f = (A_1 + B_2 \exp(B_3 \sigma^*)) (1 + B_4 \ln \dot{\epsilon}^*) (1 + A_5 T^*) \quad (1.58)$$

Here $A_1 - A_5$ are specific material constants. σ^* defines the stress triaxiality: $\sigma^* = \frac{\sigma_m}{\sigma_v}$ where σ_m is the hydrostatic pressure and σ_v the Von Mises equivalent stress. The dimensionless plastic strain rate $\dot{\epsilon}^*$ is expressed as the ratio between the equivalent plastic strain rate $\dot{\epsilon}_{pl}$ and a reference strain rate $\dot{\epsilon}_0$: $\dot{\epsilon}^* = \frac{\dot{\epsilon}_{pl}}{\dot{\epsilon}_0}$. $T^* = \frac{T - T_0}{T_f - T_0}$ depends on the ambient temperature T_0 and on the melting temperature T_f .

The complete failure occurs when $d = 1$. Børvik et al. [22] supposed that a macrocrack might appear for a critical value d_c of the damage variable less than 1. The modified failure criteria is then: $d = d_c \leq 1$. Moreover, damage evolution starts only when a threshold of the accumulated plastic strain is reached. The modified damage evolution law [22] can be written in the form:

$$\begin{aligned} \dot{d} &= 0 && \text{when } e_{pl} \leq e_d \\ \dot{d} &= \frac{d_c}{e_f - e_d} \dot{\epsilon}_{pl} && \text{when } e_{pl} > e_d \end{aligned} \quad (1.59)$$

where e_d is the threshold plastic strain for damage initiation and the failure strain e_f has a similar expression as in the original Johnson-Cook model.

1.3.3 Thermodynamics of damage

The general thermo-mechanical constitutive relations including damage can be obtained by the classical thermodynamics of irreversible processes approach, as presented for instance in [92]. This description introduces the Helmholtz free energy potential $\rho\psi(\epsilon_{ij}, d)$ depending on strains and damage variables.

The compatibility with the second principle of thermodynamics, written as the Clausius-Duhem inequality, gives the state laws:

$$\sigma_{ij} = \rho \frac{\partial \psi}{\partial \epsilon_{ij}} ; Y = -\rho \frac{\partial \psi}{\partial d} \quad (1.60)$$

together with the positiveness of the dissipation due to damage

$$Y\dot{d} \geq 0 \quad (1.61)$$

where Y is the damage energy-release rate and ρ the mass density.

In this context, the first principle of thermodynamics can be written as the general temperature equation:

$$\rho c \dot{T} + \frac{\partial q_i}{\partial x_i} = Y\dot{d} + T \left(\frac{\partial \sigma_{ij}}{\partial T} \dot{\epsilon}_{ij} - \frac{\partial Y}{\partial T} \dot{d} \right) + r \quad (1.62)$$

where T is the temperature field, q is the heat flux, c is the heat capacity and r the volume heat source. We recognize in the right member the damage dissipation and thermoelastic and damage coupling terms.

In the next chapters, the temperature equation will be deduced by homogenization from microscopic balance laws and interpreted in comparison with the phenomenological thermodynamical approach presented here.

1.4 Asymptotic homogenization

Modeling of physical phenomena in many materials is a difficult task because of heterogeneities, like inclusions, grain boundaries, voids, microcracks, ... Representation using an equivalent macroscopic material is the classical solution often used to overcome the difficulties imposed by the large number of microscopic heterogeneities. The models can be obtained either by phenomenological assumptions combined with experimental fitting at the macroscopic scale or by using an upscaling technique from microstructures inspired by small-scale observations. With the last technique, the heterogeneous material is replaced locally by a homogeneous equivalent material which properties take into account the details of the microstructure.

Homogenization methods are widely used in modeling the mechanical behavior of heterogeneous materials (e.g. [130], [117], [103]). In the case of multi-phase elastic materials, for example, the macroscopic behavior is given by effective or homogenized moduli of elasticity. The simplest method is to average the elastic properties of heterogeneous components. More complex homogenization methods, based on the elastic solution for an inclusion in an infinite matrix given by Eshelby [53], have been developed by Hill [70], Mori & Tanaka [96] and others, as reviewed by Nemat-Nasser et Hori [99].

A different method of homogenization is that based on asymptotic developments [15], [122], [10]. The asymptotic homogenization method allows to obtain the effective moduli and macroscopic equations through asymptotic expansions of the mechanical fields with respect to a microstructural size parameter. Some details about the method will be given in what follows.

Asymptotic homogenization for solids with locally periodic microcracks

The asymptotic homogenization method is used to model the behavior of materials with locally periodic microstructure. With this technique, the separation of scales is governed

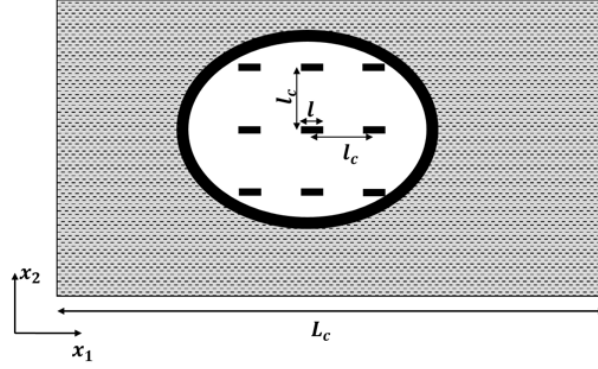


Figure 1.7: Micro-fissured medium with locally periodic distributed microcracks

by a parameter defined as the ratio between the characteristic lengths of the microscopic and macroscopic structures [9].

For a medium with locally periodic distributed microcracks depicted on Figure 1.7, the scale separation the condition becomes

$$\varepsilon = \frac{l_c}{L_c} \ll 1 \quad (1.63)$$

where l_c is the distance between the centers of neighbor micro-cracks or, equivalently, the size of the period. L_c is a macroscopic characteristic size of the solid structure. These two scales are referred to distinct systems of variables: \mathbf{y} for the microscopic scale and \mathbf{x} for the macroscopic scale. The microscopic and macroscopic variables are linked with the relation: $\mathbf{y} = \frac{\mathbf{x}}{\varepsilon}$. We define the damage variable as the normalized microcrack length: $d = \frac{l}{l_c}$, where l is the length of microcracks. The local periodicity condition allows for large-scale variations of the microcrack length l , which is assumed almost constant locally, around a material point.

The two-scale asymptotic expansion of a physical field $\Phi^\varepsilon(\mathbf{x}, t)$ is:

$$\Phi^\varepsilon(\mathbf{x}, t) = \Phi^{(0)}(\mathbf{x}, \mathbf{y}, t) + \varepsilon \Phi^{(1)}(\mathbf{x}, \mathbf{y}, t) + \varepsilon^2 \Phi^{(2)}(\mathbf{x}, \mathbf{y}, t) + \dots \quad (1.64)$$

where $\Phi^{(i)}$ are \mathbf{y} periodic. Considering the relation between \mathbf{x} and \mathbf{y} , the total spatial derivative of Φ is given by the rule:

$$\frac{d\Phi}{dx_i} = \frac{\partial\Phi}{\partial x_i} + \frac{1}{\varepsilon} \frac{\partial\Phi}{\partial y_i} \quad (1.65)$$

By applying (1.64) to the displacement u^ε and temperature T^ε , we have:

$$\mathbf{u}^\varepsilon(\mathbf{x}, t) = \mathbf{u}^{(0)}(\mathbf{x}, \mathbf{y}, t) + \varepsilon \mathbf{u}^{(1)}(\mathbf{x}, \mathbf{y}, t) + \varepsilon^2 \mathbf{u}^{(2)}(\mathbf{x}, \mathbf{y}, t) + \dots \quad (1.66)$$

$$T^\varepsilon(\mathbf{x}, t) = \mathbf{u}^{(0)}(\mathbf{x}, \mathbf{y}, t) + \varepsilon \mathbf{u}^{(1)}(\mathbf{x}, \mathbf{y}, t) + \varepsilon^2 \mathbf{u}^{(2)}(\mathbf{x}, \mathbf{y}, t) + \dots \quad (1.67)$$

The asymptotic expansions of the stress $\boldsymbol{\sigma}^\varepsilon$ and \mathbf{q}^ε are obtained using (1.65) in combination with the (1.64):

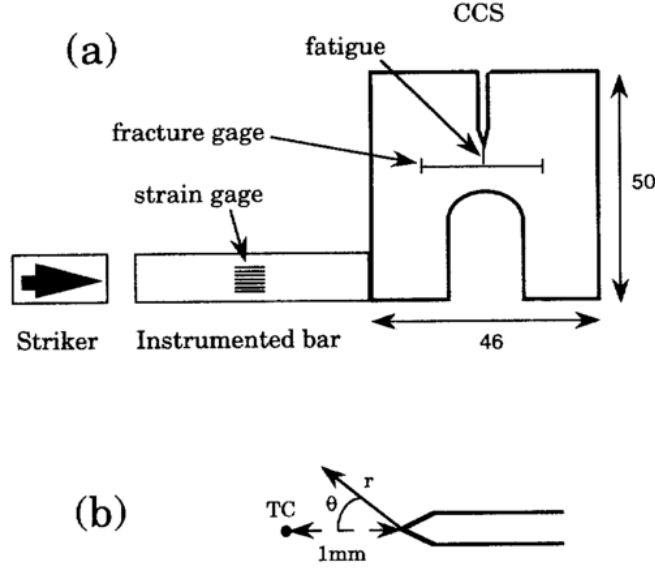


Figure 1.8: Compact compression specimen test [115]. Crack-tip temperature measurement with thermocouple.

$$\boldsymbol{\sigma}^\varepsilon(\mathbf{x}, t) = \frac{1}{\varepsilon} \boldsymbol{\sigma}^{(-1)}(\mathbf{x}, \mathbf{y}, t) + \boldsymbol{\sigma}^{(0)}(\mathbf{x}, \mathbf{y}, t) + \varepsilon \boldsymbol{\sigma}^{(1)}(\mathbf{x}, \mathbf{y}, t) + \dots \quad (1.68)$$

$$\mathbf{q}^\varepsilon(\mathbf{x}, t) = \frac{1}{\varepsilon} \mathbf{q}^{(-1)}(\mathbf{x}, \mathbf{y}, t) + \mathbf{q}^{(0)}(\mathbf{x}, \mathbf{y}, t) + \varepsilon \mathbf{q}^{(1)}(\mathbf{x}, \mathbf{y}, t) + \dots \quad (1.69)$$

Using the expansions (1.66-1.69) in the initial thermo-mechanical system we get a series of cell problems for different order of ε . The homogenized constitutive relations are obtained by solving these cell problems.

In this thesis the procedure described above will be used in combination with an energy analysis to obtain two-scale thermo-mechanical damage models.

1.5 Thermal effects in dynamic failure experiments

Thermal effects during a dynamic crack propagation in brittle materials were investigated experimentally [62], [138], [115], [116], [23], [18], [19]. Various techniques were developed for the crack-tip heating measurement.

Fuller et al. [62] used two different methods to measure the rise in temperature at the tip of a crack propagating in tensile mode with velocity between 250 and 650 $m.s^{-1}$ in commercial PMMA sheets. The first method consists on using liquid crystal film and thermocouple to measure the temperature at the crack-tip while the second is based on detection of radiation emitted by the heated tip. With these two techniques, temperature rise of about 500 K was obtained. Higher temperature rise of approximately 3200 K was detected by Weichert & Schönert [138] during dynamic fracture of glass using a very sensitive radiation thermometer. In addition to the crack-tip heating, Rittel [115], [116]

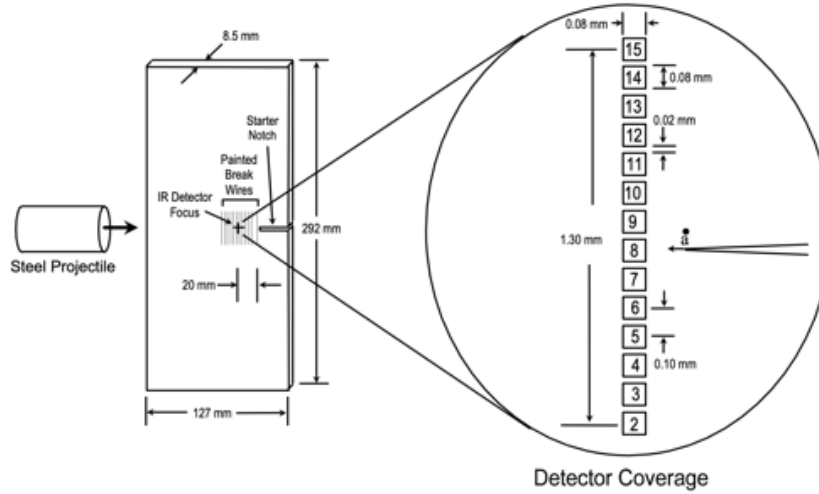


Figure 1.9: Multi-point temperature measurement in opening mode dynamic fracture experiment [17, 18].

detected significant drop of temperature prior to crack propagation through investigations on thermoelastic effects associated with dynamic fracture of polymers by using the embedded thermocouple technique. Dynamic failure tests were performed on PMMA pre-notched compact compression samples with a thermocouple placed at 1 mm of the initial notch tip recording the variation of the temperature (details in Figure 1.8). The impact loading on the CCS sample induces a dominant opening mode of crack propagation, starting from the pre-existing notch. The recorded thermal signals show significant temperature drop, between -30 and -60 K , prior to crack initiation. Heating effects due to crack propagation were also reported with a temperature increase in the range $30 - 60\text{ K}$.

It is important to note that these reported results were obtained by temperature measurements on one point. Multi-point infrared temperature detectors were used in the dynamic fracture experiments performed by Bjerke et al. [17, 18, 19], for high-speed cracks in PMMA propagating in opening or shear modes.

Figure 1.9 presents the configuration of the opening mode experiment of [17, 18]. Symmetrical impact loading is applied on a rectangular pre-notched PMMA panel in order to generate a dominated mode I crack propagation. The thermal signals were recorded on points located at 20 mm at the initial notch tip. The results reported in [18] revealed that crack-tip heating depends on the crack-tip velocity: temperature rise of 23 K was found for crack-tip speed of 300 m.s^{-1} while 73 K was recorded for a crack propagating at 600 m.s^{-1} . Unlike the results obtained in [115], [116] small temperature drop of about $2 - 3\text{ K}$ prior to crack propagation was observed. It was shown that for PMMA the region of temperature increase had a lateral span of $300\text{ }\mu\text{m}$ from the crack tip. This localization region in PMMA was found to be smaller than in Polycarbonate, a more ductile polymer in which important plastic deformations occur near the tip of the crack leading to more substantial heating.

The case of a dynamic shear crack was studied using a pre-notched rectangular panel

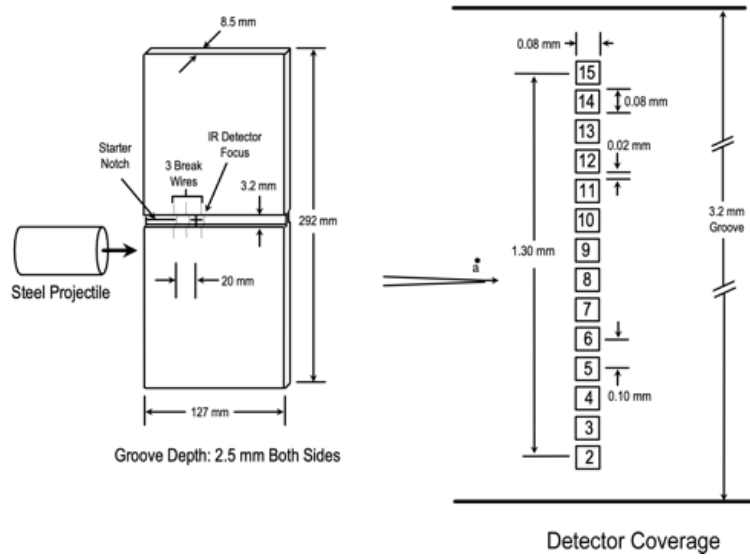


Figure 1.10: Multi-point temperature measurement in shear mode dynamic fracture experiment [17, 19].

in PMMA with side grooves, as shown in Figure 1.10). The shear dominated fracture was achieved through an asymmetrical impact loading. Thermal signals recorded in the same region as for the opening mode show increase of 85 K at the moving crack tip, approaching the glass transition temperature. Localization of the heating in the shear dominated fracture was found to be more pronounced, with a lateral span $\leq 140\ \mu\text{m}$, compared to the opening mode.

Chapter 2

Two-scale dynamic damage model for mode I microcracking with heat dissipation

Contents

2.1	Introduction	25
2.2	Two-scale thermoelastic fracture problem	27
2.3	Asymptotic developments and homogenization analysis	30
2.4	Dynamic damage evolution	36
2.5	Local macroscopic response	40
2.5.1	Homogenized coefficients	40
2.5.2	Local response analysis	42
2.6	Numerical Simulation of the CCS Impact Test	48
2.7	Heat conduction versus adiabatic conditions	51
2.7.1	Single element test	51
2.7.2	Numerical simulations of an impact test	52
2.8	Conclusions	56

2.1 Introduction

The evolution of microcracks plays an essential role in the rapid failure of brittle materials like ceramics, rocks or polymers. This was clearly proved, for instance, by the experimental observations of [110, 124, 111, 125, 36] on the dynamic fracture of nominally brittle polymers. The morphology of the fracture surface reveals that nucleation, growth and coalescence of microcracks represent the dominant failure micromechanism.

The formation of microbranches on the main crack faces can explain the dramatic increase of dissipated energy and the saturation effects in the crack-tip velocity below the theoretical limit speed.

Despite the important progresses of Fracture Mechanics to reproduce the dynamic effects of failure (e.g.,[59],[112]), the theory has limited predictive capacity for complex rupture patterns. The case of microbranching instabilities is an example among others. The reported microscopic observations during fast failure in brittle materials suggest that a proper model could be obtained by incorporating the microcracking mechanism. Since it takes place at scales smaller than that of the solid structure, a multiscale approach with propagating microcracks may represent the appropriate modeling framework.

The thermo-mechanical couplings represent another significant aspect of the fast failure in brittle solids. Temperature measurements for opening mode cracks, like those reported in [62, 138, 115, 116, 23, 18] for glass and PMMA materials, revealed a significant temperature rise in a highly localized area surrounding the crack tip during propagation and a temperature drop ahead the crack-tip in the fracture initiation phase. After a cooling regime prior to crack initiation, during the rapid mode I growth the crack tip behaves like a moving heat source. Since the plasticity effects can be neglected and the energy needed for the new crack surface formation is much smaller than the total energy expended in the crack tip region, other dissipative processes, like the craze formation and breakdown in polymers (as discussed in [18],[54]), are responsible for the tip heating effect.

In order to describe these specific thermal behaviors it is necessary to adequately model the thermo-mechanical coupling at the front of a running crack. In particular, one needs to establish the link between the energy dissipation at the moving tip and the corresponding heat generation. Attempts to model such thermofracture heating effects in the context of Fracture Mechanics have been made for instance in [25, 26, 135]. These authors consider crack models with Dirac-type heat sources located at the tip point and which intensity represents the excess of energy release rate with respect to that necessary for the new crack surface formation.

More recently, [18] proposed a thermally dissipative cohesive zone model for dynamic fracture of amorphous polymers. Their model is based on the assumption that the excess supplied energy in the crack-tip region is converted to heat within the cohesive zone that models the crazing process. A model involving heat generation by plastic dissipation in the bulk and a thermal cohesive-zone has been studied in [54] under quasi-static conditions. As concerns the dynamic failure approach of [18], comparison with experiments showed good agreement for the low speed fracture case, i.e. crack-tip speed up to $0.2C_R$, where C_R is the Rayleigh wave velocity. For faster cracks, the authors comment: "For higher speed fracture where subsurface damage becomes prominent, the line dissipation model of a cohesive zone is inadequate, and a distributed damage model is needed". To our knowledge, a damage model able to predict the heating effects during rapid failure in brittle materials has not been proposed in the literature and this is the aim of the present contribution.

The distributed damage approaches proved to be an efficient tool to model dynamic failure in brittle materials. Phenomenological rate-dependent models have been considered by introducing viscous-type damage laws (e.g. [50],[3],[134]) or gradient damage

and phase-field models (e.g. [24], [133], [20], [71], [126], [90]). Extensions that incorporate the thermo-mechanical couplings are given in [95, 128, 34]. Microcrack informed models were proposed in the dynamic failure context, among other contributions, in [97, 113, 73, 100, 16, 82, 72].

The objective of the present work is to construct a two-scale thermomechanical damage model in dynamics that accounts for microcracks evolution and thermofracture heating effect. Although the rapid failure processes can be reasonably described under adiabatic conditions at the macroscopic scale, the microscopic conduction effects may still be important. This motivates the adoption of the point heat source model [25, 26, 135] at the small-scale level, at the moving tips of the microcracks. The propagation of microcracks is assumed to follow a Griffith type criterion formulated with the dynamic energy release rate.

Starting with the fully coupled dynamic thermoelastic fracture problem at the microscale, we use the homogenization method developed in [37, 82, 41], based on asymptotic developments, to obtain the new thermo-damage model. The upscaling procedure leads to distributed heat sources, depending on the damage energy-release rate, in the homogenized temperature equation and a damage evolution law expressed with the thermal and the mechanical fields.

Investigations of the local response of the new model are performed to illustrate its capacity for predicting strain-rate and microstructural size effects and specific thermal behaviors like the existence of cooling and heating regimes associated, respectively, to damage initiation and propagation. Structural numerical simulations are also performed to reproduce the temperature field measurements during rapid failure of PMMA samples in a Compact Compression Test [115, 116, 23], showing good agreement between theoretical predictions and experimental results.

This chapter is organized as follows. In 2.2 we formulate the thermoelastic fracture problem for a solid with a distribution of microcracks propagating dynamically. The asymptotic homogenization analysis is performed in section 2.3 for the thermoelasticity system and in section 2.4 for the damage evolution law. Numerical simulations of the local effective response of the model are presented in section 2.5. The results of structural computations for the Compact Compression Test in PMMA samples and the comparison with the experimental data are given in section 2.6.

In the last part of the chapter we present a comparison between models with heat conduction and adiabatic assumptions concerning the temperature evolution during dynamic damage growth. It will be showed that the adiabatic conditions represent a reasonable approximation for the description of rapid failure.

2.2 Two-scale thermoelastic fracture problem

Consider a solid containing a large number of small cracks. When their lengths are much smaller than the size of the whole structure, we distinguish between the macroscopic properties at the scale of the solid body and the microscopic ones characterizing the local behavior in the vicinity of one microcrack.

The distribution of microcracks in the solid is assumed to be locally periodic, as

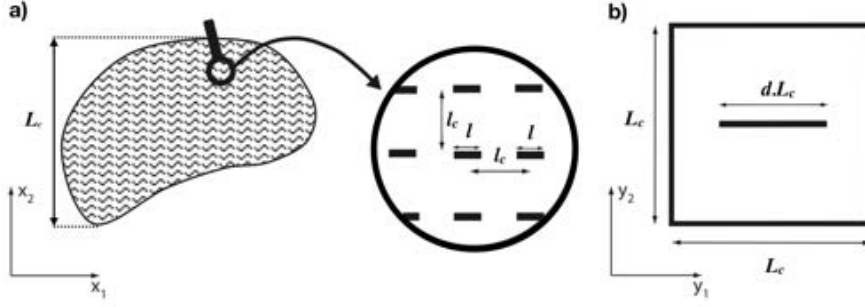


Figure 2.1: a) Micro-fissured medium with locally periodic microstructure with l_c the size of a period, l the local micro-crack length and L_c the characteristic length of the macro-structure. b) Reference cell of size L_c with rescaled crack length $d.L_c$.

illustrated in Figure 2.1, all of them being straight and parallel to the x_1 axis.

Let l be the microcrack length and l_c the size of the periodicity cells. The local periodicity means slow small-scale variations of l , with fixed l_c , such that locally the microstructure may be considered periodic.

If L_c is a characteristic length of the macrostructure, as illustrated in Figure 2.1, we introduce the parameter

$$\varepsilon = \frac{l_c}{L_c} \quad (2.1)$$

as a measure of the difference between microscopic and macroscopic scales of the solid body.

We consider plane strain deformations and we denote by \mathcal{B} the two-dimensional solid domain and by \mathcal{C} the union of all the micro-cracks inside \mathcal{B} . The coupled nonlinear equations of dynamic thermoelasticity:

$$c \frac{\partial T^\varepsilon}{\partial t} + \alpha(3\lambda + 2\mu)T^\varepsilon \frac{\partial e_{xjj}(\mathbf{u}^\varepsilon)}{\partial t} + \frac{\partial q_j^\varepsilon}{\partial x_j} = 0 \quad (2.2)$$

$$\rho \frac{\partial^2 u_i^\varepsilon}{\partial t^2} - \frac{\partial \sigma_{ij}^\varepsilon}{\partial x_j} = 0 \quad (2.3)$$

hold true in the solid part of \mathcal{B} . Here c is the specific heat, α is the coefficient of thermal expansion, λ and μ are the Lamé elastic coefficients and ρ is the mass density.

The relation (2.2) is the nonlinear form of the temperature equation. Since thermoelastic fracture problems may involve important temperature variations, in our analysis we will follow [25, 26] by using the non-linearized thermal equation.

The temperature field T^ε and the heat flux \mathbf{q}^ε are related by Fourier law:

$$q_j^\varepsilon = -k \frac{\partial T^\varepsilon}{\partial x_j} \quad (2.4)$$

with k the heat conduction coefficient.

The components of the strain tensor calculated with respect to x_i variables using the displacement field \mathbf{u}^ε are denoted by $e_{xkl}(\mathbf{u}^\varepsilon) = \frac{1}{2} \left(\frac{\partial u_k^\varepsilon}{\partial x_l} + \frac{\partial u_l^\varepsilon}{\partial x_k} \right)$ and the constitutive law for the stress tensor $\boldsymbol{\sigma}^\varepsilon$ in an isotropic solid reads:

$$\sigma_{ij}^\varepsilon = \lambda e_{xkk}(\mathbf{u}^\varepsilon) \delta_{ij} + 2\mu e_{xij}(\mathbf{u}^\varepsilon) - \alpha(3\lambda + 2\mu)(T^\varepsilon - T_0) \delta_{ij} \quad (2.5)$$

with T_0 being the initial temperature.

Traction-free and thermally isolating boundary conditions are assumed on the crack faces

$$\boldsymbol{\sigma}^\varepsilon \mathbf{N} = 0 \quad ; \quad \mathbf{q}^\varepsilon \mathbf{N} = 0 \quad (2.6)$$

where \mathbf{N} is the unit normal vector on the crack line, as shown in Fig. 2.2. Additional conditions on the outer boundary of \mathcal{B} and initial conditions for the temperature, displacement and velocity fields inside the solid domain should be specified for the formulation of the thermoelastic problem.

The dynamic propagation of microcracks is described by a Griffith criterion involving the energy-release rate [59, 112]:

$$\mathcal{G}^{d\varepsilon} = \lim_{r \rightarrow 0} \int_{\Gamma_r} ((\mathcal{U}^\varepsilon + \mathcal{K}^\varepsilon) n_1 - \sigma_{ij}^\varepsilon n_j \frac{\partial u_i^\varepsilon}{\partial x_1}) ds \quad (2.7)$$

expressing the available energy for crack propagation. Here Γ_r is a closed circular contour of radius r encircling the crack tip and \mathbf{n} is its outward unit normal, as represented in Figure 2.2. \mathcal{U}^ε is the internal energy:

$$\mathcal{U}^\varepsilon = \frac{1}{2} (\lambda e_{xii}(\mathbf{u}^\varepsilon) e_{xjj}(\mathbf{u}^\varepsilon) + 2\mu e_{xij}(\mathbf{u}^\varepsilon) e_{xij}(\mathbf{u}^\varepsilon)) + (3\lambda + 2\mu) \alpha T_0 e_{xkk}(\mathbf{u}^\varepsilon) + c T^\varepsilon \quad (2.8)$$

and \mathcal{K}^ε is the kinetic energy:

$$\mathcal{K}^\varepsilon = \frac{1}{2} \rho \frac{\partial \mathbf{u}^\varepsilon}{\partial t} \frac{\partial \mathbf{u}^\varepsilon}{\partial t} \quad (2.9)$$

Microcracks propagate when $\mathcal{G}^{d\varepsilon} = \mathcal{G}_c$, with \mathcal{G}_c being the critical fracture energy of the material.

The heat flow from a crack tip during propagation can be defined as the limit

$$D^\varepsilon = \lim_{r \rightarrow 0} \int_{\Gamma_r} \mathbf{q}^\varepsilon \mathbf{n} ds \quad (2.10)$$

Following the approaches of [25, 26], [135], we consider the crack tips as moving heat sources. A part 2γ of the energy dissipated during fracture is needed for the formation of new crack surfaces while the rest is converted to heat through specific material failure mechanisms, like the process of craze formation and breakdown in brittle amorphous polymers. If we denote by $v_p = \frac{1}{2} \frac{dl}{dt}$ the velocity of a microcrack tip, then the local energy balance during its propagation reads

$$D^\varepsilon = v_p (\mathcal{G}^{d\varepsilon} - 2\gamma) \quad (2.11)$$

For some materials the surface energy term 2γ is negligible when compared with the energy release rate $\mathcal{G}^{d\varepsilon}$. As [18] remark, the surface energy of some polymers is several orders of

magnitude lower than the fracture energy. For example, [14] estimates the surface energy of PMMA as 0.1 J/m^2 while the measured values of the energy release rate are 3-4 orders of magnitude higher, depending on the crack velocity. In the case of polystyrene, [139] reported a surface energy of 0.04 J/m^2 , which is negligible in comparison to the critical fracture energy.

In this case, (2.11) can be replaced by the approximate relation

$$D^\varepsilon = v_p \mathcal{G}^{d\varepsilon} \quad (2.12)$$

In what follows, the relation (2.12) will be adopted. However, the present approach may be easily adapted to the case of non-negligible surface energy, by replacing the equation (2.12) by (2.11).

The relations (2.10-2.12) express the link between the energy dissipation and the heat production during failure and represent a supplementary condition to be imposed at the moving tips of microcracks. This condition introduces a new thermo-mechanical coupling for the solid body.

2.3 Asymptotic developments and homogenization analysis

The asymptotic homogenization method [122, 56] is employed in this section to obtain the macroscopic thermoelasticity equations from the initial problem described previously. For bodies without cracks, similar techniques have been used in coupled dynamic thermoelasticity by [52, 57, 102, 9] among other authors. In the present development we focus on the influence of microcracks with the specific singularities of the fields, the damage dependence of the effective thermoelastic coefficients and the upscaling of the temperature equation with the non-classical heat source conditions.

In the previous section, the characteristic length of the microstructure l_c has been introduced as the size of the microscopic period and also the mutual distance between neighbor microcracks. The damage variable d may be defined as the normalized microcrack length:

$$d = \frac{l}{l_c} \quad (2.13)$$

The local periodicity assumption for the length l allows for large-scale spatial variations of the damage variable d .

To characterize the field variations at different scales, we distinguish between the macroscopic variable \mathbf{x} and the microscopic variable \mathbf{y} , linked by the relation $\mathbf{y} = \frac{\mathbf{x}}{\varepsilon}$, with ε defined in (2.1). The scaling of the microscopic period by this transformation leads to a reference cell Y , of size L_c and containing the crack CY of length $d.L_c$, as illustrated in Figure 2.2.

For a field f depending on both \mathbf{x} and \mathbf{y} , the total spatial derivative can be calculated by the formula $\frac{df}{dx_i} = \frac{\partial f}{\partial x_i} + \frac{1}{\varepsilon} \frac{\partial f}{\partial y_i}$.

In what follows, we adopt the separation of scales assumption

$$\varepsilon = \frac{l_c}{L_c} \ll 1 \quad (2.14)$$

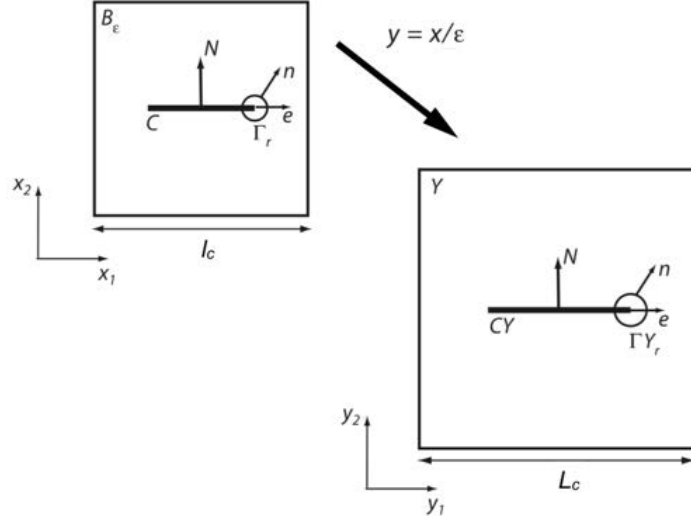


Figure 2.2: Scaling of the microscopic period of the material to the reference cell.

This means that the scale of microcracks is small in comparison with that of the solid body. Variations in \mathbf{y} do not have much influence on \mathbf{x} and both variables should be taken into account in the description of the physical fields, being treated as independent variables.

The displacement \mathbf{u}^ε and the temperature T^ε fields are developed with respect to the small parameter ε in the form:

$$\mathbf{u}^\varepsilon(\mathbf{x}, t) = \mathbf{u}^{(0)}(\mathbf{x}, \mathbf{y}, t) + \varepsilon \mathbf{u}^{(1)}(\mathbf{x}, \mathbf{y}, t) + \varepsilon^2 \mathbf{u}^{(2)}(\mathbf{x}, \mathbf{y}, t) + \dots \quad (2.15)$$

$$T^\varepsilon(\mathbf{x}, t) = T^{(0)}(\mathbf{x}, \mathbf{y}, t) + \varepsilon T^{(1)}(\mathbf{x}, \mathbf{y}, t) + \varepsilon^2 T^{(2)}(\mathbf{x}, \mathbf{y}, t) + \dots \quad (2.16)$$

where $\mathbf{u}^{(i)}(\mathbf{x}, \mathbf{y}, t)$ and $T^{(i)}(\mathbf{x}, \mathbf{y}, t)$, $\mathbf{x} \in B$, $\mathbf{y} \in Y$ are Y -periodic.

Using these developments in the equations (2.4-2.5) we obtain:

$$\boldsymbol{\sigma}^\varepsilon(\mathbf{x}, t) = \frac{1}{\varepsilon} \boldsymbol{\sigma}^{(-1)}(\mathbf{x}, \mathbf{y}, t) + \boldsymbol{\sigma}^{(0)}(\mathbf{x}, \mathbf{y}, t) + \varepsilon \boldsymbol{\sigma}^{(1)}(\mathbf{x}, \mathbf{y}, t) + \varepsilon^2 \boldsymbol{\sigma}^{(2)}(\mathbf{x}, \mathbf{y}, t) + \dots \quad (2.17)$$

$$\mathbf{q}^\varepsilon(\mathbf{x}, t) = \frac{1}{\varepsilon} \mathbf{q}^{(-1)}(\mathbf{x}, \mathbf{y}, t) + \mathbf{q}^{(0)}(\mathbf{x}, \mathbf{y}, t) + \varepsilon \mathbf{q}^{(1)}(\mathbf{x}, \mathbf{y}, t) + \varepsilon^2 \mathbf{q}^{(2)}(\mathbf{x}, \mathbf{y}, t) + \dots \quad (2.18)$$

where

$$\sigma_{ij}^{(-1)} = \lambda e_{ykk}(\mathbf{u}^{(0)}) \delta_{ij} + 2\mu e_{yij}(\mathbf{u}^{(0)}) \quad (2.19)$$

$$\begin{aligned} \sigma_{ij}^{(0)} = & \lambda(e_{xkk}(\mathbf{u}^{(0)}) + e_{ykk}(\mathbf{u}^{(1)})) \delta_{ij} + 2\mu(e_{xij}(\mathbf{u}^{(0)}) + e_{yij}(\mathbf{u}^{(1)})) \\ & - (3\lambda + 2\mu)\alpha(T^{(0)} - T_0) \delta_{ij} \end{aligned} \quad (2.20)$$

$$\begin{aligned} \sigma_{ij}^{(1)} = & \lambda(e_{xkk}(\mathbf{u}^{(1)}) + e_{ykk}(\mathbf{u}^{(2)})) \delta_{ij} + 2\mu(e_{xij}(\mathbf{u}^{(1)}) + e_{yij}(\mathbf{u}^{(2)})) \\ & - (3\lambda + 2\mu)\alpha T^{(1)} \end{aligned} \quad (2.21)$$

and

$$q_j^{(-1)} = -k \frac{\partial T^{(0)}}{\partial y_j}; \quad q_j^{(0)} = -k \left(\frac{\partial T^{(0)}}{\partial x_j} + \frac{\partial T^{(1)}}{\partial y_j} \right); \quad q_j^{(1)} = -k \left(\frac{\partial T^{(1)}}{\partial x_j} + \frac{\partial T^{(2)}}{\partial y_j} \right) \quad (2.22)$$

The asymptotic developments of momentum and temperature equations (2.2-2.3) lead to problems of order ε^α , with $\alpha = -2, -1, 0$, in the form:

$$\frac{\partial q_j^{(-1)}}{\partial y_j} = 0 \quad ; \quad \frac{\partial \sigma_{ij}^{(-1)}}{\partial y_j} = 0 \quad (2.23)$$

$$(3\lambda + 2\mu)\alpha T^{(0)} \frac{\partial e_{yij}(u^{(0)})}{\partial t} + \frac{\partial q_j^{(-1)}}{\partial x_j} + \frac{\partial q_j^{(0)}}{\partial y_j} = 0 \quad ; \quad \frac{\partial \sigma_{ij}^{(-1)}}{\partial x_j} + \frac{\partial \sigma_{ij}^{(0)}}{\partial y_j} = 0 \quad (2.24)$$

$$c \frac{\partial T^{(0)}}{\partial t} + (3\lambda + 2\mu)\alpha T^{(0)} \left(\frac{\partial e_{xij}(u^{(0)})}{\partial t} + \frac{\partial e_{yij}(u^{(1)})}{\partial t} \right) + \frac{\partial q_j^{(0)}}{\partial x_j} + \frac{\partial q_j^{(1)}}{\partial y_j} = 0 \quad ;$$

$$\frac{\partial \sigma_{ij}^{(0)}}{\partial x_j} + \frac{\partial \sigma_{ij}^{(1)}}{\partial y_j} - \rho \frac{\partial^2 u^{(0)}}{\partial x_j^2} = 0 \quad (2.25)$$

Corresponding boundary conditions are obtained from (2.6) for the terms of different orders $\sigma^{(m)}$ and $q^{(m)}$:

$$\sigma_{ij}^{(m)} N_j = 0 \quad ; \quad q_j^{(m)} N_j = 0 \quad m = -1, 0, 1 \quad (2.26)$$

At the microcrack tips, a supplementary condition is given by (2.12) relating the energy-release rate (2.7) and the heat dissipation term (2.10). Using the development (2.16) and the link between length elements in the physical and reference cells $ds = \varepsilon ds_y$, we get:

$$D^\varepsilon = D^{(0)} + \varepsilon D^{(1)} + \varepsilon^2 D^{(2)} + \dots \quad (2.27)$$

where

$$D^{(0)} = \lim_{r \rightarrow 0} \int_{\Gamma_{Y_r}} -k \frac{\partial T^{(0)}}{\partial y_j} n_j ds_y \quad ; \quad D^{(1)} = \lim_{r \rightarrow 0} \int_{\Gamma_{Y_r}} -k \left(\frac{\partial T^{(0)}}{\partial x_j} + \frac{\partial T^{(1)}}{\partial y_j} \right) n_j ds_y$$

$$D^{(2)} = \lim_{r \rightarrow 0} \int_{\Gamma_{Y_r}} -k \left(\frac{\partial T^{(1)}}{\partial x_j} + \frac{\partial T^{(2)}}{\partial y_j} \right) n_j ds_y \quad (2.28)$$

The asymptotic development of the energy release rate can be written from (2.7) in the form:

$$\mathcal{G}^{d\varepsilon} = \frac{1}{\varepsilon} \mathcal{G}^{(-1)} + \mathcal{G}^{(0)} + \varepsilon \mathcal{G}^{(1)} + \dots \quad (2.29)$$

The complete expressions of the terms appearing in this relation are given in the Appendix A. Introduction of the expansions of $\mathcal{G}^{d\varepsilon}$ and D^ε in the criterion (2.11) provides the link between different orders terms of heating dissipation and energy-release rate :

$$D^{(0)} = \frac{1}{2} \frac{dd}{dt} L_c \mathcal{G}^{(-1)} \quad ; \quad D^{(1)} = \frac{1}{2} \frac{dd}{dt} L_c \mathcal{G}^{(0)} \quad ; \quad D^{(2)} = \frac{1}{2} \frac{dd}{dt} L_c \mathcal{G}^{(1)} \quad (2.30)$$

At the order ε^{-2} , the problem for $\mathbf{u}^{(0)}$ and $T^{(0)}$ results from (2.23), (2.26) and (2.30) as:

$$\frac{\partial}{\partial y_j} (\lambda e_{ykk}(\mathbf{u}^{(0)}) \delta_{ij} + 2\mu e_{yij}(\mathbf{u}^{(0)})) = 0 \quad \text{in} \quad Y \quad (2.31)$$

$$(\lambda e_{ykk}(\mathbf{u}^{(0)}) \delta_{ij} + 2\mu e_{yij}(\mathbf{u}^{(0)})) N_j = 0 \quad \text{on} \quad CY \quad (2.32)$$

and the thermal equations

$$\frac{\partial^2 T^{(0)}}{\partial y_1^2} + \frac{\partial^2 T^{(0)}}{\partial y_2^2} = 0 \quad \text{in } Y \quad (2.33)$$

$$\frac{\partial T^{(0)}}{\partial y_j} N_j = 0 \quad \text{on } CY \quad (2.34)$$

$$\lim_{r \rightarrow 0} \int_{\Gamma Y_r} -k \frac{\partial T^{(0)}}{\partial y_j} n_j ds_y = \frac{1}{2} \frac{dd}{dt} L_c \mathcal{G}^{(-1)} \quad \text{at } (y_1, y_2) = (\pm \frac{dL_c}{2}, 0) \quad (2.35)$$

In the last condition, considered at both microcrack tips in the reference cell, the term $\mathcal{G}^{(-1)}$ is given by the expression (A.2). Periodicity conditions are assumed on the opposite exterior boundaries of Y .

Choosing $\mathbf{u}^{(0)} = \mathbf{u}^{(0)}(\mathbf{x}, t)$ and $T^{(0)} = T^{(0)}(\mathbf{x}, t)$ independent of the y variables, we can verify the system of equations (2.31 - 2.35). They represent the macroscopic displacement and temperature fields.

The next order (ε^{-1}) problem, for $\mathbf{u}^{(1)}$ and $T^{(1)}$, can be deduced from Eqs (2.24), (2.26) and the second relation (2.30) as:

$$\frac{\partial}{\partial y_j} (\lambda e_{ykk}(\mathbf{u}^{(1)}) \delta_{ij} + 2\mu e_{yij}(\mathbf{u}^{(1)})) = 0 \quad \text{in } Y \quad (2.36)$$

$$\begin{aligned} (\lambda e_{ykk}(\mathbf{u}^{(1)}) \delta_{ij} + 2\mu e_{yij}(\mathbf{u}^{(1)})) N_j &= -(\lambda e_{xkk}(\mathbf{u}^{(0)}) \delta_{ij} + 2\mu e_{xij}(\mathbf{u}^{(0)})) \\ &\quad - (3\lambda + 2\mu) \alpha (T^{(0)} - T_0) \delta_{ij} N_j \quad \text{on } CY \end{aligned} \quad (2.37)$$

and

$$\frac{\partial^2 T^{(1)}}{\partial y_1^2} + \frac{\partial^2 T^{(1)}}{\partial y_2^2} = 0 \quad \text{in } Y \quad (2.38)$$

$$\frac{\partial T^{(1)}}{\partial y_j} N_j = -\frac{\partial T^{(0)}}{\partial x_j} N_j \quad \text{on } CY \quad (2.39)$$

$$\lim_{r \rightarrow 0} \int_{\Gamma Y_r} -k \left(\frac{\partial T^{(0)}}{\partial x_j} + \frac{\partial T^{(1)}}{\partial y_j} \right) n_j ds_y = \frac{1}{2} \frac{dd}{dt} L_c \mathcal{G}^{(0)} \quad \text{at } (y_1, y_2) = (\pm \frac{dL_c}{2}, 0) \quad (2.40)$$

On the external boundaries of Y periodicity conditions complete the formulation of these cell problems.

For given $\mathbf{u}^{(0)}(\mathbf{x}, t)$ and $T^{(0)}(\mathbf{x}, t)$, the solution $\mathbf{u}^{(1)}$ of (2.36-2.37) has the classical $r^{1/2}$ singularity as (y_1, y_2) approaches the crack tips. In the expression (A.3) of $\mathcal{G}^{(0)}$ the integrand is not singular enough to get a non-vanishing limit, such that the right member of (2.40) is equal to 0.

The particular form of the boundary condition (2.37) shows that the general solution of (2.36-2.37), for the first-order corrector $\mathbf{u}^{(1)}$, is of the form:

$$\mathbf{u}^{(1)}(\mathbf{x}, \mathbf{y}, t) = \boldsymbol{\xi}^{pq}(\mathbf{y}) e_{xpq}(\mathbf{u}^{(0)})(\mathbf{x}, t) + \phi(\mathbf{x}, t) (T^{(0)} - T_0) \quad (2.41)$$

Here the characteristic functions $\boldsymbol{\xi}^{pq}$ are obtained by solving the unit-cell problem:

$$\frac{\partial}{\partial y_j} (\lambda e_{ykk}(\boldsymbol{\xi}^{pq}) \delta_{ij} + 2\mu e_{yij}(\boldsymbol{\xi}^{pq})) = 0 \quad \text{in } Y \quad (2.42)$$

$$(\lambda e_{ykk}(\boldsymbol{\xi}^{pq}) \delta_{ij} + 2\mu e_{yij}(\boldsymbol{\xi}^{pq})) N_j = -(\lambda \delta_{ij} \delta_{pq} + \mu (\delta_{ip} \delta_{jq} + \delta_{iq} \delta_{jp})) N_j \quad \text{on } CY \quad (2.43)$$

while ϕ is the solution of the second problem:

$$\frac{\partial}{\partial y_j}(\lambda e_{ykk}(\phi)\delta_{ij} + 2\mu e_{yij}(\phi)) = 0 \quad \text{in } Y \quad (2.44)$$

$$(\lambda e_{ykk}(\phi)\delta_{ij} + 2\mu e_{yij}(\phi))N_j = (3\lambda + 2\mu)\alpha\delta_{ij}N_j \quad \text{on } CY \quad (2.45)$$

The temperature corrector $T^{(1)}$ is obtained from (2.38-2.40) and depends linearly on the right member of (2.39), with $N_1 = 0$, $N_2 = 1$:

$$T^{(1)}(\mathbf{x}, \mathbf{y}, t) = \theta(\mathbf{y})\frac{\partial T^{(0)}}{\partial x_2}(\mathbf{x}, t) \quad (2.46)$$

where θ is solution of the following unit cell problem:

$$\frac{\partial^2 \theta}{\partial y_1^2} + \frac{\partial^2 \theta}{\partial y_2^2} = 0 \quad \text{in } Y \quad (2.47)$$

$$\frac{\partial \theta}{\partial y_2} = -1 \quad \text{on } CY \quad (2.48)$$

$$\lim_{r \rightarrow 0} \int_{\Gamma_{Y_r}} \frac{\partial \theta}{\partial y_j} n_j ds_y = 0 \quad \text{at } (y_1, y_2) = (\pm \frac{dL_c}{2}, 0) \quad (2.49)$$

We note that the solutions of the unit cell problems (2.42-2.43), (2.44-2.45) and (2.47-2.49) depend on the normalized microcrack length d .

At the order ε^0 , we get the following problems for thermal and displacement fields:

$$\begin{aligned} k\left(\frac{\partial^2 T^{(0)}}{\partial x_1^2} + \frac{\partial^2 T^{(0)}}{\partial x_2^2} + 2\left(\frac{\partial^2 T^{(1)}}{\partial x_1 \partial y_1} + \frac{\partial^2 T^{(1)}}{\partial x_2 \partial y_2}\right) + \frac{\partial^2 T^{(2)}}{\partial y_1^2} + \frac{\partial^2 T^{(2)}}{\partial y_2^2}\right) \\ - (3\lambda + 2\mu)\alpha T^{(0)} \frac{\partial}{\partial t} (e_{x11}(\mathbf{u}^{(0)}) + e_{x22}(\mathbf{u}^{(0)})) \\ + e_{y11}(\mathbf{u}^{(1)}) + e_{y22}(\mathbf{u}^{(1)}) = c \frac{\partial T^{(0)}}{\partial t} \quad \text{in } Y \end{aligned} \quad (2.50)$$

$$\frac{\partial T^{(1)}}{\partial x_2} + \frac{\partial T^{(2)}}{\partial y_2} = 0 \quad \text{on } CY \quad (2.51)$$

$$\lim_{r \rightarrow 0} \int_{\Gamma_{Y_r}} -k\left(\frac{\partial T^{(1)}}{\partial x_j} + \frac{\partial T^{(2)}}{\partial y_j}\right) n_j ds_y = \frac{1}{2} \frac{dd}{dt} L_c \mathcal{G}^{(1)} \quad \text{at } (y_1, y_2) = (\pm \frac{dL_c}{2}, 0) \quad (2.52)$$

and

$$\begin{aligned} \frac{\partial}{\partial x_j}(\lambda(e_{xkk}(\mathbf{u}^{(0)}) + e_{ykk}(\mathbf{u}^{(1)}))\delta_{ij} + 2\mu(e_{xij}(\mathbf{u}^{(0)}) + e_{yij}(\mathbf{u}^{(1)}))) \\ - (3\lambda + 2\mu)\alpha(T^{(0)} - T_0)\delta_{ij} + \frac{\partial}{\partial y_j}(\lambda(e_{xkk}(\mathbf{u}^{(1)}) + e_{ykk}(\mathbf{u}^{(2)}))\delta_{ij} \\ + 2\mu(e_{xij}(\mathbf{u}^{(1)}) + e_{yij}(\mathbf{u}^{(2)}))) - (3\lambda + 2\mu)\alpha T^{(1)}\delta_{ij} = \rho \frac{\partial^2 \mathbf{u}_i^{(0)}}{\partial t^2} \quad \text{in } Y \end{aligned} \quad (2.53)$$

$$\begin{aligned} (\lambda(e_{xkk}(\mathbf{u}^{(1)}) + e_{ykk}(\mathbf{u}^{(2)}))\delta_{ij} + 2\mu(e_{xkk}(\mathbf{u}^{(1)}) + e_{yij}(\mathbf{u}^{(2)}))) \\ - (3\lambda + 2\mu)\alpha T^{(1)}\delta_{ij} N_j = 0 \quad \text{on } CY \end{aligned} \quad (2.54)$$

In order to deduce the effective thermo-mechanical balance laws we apply the mean value operator $\langle \cdot \rangle = (1/|Y|) \int_Y \cdot dy$, with $|Y| = L_c^2$ the area of Y , to (2.50) and (2.53). Integration by parts, use of the periodicity conditions and the crack-tip relations of the form (2.52) lead to:

$$c^{eff} \frac{\partial T^{(0)}}{\partial t} + T^{(0)} \beta_{ij}^{eff} \frac{\partial e_{xij}(\mathbf{u}^{(0)})}{\partial t} + \frac{\partial Q_i^{(0)}}{\partial x_i} = \frac{\mathcal{G}^{(1)}}{L_c} \frac{dd}{dt} \quad (2.55)$$

$$\rho^{eff} \frac{\partial^2 \mathbf{u}_i^{(0)}}{\partial t^2} - \frac{\partial \Sigma_{ij}^{(0)}}{\partial x_j} = 0 \quad (2.56)$$

where the macroscopic stress $\Sigma_{ij}^{(0)} = \langle \sigma_{ij}^{(0)} \rangle$ and heat flux $Q_i^{(0)} = \langle q_i^{(0)} \rangle$ are given by

$$\Sigma_{ij}^{(0)} = C_{ijkl}^{eff} e_{xkl}(\mathbf{u}^{(0)}) - \varphi_{ij}^{eff} (T^{(0)} - T_0) \quad (2.57)$$

$$Q_i^{(0)} = -k_{ij}^{eff} \frac{\partial T^{(0)}}{\partial x_j} \quad (2.58)$$

As concerns the expressions of the homogenized coefficients, we obtain for the effective specific heat coefficient:

$$c^{eff} = c + T^{(0)} S^* \quad (2.59)$$

with the thermal modulus S^* given by

$$S^* = \frac{1}{|Y|} \int_Y (3\lambda + 2\mu) \alpha (e_{y11}(\boldsymbol{\phi}) + e_{y22}(\boldsymbol{\phi})) dy \quad (2.60)$$

The effective elastic moduli C_{ijkl}^{eff} are computed with the cell solutions as:

$$C_{ijkl}^{eff} = \frac{1}{|Y|} \int_Y (\lambda \delta_{ij} \delta_{kl} + \mu (\delta_{ik} \delta_{jl} + \delta_{il} \delta_{jk}) + \lambda e_{yymm}(\boldsymbol{\xi}^{kl}) \delta_{ij} + 2\mu e_{yij}(\boldsymbol{\xi}^{kl})) dy \quad (2.61)$$

and the homogenized mass density:

$$\rho^{eff} = \frac{1}{|Y|} \int_Y \rho dy \quad (2.62)$$

For the thermal expansion coefficients we obtain the formulae

$$\beta_{ij}^{eff} = \frac{1}{|Y|} \int_Y \alpha (3\lambda + 2\mu) (\delta_{ij} + e_{yymm}(\boldsymbol{\xi}^{ij})) dy \quad (2.63)$$

$$\varphi_{ij}^{eff} = \frac{1}{|Y|} \int_Y (\alpha (3\lambda + 2\mu) \delta_{ij} - C_{ijkl} e_{ykl}(\boldsymbol{\phi})) dy \quad (2.64)$$

and we prove the equality $\beta_{ij}^{eff} = \varphi_{ij}^{eff}$ using the corresponding cell problems for the characteristic functions.

The homogenized thermal conduction components are:

$$k_{11}^{eff} = \frac{1}{|Y|} \int_Y k dy ; k_{12}^{eff} = \frac{1}{|Y|} \int_Y k \frac{\partial \theta}{\partial y_1} dy ; k_{22}^{eff} = \frac{1}{|Y|} \int_Y k (1 + \frac{\partial \theta}{\partial y_2}) dy \quad (2.65)$$

We remark that the effective coefficients S^* , C_{ijkl}^{eff} , φ_{ij}^{eff} and k_{ij}^{eff} depend on the damage variable d . This dependence will be illustrated numerically in Section 5 for a particular set of initial material constants and different microcrack lengths.

As concerns the homogenized temperature equation (2.55), the development in the next section will allow us to express the right member as a fully macroscopic dissipation term.

2.4 Dynamic damage evolution

In order to obtain a complete thermoelastic damage problem, we have to supplement the equations (2.55-2.58) with an evolution equation for the damage variable $d(x_i, t)$. Based on previous contributions [37, 82, 41], we develop in this Section a microfracture-to-damage homogenization approach in the non-classical framework of dynamic thermoelastic fracture with heat production. In the particular case when the heating term in the right of (2.55) is neglected, the final product of this Section will be a new thermo-elastic damage law in dynamics.

An energy analysis will be performed with the solutions of the cell problems formulated in the previous section, in the case of propagating microcracks. We will assume that, in the reference cell Y , the crack CY of length $d(t) \cdot L_c$ extends symmetrically, the two tips moving with the velocity $\frac{1}{2} \frac{dd}{dt} \cdot L_c$. In order to properly account for the singularity of the fields and the energy flow at microcrack tips during this evolution, we will first work on the domain Y_r representing the cell Y without the interiors of the cercles ΓY_r^g and ΓY_r^d (see Fig. 2.2). We also denote by CY_r the part of the crack line inside Y_r . The fields defined on Y with the crack CY will then be recovered by taking the limit $r \rightarrow 0$.

Multiplication of the equation (2.36) by $\dot{u}_i^{(1)}$, integration on Y_r , use of periodicity conditions and Reynolds transport theorem lead to the energy balance:

$$\begin{aligned} & \frac{d}{dt} \int_{Y_r} \frac{1}{2} C_{ijkl} e_{ykl}(\mathbf{u}^{(1)}) e_{yij}(\mathbf{u}^{(1)}) dy \\ & + \int_{\Gamma Y_r^g \cup \Gamma Y_r^d} \left(\frac{1}{2} C_{ijkl} e_{ykl}(\mathbf{u}^{(1)}) e_{yij}(\mathbf{u}^{(1)}) \frac{1}{2} \frac{dd}{dt} L_c n_1 + C_{ijkl} e_{ykl}(\mathbf{u}^{(1)}) n_j \dot{u}_i^{(1)} \right) ds_y \\ & = \int_{CY_r} C_{ijkl} e_{ykl}(\mathbf{u}^{(1)}) N_j \left[\dot{u}_i^{(1)} \right] ds_y \end{aligned} \quad (2.66)$$

where we have used the compact notation $C_{ijkl} = \lambda \delta_{ij} \delta_{kl} + \mu (\delta_{ik} \delta_{jl} + \delta_{il} \delta_{jk})$ for the initial elastic coefficients. The brackets $[f] = f^+ - f^-$ denote the jump of f over the crack faces, with the $+$ value on the side given by the orientation of the normal vector \mathbf{N} , as illustrated in Fig. 2.2.

The singularity of field $\dot{u}_i^{(1)}$ allows us [59, 25] to use the local relation $\dot{u}_i^{(1)} \simeq -\frac{1}{2} \frac{dd}{dt} L_c \frac{\partial u_i^{(1)}}{\partial y_1}$ in the vicinity of the crack tips. In this way, by taking the limit we retrieve the energy-release rate term $\mathcal{G}^{(1)}$, given in (A.8), for the two crack tips and the previous relation

becomes:

$$\begin{aligned} \frac{d}{dt} \int_Y \frac{1}{2} C_{ijkl} e_{ykl}(\mathbf{u}^{(1)}) e_{yij}(\mathbf{u}^{(1)}) dy + \frac{dd}{dt} L_c \mathcal{G}^{(1)} \\ = \int_{CY} C_{ijkl} e_{ykl}(\mathbf{u}^{(1)}) N_j [\dot{u}_i^{(1)}] ds_y \end{aligned} \quad (2.67)$$

A similar procedure can be applied starting with the equation (2.31) in the slightly modified form

$$\frac{\partial}{\partial y_j} (C_{ijkl} e_{xkl}(\mathbf{u}^{(0)}) - \beta T^{(0)} \delta_{ij}) = 0$$

with $\beta = \alpha(3\lambda + 2\mu)$. Using the fact that $\mathbf{u}^{(0)}$ and $T^{(0)}$ do not depend on y_i variables, we obtain:

$$\begin{aligned} \int_Y (C_{ijkl} e_{xkl}(\mathbf{u}^{(0)}) - \beta T^{(0)} \delta_{ij}) e_{yij}(\dot{\mathbf{u}}^{(1)}) dy \\ - \int_{CY} (C_{ijkl} e_{xkl}(\mathbf{u}^{(0)}) - \beta T^{(0)} \delta_{ij}) N_j [\dot{u}_i^{(1)}] ds_y = 0 \end{aligned} \quad (2.68)$$

Combining (2.67) and (2.68) and using the boundary condition (2.37) on the crack faces allow us to obtain

$$\begin{aligned} \frac{d}{dt} \int_Y \frac{1}{2} C_{ijkl} e_{ykl}(\mathbf{u}^{(1)}) e_{yij}(\mathbf{u}^{(1)}) dy + \int_Y (C_{ijkl} e_{xkl}(\mathbf{u}^{(0)}) - \beta T^{(0)} \delta_{ij}) e_{yij}(\dot{\mathbf{u}}^{(1)}) dy \\ + \frac{dd}{dt} L_c \mathcal{G}^{(1)} = - \int_{CY} (\beta T_0 \delta_{ij}) N_j [\dot{u}_i^{(1)}] ds_y = - \frac{d}{dt} \int_Y \beta T_0 \delta_{ij} e_{yij}(\mathbf{u}^{(1)}) dy \end{aligned} \quad (2.69)$$

where the last equality results by integration of $\frac{\partial}{\partial y_j} (\alpha(\beta T_0 \delta_{ij})) = 0$.

In the second term of (2.69) we can interchange the time derivative so that to obtain the equivalent identity:

$$\begin{aligned} \frac{1}{2} \frac{d}{dt} \int_Y (C_{ijkl} (e_{xkl}(\mathbf{u}^{(0)}) + e_{ykl}(\mathbf{u}^{(1)})) - \beta(T^{(0)} - T_0)) e_{yij}(\mathbf{u}^{(1)}) dy \\ + \frac{1}{2} \frac{d}{dt} \int_Y (C_{ijkl} e_{xkl}(\mathbf{u}^{(0)}) - \beta(T^{(0)} - T_0)) e_{yij}(\mathbf{u}^{(1)}) dy + \frac{dd}{dt} L_c \mathcal{G}^{(1)} \\ = \int_Y (C_{ijkl} e_{xkl}(\dot{\mathbf{u}}^{(0)}) - \beta \dot{T}^{(0)} \delta_{ij}) e_{yij}(\mathbf{u}^{(1)}) dy \end{aligned} \quad (2.70)$$

On the other hand, if the equation (2.36) in its equivalent form

$$\frac{\partial}{\partial y_j} (C_{ijkl} (e_{xkl}(\mathbf{u}^{(0)}) + e_{ykl}(\mathbf{u}^{(1)})) - \beta(T^{(0)} - T_0) \delta_{ij}) = 0$$

is multiplied by u_i and integrated over Y , and the crack face conditions (2.37) are used, we get:

$$\int_Y (C_{ijkl} (e_{xkl}(\mathbf{u}^{(0)}) + e_{ykl}(\mathbf{u}^{(1)})) - \beta(T^{(0)} - T_0) \delta_{ij}) e_{yij}(\mathbf{u}^{(1)}) dy = 0 \quad (2.71)$$

With this last relation the identity (2.69) reduces to

$$\begin{aligned} \frac{dd}{dt} L_c \mathcal{G}^{(1)} &= \int_Y C_{ijkl} e_{ykl}(\mathbf{u}^{(1)}) dy e_{xij}(\dot{\mathbf{u}}^{(0)}) - \int_Y \beta e_{ykl}(\mathbf{u}^{(1)}) \delta_{kl} dy \dot{T}^{(0)} \\ &- \frac{1}{2} \frac{d}{dt} \int_Y C_{ijkl} e_{ykl}(\mathbf{u}^{(1)}) dy e_{xij}(\mathbf{u}^{(0)}) + \frac{1}{2} \frac{d}{dt} \int_Y \beta e_{ykl}(\mathbf{u}^{(1)}) \delta_{kl} dy (T^{(0)} - T_0) \end{aligned} \quad (2.72)$$

In order to evaluate the integrals in the right member of (2.72) we use the particular structure (2.41) of the first order corrector $\mathbf{u}^{(1)}$ together with the expressions (2.61), (2.63) and (2.60) of the effective coefficients C_{ijmn}^{eff} , β_{ij}^{eff} and S^* , respectively. We obtain in this way :

$$\int_Y C_{ijkl} e_{ykl}(\mathbf{u}^{(1)}) dy = L_c^2 ((C_{ijmn}^{eff} - C_{ijmn}) e_{xmn}(\mathbf{u}^{(0)}) - (\beta_{ij}^{eff} - \beta \delta_{ij}) (T^{(0)} - T_0)) \quad (2.73)$$

$$\int_Y \beta e_{ykl}(\mathbf{u}^{(1)}) \delta_{kl} dy = L_c^2 ((\beta_{ij}^{eff} - \beta \delta_{ij}) e_{xij}(\mathbf{u}^{(0)}) + S^* (T^{(0)} - T_0)) \quad (2.74)$$

With these expressions replaced in (2.72) we finally obtain

$$\begin{aligned} \frac{dd}{dt} \left(\frac{\mathcal{G}^{(1)}}{L_c} + \frac{1}{2} \frac{dC_{ijkl}^{eff}}{dd} e_{xkl}(\mathbf{u}^{(0)}) e_{xij}(\mathbf{u}^{(0)}) - \frac{d\beta_{ij}^{eff}}{dd} (T^{(0)} - T_0) e_{xij}(\mathbf{u}^{(0)}) \right. \\ \left. - \frac{1}{2} \frac{dS^*}{dd} (T^{(0)} - T_0)^2 \right) = 0 \end{aligned} \quad (2.75)$$

For evolving microcracks ($\frac{dd}{dt} \neq 0$), the last relation establishes a link between the first-order energy-release rate term $\mathcal{G}^{(1)}$ and the macroscopic quantity:

$$\mathcal{Y} = -\frac{1}{2} \frac{dC_{ijkl}^{eff}}{dd} e_{xkl}(\mathbf{u}^{(0)}) e_{xij}(\mathbf{u}^{(0)}) + \frac{d\beta_{ij}^{eff}}{dd} (T^{(0)} - T_0) e_{xij}(\mathbf{u}^{(0)}) + \frac{1}{2} \frac{dS^*}{dd} (T^{(0)} - T_0)^2 \quad (2.76)$$

which represents the volumetric density of damage energy release rate.

Used in combination with a microscopic crack propagation criterion, the equation (2.75) provides the macroscopic damage law. Consider a Griffith type criterion $\mathcal{G}^{d\epsilon} = \mathcal{G}_c$, with $\mathcal{G}_c(v_p)$ the critical fracture energy that may depend on the crack speed $v_p = \frac{l_c}{2} \frac{dd}{dt}$. For rapid propagation it may be showed [59, 112] that

$$\mathcal{G}^{d\epsilon} = g(v_p) \mathcal{G}^\epsilon \simeq \left(1 - \frac{v_p}{C_R}\right) \mathcal{G}^\epsilon \quad (2.77)$$

where $g(v_p)$ is a universal function of the crack speed that may be approximated, for mode I propagation, by $g(v_p) \simeq 1 - \frac{v_p}{C_R}$. Here C_R is the Rayleigh wave velocity and the quantity \mathcal{G}^ϵ is the instantaneous quasi-static energy release rate corresponding to a given microcrack length.

The asymptotic development (A.1-A.9) of $\mathcal{G}^{d\epsilon}$ given in the Appendix A show the link with the quasi-static energy release rate: $\mathcal{G}^\epsilon = \epsilon \mathcal{G}^{(1)}$. As remarked in the Appendix A, the development (A.1) is incomplete in the sense that it corresponds to the approximation given by the consideration of only the first order correctors. A better solution for capturing the dynamic effects is to use the expression (2.77) of $\mathcal{G}^{d\epsilon}$ together with $\mathcal{G}^\epsilon = \epsilon \mathcal{G}^{(1)}$, as

proposed in [41] for the purely elastic case. In this way, we have $\mathcal{G}^{d\varepsilon} = \varepsilon g(v_p)\mathcal{G}^{(1)}$ and we can write (2.75) in the form:

$$\frac{dd}{dt} \left(\frac{\mathcal{G}_c(v_p)}{\varepsilon g(v_p)L_c} - \mathcal{Y} \right) = 0 \quad (2.78)$$

As a linear approximation of the crack-speed dependent fracture energy (e.g. [18], [36]), we consider $\mathcal{G}_c(v_p) = \mathcal{G}_{c0}(1 + a.v_p)$ with constant parameters \mathcal{G}_{c0} and a . In this case, the use of the expression of the velocity $v_p = \frac{l_c}{2} \frac{dd}{dt}$ leads to the following damage evolution law:

$$\frac{dd}{dt} = \frac{2C_R}{l_c} \left\langle 1 - \frac{\mathcal{G}_{c0}(1 + aC_R)}{l_c\mathcal{Y} + aC_R\mathcal{G}_{c0}} \right\rangle \quad (2.79)$$

where $\langle . \rangle$ represents the positive part. We note that the microstructural length l_c is present in the equation (2.79).

It is important to note that, in order to incorporate realistic effects related to the velocity dependence of the energy of fracture, in the damage law (2.79) we considered the microscopic fracture energy $\mathcal{G}_c(v_p)$ as a function of the microcrack speed. As observed by [124, 125], the crack-speed dependency of the fracture energy is the results of micro-branching effects requiring larger energy for the propagation of the multi-crack system. In a perfect two-scale description, evolving multi-crack systems should be incorporated at the small scale. However, this would lead to insurmountable difficulties related to the energetic description of the arrest of the branches together with the propagation of the main microcrack, to the speed influence on the geometry of the multi-crack system producing damage-rate dependent effective coefficients and making difficult the obtention of the damage evolution law or to the non-uniqueness of the cell solutions related to micro-branching instabilities and compromising the well-definiteness of the homogenized response. To avoid all these difficulties, we proposed a relatively simple solution to incorporate the velocity effects in the damage law. This allowed us to rigorously obtain the damage evolution law by homogenization and, as we will see in the last section, to have good agreements between the model predictions and the experimental results.

The damage energy-release rate \mathcal{Y} is calculated with the displacement and temperature fields such that (2.79) forms with the equations (2.55-2.58) a coupled thermoelastic and damage system. In order to obtain the temperature equation in a completely macroscopic form, we should replace the expression of

$$\mathcal{G}^{(1)} = \frac{\mathcal{G}_{c0}(1 + a.v_p)}{\varepsilon g(v_p)} = \frac{\mathcal{G}_{c0}L_cC_R(2 + a.l_c\frac{dd}{dt})}{l_c(2C_R - l_c\frac{dd}{dt})}$$

In this way (2.55) becomes:

$$c^{eff} \frac{\partial T^{(0)}}{\partial t} + T^{(0)} \beta_{ij}^{eff} \frac{\partial e_{xij}(\mathbf{u}^{(0)})}{\partial t} + \frac{\partial Q_i^{(0)}}{\partial x_i} = \frac{\mathcal{G}_{c0}C_R(2 + a.l_c\frac{dd}{dt})}{l_c(2C_R - l_c\frac{dd}{dt})} \frac{dd}{dt} \quad (2.80)$$

as the macroscopic temperature equation in which the right member source term represents the damage dissipation as heat.

Finally, we note that the expression of the heat production term in the equation (2.80) is the consequence of the particular expressions considered for $g(v_p)$ and $\mathcal{G}_c(v_p)$. The

general form of the right member in the macroscopic temperature equation is $\frac{\mathcal{G}_c(\frac{l_c}{2} \frac{dd}{dt})}{l_c g(\frac{l_c}{2} \frac{dd}{dt})} \frac{dd}{dt}$. For the examples given in the next sections the particular expression (2.80) is adopted.

2.5 Local macroscopic response

The objective of this section is the study of the local macroscopic behavior predicted by the new damage model. We first analyse the effective coefficients as functions of the damage variable using interpolations of their numerical values computed with the numerical solutions of the cell problems for a number of microcrack lengths. Then we illustrate the local macroscopic response of the model for uniaxial loadings with special emphasis on the influence of microscopic dissipation as heat, the loading rate, the size of the microstructure and the initial damage value.

The material parameters used for the computations correspond to a PMMA polymer : the dynamic Young modulus $E = 5 \text{ GPa}$, the Poisson ratio $\nu = 0.37$, the mass density $\rho = 1180 \text{ kg.m}^{-3}$, the thermal expansion coefficient $\alpha = 10^{-4} \text{ K}^{-1}$, the heat capacity $c = 10^6 \text{ J.m}^{-3}.\text{K}^{-1}$ and the thermal conductivity $k = 0.2 \text{ W.m}^{-1}.\text{K}^{-1}$.

For the fracture energy, we adopt the approximation given in the previous section $\mathcal{G}_c(v_p) = \mathcal{G}_{c0}(1 + a.v_p)$ with $\mathcal{G}_{c0} = 400 \text{ J.m}^{-2}$ and $a = 0.025 \text{ s.m}^{-1}$. This choice of parameters is consistent with the values of the fracture energy at different crack tip speeds reported in the literature (e.g., [18], [36]) for PMMA polymers.

2.5.1 Homogenized coefficients

The effective coefficients are calculated with the formulae (2.59-2.65) using the characteristic functions ξ^{pq} , ϕ and θ that are solutions of the cell problems (2.42-2.43), (2.44-2.45) and (2.47-2.49), respectively.

For 11 values of the normalized microcrack length $d \in [0, 1]$, these characteristic functions are computed numerically with the Finite Element method, using the FEM software COMSOL Multiphysics. The corresponding numerical values of the effective coefficients are then interpolated with polynomial functions of the damage variable. In the extreme case of a completely broken cell ($d = 1$), analytical solutions of the cell problems can be obtained and used for to calculate the effective coefficients at failure limit.

In Figure 2.3 the homogenized elastic coefficients $C_{ijkl}^{eff}(d)$ are represented versus the damage variable d . They are normalized with those for $d = 0$, corresponding to the virgin material. Both the discrete numerical values, computed with the finite element solutions, and the interpolation curves are shown.

While the solid matrix is assumed to be isotropic, corresponding to the effective elastic coefficients $C_{ijkl}^{eff}(0)$, the presence of microcracks induces an orthotropic effective response. The effective coefficients have a nonlinear dependence on the damage variable, with a more abrupt loss of rigidity when approaching the limit state $d = 1$. At failure, when the crack completely separates the cell into two distinct parts, vanishing response is obtained for loadings in the normal direction, given by the coefficients C_{2222}^{eff} and C_{1122}^{eff} , and in shear loadings by C_{1212}^{eff} . Only partial degradation is obtained in the response to loadings parallel to the crack direction, as observed for $C_{1111}^{eff}(d)$. Analytical solution calculations allow us

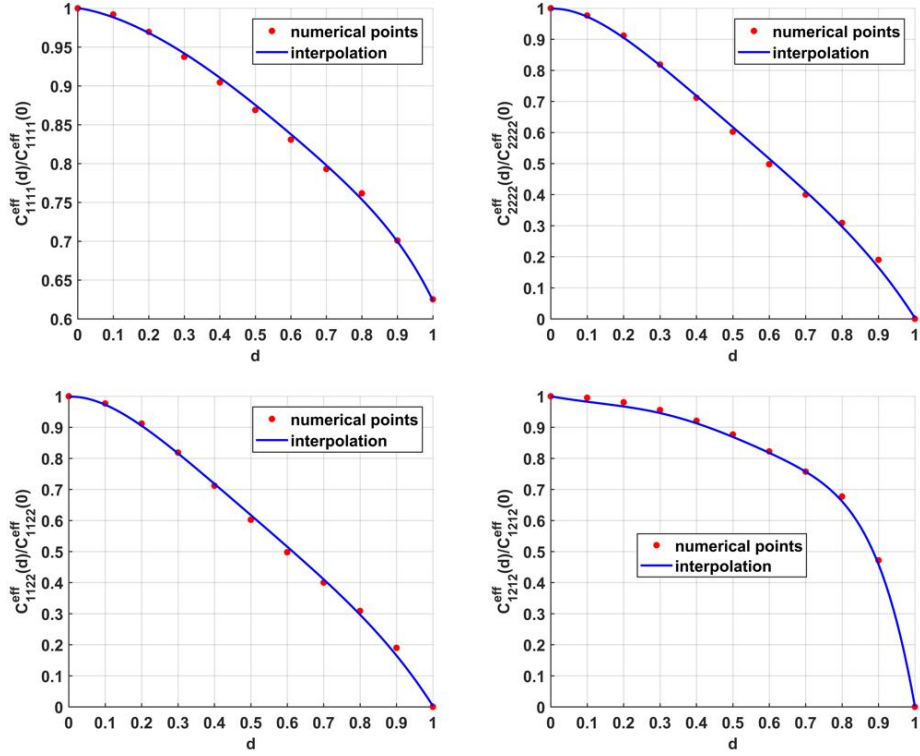


Figure 2.3: Homogenized coefficients C_{ijkl}^{eff} versus the damage variable d : computed values and interpolation curves.

to obtain the expression of the coefficient $C_{1111}^{eff}(1) = \frac{E}{1-\nu^2}$ for a completely fractured cell. This corresponds to the last point value in Figure 2.3.

The effective stress-temperature moduli β_{ij}^{eff} are represented in Figure 2.4. With the increase of the damage value, the upper and lower parts a cell are progressively separated by a traction-free and thermally isolating crack and the thermo-mechanical coupling is reduced. In particular, as a consequence of the microcrack orientation, the coefficient β_{22}^{eff} is vanishing at the complete failure limit. As expected, the thermal expansion is less affected in the direction of the crack line. In fact, the analytical solution of the cell problem for $d = 1$ gives the expression $\beta_{11}^{eff}(1) = \frac{E\alpha}{1-\nu}$ for this non-vanishing coefficient.

As concerns the thermal modulus S^* , that appears in the expression of the effective specific heat $c^{eff} = c + T^{(0)}S^*$, it is represented in the left side of the Figure 2.5 as function of damage variable. The virgin material ($d = 0$) has the heat capacity c , while for a given $d \neq 0$ the effective specific heat is increasing with the increase of S^* . The presence of a thermally isolating crack in the cell determine the necessity of more heating to increase the temperature with a unit value. At $d = 1$ we determine the analytical expression $S^*(1) = E\alpha^2 \frac{1+\nu}{(1-2\nu)(1-\nu)}$ provided by the analytical solution of the problem (2.44-2.45).

On the right side of Figure 2.5 the effective thermal conduction coefficient $k_{22}^{eff}(d)$ is represented vs the damage value. The virgin material has isotropic conductivities $k_{11}^{eff}(0) = k$, $k_{22}^{eff}(0) = k$ and $k_{12}^{eff}(0) = 0$, while the presence of a crack induces anisotropy

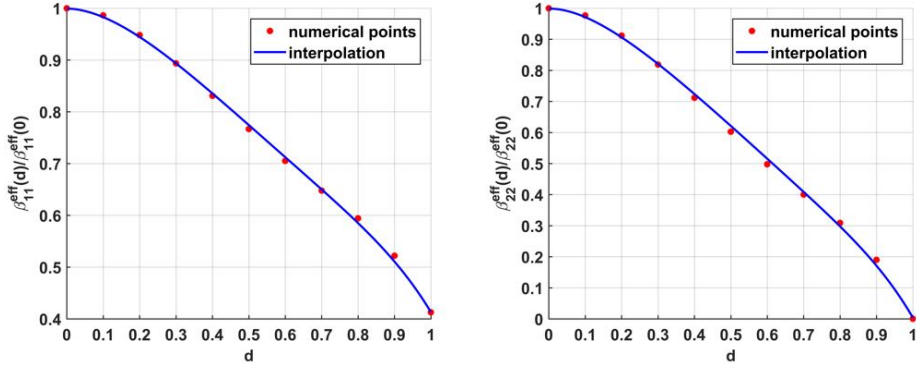


Figure 2.4: Effective stress-temperature moduli β_{11}^{eff} and β_{22}^{eff} versus damage.

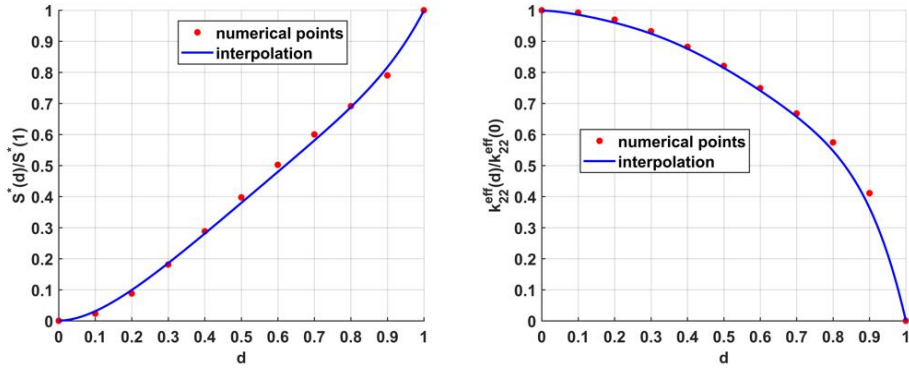


Figure 2.5: Effective thermal modulus $S^*(d)$ and conductivity coefficient $k_{22}^{eff}(d)$.

by reduction of $k_{22}^{eff}(d)$ and a constant conductivity $k_{11}^{eff}(d) = k$. This is the consequence of the thermally isolating crack-face conditions. For larger values of d the overall conductivity in the direction normal to the crack is decreasing to $k_{22}^{eff}(1) = 0$, corresponding to isolating a crack traversing completely the cell.

2.5.2 Local response analysis

In order to analyse the homogenized response of the new damage model, we impose a strain history $e_{x22}(u^{(0)})(t)$, with constant strain rate \dot{e}_{x22} , as the only non-vanishing strain component. Under this loading, we determine the local response of the model in effective stress, damage and temperature by solving the equations (2.79) and (2.80). For the description of rapid failure phenomena, we assume adiabatic conditions at the macroscopic level by neglecting the conduction term in (2.80). In this case, we have a coupled system of nonlinear differential equations for $T^0(t)$ and $d(t)$ that is solved numerically using a forward Euler finite-difference scheme.

Unless specified, the material parameters are those given in the beginning of this section. The initial temperature is $T_0 = 20^\circ C$, $d_0 = 0.1$ and the strain rate value is

$\dot{e}_{x22} = 5000 \text{ s}^{-1}$. The interpolated effective coefficients are used in the computations.

2.5.2.1 Influence of the heat sources

We first analyse the influence of heating during damage evolution. The temperature equation (2.80) is solved with and without the right member, together with the damage evolution law (2.79).

The obtained temperatures are plotted in Figure 2.6 versus the applied strain $e_{x22}(u^{(0)})$. The results are presented for three values of the microstructural length: $l_c = 10^{-4} \text{ m}$; $l_c = 10^{-5} \text{ m}$ and $l_c = 10^{-6} \text{ m}$. The continuous lines represent the temperature $T^{(0)}$ when the crack-tip dissipation as heat is taken into account, while the dotted line corresponds to temperature evolutions without heating sources.

In the first stage, when the crack propagation has not been activated, we note a cooling effect, identical for the two models. This is in accordance with the experimental observations (e.g., [116], [23]) reporting temperature decrease near the crack tip during the initiation phase of dynamic fracture and will be discussed in the next section where such an experiment will be reproduced numerically.

Once the propagation starts, the crack-tip heating is activated and influences the evolution of $T^{(0)}$ which is increasing. When the heating term is neglected, the temperature is still decreasing during microcrack growth. For smaller sizes of the microstructure, the increase of the temperature is more important and more rapid. As will be observed in the next example, in this case the microcrack propagation is more rapid leading to higher dissipation rates at the tips and the temperature can thus increase up to a few hundreds of degrees.

2.5.2.2 Influence of the microstructural size l_c

To get more insight on the influence of the microstructural length l_c on the thermo-mechanical response of the model, we represent in Figure 2.7 the macroscopic stress $\Sigma_{22}^{(0)}$, damage variable d and temperature $T^{(0)}$ versus the applied strain $e_{x22}(u^{(0)})$, for three lengths: $l_c = 5 \times 10^{-4} \text{ m}$; $l_c = 5 \times 10^{-5} \text{ m}$ and $l_c = 5 \times 10^{-6} \text{ m}$.

Fine microstructures are more resistant to damage initiation since smaller microcracks are more difficult to propagate. It can be observed that, once the propagation initiated, the response of large microstructures is more ductile. This is the consequence of the fact that, for larger periods, a larger part of the supplied energy is stored as kinetic and elastic energy in the vicinity of the microcrack lips during propagation such that a smaller amount of energy remains available for damage.

The process is accompanied by a temperature drop in the elastic regime followed by a reverse tendency during damage growth. For small l_c , the damage propagates rapidly with more dissipated energy converted to heat. This leads to a more rapid temperature rise up to quite elevated values. For large l_c , the damage rate is less important and so is the corresponding dissipation heating. Consequently, the temperature evolution is not so rapid and its final value is smaller.

Figure 2.8 shows the final values of the temperature, at complete failure, and its minimum values, corresponding to the end of the elastic cooling phase, for different sizes

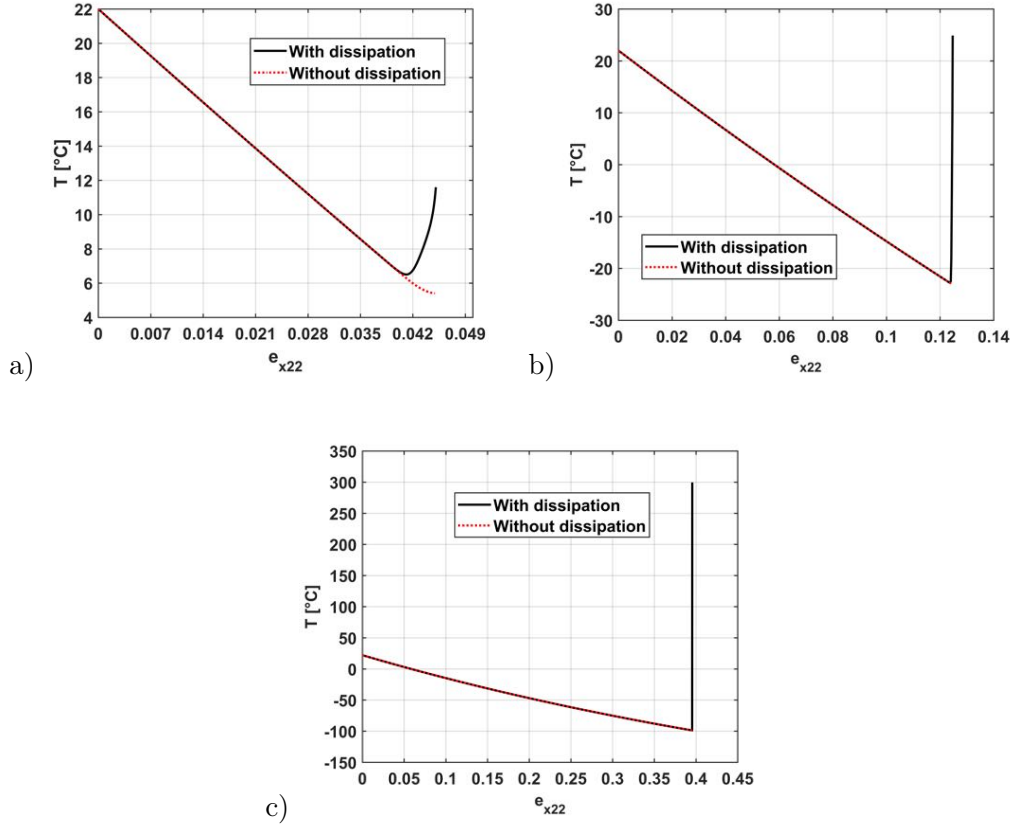


Figure 2.6: Temperature $T^{(0)}$ versus the applied strain $e_{x22}(u^{(0)})(t)$, for three sizes of the microstructure: a) $l_c = 10^{-4} m$; b) $l_c = 10^{-5} m$; c) $l_c = 10^{-6} m$. Evolutions with (continuous line) or without (dotted line) crack tip heating.

of the microstructure. For l_c of the order of a few microns, the temperature at failure may be of hundreds of degrees while for l_c of some tens of microns we reach an asymptotic value of about ten degrees Celsius. For small values of l_c the evolution of $T^{(0)}$ passes through low negative values, while for higher microstructural lengths the minimum temperature is of about $0^\circ C$.

Globally, the damage behavior for finer microstructures is more brittle with higher dynamic tensile strength and this induces more substantial temperature variations during both cooling and heating regimes.

2.5.2.3 Influence of the rate of loading

We study now the influence of the loading rate. The effective stress, damage and temperature are represented in Fig. 2.9 for three strain rates: $\dot{e}_{x22} = 100 s^{-1}$, $\dot{e}_{x22} = 1000 s^{-1}$, $\dot{e}_{x22} = 10000 s^{-1}$. The microscopic length parameter is chosen $l_c = 3 \times 10^{-4} m$.

As already observed in the purely mechanical case [82], the increase of the loading rate induces more ductility in the macroscopic response of the material. This is the consequence of the inertial effects incorporated in the damage model. At high strain

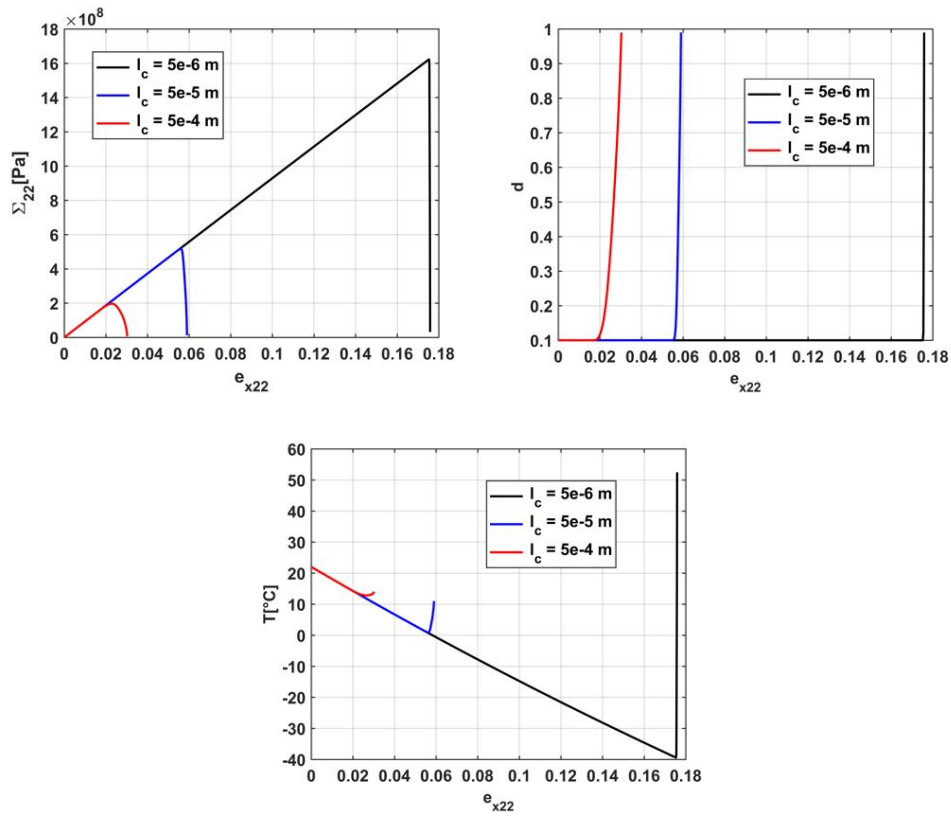


Figure 2.7: Influence of size of the microstructure on the effective stress, damage and temperature for: $l_c = 5 \times 10^{-4}$ m; $l_c = 5 \times 10^{-5}$ m; $l_c = 5 \times 10^{-6}$ m.

rates, a more important part of the supplied energy is stored as kinetic energy around microcrack tips, causing a slowing effect in the propagation of microcracks. Consequently,

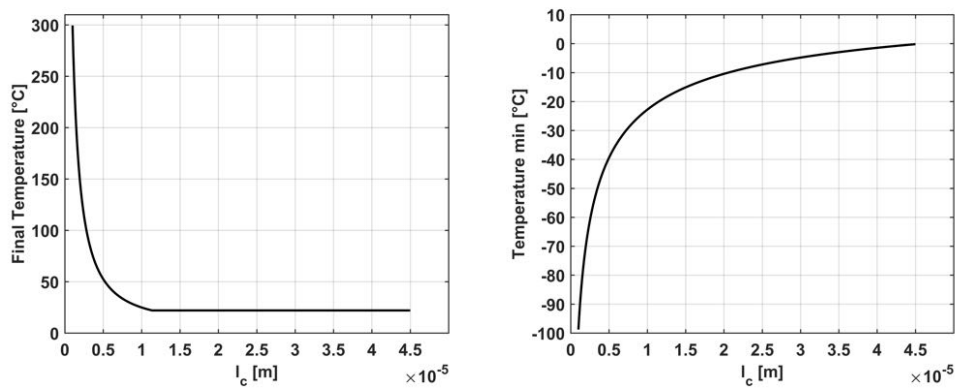


Figure 2.8: Final value of the temperature (at $d = 1$) and its minimal value (at the end of the cooling phase) versus the size of the microstructure l_c .

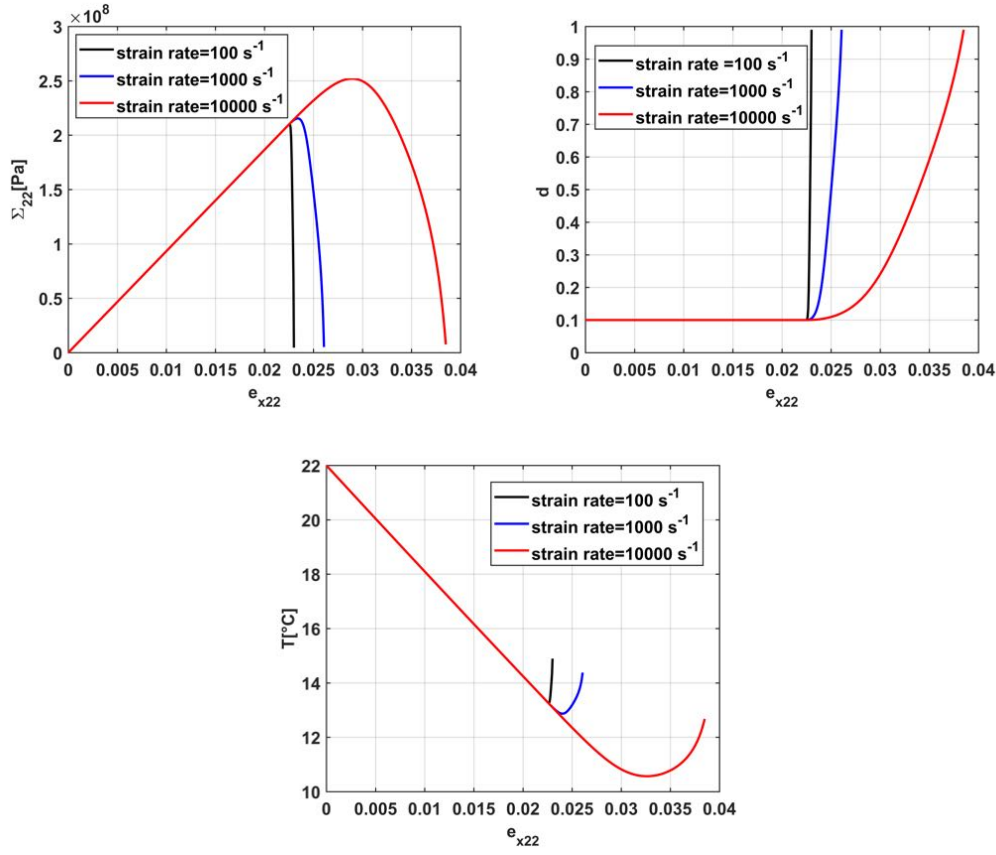


Figure 2.9: Effective stress, damage and temperature for different strain rates: $\dot{e}_{x22} = 100 \text{ s}^{-1}$, $\dot{e}_{x22} = 1000 \text{ s}^{-1}$ and $\dot{e}_{x22} = 10000 \text{ s}^{-1}$.

the dynamic strength is increased and the response in the evolving damage regime is more ductile, as can be observed in the plotted stress and damage evolutions.

When the damage initiation is retarded, the cooling regime is extended as show the temperature curves in Fig. 2.9. Since the damage rate controls the amount of energy converted to heat, for higher loading rates the model predicts lower heat production during the propagation phase. Finally, the temperature curves in Fig. 2.9 are the consequence of the competition between the duration of the heating regime and the amount of energy dissipated as heat. For high strain rates, the dissipation is less important but the heating time is longer, while for slower strain evolutions more substantial amounts of energy are dissipated in shorter times, due to the rapid damage growth.

It worths remarking that for smaller microstructural sizes the ductility is substantially reduced and the heating increases considerably leading to elevated final temperatures for a larger range of strain rates. This effect can be observed by comparison with the temperature curves in Figures 2.6 and 2.7.

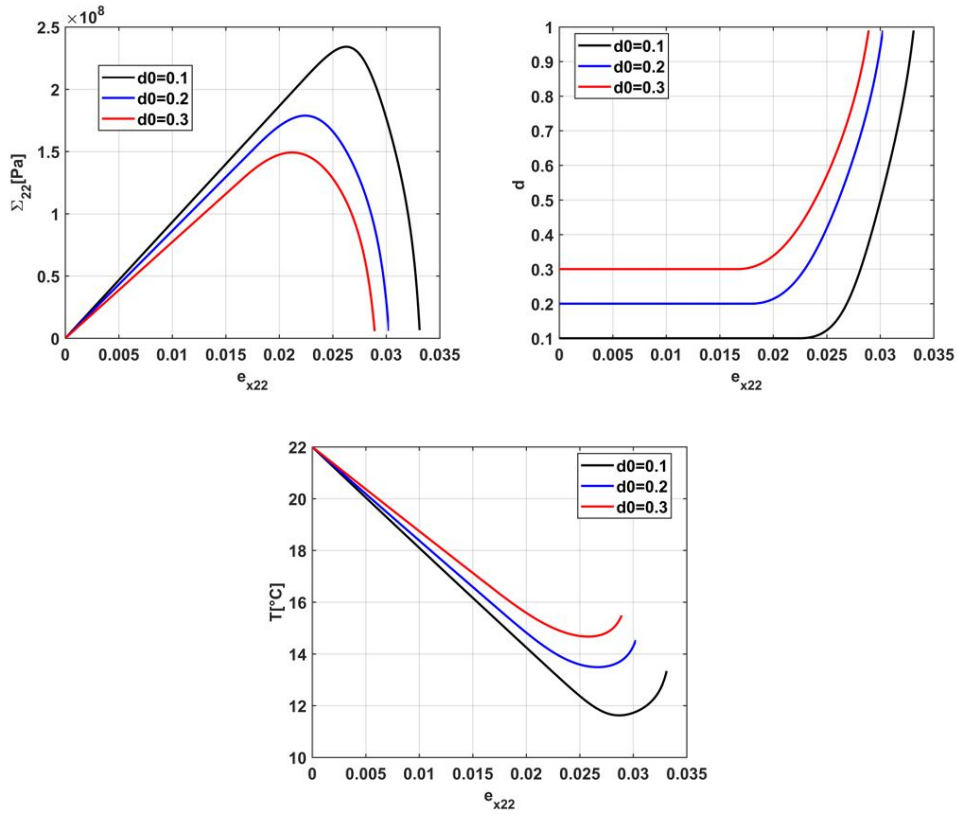


Figure 2.10: Macroscopic fields for initial values of damage: $d_0 = 0.1$, $d_0 = 0.2$ and $d_0 = 0.3$.

2.5.2.4 Influence of the initial damage

We finally study the role of the initial value of damage d_0 . The response of the model is represented in Fig. 2.10 for $d_0 = 0.1$, $d_0 = 0.2$ and $d_0 = 0.3$ and the small-scale length $l_c = 3 \times 10^{-4} m$.

As expected, smaller values of d_0 lead to higher tensile strengths, retarded damage initiation but followed by a more rapid evolution. The stiffness decreases with the increase of the initial damage.

The retarded damage initiation increases the elastic cooling regime such that the minimum temperature is lower for smaller d_0 . During the propagation phase, the faster evolution of damage obtained for smaller d_0 leads to increased heating such that the temperature rise is more important. For higher values of d_0 , the heating phase starts earlier and the final temperature is higher even if the damage rate and the associated heating are smaller.

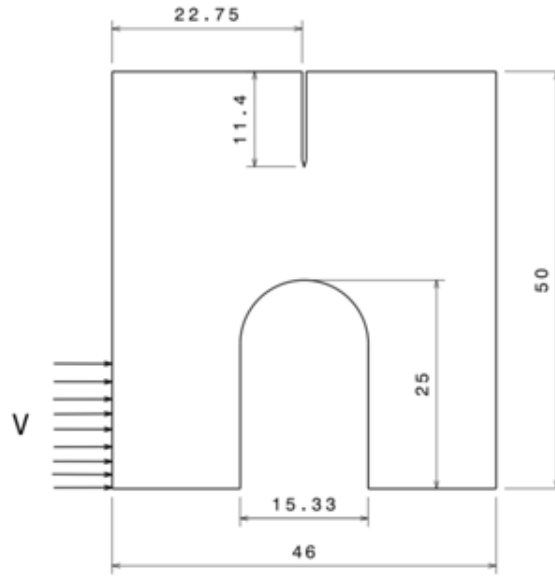


Figure 2.11: Geometry of the specimen, with dimensions in *mm*. The impact velocity V is applied over a region of 16.5 mm .

2.6 Numerical Simulation of the CCS Impact Test

We present in this section numerical simulations of the Compact Compression Specimen (CCS) test and we compare the results with the experimental data reported in [115, 116, 23] for thermal evolutions during failure initiation and propagation phases.

The geometry of the CCS specimen is shown in Figure 2.11. The material is the commercial polymethylmethacrylate (PMMA). An impact loading is applied through a Hopkinson steel bar of 16.5 mm diameter such that tensile failure is initiated in the upper part, at the tip of a pre-existing notch where a small fatigue crack has been processed. Impact velocities in the range $8 - 65\text{ m/s}$ have been applied. The specimen is instrumented with a fracture gage and an embedded thermocouple, allowing measurements of the fracture time and the temperature in the vicinity of the tip. The fracture gage and the thermocouple are placed at 1 mm distance ahead of the fatigue crack tip.

Under impact loading, mixed mode fracture is initiated at the tip of the pre-existing crack and traverses the specimen vertically following a slightly curved path in dominant mode I propagation. The measurements show that, prior to failure initiation, the near-tip temperature can drop by several tens of degrees. This cooling phase is followed by a significant temperature rise during the fracture growth, the crack tip behaving like a heat source. In this heating phase, the temperatures at the tip can mount up to a few tens of degrees higher than the initial temperature of the specimen. Such thermal variations indicate the necessity of adopting a thermo-mechanical framework for the modeling of dynamic failure.

As shown for instance in [23] and [18], adiabatic conditions can be reasonably assumed in the description of such dynamic fracture tests and for short time intervals around the

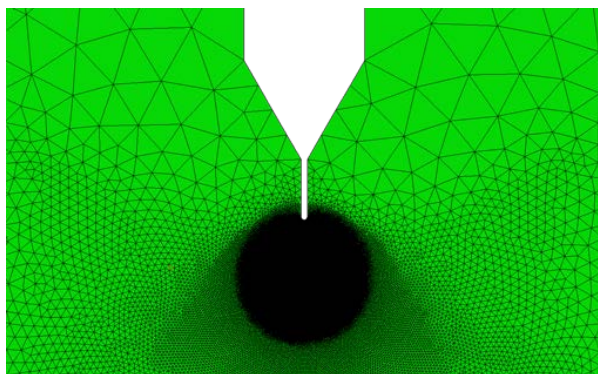


Figure 2.12: Local geometry near the notch tip and finite element mesh with refinement in the failure initiation zone.

failure initiation instant. In the present simulations we assume macroscopic adiabatic conditions by neglecting the conduction term in the left-hand side of the temperature equation (2.80).

To simulate the compact compression experiment, we implemented the thermoelastic damage model as a ABAQUS VUMAT user material subroutine using explicit time integration. Under the adiabaticity condition, dynamic elasticity computations can be performed in Abaqus Explicit with the complete resolution of the temperature and damage equations in the user subroutine. On a time step and for given strain increments in an integration point of the FE mesh, we first solve the damage law (2.79) using a Euler forward scheme, with the temperature value at the beginning of the step and a non-decreasing numerical condition for damage. Then, with the computed damage at the end of the time step, a forward Euler scheme is also employed for the adiabatic temperature equation (2.80). After the computation of the new values of temperature and damage, the stress components are updated according to the constitutive relation (2.57).

A FE mesh is constructed with plane strain 3-nodes linear elements CPE3. The local geometry near the notch tip and the finite element mesh refined in the region of expected rupture initiation are shown in Figure 2.12. The length of the "fatigue crack" is 0.5 mm and its thickness is 0.05 mm with a rounded tip (magnified in Fig. 2.13). The element size in the region near the tip is about 0.003 mm . The impact loading is modeled by an applied velocity $V = 30\text{ m/s}$ over a boundary zone of 16.5 mm , as in Fig. 2.11, corresponding to the diameter of the Hopkinson bar.

The material parameters of the PMMA material are those given in the beginning of Section 5 and the microstructural length value is chosen as $l_c = 6 \times 10^{-5}\text{ m}$. Since the relevant macroscopic dimensions L_c of the specimen are of order of tens of millimeters, the separation of scales assumption (2.14) is verified.

In the left side of Figure 2.13, the computed damage variable d is represented. Element deletion is activated at the damage value $d = 0.99$. We note the initiation of a macrocrack with a kink angle with respect to the vertical direction; such a failure path deviation can be retrieved in the experimental observations [115]. Microbranching effects are observed in the damaged zone.

The computed temperature field near the tip of the propagating macrocrack is shown

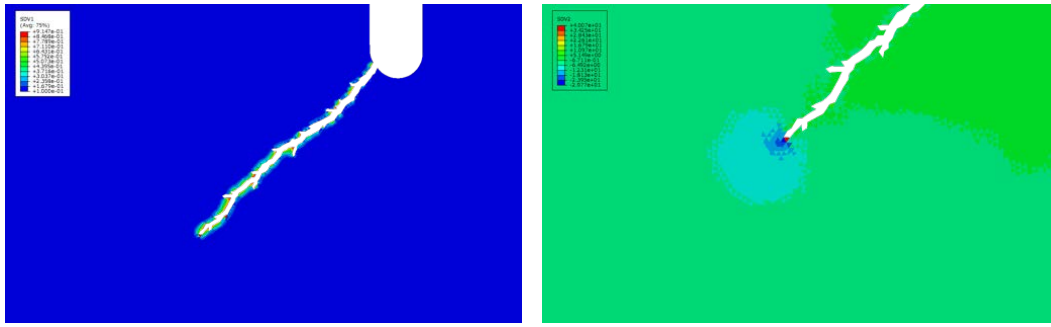


Figure 2.13: Left: damage variable represented with element deletion at complete failure. Right: temperature field with cooling and heating zones near the moving tip.

in the right image of Figure 2.13. Ahead of the tip a cooling zone is present, with a minimum relative temperature of about -30°C , while the tip is behaving like a heat source with a maximum relative temperature of about 40°C . In Figure 2.13, the temperature is represented without average element output at nodes. The obtained temperature distribution is the consequence of the small-scale heating accounted by the damage model.

We note that the highly localized heat source in Fig. 2.13 is in agreement with experimental results of [62] who estimated the width of the hot zone along the crack path to be about $1 - 3 \mu\text{m}$, which also corresponds to the observed maximal craze thickness in PMMA (e.g., [48]).

The measured values of the temperature at 1 mm from the tip of the notch reported in [115] are given in Figure 2.14 together with the corresponding computed values in four elements situated in the same region. Similar temperature variations can be noticed: a cooling regime with a temperature drop of about $25 - 30^{\circ}\text{C}$ from the initial value

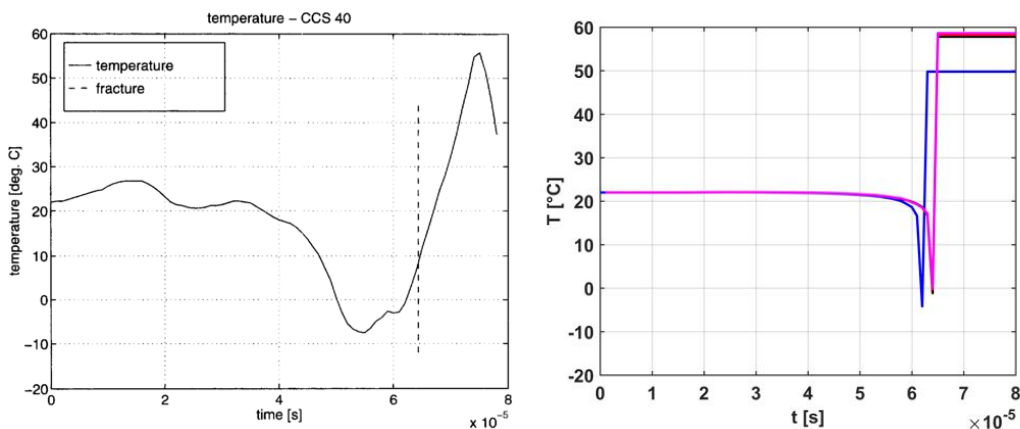


Figure 2.14: Temperature variation at 1 mm from the tip of the notch: measured values (left) from [115] and computed values (right) in 4 neighbor elements in the area of the thermocouple location.

$T_0 = 22^\circ C$, followed by a heating regime in which the rise of the temperature may be of $30 - 35^\circ C$.

These results confirm the capacity of the model to correctly predict the thermal evolutions associated with the dynamic failure of brittle materials.

2.7 Heat conduction versus adiabatic conditions

In the analysis of the previous sections, we assumed adiabatic heating for the evolution of temperature. The thermo-mechanical damage model was implemented with the solution of the equation (2.80), in which the conduction term has been neglected, and the damage law (2.79). In this section we analyse the prediction of the model without the adiabaticity assumption. Our aim is to verify if the adiabatic conditions assumed at the macroscopic level represent are reasonable for the damage model predictions.

We implemented the model in a VUMAT user material subroutine for a fully coupled thermal-stress analysis in ABAQUS. On a time step, the damage law (2.79) is solved at every integration point for given strain increments and temperature. The stresses are updated using the obtained damage value. The fully coupled thermal-stress analysis of ABAQUS allows us to obtain the value of temperature required for the next time step [1]. As in the previous section, a Euler forward scheme is used to solve the damage law. Numerical simulations are performed with the explicit temperature-displacement analysis [1]. The results are compared with those obtained using the implementation in the previous section.

2.7.1 Single element test

As a simple check of the numerical implementation, we first consider a single element test as represented in Figure 2.15. On a square of 1 mm side, we apply along the x_1 -axis a velocity boundary condition on the right side while the left side is fixed. The displacements of the top and bottom boundaries along the x_2 -axis are suppressed with the boundary

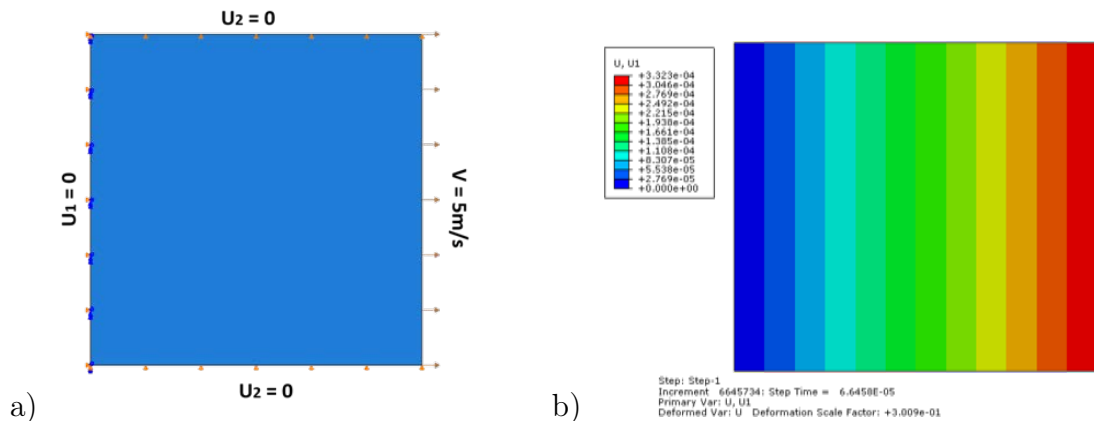


Figure 2.15: One-element test : a) boundary conditions and b) displacement u_1 .

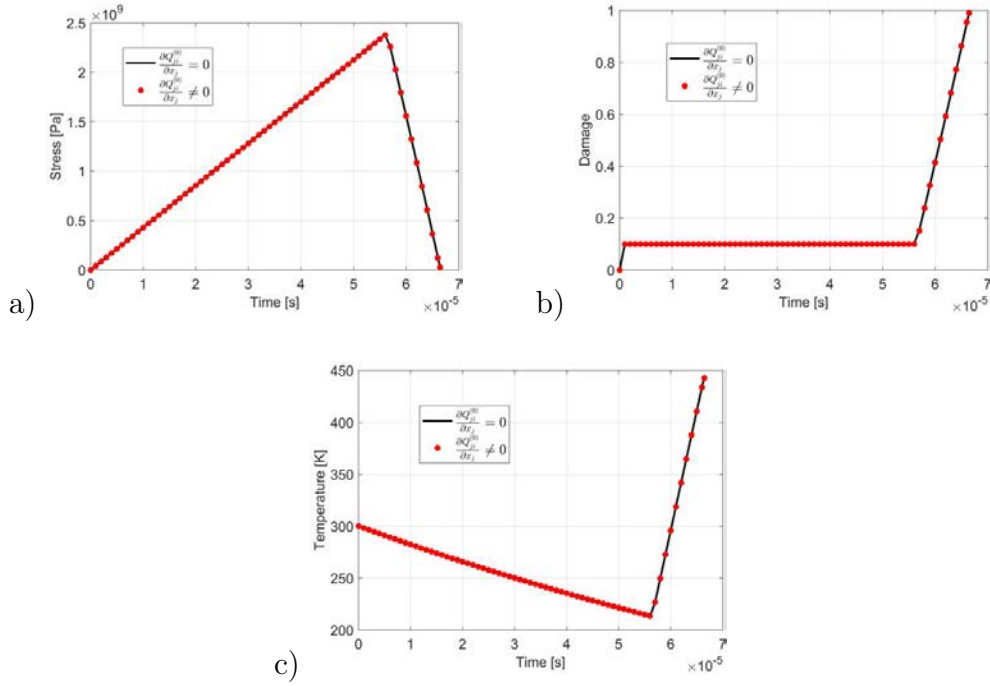


Figure 2.16: Stress Σ_{11} , damage variable d and macroscopic temperature $T^{(0)}$ obtained with and without adiabatic assumption

condition $u_2 = 0$. The plane stress 4-node bilinear displacement and temperature reduced integration with hourglass control element CPS4RT is used for the ABAQUS fully coupled thermal-stress analysis. The loading velocity is $V = 5 \text{ m.s}^{-1}$ giving the corresponding strain rate of 5000 s^{-1} .

For this FEM analysis we consider the microstructural size $l_c = 10^{-6} \text{ m}$ while initial values of the damage variable and temperature are $d_0 = 0.1$ and $T_0 = 300 \text{ K}$, correspondingly. We adopt for the fracture energy $\mathcal{G}_c = 400 \times (1 + 0.025 \times v_p) \text{ J.m}^{-2}$.

As expected, the results obtained with the analysis exhibit spatial variation of the displacement in the horizontal direction (Figure 2.15) while in the vertical direction no displacement is obtained. In the case of single element, heat flux is not involved in the FEM computation. In these conditions, numerical predictions of damage, temperature and stress evolutions obtained with and without the assumptions of adiabatic heating are similar as shown in Figure 2.16.

2.7.2 Numerical simulations of an impact test

In [18], an experimental setup for simultaneous detection of thermal effects and crack-tip speed measurement during dynamic crack propagation is presented. An array of infrared detectors was used for thermal signal measurements while a propagation gage made with conducting silver paint lines allows the monitoring of crack evolution. A cylindrical steel projectile with a diameter of 38 mm is accelerated with velocity ranging between 8 and $40 \text{ m} \times \text{s}^{-1}$ in order to symmetrically impact rectangular pre-notched PMMA specimens, as represented in Figure 2.17. Mode I crack growth is then induced in the specimen. The

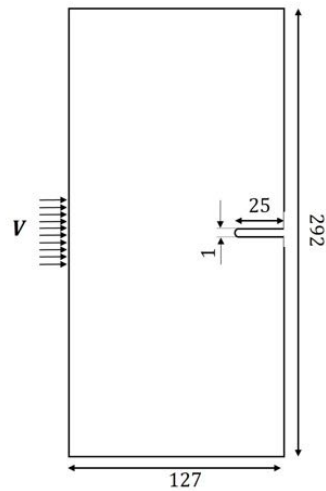


Figure 2.17: Rectangular PMMA specimen with initial notch subjected to impact loading

variation of temperature is detected on a location at $\sim 15 - 20 \text{ mm}$ of the initial notch tip.

We use our thermo-mechanical damage model to perform the numerical simulations of this experimental test [18]. The details of the FE mesh configuration are showed on Figure 2.18. This mesh is constructed with 3-nodes plane stress elements CPS3T. The average element size in the refined region near the initial notch tip is $1 \mu\text{m}$ and the dimensions of the model specimen in Figure 2.18 are scaled with 1/10 ratio. The impact loading is applied by defining a constant velocity of $8 \text{ m} \times \text{s}^{-1}$ in a symmetrical way on a boundary

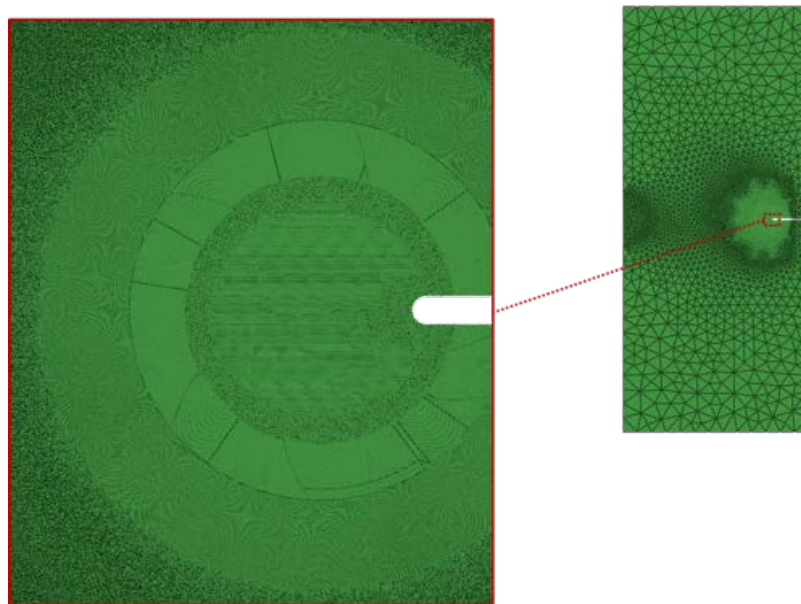


Figure 2.18: FE mesh with refinement near the initial notch tip.

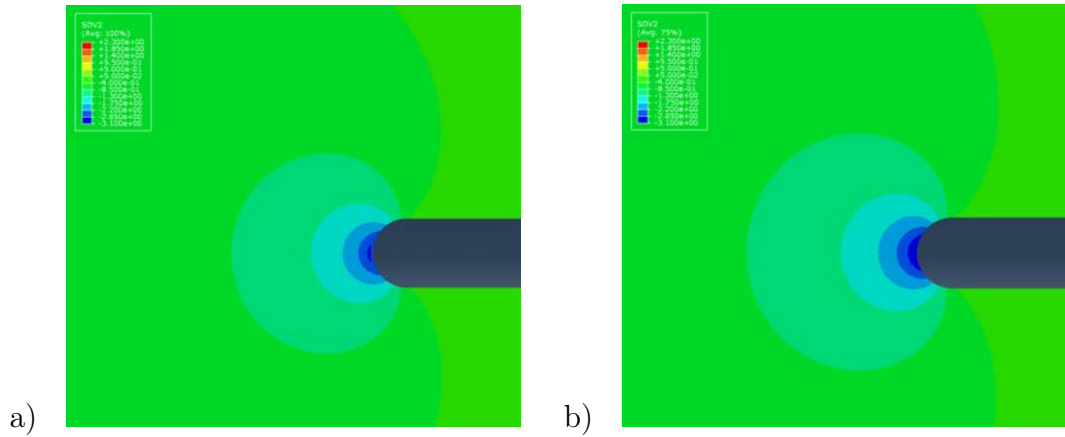


Figure 2.19: Temperature contours during the crack initiation regime: simulations with (a) and without (b) heat conduction.

of 3.8 mm and the initial value of the temperature $T_0 = 300\text{ K}$ is defined.

The Figures 2.19 and 2.20 show the temperature contours during the initiation and the propagation regimes, respectively, obtained by computations with (a) and without (b) heat conduction. We observe that the temperature contours ranging in $-3\text{ K} < \Delta T < 30\text{ K}$ are relatively similar. The results are also consistent with the observations of other authors (e.g. [23]) concerning the validity of the adiabatic conditions for short time scales during rapid failure.

In Figure 2.21 we show the evolution of temperature in a point situated at a distance of 0.6 mm from the initial notch tip. The two simulations exhibit a temperature drop which is the effect of the thermoelastic coupling term in (2.80) followed by temperature rise due to rapid damage propagation.

We end this section by considering the FE model specimen with the real dimensions given in Figure 2.17 and comparing the numerical results with the experimental observations for this new test. In the case of an impact velocity of $8\text{ m} \times \text{s}^{-1}$ and $l_c = 6 \times 10^{-5}\text{ m}$, the simulations predict similar evolutions of crack-tip velocity as the experimental data

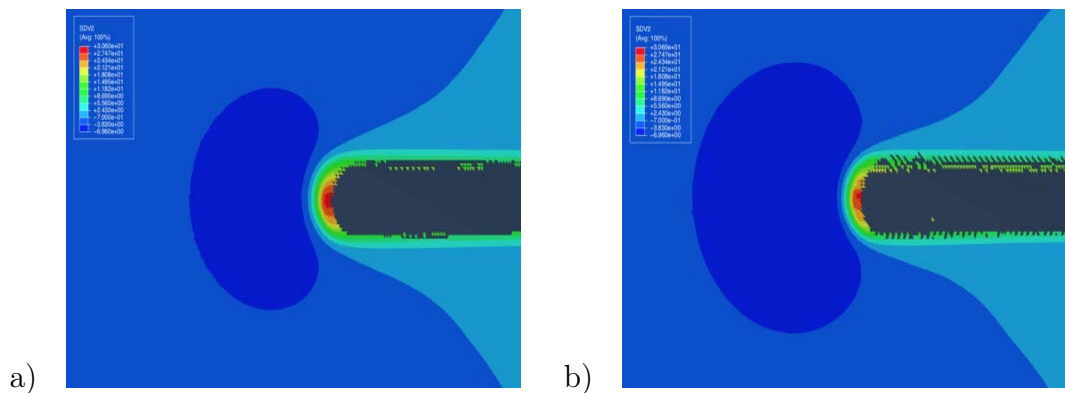


Figure 2.20: Temperature contours during the crack propagation regime: simulations with (a) and without (b) heat conduction.

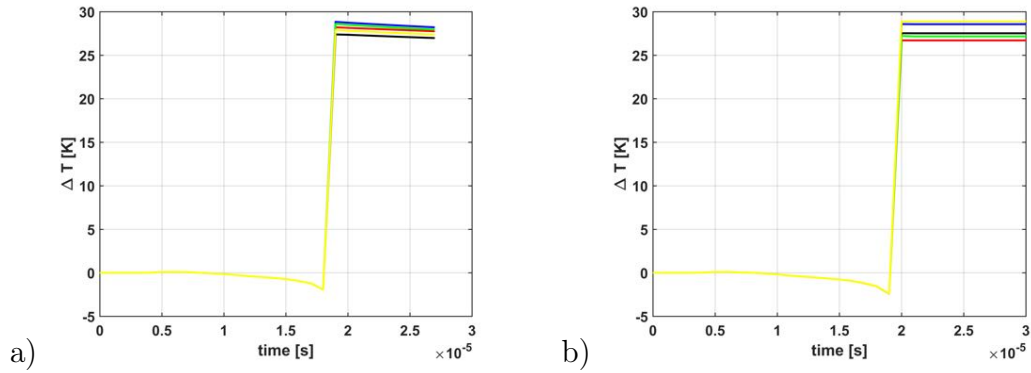


Figure 2.21: Evolutions of temperature in a point situated at a distance of 0.6 mm from the initial notch tip.

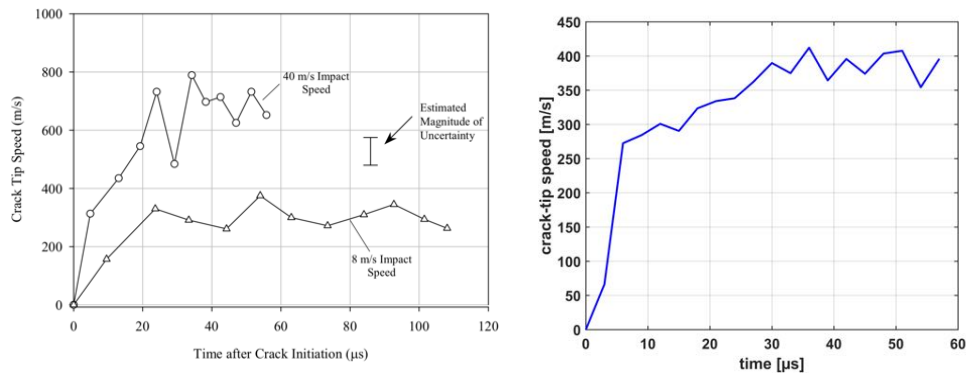


Figure 2.22: Crack-tip velocity during propagation: (a) experimental results [17] vs (b) numerical results

of [17]. As shown in Figure 2.22, the crack-tip speed reaches a value of $400\text{ m} \times \text{s}^{-1}$ at about $50\ \mu\text{s}$ after crack initiation. This value is in agreement with that measured in the experiments if we take into account the data uncertainty of $\pm 50\text{ m} \times \text{s}^{-1}$.

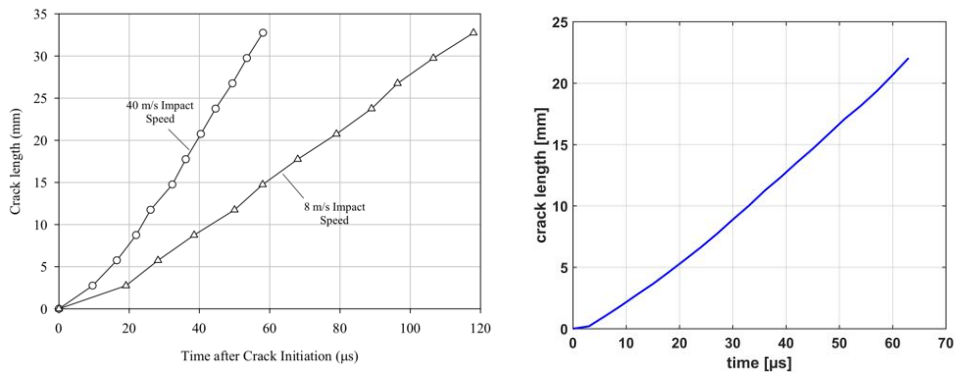


Figure 2.23: Crack length evolution with time: (a) experimental results [17] vs (b) numerical results.

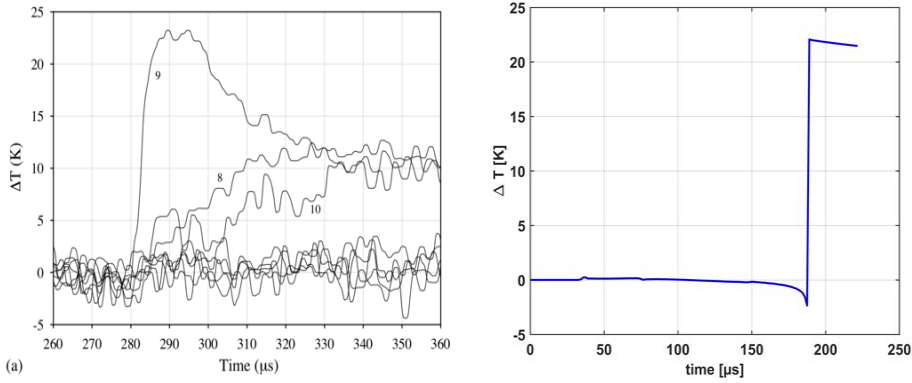


Figure 2.24: Temperature evolution with time : (a) experimental results [17] vs (b) numerical results.

Figure 2.23 gives a comparison between the FE simulations and the experimental measurements of crack length growth. The evolutions are rather similar, with some small differences. For instance, the simulations show a length of 20 mm reached at about $55 - 60\ \mu s$ while this value is obtained a little bit later, after $70\ \mu s$, in the experiments.

The thermal signal in a point at 20 mm of the initial notch tip is given by Figure (2.24). From the simulations, a rising of $\Delta T_+ = 22\text{ K}$ after a drop of $\Delta T_- = -2\text{ K}$ is obtained for the temperature evolution. These values of temperature are similar to the measured experimental values of about $\Delta T_+ = 23\text{ K}$ and $\Delta T_- = -2\text{ K}$, shown on Figure(2.24). The shift in the time axis corresponds to different initial time instants between simulations and experiment.

2.8 Conclusions

We constructed a coupled thermo-mechanical damage model for brittle materials based on dynamic evolutions of microcracks with dissipated fracture energy converted to heat at propagating tips.

Starting with a distribution of microcracks propagating according to a Griffith type criterion in dynamics and with point heat sources at the moving tips, a homogenization method based on asymptotic developments has been employed to deduce a damage evolution law coupled with the thermoelasticity system at the macroscale. The upscaling procedure leads to distributed heat sources, related to the damage energy-release rate, in the homogenized temperature equation and the damage law depend on the thermal and the mechanical fields, such that the obtained macroscopic system has strong thermo-mechanical-damage couplings.

While the failure heating effect has been addressed previously in the framework of Fracture Mechanics, through models of crack-tip heat sources (e.g., [25], [26], [135]) or thermally dissipative cohesive zones [18, 54], the present approach appears to be the first one proposing a multiscale description of the heating due to distributed damage evolution in dynamics.

The local effective response of the model has been analyzed with special emphasis on thermal evolutions. Strain-rate and size effects related to the length of the microstructure are illustrated for strain-driven evolutions of stress, damage and temperature. Cooling effects prior to damage initiation and heating during propagation have been illustrated for different model parameters.

Numerical simulations have been performed to reproduce the compact compression test for PMMA samples. Comparisons with the temperature field measurements during rapid failure reported in [115] have shown good agreement between theoretical predictions and experimental results.

The analysis in the last section of this chapter showed that the adiabaticity assumption for the evolution of temperature during dynamic crack propagation is reasonable for the simulations with the new damage model. The heat conduction model is also necessary for the study of thermally induced fracture problems, like thermal shocks [88, 141] or irradiation damage [128].

Chapter 3

Dynamic damage evolution for mode II microcracks with frictional contact

3.1 Introduction

Contents

3.1	Introduction	59
3.2	Formulation of the initial fracture problem	61
3.3	Homogenized elastodynamic equations	63
3.4	Dynamic damage law with friction effects	65
3.5	Local macroscopic behavior	67
3.5.1	Homogenized coefficients C_{mnpq} and I_{mnpq}	67
3.5.2	Local response analysis	69
3.6	Numerical simulations of mode II failure of PMMA samples under impact	72

Many complex mechanical behaviors of quasi-brittle materials under compression loadings, including the material hardening and softening, elastic stiffness degradation, induced anisotropy, irreversible deformations, have as microscopic origins the propagation of microcracks and the frictional sliding along their lips. A proper modeling of the overall behavior of quasi-brittle materials should necessarily account for the two microscopic dissipative mechanisms and their coupling. Such a description is particularly challenging in the context of dynamics, when the material response is sensitive to the rate of the applied loadings and specific interactions between the small-scale fracture and friction processes take place.

Among the various studies in the literature, one can mention the micro-mechanical approaches for stationary or evolving frictional micro-cracks in [79], [93], [2], [5], [74], [98], [136], [91], [64], [69], [85], [145], [106], [147].

In the context of dynamics, several models based on micro-mechanics have been developed to study the compressive failure response of brittle solids in the case when the

main microscopic mechanism is the tensile fracture mode. [97] studied an array of interacting and dynamically growing wing cracks and estimated the rate-dependent dynamic damage evolution. [113] developed a micro-mechanical model for ceramics based on non-interacting, uniformly distributed sliding micro-cracks subjected to dynamic compressive loading and predicted effects of the rate sensitivity on failure strength. [73] developed a model that combined damage evolution theory with dynamic crack growth under uniaxial dynamic compression. [100] developed a model based on the evolution of tensile wing micro-cracks in the case of uniaxial compression under constant strain loading. A more recent dynamic damage model inspired by the same wing crack mechanism and valid over a wide range of loading rates has been proposed by [16].

Probabilistic damage models for the description of the fragmentation processes have been proposed by [45], [60] based on the hypothesis that the increment of microcrack density is a function of the obscuration probability due to the stress release around newly formed microcracks. A specific microplane model for impact comminution of solids, inspired by the Grady's model of fragmentation and considering the kinetic energy in high-rate shear deformations as the driving force of comminution, has been formulated in [11].

Most of these models are essentially based on mode I fracture mechanisms. However, there are physical situations in which cracks are constrained to propagate in mode II. Rupture on geological faults that occurs in earthquakes is a classical example. Impact experiments of [118, 119, 109, 17, 18] on bonded or side-grooved samples of brittle polymers revealed that under high strain rate loadings a failure mode transition from opening to shear fracture takes place. In contrast with the mode I crack velocities that are much smaller than the theoretical limit, the Rayleigh wave speed c_R , the shear cracks may evolve rapidly up to c_R and may pass in the supershear regime, with tip velocities v larger than the shear wave speed c_S .

Fracture Mechanics studies on dynamic mode II cracks [58, 59, 31, 28, 29, 30, 129, 112] showed the possibility of intersonic propagation $c_S < v < c_L$, with c_L the dilatational wave speed, while the subsonic super-Rayleigh regime $c_R < v < c_S$ is non-physical since as it corresponds to negative values of the energy-release rate. In the intersonic interval, non-vanishing positive energy fluxes at the crack tip are obtained if a finite size cohesive zone model is adopted, indicating the necessity of a distributed approach. Using a phase-field fracture model [127] simulated the intersonic shear fracture of brittle specimens under impact, by triggering the crack path with a weak strip of reduced toughness, and obtained crack velocities in agreement with the experimental values in [119].

The microstructural observations of the fracture surfaces reported in [109] and [4], for mode II failure of PMMA samples under impact, revealed the existence of complex morphologies which do not correspond to *en echelon* mode I microcracks, but rather to a mode II process zone. It was also observed [17, 19] that frictional contact plays an important role during the shear failure, leading to temperature rise up to the glass transition temperature and polymer melting effects. In this context, the present contribution investigates the possibility of modeling the dynamic shear failure of brittle solids using a damage model obtained by upscaling of microstructures with rapidly evolving mode II frictional microcracks.

Damage models have been extensively employed in the last years (e.g. phase-field, delay damage laws...) for the modeling of failure in solids. A method to obtain damage

evolution laws from microcracks propagation criteria, using the asymptotic homogenization technique, has been proposed in [37] and extended to more complex microcrack evolutions in [39, 38, 61, 94, 47]. In dynamics, a damage model has been established for mode I microcracks in [82, 41] and for the antiplane mode in [6]. Heat dissipation effects have been included in the mode I dynamic damage approach in [42]. [140] proposed a quasi-static damage law for the in-plane shear-mode propagation of frictional microcracks.

The main objective of the present chapter is to develop a two-scale damage model by asymptotic homogenization from microstructures with microcracks propagating dynamically in mode II and having contact and friction conditions on their lips. The local analysis of the macroscopic response will be performed in order to reveal the main features of the new approach. At the structural level, the mode II brittle failure of PMMA specimens under impact loading will be reproduced numerically in order to illustrate the prediction capacity of the model.

This chapter is organized as follows. In section 3.2, the initial elasto-dynamic fracture problem is formulated. The next two sections are devoted to the homogenization analysis to construct the macroscopic elastodynamics equations for the microcracked solid and the dynamic damage law deduced from the microscopic propagation criterion. The analysis of the local macroscopic response of the new model is performed in Section 3.5 for the effective coefficients, the influence of small-scale friction, the strain-rate and microstructural size effects. Results of numerical simulations for dynamic shear rupture of PMMA samples under impact loading are presented and compared with the experimental data in Section 3.6.

3.2 Formulation of the initial fracture problem

We consider the dynamic evolution of an elastic solid containing a locally periodic distribution of microcracks, parallel to the x_1 axis, as illustrated in Figure 3.1. The fixed size of a period is l_c , while the variable micro-crack length is denoted by l . The local periodicity allows for different damage values in different macroscopic points, corresponding to the large-scale variations of the microcrack length.

The equations of elastodynamics can be written:

$$\frac{\partial \sigma_{ij}^\varepsilon}{\partial x_i} = \rho \frac{\partial^2 u_j^\varepsilon}{\partial t^2} \quad (3.1)$$

and the constitutive relations of linear elasticity are:

$$\sigma_{ij}^\varepsilon = a_{ijkl} e_{xkl}(\mathbf{u}^\varepsilon) \quad (3.2)$$

where \mathbf{u}^ε et $\boldsymbol{\sigma}^\varepsilon$ are the displacement and stress fields, ρ the mass density and e_{xkl} is the linearized strain tensor:

$$e_{xkl}(\mathbf{u}^\varepsilon) = \frac{1}{2} \left(\frac{\partial u_k}{\partial x_l} + \frac{\partial u_l}{\partial x_k} \right) \quad (3.3)$$

relative to the x_i variables. The elastic coefficients a_{ijkl} for an isotropic homogeneous solid have for expression:

$$a_{ijkl} = \lambda \delta_{ij} \delta_{kl} + \mu (\delta_{ik} \delta_{jl} + \delta_{il} \delta_{jk}) \quad (3.4)$$

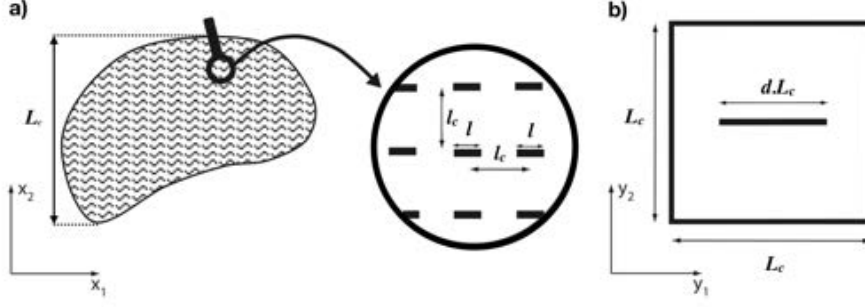


Figure 3.1: a) Micro-fissured medium with locally periodic microstructure with l_c the size of a period, l the local micro-crack length and L_c the characteristic length of the macro-structure. b) Reference cell of size L_c with rescaled crack length $d.L_c$.

where λ and μ are the Lamé constants.

Unilateral contact conditions are assumed on the crack lips. They can be expressed by the relations:

$$[\boldsymbol{\sigma}^\varepsilon \mathbf{N}] = 0, \quad \mathbf{N} \boldsymbol{\sigma}^\varepsilon \mathbf{N} < 0, \quad [\mathbf{u}^\varepsilon \cdot \mathbf{N}] = 0 \quad (3.5)$$

where $[\cdot]$ represents the jump across the crack line with respect to the unit normal vector \mathbf{N} , oriented in the direction of the x_2 axis.

In addition to the contact relations (3.5), the Coulomb friction conditions are also considered such that, in the sliding regime, we have :

$$|\mathbf{T} \boldsymbol{\sigma}^\varepsilon \mathbf{N}| = -\mu_f \mathbf{N} \boldsymbol{\sigma}^\varepsilon \mathbf{N} \quad (3.6)$$

where \mathbf{T} is the unit tangent vector to the crack, oriented in direction of x_1 axis, and μ_f is the friction coefficient.

We assume that microcracks are evolving symmetrically with respect to the center of the elementary period and following a Griffith-type propagation criterion based on the dynamic energy-release rate:

$$\mathcal{G}^{d\varepsilon} = \lim_{r \rightarrow 0} \int_{\Gamma_r} \left((U + T) \mathbf{n} \mathbf{e} - \sigma_{ij}^\varepsilon n_j \frac{\partial u_i^\varepsilon}{\partial x_1} \right) ds \quad (3.7)$$

where Γ_r is a circular contour of radius r surrounding the crack tip and U and T are, respectively, the elastic and the kinetic energy densities:

$$U = \frac{1}{2} a_{mnkl} e_{xkl}(u^\varepsilon) e_{xmn}(u^\varepsilon) ; \quad T = \frac{1}{2} \rho \frac{\partial u^\varepsilon}{\partial t} \frac{\partial u^\varepsilon}{\partial t} \quad (3.8)$$

The propagation laws for microcracks can be written in the Kuhn-Tucker form as:

$$\mathcal{G}^{d\varepsilon} - \mathcal{G}_c \leq 0; \quad \dot{l} \geq 0; \quad \dot{l} (\mathcal{G}^{d\varepsilon} - \mathcal{G}_c) = 0 \quad (3.9)$$

where l is the microcrack length, \mathcal{G}_c is the critical fracture energy of the material and \dot{l} represents the time derivative of $l(t)$. The conditions (3.9) assure that the crack propagation is irreversible and it is allowed only when the available energy for fracture $\mathcal{G}^{d\varepsilon}$ reaches the critical energy \mathcal{G}_c necessary to break the material bonds.

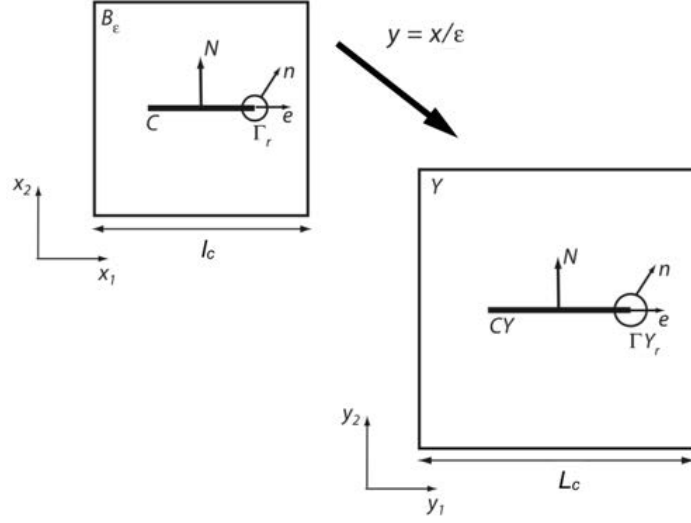


Figure 3.2: Scaling of the microscopic period of the material to the reference cell.

The objective of the next two sections is to construct a macroscopic elasto-damage model by homogenization of the present elastodynamic fracture problem.

3.3 Homogenized elastodynamic equations

In this section, we use the homogenization method based on asymptotic developments [10, 15, 122] to deduce the effective elastodynamic response of solids containing a large number of microcracks with contact and friction conditions. This section will extend the quasi-static analysis in [140] to dynamics. The results will serve as a necessary basis for the construction of the damage model in the next section.

Two coordinate systems \mathbf{x} and \mathbf{y} are introduced for the homogenization method: the \mathbf{x} variables are used to describe variations of the mechanical fields at the macroscopic scale, while \mathbf{y} variables refer to the microscopic scale. They are linked by the relation $\mathbf{y} = \frac{\mathbf{x}}{\varepsilon}$, where $\varepsilon = \frac{l_c}{L_c}$ characterizes the difference between microscopic and macroscopic scales, as in Chapter 2. The above relation transforms the physical period of size l_c , containing a crack of length l , in the unit cell Y with a crack of length $d.L_c$, with d the damage variable as shown on Figure 3.2.

Following the asymptotic homogenization method, we consider the two-scale developments of the displacement and stress fields:

$$u_i^\varepsilon(\mathbf{x}, t) = u_i^{(0)}(\mathbf{x}, \mathbf{y}, t) + \varepsilon u_i^{(1)}(\mathbf{x}, \mathbf{y}, t) + \varepsilon^2 u_i^{(2)}(\mathbf{x}, \mathbf{y}, t) + \dots \quad (3.10)$$

$$\sigma_{ij}^\varepsilon(x, t) = \frac{1}{\varepsilon} \sigma_{ij}^{(-1)}(\mathbf{x}, \mathbf{y}, t) + \sigma_{ij}^{(0)}(\mathbf{x}, \mathbf{y}, t) + \varepsilon \sigma_{ij}^{(1)}(\mathbf{x}, \mathbf{y}, t) + \dots \quad (3.11)$$

where $u_i^{(i)}(\mathbf{x}, \mathbf{y}, t)$ and $\sigma_{ij}^{(i)}(\mathbf{x}, \mathbf{y}, t)$ are periodic functions with respect to \mathbf{y} in the unit cell.

By replacing the expressions of u_i and σ_{ij} in the elastodynamic equations (3.1) and separating the terms of the same order in ε , we obtain a series of equations. The first three of them are:

$$\frac{\partial \sigma_{ij}^{(-1)}}{\partial y_i} = 0, \quad \frac{\partial \sigma_{ij}^{(-1)}}{\partial x_i} + \frac{\partial \sigma_{ij}^{(0)}}{\partial y_i} = 0, \quad \frac{\partial \sigma_{ij}^{(0)}}{\partial x_i} + \frac{\partial \sigma_{ij}^{(1)}}{\partial y_i} = \rho \frac{\partial^2 u_j^{(0)}}{\partial t^2} \quad (3.12)$$

In the same way, by replacing the two-scale developments in the constitutive relations (3.2), we obtain at the first orders in ε :

$$\sigma_{ij}^{(-1)} = a_{ijkl} e_{ykl}(\mathbf{u}^{(0)}) \quad (3.13)$$

$$\sigma_{ij}^{(0)} = a_{ijkl} (e_{xkl}(\mathbf{u}^{(0)}) + e_{ykl}(\mathbf{u}^{(1)})) \quad (3.14)$$

$$\sigma_{ij}^{(1)} = a_{ijkl} (e_{xkl}(\mathbf{u}^{(1)}) + e_{ykl}(\mathbf{u}^{(2)})) \quad (3.15)$$

Concerning the boundary conditions on the faces of the cracks, in the frictional sliding regime, we find at powers $m = -1, 0, \dots$ of ε :

$$\left[\sigma_{ij}^{(m)} N_j \right] = 0, \quad N_i \sigma_{ij}^{(m)} N_j < 0, \quad |T_i \sigma_{ij}^{(m)} N_j| = -\mu_f N_i \sigma_{ij}^{(m)} N_j \text{ on } CY^\pm \quad (3.16)$$

together with the continuity of normal displacements:

$$[\mathbf{u}^{(p)} \cdot \mathbf{N}] = 0, \quad \text{on } CY \quad (3.17)$$

for $p=0,1,\dots$

When the expression (3.13) is used in the first equation (3.12) and in the relations (3.16), for $m=-1$, we get the unit cell problem for $\mathbf{u}^{(0)}$:

$$\frac{\partial}{\partial y_i} (a_{ijkl} e_{ykl}(\mathbf{u}^{(0)})) = 0 \quad \text{in } Y \quad (3.18)$$

$$[(a_{ijkl} e_{ykl}(\mathbf{u}^{(0)})) N_j] = 0 \text{ on } CY \quad (3.19)$$

$$N_i (a_{ijkl} e_{ykl}(\mathbf{u}^{(0)})) N_j < 0 \text{ on } CY^\pm \quad (3.20)$$

$$|T_i (a_{ijkl} e_{ykl}(\mathbf{u}^{(0)})) N_j| = -\mu_f N_i (a_{ijkl} e_{ykl}(\mathbf{u}^{(0)})) N_j \text{ on } CY^\pm \quad (3.21)$$

with periodic boundary conditions on the opposite edges of the cell. This allows us to deduce the solution $\mathbf{u}^{(0)} = \mathbf{u}^{(0)}(\mathbf{x}, t)$ not depending on the microscopic variable \mathbf{y} and thus becoming the macroscopic displacement field.

The problem for $\mathbf{u}^{(1)}$ is obtained by replacing the equation (3.14) in the second relation of (3.12) and in the relations (3.16), for $m=0$:

$$\frac{\partial}{\partial y_i} (a_{ijkl} e_{ykl}(\mathbf{u}^{(1)})) = 0 \quad \text{in } Y \quad (3.22)$$

$$[(a_{ijkl} e_{ykl}(\mathbf{u}^{(1)})) N_j] = - [(a_{ijkl} e_{xkl}(\mathbf{u}^{(0)})) N_j] \text{ on } CY \quad (3.23)$$

$$N_i a_{ijkl} (e_{ykl}(\mathbf{u}^{(1)}) + e_{xkl}(\mathbf{u}^{(0)})) N_j < 0 \text{ on } CY^\pm \quad (3.24)$$

$$|T_i a_{ijkl}(e_{ykl}(\mathbf{u}^{(1)}) + e_{xkl}(\mathbf{u}^{(0)}))N_j| = -\mu_f N_i a_{ijkl}(e_{ykl}(\mathbf{u}^{(1)}) + e_{xkl}(\mathbf{u}^{(0)}))N_j \text{ on } CY^\pm \quad (3.25)$$

By introducing the macroscopic stress as the average value over the unit cell Y :

$$\Sigma_{ij}^{(0)} \equiv \langle \sigma_{ij}^{(0)} \rangle = \frac{1}{L_c^2} \int_Y a_{ijkl}(e_{xkl}(\mathbf{u}^{(0)}) + e_{ykl}(\mathbf{u}^{(1)}))dy \quad (3.26)$$

the homogenized macroscopic equation is obtained as:

$$\frac{\partial}{\partial x_j} \Sigma_{ij}^{(0)} = \rho \frac{\partial^2 u_i^{(0)}}{\partial t^2} \quad (3.27)$$

As proved in the Appendix B, the stress expression (3.26) can be used to obtain the macroscopic constitutive relation :

$$\Sigma_{ij}^{(0)} = C_{ijmn} e_{xmn}(\mathbf{u}^{(0)}) \quad (3.28)$$

where the effective coefficients C_{ijmn} are given by the relations (B.17 - B.19). We note that these coefficients depend on the normalized crack length d . This dependence will be illustrated numerically in Section 3.5.

3.4 Dynamic damage law with friction effects

In this section, the asymptotic homogenization method is used in combination with an energy analysis for microcracks propagating dynamically, in mode II, with contact and friction conditions, in order to obtain a macroscopic damage law.

The effective coefficients (B.17-B.19) depend on the damage variable d . Under the applied loadings, the microcracks are propagating and the variable $d(\mathbf{x}, t)$ will evolve in time at every material point \mathbf{x} . In order to describe this evolution, a macroscopic damage law is necessary. A specific upscaling procedure, from microcracks to damage, has been proposed in previous studies [37, 61, 140, 82] and the objective of this section is to extend this approach to the case of dynamically propagating microcracks in contact with friction.

By replacing the asymptotic expansions of the displacement \mathbf{u}^ϵ and the stress $\boldsymbol{\sigma}^\epsilon$ in (3.7) and taking into account the singularity of the mechanical fields, we obtain the expression of $\mathcal{G}^{d\epsilon}$ in the form:

$$\begin{aligned} \mathcal{G}^{d\epsilon} = & \epsilon \lim_{r \rightarrow 0} \int_{\Gamma Y_r} (-a_{ijkl} e_{ykl}(\mathbf{u}^{(1)}) n_j \left(\frac{\partial u_i^{(1)}}{\partial y_1} \right) \\ & + \frac{1}{2} a_{mnkl} e_{ykl}(\mathbf{u}^{(1)}) e_{ymn}(\mathbf{u}^{(1)}) + \frac{1}{2} \rho v^2 \left(\frac{\partial \mathbf{u}^{(1)}}{\partial y_1} \right)^2) n_1 ds_y \end{aligned} \quad (3.29)$$

where the change of variable $dS = \epsilon ds_y$ has been made, ΓY_r is the image of Γ_r in the unit cell and the microcrack tip speed has been written $v = \epsilon L_c \frac{\dot{d}}{2}$ together with the near-tip asymptotic relation [59] $\frac{\partial \mathbf{u}^\epsilon}{\partial t} \simeq -v \frac{\partial \mathbf{u}^\epsilon}{\partial x_1}$.

The dynamic energy-release rate can be expressed [59, 129] as:

$$\mathcal{G}^{d\epsilon} = g_2(v) \mathcal{G}^\epsilon \quad (3.30)$$

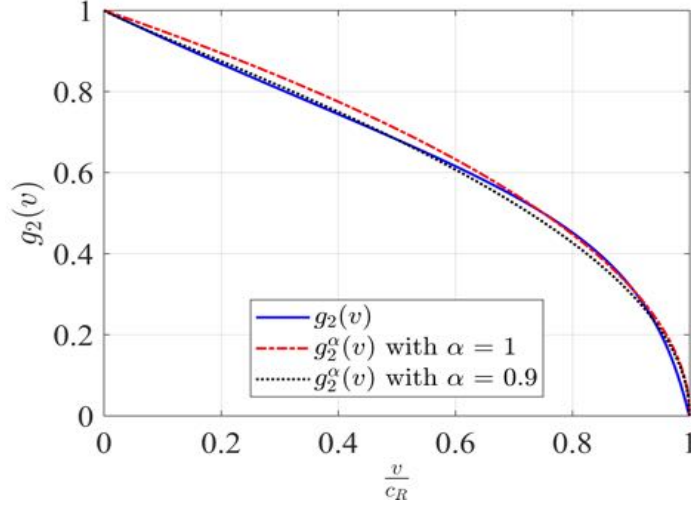


Figure 3.3: The function $g_2(v)$ and its approximations $g_2^\alpha(v)$ for $\alpha = 1$ and $\alpha = 0.9$.

where \mathcal{G}^ε is the quasi-static energy-release rate, corresponding to (3.29) without the kinetic energy term, and g_2 is a universal function, for the mode II propagation, given by the formula:

$$g_2(v) = -\sqrt{\frac{1 + \frac{v}{c_2}}{1 - \frac{v}{c_2}}} \frac{v^2(1 - \frac{v}{c_R})^2}{(1 - \nu)c_2^2 R(v) D_+^2(v)} \quad (3.31)$$

Here $c_2 = \sqrt{\frac{\mu}{\rho}}$, $c_1 = \sqrt{\frac{E(1-\nu)}{\rho(1+\nu)(1-2\nu)}}$ are respectively the shear and dilatational wave velocities, c_R is the Rayleigh wave velocity. $R(v)$ and $D_+(v)$ are functions of crack velocity v given by the expressions [129] :

$$R(v) = (1 + m_2^2)^2 - 4m_1m_2 \quad (3.32)$$

$$D_+(v) = \exp\left(\frac{1}{\pi} \int_{c_2/c_1}^1 \frac{\phi(\alpha)}{\alpha - c_2/v} d\alpha\right) \quad (3.33)$$

with

$$\phi(\alpha) = \arctan \frac{4\alpha^2 \sqrt{1 - \alpha^2} \sqrt{\alpha^2 - c_2/c_1}}{(2\alpha^2 - 1)^2} \quad (3.34)$$

and the constants $m_{1,2} = \sqrt{1 - \frac{v^2}{c_{1,2}^2}}$.

In order to find a dynamic damage law in a relatively simple form, we seek for an explicit approximation of the function $g_2(v)$. Using numerical integration for $D_+(v)$, we can compute $g_2(v)$ for v ranging from 0 to c_R . Its graphical representation is given in Figure 3.3 and compared to other simple approximation functions $g_2(v) \approx g_2^\alpha(v)$ of the form

$$g_2^\alpha(v) = \sqrt{1 - \left(\frac{v}{c_R}\right)^\alpha} \quad (3.35)$$

We remark that reasonably good approximations are obtained for $\alpha = 0.9$ and $\alpha = 1$.

Since the unit cell problem given in the previous section is the same as in quasi-statics, the analysis performed in [140] is still valid. In particular, it allows to obtain a quasi-static damage relation:

$$\left(\frac{\mathcal{G}^{(1)}}{L_c} + \left(\frac{1}{2} \frac{\partial C_{mnpq}}{\partial d} + I_{mnpq} \right) e_{xmn}(\mathbf{u}^{(0)}) e_{xpq}(\mathbf{u}^{(0)}) \right) \dot{d} = 0 \quad (3.36)$$

where the effective integral terms I_{mnpq} are described in the Appendix B. The corresponding terms in the laws (B.20) and (3.36) are related to the energy dissipated by friction on the lips of microcracks. They are absent in the case of frictionless contact or opening crack face conditions.

The term \mathcal{G}^ε in (3.36) can be expressed as $\mathcal{G}^\varepsilon = \mathcal{G}^{d\varepsilon}/g_2(v)$ from (3.30). And using the Griffith propagation criterion $\mathcal{G}^{d\varepsilon} = \mathcal{G}_c$ for $\dot{d} \neq 0$, we get the damage evolution law:

$$\frac{dd}{dt} = \frac{2c_R}{l_c} \left\langle 1 - \frac{\mathcal{G}_c^2}{\left(l_c \left(\frac{1}{2} \frac{\partial C_{mnpq}}{\partial d} + I_{mnpq} \right) e_{xmn}(\mathbf{u}^{(0)}) e_{xpq}(\mathbf{u}^{(0)}) \right)^2} \right\rangle^{1/\alpha} \quad (3.37)$$

where $\langle \cdot \rangle$ represents the positive part. If we introduce the notation $\mathcal{Y}_f = I_{mnpq} e_{xmn}(\mathbf{u}^{(0)}) e_{xpq}(\mathbf{u}^{(0)})$ for the frictional dissipation term and the damage energy-release rate $\mathcal{Y} = -\frac{1}{2} \frac{\partial C_{mnpq}}{\partial d} e_{xmn}(\mathbf{u}^{(0)}) e_{xpq}(\mathbf{u}^{(0)})$, then the evolution law can be written in a compact form:

$$\frac{dd}{dt} = \frac{2c_R}{l_c} \left\langle 1 - \frac{\mathcal{G}_c^2}{l_c^2 (\mathcal{Y} - \mathcal{Y}_f)^2} \right\rangle^{1/\alpha} \quad (3.38)$$

We note that the microscopic length l_c is present in the damage law and will be responsible for microstructural size effects.

3.5 Local macroscopic behavior

The analysis of the local response predicted by the new damage model is performed in the present section. For the numerical implementation, the material parameters of the PMMA polymer are used: dynamic Young's modulus $E = 5.5 \text{ GPa}$, Poisson's ratio $\nu = 0.35$ and mass density $\rho = 1190 \text{ kg/m}^3$. Based on the estimation in [27], where the mode II fracture toughness for PMMA was determined to be about 2.5 times the mode I toughness, we adopt for the critical fracture energy $\mathcal{G}_c = 2100 \text{ J/m}^2$. Three values of the friction coefficient $\mu_f = 0$, $\mu_f = 0.25$ and $\mu_f = 0.5$ are considered in the present analysis. The exponent for the approximation (3.35) of $g_2(v)$ is taken to be $\alpha = 1$.

3.5.1 Homogenized coefficients C_{mnpq} and I_{mnpq}

To calculate the homogenized coefficients C_{mnpq} and the integrals I_{mnpq} present in the damage law (3.37) the particular solutions of the unit cell problem (B.3-B.6) are needed. Finite Element computations with the commercial software [35] are performed to obtain the corresponding numerical solutions. Some details on the unit cell problem formulation are given in the Appendix B.

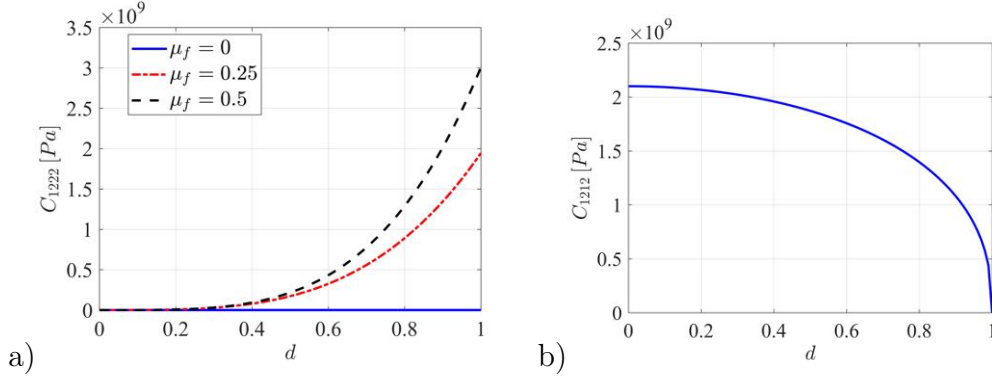


Figure 3.4: Effective moduli $C_{1222}(d)$ and $C_{1212}(d)$ for three values of the friction coefficient: $\mu_f = 0$, $\mu_f = 0.25$ and $\mu_f = 0.5$.

In order to obtain the dependence on the damage variable d , the cell problems were numerically solved for different crack lengths. With these solutions, the integral formulae (B.17-B.19) on the unit cell Y and the two integrals in (B.22) on the edges of the crack CY were evaluated. The computations were performed for 20 values of the crack length d , ranging from 0 to 1. Then, the obtained numerical values of C_{mnpq} and I_{mnpq} were computed as functions of d by polynomial interpolations. The first term in the expression (B.22) was obtained by derivation of the interpolated integral.

For $d = 0$, the effective coefficients are equal to the elastic coefficients of the undamaged material $C_{ijkl} = a_{ijkl}$, while for $d \neq 0$ the coefficients: $C_{1111} = a_{1111}$, $C_{1122} = C_{2211} = a_{1122}$, $C_{1112} = C_{1211} = 0$, $C_{2222} = a_{2222}$ are not affected by the variation of d . The computation of the integral terms in I_{ijkl} revealed that the only non-negligible coefficient is I_{2222} . In Figures 3.4 and 3.5 we represent, respectively, $C_{1222}(d)$, $C_{1212}(d)$ and $I_{2222}(d)$, corresponding to a crack orientation along the y_1 -axis and for the three values of μ_f .

The effective coefficients C_{1222} and C_{1212} are shown in Figure 3.4. C_{1222} characterizes the influence of the compression deformation $e_{x22}(\mathbf{u}^{(0)})$ on the macroscopic shear stress $\Sigma_{12}^{(0)}$. In the absence of friction, there is no such influence on the shear stress response while, in the presence of friction, the compression influence the frictional resistance giving rise shear stresses. This effect is amplified by the value of the friction coefficient and also by the size of the friction zone, controlled by the normalized microcrack length d . The two influences can be remarked in Figure 3.4a, the effective coefficient $C_{1222}(d)$ being an increasing function and having the highest values for $\mu_f = 0.5$.

As concerns the coefficient C_{1212} , the Figure 3.4b shows that it is a decreasing function of d and its behavior is not affected by the value of the friction coefficient. It represents the effect of the shear deformation of the unit cell on the macroscopic shear stress. The presence of microcracks makes easier the deformation of the cell and reduce the level of resulting shear stress. This explains the decrease of C_{1212} with respect to d . For a completely fractured cell, no shear stresses are generated since the two parts move freely.

The coefficient I_{2222} is represented in the Figure 3.5 as a function of damage d . Since these coefficients characterize the dissipation due to friction on the lips of microcracks, it is evident that they vanish for $\mu_f = 0$ and have higher values for large friction coefficients.

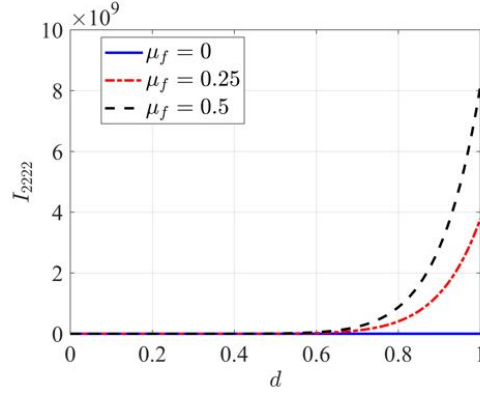


Figure 3.5: I_{2222} vs d for three values of the friction coefficient: $\mu_f = 0$, $\mu_f = 0.25$ and $\mu_f = 0.5$.

Moreover, $I_{2222}(d)$ is an increasing function since friction on larger microcracks involve more dissipation of energy. This dissipation mechanism will reduce the energy available for fracture and will delay the propagation of microcracks.

3.5.2 Local response analysis

Let us now study the local stress and damage response of the new model for a given strain history in a macroscopic point. The material parameters listed in the beginning of this section are used as an initial basis for the subsequent parametric studies. A shear strain history $e_{x12}(t)$ with constant strain rate $\dot{e}_{x12} = -8000/s$ and a fixed compression strain $e_{x22} = -5 \times 10^{-3}$ are given while the other strain components are vanishing.

In Figure 3.6 are represented the damage d and the stress $-\Sigma_{12}$ as functions of the applied strain $-e_{x12}$, for three values of the friction coefficient $\mu_f = 0$, $\mu_f = 0.25$, $\mu_f = 0.5$. The value of the initial damage is chosen $d_0 = 0.2$ and the microstructural length is $l_c = 0.003 m$. After the initial elastic regime, damage evolves and the stress-strain curve shows successive hardening and softening behavior up to complete failure. When the friction coefficient of microcracks increases, the necessary shear deformation to initiate the propagation is higher due to higher friction resistance. An important part of energy is dissipated by friction on the microcrack lips, reducing the amount of energy available for fracture. The initiation delay leads to the development of higher shear strength values.

Let us consider now the influence of the normal compression. Three different normal strain values: $e_{x22} = -10^{-3}$, $e_{x22} = -8 \times 10^{-3}$ and $e_{x22} = -1.5 \times 10^{-2}$ are considered and the corresponding responses are represented for the friction coefficient $\mu_f = 0.5$, the applied strain rate $\dot{e}_{x12} = -8000/s$, $l_c = 5 \times 10^{-3} m$ and the initial damage $d_0 = 0.2$. The Figure 3.7 shows the stress $-\Sigma_{12}$ and the damage d as a function of the strain $-e_{x12}$ for different values of e_{x22} . We observe that the increase of the compression strain produces a delay in the evolution of damage. In this case, the friction resistance is higher making the propagation of microcracks more difficult and leading to the development of higher values of the shear stress.

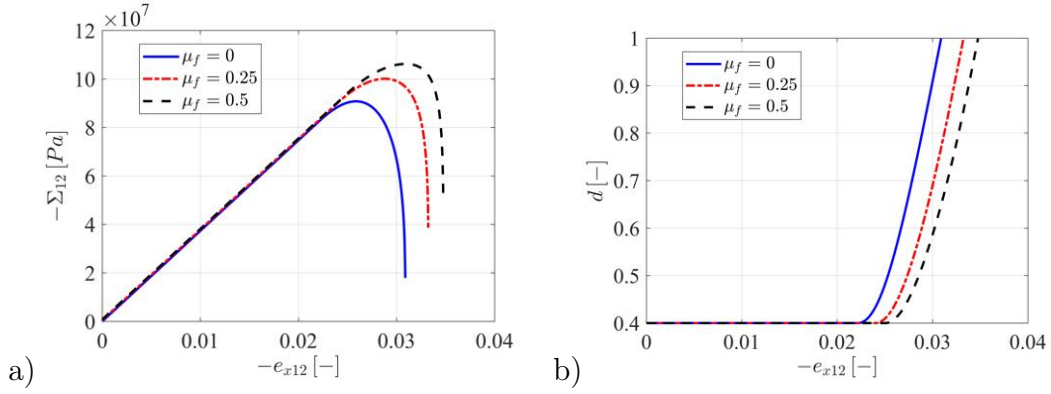


Figure 3.6: Stress $-\Sigma_{12}$ and damage d vs strain $-e_{x12}$ for three values of the friction coefficient: $\mu_f = 0$, $\mu_f = 0.25$ and $\mu_f = 0.5$.

We analyse now the local macroscopic response for different values of the strain rate: $\dot{e}_{x12} = -100 /s$, $\dot{e}_{x12} = -1000 /s$, $\dot{e}_{x12} = -10000 /s$. The stress curves $-\Sigma_{12}$ vs. $-e_{x12}$ and damage d vs $-e_{x12}$ are given in Figure 3.8 for a coefficient of friction $\mu_f = 0.5$ and for $l_c = 2 \times 10^{-3} m$.

While the response is brittle for the first two values, the loading with the highest strain rate induces some ductility in the softening regime associated with a slight increase in strength. This is a typical inertial strain-rate effect, also present in the absence of friction. It is essentially due to the formation of a non-negligible amount of kinetic energy near the crack lips which reduces the available energy for fracture. We note that this effect is less pronounced than in the case of opening of microcracks [82] where the amount of kinetic energy may be more important.

We also study the effect of the microstructural length on the local response. The tests were performed for the applied strain rate $\dot{e}_{x12} = -8000/s$ and $e_{x22} = -1 \times 10^{-3}$ and the coefficient of friction $\mu_f = 0.5$. Three sizes of microstructure were considered: $l_c = 5 \times 10^{-3} m$, $l_c = 5 \times 10^{-4} m$ and $l_c = 5 \times 10^{-5} m$ and the results are presented in Figure 3.9. We observe that the shear strength increases and damage initiation is delayed as the

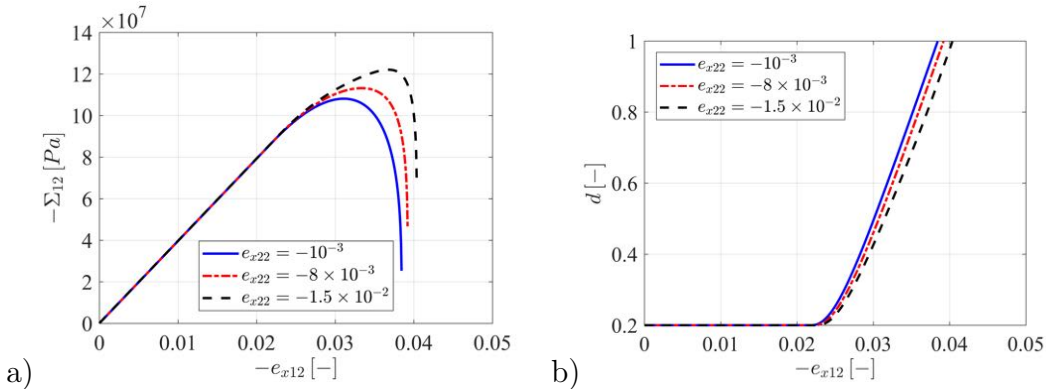


Figure 3.7: Stress $-\Sigma_{12}$ and damage d responses for three values of the compressive strain.

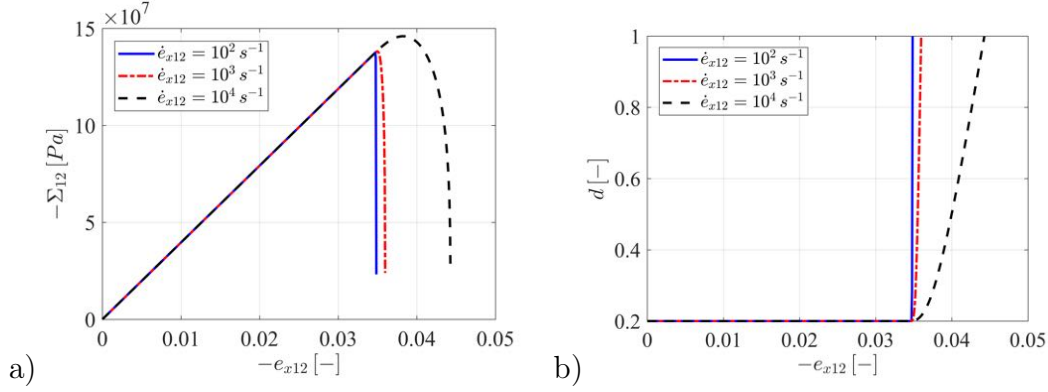


Figure 3.8: Stress $-\Sigma_{12}$ and damage d response for three values of the strain rate: $\dot{e}_{x12} = -100 / \text{s}$, $\dot{e}_{x12} = -1000 / \text{s}$, $\dot{e}_{x12} = -10000 / \text{s}$.

size of the microstructure decreases. This is the typical Fracture Mechanics size effect transferred to the damage model at the macroscopic level: larger microcracks propagate much easier than smaller ones. The finer the microstructure, the stronger the material.

Finally, we consider the case of crack-velocity dependent fracture energy $\mathcal{G}_c(v)$. As we will illustrate in the next section, this dependency is necessary to recover the experimental results. For mode I dynamic fracture, the dependency $\mathcal{G}_c(v)$ has been studied by different authors, e.g. [18, 36]. To our knowledge, such results are not available for the mode II failure. Similarly to the opening mode case [42], we consider the linear approximation $\mathcal{G}_c(v) = \mathcal{G}_{c0}(1 + a.v)$.

In Figure 3.10 the stress and damage curves are plotted for $\mathcal{G}_{c0} = 2100 \text{ J/m}^2$, for both $a = 0$ and $a = 0.01$. The other parameters are $\dot{e}_{x12} = -8000 / \text{s}$, $e_{x22} = -1 \times 10^{-3}$, $l_c = 1 \times 10^{-3} \text{ m}$ and $\mu_f = 0.5$. As expected, the increase of the fracture energy with the velocity of the cracks leads to a damage delay and the corresponding peak stress increase. The influence of non-vanishing a will be important for the macroscopic simulations presented in the next section.

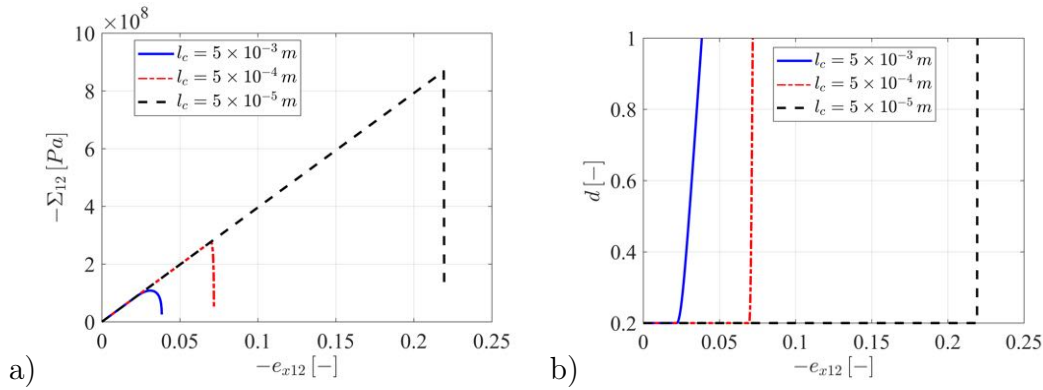


Figure 3.9: Stress $-\Sigma_{12}$ and damage d vs strain $-e_{x12}$ for micro-structural lengths: $l_c = 5 \times 10^{-3} \text{ m}$, $l_c = 5 \times 10^{-4} \text{ m}$ and $l_c = 5 \times 10^{-5} \text{ m}$.

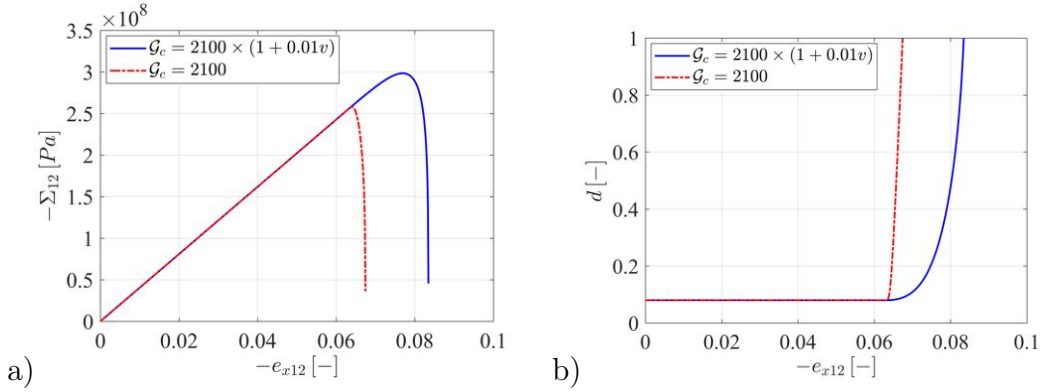


Figure 3.10: Stress $-\Sigma_{12}$ and damage d vs strain $-e_{x12}$, for constant and crack-velocity dependent fracture energy.

3.6 Numerical simulations of mode II failure of PMMA samples under impact

We investigate here the capacity of the damage model to reproduce quantitatively the experimental results in [109] concerning the rapid shear failure of PMMA samples under impact loading. The authors showed that, by increasing the impact speed, the failure dominated by normal stress changes to a shear stress dominated failure oriented in the loading direction. Since the fracture toughness in mode II is much larger than in mode I [27, 109], side-grooved specimens are used in order to promote the shear failure mode.

The geometry of the specimen is given in Figure 3.11a. The dimensions are defined as $W = 100 \text{ mm}$, $2H = 400 \text{ mm}$ and $T = 6.35 \text{ mm}$. The grooves at both sides of the sample have the depth $D_g = 1.5 \text{ mm}$ and the height $H_g = 3.2 \text{ mm}$. The length of the initial

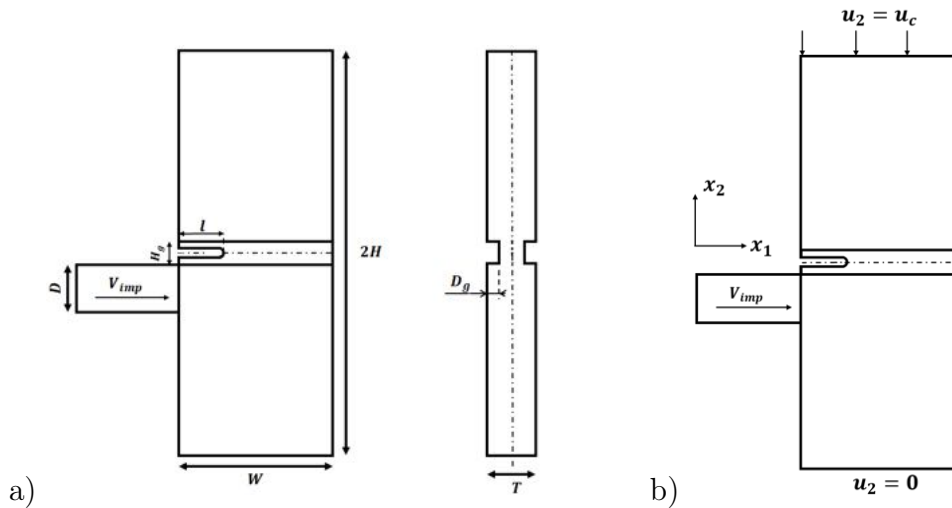


Figure 3.11: Geometry of the specimen and applied loadings: a) impact, b) impact and normal compression.

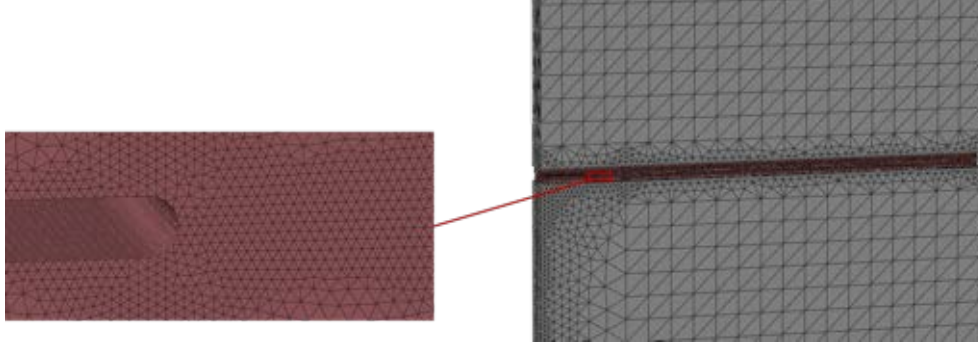


Figure 3.12: Details of the mesh used in the FE simulations.

notch is $l = 19\text{ mm}$ and its thickness is 0.3 mm . As shown Figure 3.11a, asymmetric impact loading with the velocity $V_{imp} = 60\text{ m/s}$ is applied over a zone of $D = 50\text{ mm}$, corresponding to the diameter of the projectile used for the experiments.

The applied loading generates a dominant shear stress state at the tip of the initial notch and initiate the shear failure along the groove. The dimensions of the specimen are such that, during the first $100\ \mu\text{s}$, there is not effect of the reflected waves from the far boundaries, the only loading being that of the projectile. The observations in [109] show the formation of a shear crack along the groove and a kinked mode I crack inclined at some angle with respect to the loading direction. This latter opening crack was missing in some experiments, only the shear crack being present. Since the model developed in the present contribution is based on mode II microcracks, our aim is to reproduce the formation of the macroscopic shear fracture.

The numerical values of the dynamic Young's modulus E , the Poisson's ratio ν and the mass density ρ for the PMMA material are given in the Table 1. Also given are the friction coefficient μ_f , the microstructural length l_c , the initial damage d_0 and the exponent α in the approximation (3.35) of $g_2(v)$. The critical fracture energy is assumed to be velocity dependent $\mathcal{G}_c = \mathcal{G}_{c0} \times (1 + a.v)$. The choice of the parameters is discussed below.

The damage model has been implemented in the commercial Finite Element software [1], as a VUMAT user material subroutine. Dynamic elasticity computations can be performed in Abaqus Explicit with the resolution of the damage equation in the user subroutine. On a time step and for given strain increments in an integration point of the FE mesh, the damage law (3.38) is numerically integrated using a Euler forward scheme. Only the in-plane strain components are considered in the expression of the energy terms \mathcal{Y} and \mathcal{Y}_f in the damage law (3.38).

In order to account for the effect of the grooves on the initiation of the shear failure, a

Table 3.1: Parameters used in the simulations of the asymmetric impact test.

$E\text{ (GPa)}$	$\nu\text{ (-)}$	$\rho\text{ (kg/m}^3\text{)}$	$\mu_f\text{ (-)}$	$l_c\text{ (m)}$	$d_0\text{ (-)}$	$\alpha\text{ (-)}$	$\mathcal{G}_{c0}\text{ (J/m}^2\text{)}$	$a\text{ (s/m)}$
5.5	0.35	1190	0.5	8×10^{-5}	0.08	1	2100	0.0075

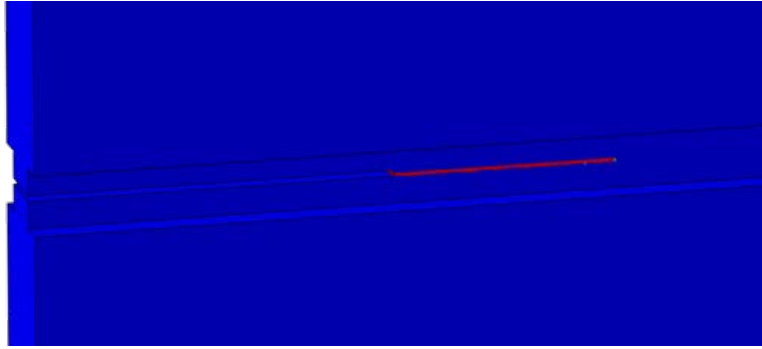


Figure 3.13: Damage band propagation inside the groove.

3D FE discretization is adopted. A FE mesh is constructed using four nodes tetrahedral linear elements C3D4. The details of the mesh are given in Figure 3.12. A refinement is considered in the groove, along the expected path of the damage band, with the element size of $5 \times 10^{-2} \text{ mm}$.

Under the impact loading, damage localization occurs starting from the tip of the notch and the damage band propagates in the groove. The complete failure corresponds to a critical value of the damage parameter $d = 0.99$ at the integration point. When this state is reached, the respective element is deleted and unilateral contact with friction conditions are introduced between the new formed boundaries of the macroscopic crack. In this evolution, the damage localization is a consequence of the softening response of the model [40] and transition to discontinuous crack is performed numerically at complete failure. Other approaches, like the one in [146] where the localization process is described with a traction-based friction-damage law on the newly formed macrocrack, may be adapted in future studies to the dynamic damage model proposed in the present contribution.

A typical evolution of the damage band initiated at the notch tip and evolving in the groove is represented in Figure 3.13. The trajectory is relatively straight, in the loading direction. This corresponds to the experimental observations of the shear crack by [109]. The authors also give the tip positions at different instants of time; they are represented in Figures 3.15-3.17 with red square symbols.

In Figure 3.14 the lines of constant shear stress Σ_{12} are represented near the tip of the damage band at $40 \mu\text{s}$ and $60 \mu\text{s}$, respectively. When approaching the tip, the absolute

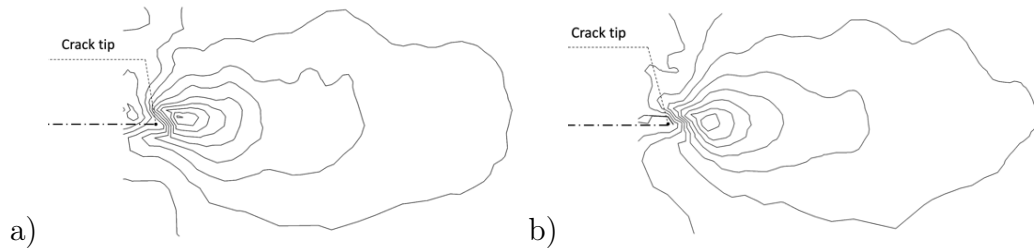


Figure 3.14: Lines of constant shear stress Σ_{12} at: a) $40 \mu\text{s}$ and b) $60 \mu\text{s}$. The absolute values of Σ_{12} are increasing when approaching the tip of the damage band.

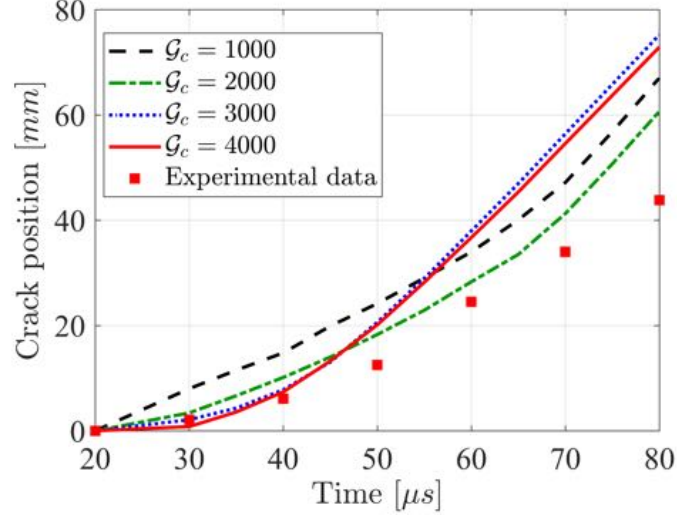


Figure 3.15: Variation of the crack-tip position with time for constant values of \mathcal{G}_c .

values of Σ_{12} are increasing, with a maximum in the immediate vicinity of the damage front. With respect to the angle at the tip, they are maximal approximately on the (horizontal) damage line, ahead of the tip. This distribution is characteristic to dominant mode II crack propagation [112].

To explore the possibility of reproducing the experimental data for the crack-tip evolution, we first considered the case of constant fracture energy $\mathcal{G}_c = \mathcal{G}_{c0}$. In Figure 3.15 the variation of the crack tip position with time is represented for four constant values of \mathcal{G}_c . A tendency of approaching the experimental points is observed when one increases the fracture energy but this is effective only on the interval up to $40 \mu s$. For large values of \mathcal{G}_c , the propagation is more rapid. Since the increase of the critical energy first delayed the propagation, much more energy is stored in the sample leading to more rapid propagation in a second stage.

In these simulations the value of the microstructural length is $l_c = 8 \times 10^{-5} m$. Note that this value is close to the one considered for the mode I failure $l_c = 6 \times 10^{-5} m$ in the compact compression specimen impact test [42]. The particular influence of \mathcal{G}_c in Figure 3.15 is also obtained when the critical energy is kept constant but the length ε is decreased. For smaller microstructures, the propagation is also delayed initially and the same acceleration effect in the later stage is retrieved.

The next step of our investigation is to consider velocity-dependent fracture energy $\mathcal{G}_c = \mathcal{G}_{c0} \times (1 + a.v)$. For the initial value $\mathcal{G}_{c0} = 2100 J/m^2$ was found to be a good choice. Relatively good approximations of the experimental data are obtained for a in the range $0.0075 - 0.0125 s/m$. We note that the value $\mathcal{G}_{c0} = 2100 J/m^2$ is consistent with the estimation of [27] who determined that the ratio between mode II and mode I fracture toughness is about 2.5. This would correspond to a mode I fracture energy of $336 J/m^2$ which is in the range of acceptable values for the PMMA material.

The predicted crack tip position at different instants of time and for $a = 0.0075 s/m$ is represented in Figure 3.17. This rapid evolution is typical for a shear crack. The

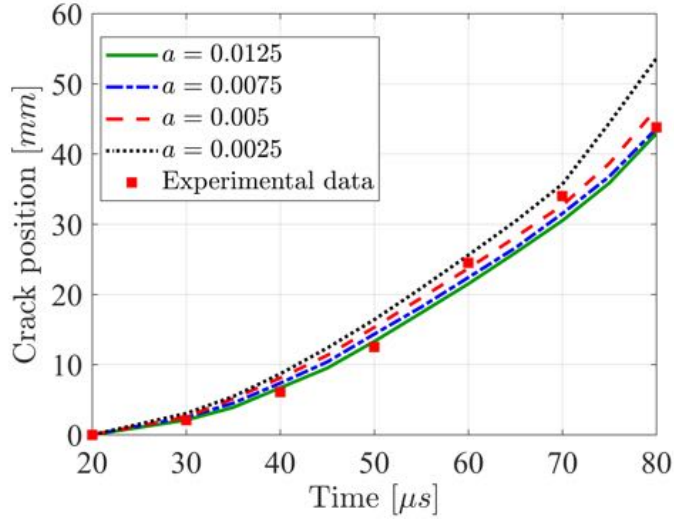


Figure 3.16: Crack-tip position vs time for different values of a and variable fracture energy $\mathcal{G}_c = 2100 \times (1 + a.v)$.

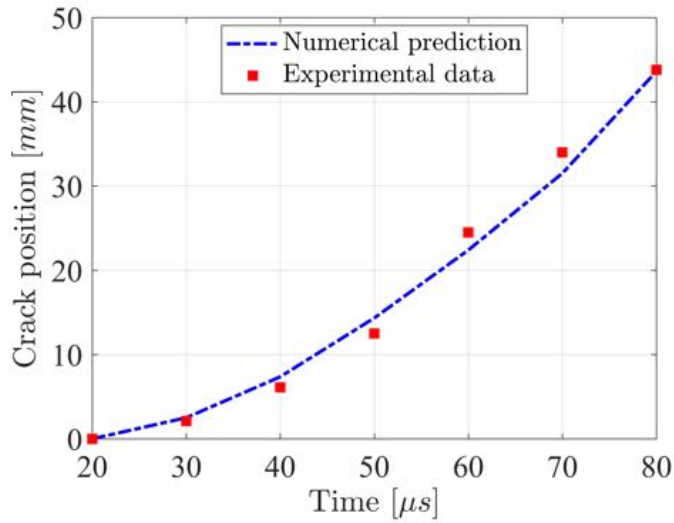


Figure 3.17: Crack-tip position vs time for $\mathcal{G}_c = 2100 \times (1 + 0.0075.v)$.

crack velocity is increased in $80 \mu s$ up to a value close to the Rayleigh wave speed, which is $1222.1 m/s$ for the considered material parameters. This corresponds to the measures reported in [109]. It is known that mode I cracks usually do not evolve up to the theoretical limit which is the Rayleigh wave velocity, but have a lower limit speed due to the development of micro-branching instabilities [112].

In order to evaluate the influence of the friction on fracture evolution, we also simulated the impact test in the case of frictionless contact $\mu_f = 0$ on microcracks. For the sake of comparison, we plotted in Figure 3.18 the crack-tip positions vs time for $\mu_f = 0$ and $\mu_f = 0.5$, respectively. It can be remarked that the presence of friction slows down the

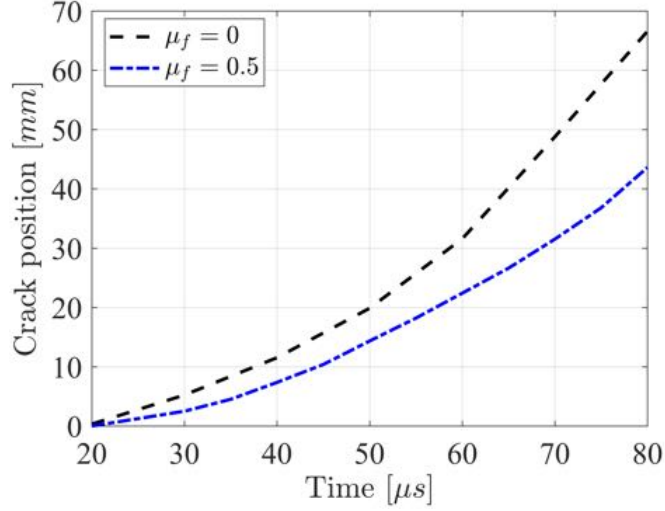


Figure 3.18: Crack-tip position vs time for $\mu_f = 0$ and $\mu_f = 0.5$.

fracture evolution. This influence at the structural level is related to that revealed by the local analysis and shows the necessity of including frictional effects on microcracks in the modeling of failure of quasi-brittle materials.

We finally study the influence of the normal compression on the macroscopic crack growth. For this, in addition to the impact loading, a normal displacement is applied on the top boundary of the specimen while the bottom is blocked in the vertical direction x_2 . No constraints are imposed in the impact direction x_1 on these two boundaries. The new loading is illustrated in Figure 3.11b. In order to have an effective compression in the groove before impact, the applied displacement is chosen in the form:

$$u_2(t) = \frac{u_c}{t_0}t \quad \text{for } t \leq t_0 \quad ; \quad u_2(t) = u_c \quad \text{for } t \geq t_0 \quad (3.39)$$

with $t_0 = 100 \mu s$ and the impact velocity $V_{imp} = 60 m/s$ is applied starting from $t_1 = 200 \mu s$.

In Figure 3.19, the crack tip advancement has been represented for different values of the applied normal displacement $u_c = 0 m$, $u_c = -0.0025 m$, $u_c = -0.005 m$ and $u_c = -0.0075 m$, respectively. As expected, when u_c is increased the fracture propagation is delayed as a consequence of the increased frictional resistance. We retrieve at the level of the macrostructure the influence of the normal compression discussed in the local analysis. This influence cannot be captured using a damage model not accounting for frictional effects.

Conclusions

A new dynamic damage model taking into account the dissipation due to friction on the lips of microcracks has been proposed. The damage evolution law is obtained by asymptotic homogenization from a microscopic Griffith-type propagation criterion in mode II.

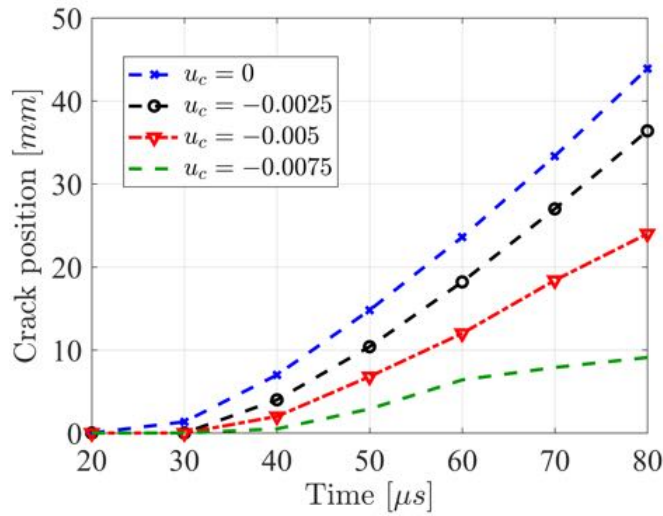


Figure 3.19: Crack-tip position vs time for different values of the applied normal displacement u_c at the top of the specimen.

Unilateral contact with friction conditions have been assumed on the lips of microcracks. The macroscopic damage law contains a length parameter characterizing the mutual distance between neighbor microcracks. Microstructural size effects, strain-rate sensitivity and friction influence are analyzed at the local and structural levels.

Numerical simulations of the impact test on PMMA samples are presented. For high impact velocities, the shear failure mode is activated in grooved specimens. It was found that the model predictions are in good agreement with the experimental data.

Further developments of the present model may explore the possibility to reproduce simultaneous mode I and mode II propagation by combination with the damage model in [82, 41], the prediction of the intersonic shear failure by replication of the experiments in [119] or the inclusion of frictional heating effects using an approach similar to that developed in [42] for mode I failure.

Chapter 4

Thermo-mechanical couplings in dynamic shear failure

Contents

4.1	Introduction	79
4.2	Thermoelastic fracture problem formulation	81
4.3	Asymptotic homogenization analysis	83
4.4	Dynamic damage law	90
4.5	Local macroscopic response	94
4.5.1	Homogenized coefficients	94
4.5.2	Macroscopic response	97
4.6	Numerical simulations of heating in mode II failure under impact	102
4.7	Conclusions	105

4.1 Introduction

The material response of quasi-brittle solids under compression loadings involving complex features like hardening and softening, stiffness degradation, induced anisotropy, irreversible deformations and thermal changes are the result of microscopic evolutions of microcracks with frictional sliding on their lips. The dynamic behavior of these materials is often associated with important thermal changes originated by small-scale dissipation processes related to microcrack propagation and frictional heating. In order to properly account for such mechanisms and their coupling, a multiscale modeling framework is well suited. The objective of the present contribution is to construct a two-scale thermomechanical damage model based on dynamic evolutions of mode II microcracks with associated heat dissipation effects due to their propagation and frictional sliding.

Micromechanical approaches for stationary or evolving frictional micro-cracks have been developed, among others, in [79], [93], [2], [5], [74], [98], [136], [91], [64], [69], [85],

[145], [147]. In dynamics, models based on micro-mechanics have been developed to study the compressive failure response of brittle solids in the case when the main microscopic mechanism is the tensile fracture mode. A study of an array of interacting and dynamically growing wing cracks and the corresponding rate-dependent dynamic damage evolution has been performed in [97]. In [113] the authors developed a micro-mechanical model for ceramics based on non-interacting, uniformly distributed sliding micro-cracks subjected to dynamic compressive loading and predicted effects of the rate sensitivity on failure strength. A model that combines damage evolution theory with dynamic crack growth under uniaxial dynamic compression has been proposed in [73]. Also, in [100] a model based on the evolution of tensile wing micro-cracks in the case of uniaxial compression under constant strain loading is developed. A more recent dynamic damage model inspired by the same wing crack mechanism and valid over a wide range of loading rates has been proposed in [16]. In [127] a phase-field fracture model has been used to simulate the intersonic shear fracture of brittle specimens under impact [119].

Thermal effects play an important role in the description of dynamic failure. Temperature measurements for opening or shear mode cracks, like those reported in [115, 116, 18, 19] for brittle polymers, revealed a significant temperature rise in a highly localized area surrounding the crack tip during propagation. Attempts to model such heating effects in the context of Fracture Mechanics have been made for instance in [25, 135] by considering crack models with Dirac-type heat sources located at the tip point and which intensity represents the excess of energy release rate with respect to that necessary for the new crack surface formation. In [18] the authors proposed a thermally dissipative cohesive zone model for dynamic fracture of amorphous polymers. Their model is based on the assumption that the excess supplied energy in the crack-tip region is converted to heat within the cohesive zone that models the crazing process. More recently, a multiscale damage approach has obtained [42] for mode I dynamic failure with moving heat sources at the tips of microcracks.

A second source of heating for shear rupture is the frictional sliding on the crack lips. For brittle materials under impact loading, the frictional heating on cracks has been considered for instance in [33]. Earthquakes motion is generally associated with the development of important densities of microcracks and the frictional heating effects play an important role in the description of seismic events [83, 55, 120]. In [46] a statistical approach has been developed to predict the dynamic response of brittle reactive materials with myriad of microcracks under impact and including the hot spot formation by frictional heating. A phase field damage model that includes heat sources due to frictional heating at the crack surfaces and heat dissipation during crack propagation has been used in [67, 49] to illustrate the nucleation of hot spots in energetic materials.

Impact experiments reported in [118, 119, 109, 17, 18] on bonded or side-grooved samples of brittle polymers revealed that under high strain rate loadings a failure mode transition from opening to shear fracture takes place. In contrast with the mode I crack velocities that are much smaller than the theoretical limit, the Rayleigh wave speed c_R , the shear cracks may evolve rapidly up to c_R and may pass in the supershear regime, with tip velocities v larger than the shear wave speed c_S . The microstructural observations of the fracture surfaces [109, 4], for mode II failure of PMMA samples under impact, revealed the existence of complex morphologies which do not correspond to *en echelon* mode

I microcracks, but rather to a mode II process zone. It was also observed [17, 19] that frictional contact plays an important role during the shear failure, leading to temperature rise up to the glass transition temperature and polymer melting effects. In this context, the present contribution investigates the possibility of modeling the dynamic shear failure of brittle solids using a thermomechanical damage model obtained by upscaling of microstructures with rapidly evolving mode II frictional microcracks and the associated thermal effects.

A method to obtain damage evolution laws from microcracks propagation criteria, using the asymptotic homogenization technique, has been proposed in [37]. In dynamics, a damage model has been established for mode I microcracks in [82, 41] and heat dissipation effects have been included in the mode I dynamic damage approach in [42]. For microcracks with contact and friction, a quasi-static damage law has been obtained in [140] and it has been extended to dynamics in [8]. The purpose of the present work is the construction of a two-scale thermomechanical damage model by homogenization in the case of dynamic mode II evolutions of microcracks having contact and friction conditions on their lips and with crack-tip and frictional heating sources.

This chapter is organized as follows. In Section 4.2, the thermoelastic dynamic fracture problem is formulated. The next two sections are devoted to the homogenization analysis for the macroscopic temperature and elastodynamics equations for the microcracked solid and the dynamic damage law deduced from the microscopic propagation criterion. The analysis of the local macroscopic response of the new model is performed in Section 4.5 for the effective coefficients, the influence of small-scale friction, the strain-rate and microstructural size, the thermal evolutions accompanying the damage processes. Results of numerical simulations for dynamic shear rupture of PMMA samples under impact loading and the associated thermal evolutions are presented and compared with the experimental data in the last section.

4.2 Thermoelastic fracture problem formulation

For a solid containing a large number of cracks that are small with respect to the size of the whole structure, we distinguish between the macroscopic properties at the scale of the solid body and the microscopic ones characterizing the local behavior in the vicinity of one microcrack.

The distribution of microcracks in the solid B is assumed to be locally periodic, as illustrated in Figure 4.1, all of them being straight and parallel to the x_1 axis. We denote by l the microcrack length and by l_c the size of the period. The local periodicity means slow spatial variations of l , with fixed l_c , such that locally the microstructure may be considered periodic.

If L_c is a characteristic length of the solid body B , as in Fig. 4.1, then the small parameter $\varepsilon = \frac{l_c}{L_c}$, is a measure of the difference between microscopic and macroscopic scales. The mechanical and thermal fields describing the corresponding two-scale multi-fracture problem will be denoted with an upper index ε .

The thermo-mechanical evolutions in a material point of the solid are described by

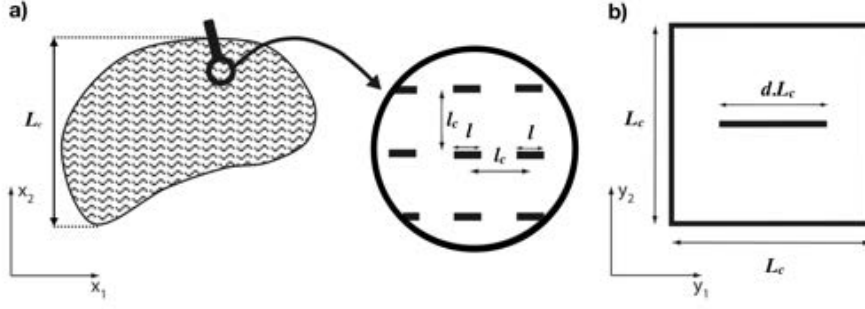


Figure 4.1: a) Solid body with locally periodic microstructure with l_c the size of a period, l the micro-crack length and L_c the characteristic length of the macro-structure. b) Reference cell of size L_c with rescaled crack length $d.L_c$.

the nonlinear equations of dynamic thermoelasticity

$$c \frac{\partial T^\varepsilon}{\partial t} + b_{ij} T^\varepsilon \frac{\partial e_{xij}(\mathbf{u}^\varepsilon)}{\partial t} + \frac{\partial q_j^\varepsilon}{\partial x_j} = 0 \quad (4.1)$$

$$\rho \frac{\partial^2 u_i^\varepsilon}{\partial t^2} - \frac{\partial \sigma_{ij}^\varepsilon}{\partial x_j} = 0 \quad (4.2)$$

where c is the specific heat and ρ the density of the material, $b_{ij} = \alpha(3\lambda + 2\mu)\delta_{ij}$ is the tensor of isotropic thermoelastic coupling coefficients, with λ , μ the Lamé constants and α the thermal expansion coefficient. The strain tensor calculated with respect to x_i variables is denoted by $e_{xij}(\mathbf{u}^\varepsilon) = \frac{1}{2} \left(\frac{\partial u_i^\varepsilon}{\partial x_j} + \frac{\partial u_j^\varepsilon}{\partial x_i} \right)$.

The heat flux vector \mathbf{q}^ε is given by the Fourier law:

$$q_j^\varepsilon = -k \frac{\partial T^\varepsilon}{\partial x_j} \quad (4.3)$$

where k is the thermal conduction coefficient of the material, while the thermoelastic constitutive relations for stresses are

$$\sigma_{ij}^\varepsilon = a_{ijkl} e_{xkl}(\mathbf{u}^\varepsilon) - b_{ij}(T^\varepsilon - T_0) \quad (4.4)$$

with $a_{ijkl} = \lambda \delta_{ij} \delta_{kl} + \mu(\delta_{ik} \delta_{jl} + \delta_{il} \delta_{jk})$ being the isotropic elastic moduli.

On each crack faces unilateral contact conditions are assumed:

$$[\boldsymbol{\sigma}^\varepsilon \mathbf{N}] = 0; \quad \mathbf{N} \boldsymbol{\sigma}^\varepsilon \mathbf{N} < 0; \quad [\mathbf{u}^\varepsilon \mathbf{N}] = 0 \quad (4.5)$$

together with the Coulomb friction law:

$$|\mathbf{T} \boldsymbol{\sigma}^\varepsilon \mathbf{N}| = -\mu_f \mathbf{N} \boldsymbol{\sigma}^\varepsilon \mathbf{N} \quad (4.6)$$

In these relations, \mathbf{N} is the unit vector normal to the crack, as shown in Fig. 4.2, \mathbf{T} is a unit vector tangent to the crack line, μ_f is the friction coefficient and $[\cdot]$ indicates the jump across the crack faces.

The frictional sliding between the crack faces gives rise to heating. A superficial heat source [142, 143] equal to the frictional power, calculated with the shear stress and the relative sliding velocity, is considered together with the continuity of the temperature field across the crack surface:

$$[\mathbf{q}^\varepsilon \mathbf{N}] = \mu_f \mathbf{N} \boldsymbol{\sigma}^\varepsilon \mathbf{N} \left[\frac{\partial \mathbf{u}^\varepsilon}{\partial t} \mathbf{T} \right] ; \quad [T^\varepsilon] = 0 \quad (4.7)$$

The sign in the right member of the first relation corresponds to negative relative velocities, as will be the case in the examples of the last section.

A second dissipation effect is linked to crack propagation. Most of the energy dissipated for rupture is converted into heat and the crack tips are behaving like moving heat sources [25, 135, 42]. If we define the heat flow from the crack tip as the limit

$$D^\varepsilon = \lim_{r \rightarrow 0} \int_{\Gamma_r} \mathbf{q}^\varepsilon \mathbf{n} \, ds \quad (4.8)$$

where Γ_r is a small contour shrinking to the tip as represented in Fig. 4.2, then the local balance of energy during propagation reads

$$D^\varepsilon = v_p \mathcal{G}^{d\varepsilon} \quad (4.9)$$

with $v_p = \frac{1}{2} \frac{dl}{dt}$ being the crack-tip velocity. The term $\mathcal{G}^{d\varepsilon}$ represents the dynamic energy release-rate

$$\mathcal{G}^{d\varepsilon} = \lim_{r \rightarrow 0} \int_{\Gamma_r} ((\mathcal{U}^\varepsilon + \mathcal{K}^\varepsilon) n_1 - \sigma_{ij}^\varepsilon n_j \frac{\partial u_i^\varepsilon}{\partial x_1}) ds \quad (4.10)$$

calculated with the internal energy:

$$\mathcal{U}^\varepsilon = \frac{1}{2} a_{ijkl} e_{xkl}(\mathbf{u}^\varepsilon) e_{xij}(\mathbf{u}^\varepsilon) + b_{ij} T_0 e_{xij}(\mathbf{u}^\varepsilon) + c T^\varepsilon \quad (4.11)$$

and the kinetic energy

$$\mathcal{K}^\varepsilon = \frac{1}{2} \rho \frac{\partial \mathbf{u}^\varepsilon}{\partial t} \frac{\partial \mathbf{u}^\varepsilon}{\partial t} \quad (4.12)$$

For the propagation of the cracks, we consider a Griffith-type criterion $\mathcal{G}^{d\varepsilon} = \mathcal{G}_c$, with \mathcal{G}_c the critical fracture energy. In this case the relation (4.9) becomes $D^\varepsilon = v_p \mathcal{G}_c$.

4.3 Asymptotic homogenization analysis

The previous multi-fracture problem will be upscaled to obtain an equivalent macroscopic formulation in this section. The asymptotic homogenization method [122, 56] will be used to deduce the macroscopic thermoelasticity equations from the initial problem described previously. A similar approach has been used for coupled dynamic thermoelasticity by [52, 57, 102, 9] in the case of solids without cracks. For thermoelastic microcracked solids in dynamics, the method has been used in [42] in the case of opening microcracks. In this section, we focus on the influence of the contact and frictional conditions on

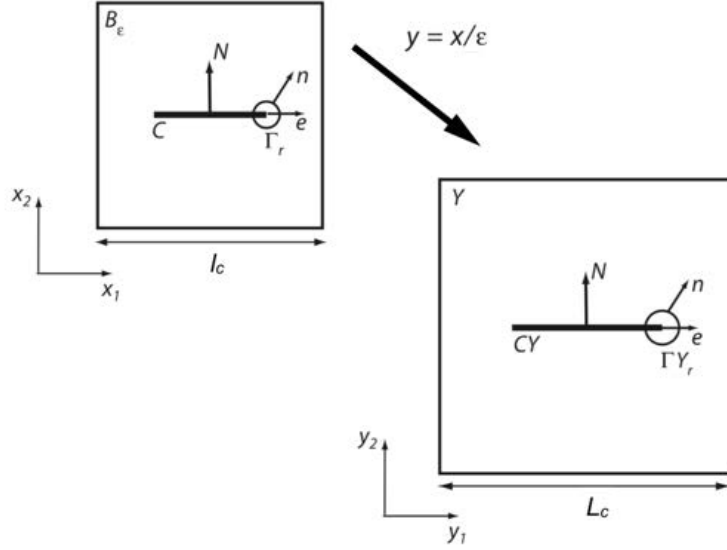


Figure 4.2: Scaling of the microscopic period B_ε with a crack C into the reference cell Y with the crack CY . The unit vectors \mathbf{n} and \mathbf{e} indicate the normal to the crack-tip contours Γ_r and Γ_{Y_r} and, respectively, the propagation direction.

shearing microcracks and of the non-classical heat sources associated with friction and rupture dissipations. The analysis performed here for the coupled thermoelastic system will be completed in Section 4.4 with the construction of the thermoelastic damage law by homogenization.

We introduce the damage variable $d = \frac{l}{l_c}$ as the microcrack length normalized by the size of the microscopic period. The local periodicity assumption for the length l , with constant l_c , will assure large-scale spatial variations of the damage variable d .

In what follows, we assume that the scale of microcracks is small in comparison with that of the solid body. This is expressed by the separation of scales condition

$$\varepsilon = \frac{l_c}{L_c} \ll 1 \quad (4.13)$$

Small-scale variations of the thermomechanical fields do not have much influence at the large scale. Two different systems of space variables will be considered for the two scales and both should be taken into account in the description of the physical fields, being treated as independent variables.

We will distinguish between the macroscopic variable \mathbf{x} and the microscopic variable \mathbf{y} , linked by the relation $\mathbf{y} = \frac{\mathbf{x}}{\varepsilon}$. For a field f depending on both \mathbf{x} and \mathbf{y} , the total spatial derivative can be calculated by the formula $\frac{df}{dx_i} = \frac{\partial f}{\partial x_i} + \frac{1}{\varepsilon} \frac{\partial f}{\partial y_i}$. The scaling of the microscopic period B_ε , containing a crack C , by this transformation leads to a reference cell Y , of size L_c and containing the crack CY of length $d.L_c$, as illustrated in Figure 4.2.

Asymptotic developments with respect to ε for the temperature and displacement

fields are considered:

$$\mathbf{u}^\varepsilon(\mathbf{x}, t) = \mathbf{u}^{(0)}(\mathbf{x}, \mathbf{y}, t) + \varepsilon \mathbf{u}^{(1)}(\mathbf{x}, \mathbf{y}, t) + \varepsilon^2 \mathbf{u}^{(2)}(\mathbf{x}, \mathbf{y}, t) + \dots \quad (4.14)$$

$$T^\varepsilon(\mathbf{x}, t) = T^{(0)}(\mathbf{x}, \mathbf{y}, t) + \varepsilon T^{(1)}(\mathbf{x}, \mathbf{y}, t) + \varepsilon^2 T^{(2)}(\mathbf{x}, \mathbf{y}, t) + \dots \quad (4.15)$$

where $\mathbf{u}^{(i)}(x, y, t)$ and $T^{(i)}(x, y, t)$, $\mathbf{x} \in B$ and $\mathbf{y} \in Y$ are Y -periodic.

Using these expansions in the equations (4.3-4.4) we get for the heat flux and stress fields:

$$\mathbf{q}^\varepsilon(\mathbf{x}, t) = \frac{1}{\varepsilon} \mathbf{q}^{(-1)}(\mathbf{x}, \mathbf{y}, t) + \mathbf{q}^{(0)}(\mathbf{x}, \mathbf{y}, t) + \varepsilon \mathbf{q}^{(1)}(\mathbf{x}, \mathbf{y}, t) + \varepsilon^2 \mathbf{q}^{(2)}(\mathbf{x}, \mathbf{y}, t) + \dots \quad (4.16)$$

$$\boldsymbol{\sigma}^\varepsilon(\mathbf{x}, t) = \frac{1}{\varepsilon} \boldsymbol{\sigma}^{(-1)}(\mathbf{x}, \mathbf{y}, t) + \boldsymbol{\sigma}^{(0)}(\mathbf{x}, \mathbf{y}, t) + \varepsilon \boldsymbol{\sigma}^{(1)}(\mathbf{x}, \mathbf{y}, t) + \varepsilon^2 \boldsymbol{\sigma}^{(2)}(\mathbf{x}, \mathbf{y}, t) + \dots \quad (4.17)$$

with

$$q_j^{(-1)} = -k \frac{\partial T^{(0)}}{\partial y_j} ; \quad q_j^{(0)} = -k \left(\frac{\partial T^{(0)}}{\partial x_j} + \frac{\partial T^{(1)}}{\partial y_j} \right) ; \quad q_j^{(1)} = -k \left(\frac{\partial T^{(1)}}{\partial x_j} + \frac{\partial T^{(2)}}{\partial y_j} \right) \quad (4.18)$$

and

$$\sigma_{ij}^{(-1)} = a_{ijkl} e_{ykl}(\mathbf{u}^{(0)}) \quad (4.19)$$

$$\sigma_{ij}^{(0)} = a_{ijkl} (e_{xkl}(\mathbf{u}^{(0)}) + e_{ykl}(\mathbf{u}^{(1)})) - b_{ij} (T^{(0)} - T_0) \quad (4.20)$$

$$\sigma_{ij}^{(1)} = a_{ijkl} (e_{xkl}(\mathbf{u}^{(1)}) + e_{ykl}(\mathbf{u}^{(2)})) - b_{ij} T^{(1)} \quad (4.21)$$

When these developments are replaced in the momentum and temperature equations (4.1-4.2) one obtains problems of order ε^n , with $n = -2, -1, 0$, in the form:

$$\frac{\partial q_j^{(-1)}}{\partial y_j} = 0 ; \quad \frac{\partial \sigma_{ij}^{(-1)}}{\partial y_j} = 0 \quad (4.22)$$

$$b_{ij} T^{(0)} \frac{\partial e_{yij}(u^{(0)})}{\partial t} + \frac{\partial q_j^{(-1)}}{\partial x_j} + \frac{\partial q_j^{(0)}}{\partial y_j} = 0 ; \quad \frac{\partial \sigma_{ij}^{(-1)}}{\partial x_j} + \frac{\partial \sigma_{ij}^{(0)}}{\partial y_j} = 0 \quad (4.23)$$

$$c \frac{\partial T^{(0)}}{\partial t} + b_{ij} T^{(0)} \left(\frac{\partial e_{xij}(u^{(0)})}{\partial t} + \frac{\partial e_{yij}(u^{(1)})}{\partial t} \right) + \frac{\partial q_j^{(0)}}{\partial x_j} + \frac{\partial q_j^{(1)}}{\partial y_j} = 0 ;$$

$$\rho \frac{\partial^2 u^{(0)}}{\partial t^2} - \frac{\partial \sigma_{ij}^{(0)}}{\partial x_j} - \frac{\partial \sigma_{ij}^{(1)}}{\partial y_j} = 0 \quad (4.24)$$

From the boundary conditions (4.5-4.6), for $m = -1, 0, 1$, we deduce:

$$\left[\sigma_{ij}^{(m)} N_j \right] = 0 ; \quad N_i \sigma_{ij}^{(m)} N_j < 0 ; \quad \left[u_i^{(m+1)} N_i \right] = 0 \quad (4.25)$$

$$\left| T_i \sigma_{ij}^{(m)} N_j \right| = -\mu_f N_i \sigma_{ij}^{(m)} N_j \quad (4.26)$$

while the thermal conditions (4.7) lead to

$$\left[q_j^{(-1)} N_j \right] = \mu_f N_i \sigma_{ij}^{(-1)} N_j \left[\frac{\partial u_m^{(0)}}{\partial t} T_m \right]; \quad [T^{(0)}] = 0 \quad (4.27)$$

$$\left[q_j^{(0)} N_j \right] = \mu_f \left(N_i \sigma_{ij}^{(-1)} N_j \left[\frac{\partial u_m^{(1)}}{\partial t} T_m \right] + N_i \sigma_{ij}^{(0)} N_j \left[\frac{\partial u_m^{(0)}}{\partial t} T_m \right] \right); \quad [T^{(1)}] = 0 \quad (4.28)$$

$$\left[q_j^{(1)} N_j \right] = \mu_f \left(N_i \sigma_{ij}^{(-1)} N_j \left[\frac{\partial u_m^{(2)}}{\partial t} T_m \right] + N_i \sigma_{ij}^{(0)} N_j \left[\frac{\partial u_m^{(1)}}{\partial t} T_m \right] \right) + \mu_f \left(N_i \sigma_{ij}^{(1)} N_j \left[\frac{\partial u_m^{(0)}}{\partial t} T_m \right] \right); \quad [T^{(2)}] = 0 \quad (4.29)$$

The development of the crack-tip heat flow (4.8) is calculated, using the link between the length elements in the physical and reference cells $ds = \varepsilon ds_y$, as:

$$D^\varepsilon = D^{(0)} + \varepsilon D^{(1)} + \varepsilon^2 D^{(2)} + \dots \quad (4.30)$$

with

$$D^{(0)} = \lim_{r \rightarrow 0} \int_{\Gamma_{Y_r}} -k \frac{\partial T^{(0)}}{\partial y_j} n_j ds_y; \quad D^{(1)} = \lim_{r \rightarrow 0} \int_{\Gamma_{Y_r}} -k \left(\frac{\partial T^{(0)}}{\partial x_j} + \frac{\partial T^{(1)}}{\partial y_j} \right) n_j ds_y; \quad D^{(2)} = \lim_{r \rightarrow 0} \int_{\Gamma_{Y_r}} -k \left(\frac{\partial T^{(1)}}{\partial x_j} + \frac{\partial T^{(2)}}{\partial y_j} \right) n_j ds_y \quad (4.31)$$

As concerns the energy release rate (4.10) it can be developed in the form:

$$\mathcal{G}^{d\varepsilon} = \frac{1}{\varepsilon} \mathcal{G}^{(-1)} + \mathcal{G}^{(0)} + \varepsilon \mathcal{G}^{(1)} + \dots \quad (4.32)$$

where the terms of different orders are:

$$\mathcal{G}^{(-1)} = \lim_{r \rightarrow 0} \int_{\Gamma_{Y_r}} \left(\frac{1}{2} a_{ijkl} e_{ykl}(\mathbf{u}^{(0)}) e_{yij}(\mathbf{u}^{(0)}) n_1 - a_{ijkl} e_{ykl}(\mathbf{u}^{(0)}) n_j \frac{\partial u_i^{(0)}}{\partial y_1} \right) ds_y \quad (4.33)$$

$$\mathcal{G}^{(0)} = \lim_{r \rightarrow 0} \int_{\Gamma_{Y_r}} \left(\left(a_{ijkl} e_{ykl}(\mathbf{u}^{(0)}) (e_{xij}(\mathbf{u}^{(0)}) + e_{yij}(\mathbf{u}^{(1)})) + b_{ij} T_0 e_{yij}(\mathbf{u}^{(0)}) \right) n_1 - a_{ijkl} (e_{xkl}(\mathbf{u}^{(0)}) + e_{ykl}(\mathbf{u}^{(1)})) n_j \frac{\partial u_i^{(0)}}{\partial y_1} - a_{ijkl} e_{ykl}(\mathbf{u}^{(0)}) n_j \left(\frac{\partial u_i^{(0)}}{\partial x_1} + \frac{\partial u_i^{(1)}}{\partial y_1} \right) \right) ds_y \quad (4.34)$$

$$\begin{aligned}
 \mathcal{G}^{(1)} = & \lim_{r \rightarrow 0} \int_{\Gamma Y_r} \left(\left(\frac{1}{2} a_{ijkl} \left(2e_{ykl}(\mathbf{u}^{(0)}) (e_{xij}(\mathbf{u}^{(0)}) + e_{yij}(\mathbf{u}^{(1)})) \right. \right. \right. \\
 & \left. \left. \left. + (e_{xij}(\mathbf{u}^{(0)}) + e_{yij}(\mathbf{u}^{(1)})) (e_{xkl}(\mathbf{u}^{(0)}) + e_{ykl}(\mathbf{u}^{(1)})) \right) \right. \\
 & \left. + b_{ij} T_0 (e_{xij}(\mathbf{u}^{(0)}) + e_{yij}(\mathbf{u}^{(1)})) + c T^{(0)} + \frac{\rho}{8} \frac{\partial u_i^{(0)}}{\partial y_1} \frac{\partial u_i^{(0)}}{\partial y_1} \left(\frac{dd}{dt} \right)^2 \right) n_1 \\
 & - \left(a_{ijkl} e_{ykl}(\mathbf{u}^{(0)}) n_j \left(\frac{\partial u_i^{(1)}}{\partial x_1} + \frac{\partial u_i^{(2)}}{\partial y_1} \right) \right. \\
 & \left. + \left(a_{ijkl} (e_{xkl}(\mathbf{u}^{(0)}) + e_{ykl}(\mathbf{u}^{(1)})) - b_{ij} (T^{(0)} - T_0) \right) n_j \left(\frac{\partial u_i^{(0)}}{\partial x_1} + \frac{\partial u_i^{(1)}}{\partial y_1} \right) \right. \\
 & \left. + \left(a_{ijkl} (e_{xkl}(\mathbf{u}^{(1)}) + e_{ykl}(\mathbf{u}^{(2)})) - b_{ij} T^{(1)} \right) n_j \frac{\partial u_i^{(0)}}{\partial y_1} \right) ds_y \quad (4.35)
 \end{aligned}$$

For the velocity field the local relation $\frac{\partial u_i^\varepsilon}{\partial t} \simeq -\frac{d(l/2)}{dt} \frac{\partial u_i^\varepsilon}{\partial x_1} = -\frac{\varepsilon L_c}{2} \frac{dd}{dt} \frac{\partial u_i^\varepsilon}{\partial x_1}$ in the vicinity of the crack tips [59, 25] has been used. Introduction of the expansions of $\mathcal{G}^{d\varepsilon}$ and D^ε in the energy relation (4.9) provides the link between different orders terms of heat dissipation and energy-release rate :

$$D^{(0)} = \frac{1}{2} \frac{dd}{dt} L_c \mathcal{G}^{(-1)} ; \quad D^{(1)} = \frac{1}{2} \frac{dd}{dt} L_c \mathcal{G}^{(0)} ; \quad D^{(2)} = \frac{1}{2} \frac{dd}{dt} L_c \mathcal{G}^{(1)} \quad (4.36)$$

From Equations (4.22), (4.25), (4.26), (4.27) and (4.36), we deduce at the order ε^{-2} the problems for $\mathbf{u}^{(0)}$ and $T^{(0)}$ as:

$$\frac{\partial}{\partial y_j} \left(a_{ijkl} e_{ykl}(\mathbf{u}^{(0)}) \right) = 0 \quad \text{in} \quad Y \quad (4.37)$$

$$[a_{ijkl} e_{ykl}(\mathbf{u}^{(0)}) N_j] = 0 ; \quad [u_i^{(0)} N_i] = 0 ; \quad N_i a_{ijkl} e_{ykl}(\mathbf{u}^{(0)}) N_j < 0 \quad (4.38)$$

$$| T_i a_{ijkl} e_{ykl}(\mathbf{u}^{(0)}) N_j | = -\mu_f N_i a_{ijkl} e_{ykl}(\mathbf{u}^{(0)}) N_j \quad (4.39)$$

on CY and

$$-k \left(\frac{\partial^2 T^{(0)}}{\partial y_1^2} + \frac{\partial^2 T^{(0)}}{\partial y_2^2} \right) = 0 \quad \text{in} \quad Y \quad (4.40)$$

$$[T^{(0)}] = 0 ; \quad \left[-k \frac{\partial T^{(0)}}{\partial y_j} N_j \right] = \mu_f N_i a_{ijkl} e_{ykl}(\mathbf{u}^{(0)}) \left[\frac{\partial u_m^{(0)}}{\partial t} T_m \right] N_j \quad (4.41)$$

$$\lim_{r \rightarrow 0} \int_{\Gamma Y_r} -k \frac{\partial T^{(0)}}{\partial y_j} n_j ds_y = \frac{1}{2} \frac{dd}{dt} L_c \mathcal{G}^{(-1)} \quad \text{at} \quad (y_1, y_2) = \left(\pm \frac{dL_c}{2}, 0 \right) \quad (4.42)$$

The solution is obtained by choosing the macroscopic displacements and temperature fields $\mathbf{u}^{(0)}(\mathbf{x}, \mathbf{t})$ and $T^{(0)}(\mathbf{x}, \mathbf{t})$, independent of the microscopic variables y_i , which verify the systems (4.37 - 4.39) and (4.40 - 4.42).

At the order ε^{-1} , from (4.23), (4.25), (4.26), (4.28) and (4.36) we get the problems for $\mathbf{u}^{(1)}$ and $T^{(1)}$ in the form:

$$\frac{\partial}{\partial y_j} (a_{ijkl} e_{ykl}(\mathbf{u}^{(1)})) = 0 \quad \text{in } Y \quad (4.43)$$

$$\left[\left(a_{ijkl} (e_{xkl}(\mathbf{u}^{(0)}) + e_{ykl}(\mathbf{u}^{(1)})) - b_{ij} (T^{(0)} - T_0) \right) N_j \right] = 0 \quad (4.44)$$

$$N_i \left(a_{ijkl} (e_{xkl}(\mathbf{u}^{(0)}) + e_{ykl}(\mathbf{u}^{(1)})) - b_{ij} (T^{(0)} - T_0) \right) N_j < 0 \quad (4.45)$$

$$\left| T_i \left(a_{ijkl} (e_{xkl}(\mathbf{u}^{(0)}) + e_{ykl}(\mathbf{u}^{(1)})) - b_{ij} (T^{(0)} - T_0) \right) N_j \right| = \quad (4.46)$$

$$-\mu_f N_i \left(a_{ijkl} (e_{xkl}(\mathbf{u}^{(0)}) + e_{ykl}(\mathbf{u}^{(1)})) - b_{ij} (T^{(0)} - T_0) \right) N_j \\ [u_i^{(1)} N_i] = 0 \quad (4.47)$$

on CY and

$$-k \left(\frac{\partial^2 T^{(1)}}{\partial y_1^2} + \frac{\partial^2 T^{(1)}}{\partial y_2^2} \right) = 0 \quad \text{in } Y \quad (4.48)$$

$$[T^{(1)}] = 0; \quad \left[-k \frac{\partial T^{(1)}}{\partial y_j} N_j \right] = - \left[-k \frac{\partial T^{(0)}}{\partial x_j} N_j \right] \quad \text{on } CY \quad (4.49)$$

$$\lim_{r \rightarrow 0} \int_{\Gamma Y_r} -k \left(\frac{\partial T^{(0)}}{\partial x_j} + \frac{\partial T^{(1)}}{\partial y_j} \right) n_j ds_y = \frac{1}{2} \frac{dd}{dt} L_c \mathcal{G}^{(0)} \text{ at } (y_1, y_2) = \left(\pm \frac{dL_c}{2}, 0 \right) \quad (4.50)$$

On the external boundaries of Y , periodicity conditions complete the formulation of the cell problems.

Since $\mathbf{u}^{(0)}$ is not depending on \mathbf{y} , the expressions (4.33-4.34) show that $\mathcal{G}^{(-1)}$ and $\mathcal{G}^{(0)}$ are vanishing. As remarked in [42], the kinetic energy do not contribute to $\mathcal{G}^{(-1)}$ unless higher order correctors are considered for the thermomechanical fields.

Let us define a system of generators for the macroscopic strains \mathbf{E}^{pq} that respect the contact boundary conditions. An example used in the simulations is given in the Appendix C. The macroscopic strains are obtained as linear combination of the elements of this system as:

$$e_{xij}(\mathbf{u}^{(0)}) = \varrho_{pq}(\mathbf{u}^{(0)}) E_{ij}^{pq} \quad (4.51)$$

Based on the previous boundary-value problem for the first-order corrector $\mathbf{u}^{(1)}$ we deduce its general expression in the form:

$$\mathbf{u}^{(1)}(\mathbf{x}, \mathbf{y}, t) = \boldsymbol{\xi}^{pq}(\mathbf{y}) \varrho_{pq}(\mathbf{u}^{(0)})(\mathbf{x}, t) + \boldsymbol{\phi}(\mathbf{y})(T^{(0)}(\mathbf{x}, t) - T_0) \quad (4.52)$$

where $\boldsymbol{\xi}^{pq}$ is the solution of:

$$\frac{\partial}{\partial y_j} (a_{ijkl} e_{ykl}(\boldsymbol{\xi}^{pq})) = 0 \quad \text{in } Y \quad (4.53)$$

$$\left[a_{ijkl} e_{ykl}(\boldsymbol{\xi}^{pq}) N_j \right] = - \left[a_{ijkl} E_{kl}^{pq} N_j \right] \quad (4.54)$$

$$N_i a_{ijkl} (e_{ykl}(\boldsymbol{\xi}^{pq}) + E_{kl}^{pq}) N_j < 0 \quad (4.55)$$

$$\left| T_i a_{ijkl} (e_{ykl}(\boldsymbol{\xi}^{pq}) + E_{kl}^{pq}) N_j \right| = -\mu_f N_i a_{ijkl} (e_{ykl}(\boldsymbol{\xi}^{pq}) + E_{kl}^{pq}) N_j \quad (4.56)$$

$$[\xi_i^{pq} N_i] = 0 \quad (4.57)$$

while ϕ is obtained by solving for the unit cell the problem:

$$\frac{\partial}{\partial y_j} (a_{ijkl} e_{ykl}(\phi)) = 0 \quad \text{in } Y \quad (4.58)$$

$$\left[a_{ijkl} e_{ykl}(\phi) N_j \right] = \left[b_{ij} N_j \right] \quad (4.59)$$

$$N_i (a_{ijkl} e_{ykl}(\phi) - b_{ij}) N_j < 0 \quad (4.60)$$

$$|T_i (a_{ijkl} e_{ykl}(\phi) - b_{ij}) N_j| = -\mu_f N_i (a_{ijkl} e_{ykl}(\phi) - b_{ij}) N_j \quad (4.61)$$

$$[\phi_i N_i] = 0 \quad (4.62)$$

Taking into account the orientation of the microcrack, with $N_1 = 0$ and $N_2 = 1$, the solution of (4.48 - 4.50) has the general form

$$T^{(1)} = \theta(\mathbf{y}) \frac{\partial T^{(0)}}{\partial x_2}(\mathbf{x}, t) \quad (4.63)$$

where θ is obtained by solving the cell problem:

$$-k \left(\frac{\partial^2 \theta}{\partial y_1^2} + \frac{\partial^2 \theta}{\partial y_2^2} \right) = 0 \quad \text{in } Y \quad (4.64)$$

$$\left[\frac{\partial \theta}{\partial y_2} \right] = 0; \quad [\theta] = 0 \quad \text{on } CY \quad (4.65)$$

$$\lim_{r \rightarrow 0} \int_{\Gamma_{Y_r}} -k \left(\frac{\partial \theta}{\partial y_1} n_1 + \frac{\partial \theta}{\partial y_2} n_2 \right) ds_y = 0 \quad \text{at } (y_1, y_2) = \left(\pm \frac{dL_c}{2}, 0 \right) \quad (4.66)$$

More details about the formulation of these unit-cell solutions and their compatibility with the contact conditions on the crack faces are given in the Appendix C.

At the order ε^0 , we obtain for temperature and displacement fields:

$$c \frac{\partial T^{(0)}}{\partial t} + b_{ij} T^{(0)} \frac{\partial}{\partial t} (e_{xij}(\mathbf{u}^{(0)}) + e_{yij}(\mathbf{u}^{(1)})) + \frac{\partial q_j^{(0)}}{\partial x_j} + \frac{\partial q_j^{(1)}}{\partial y_j} = 0 \quad \text{in } Y \quad (4.67)$$

$$[T^{(2)}] = 0; \quad [q_j^{(1)} N_j] = \mu_f N_i \sigma_{ij}^{(0)} N_j \left[\frac{\partial u_m^{(1)}}{\partial t} T_m \right] \quad \text{on } CY \quad (4.68)$$

$$\lim_{r \rightarrow 0} \int_{\Gamma_{Y_r}} q_j^{(1)} n_j ds_y = \frac{1}{2} \frac{dd}{dt} L_c \mathcal{G}^{(1)} \quad \text{at } (y_1, y_2) = \left(\pm \frac{dL_c}{2}, 0 \right) \quad (4.69)$$

and

$$\rho \frac{\partial^2 u_i^{(0)}}{\partial t^2} - \frac{\partial \sigma_{ij}^{(0)}}{\partial x_j} - \frac{\partial \sigma_{ij}^{(1)}}{\partial y_j} = 0 \quad \text{in } Y \quad (4.70)$$

$$|T_i \sigma_{ij}^{(1)} N_j| = -\mu_f N_i \sigma_{ij}^{(1)} N_j \quad \text{on } CY \quad (4.71)$$

$$[\sigma_{ij}^{(1)} N_j] = 0; \quad N_i \sigma_{ij}^{(1)} N_j < 0; \quad [u_i^{(1)} N_i] = 0 \quad \text{on } CY \quad (4.72)$$

To obtain the macroscopic thermo-mechanical equations we apply the mean value operator $\langle \cdot \rangle = \frac{1}{|Y|} \int_Y \cdot dy$, with $|Y| = L_c^2$, to (4.67) and (4.70). Integration by parts and

use of the periodicity and boundary conditions on microcracks lead to:

$$(c + T^{(0)}S^*)\frac{\partial T^{(0)}}{\partial t} + T^{(0)}\beta_{ij}\frac{\partial e_{xij}(\mathbf{u}^{(0)})}{\partial t} + \frac{\partial Q_j^{(0)}}{\partial x_j} = \quad (4.73)$$

$$\begin{aligned} \frac{\mathcal{G}^{(1)}}{L_c}\frac{dd}{dt} + \frac{1}{L_c^2}\int_{CY}\sigma_{ij}^{(0)}N_j\left[\dot{u}_i^{(1)}\right]ds_y \\ \rho^{eff}\frac{\partial^2 u_i^{(0)}}{\partial t^2} - \frac{\partial \Sigma_{ij}^{(0)}}{\partial x_j} = 0 \end{aligned} \quad (4.74)$$

with the macroscopic stress $\Sigma_{ij}^{(0)} = \langle \sigma_{ij}^{(0)} \rangle$ and heat flux $Q_j^{(0)} = \langle q_j^{(0)} \rangle$:

$$\Sigma_{ij}^{(0)} = C_{ijpq}e_{xpq}(\mathbf{u}^{(0)}) - \vartheta_{ij}(T^{(0)} - T_0) \quad (4.75)$$

$$Q_i^{(0)} = -k_{ij}^{eff}\frac{\partial T^{(0)}}{\partial x_j} \quad (4.76)$$

The particular expressions of the effective moduli S^* , C_{ijpq} , ρ^{eff} , ϑ_{ij} and k_{ij}^{eff} are given in the Appendix C. They are calculated with the unit-cell solutions and depend on the normalized crack length d .

As concerns the source terms in the right member of the equation (4.73), their macroscopic expressions will be obtained in the next section. It is important to note that the first one is calculated as a limit at the microcrack tips and represents the heating due to the damage evolution. The second term is obtained as an integral on microcracks and expresses the frictional heating effect. When damage is not evolving only the second term will be non-vanishing, while for propagating microcracks without friction only the first term remains in (4.73).

4.4 Dynamic damage law

The asymptotic homogenization method is used here in combination with an energy analysis for microcracks propagating dynamically, in mode II, with frictional contact and heating conditions, in order to obtain a macroscopic damage law. A specific upscaling procedure, from microcracks to damage, has been proposed in previous studies [37, 140, 82, 42] and the objective of this section is to extend this approach to account for thermal effects in the case of dynamically propagating mode II microcracks with contact and friction.

Starting from similar cell problems as in the previous section, in [37, 140] the following energy balance has been established:

$$\begin{aligned} \frac{d}{dt}\int_Y\frac{1}{2}a_{ijkl}e_{ykl}(\mathbf{u}^{(1)})e_{yij}(\mathbf{u}^{(1)})dy + \frac{dd}{dt}L_c\mathcal{G}^{(1)} \\ = \int_{CY}a_{ijkl}e_{ykl}(\mathbf{u}^{(1)})N_j\left[\dot{u}_i^{(1)}\right]ds_y \end{aligned} \quad (4.77)$$

The equivalent form of the equation (4.37):

$$\frac{\partial}{\partial y_j}\left(a_{ijkl}e_{xkl}(\mathbf{u}^{(0)}) - b_{ij}(T^{(0)} - T_0)\right) = 0 \quad (4.78)$$

multiplied by $\dot{u}_i^{(1)}$ and integrated over Y leads to:

$$\begin{aligned} & \int_{CY} (a_{ijkl}e_{xkl}(\mathbf{u}^{(0)}) - b_{ij}(T^{(0)} - T_0))N_j[\dot{u}_i^{(1)}]ds_y = \\ & \int_Y (a_{ijkl}e_{xkl}(\mathbf{u}^{(0)}) - b_{ij}(T^{(0)} - T_0))e_{yij}(\dot{\mathbf{u}}^{(1)})dy \end{aligned} \quad (4.79)$$

Combination of the relations (4.77) and (4.79) gives:

$$\begin{aligned} & \int_{CY} \left(a_{ijkl}(e_{xkl}(\mathbf{u}^{(0)}) + e_{ykl}(\mathbf{u}^{(1)})) - b_{ij}(T^{(0)} - T_0) \right) N_j [\dot{u}_i^{(1)}] ds_y \\ & = \frac{dd}{dt} L_c \mathcal{G}^{(1)} + \frac{d}{dt} \int_Y \frac{1}{2} a_{ijkl} e_{ykl}(\mathbf{u}^{(1)}) e_{yij}(\mathbf{u}^{(1)}) dy \\ & \quad + \int_Y (a_{ijkl}e_{xkl}(\mathbf{u}^{(0)}) - b_{ij}(T^{(0)} - T_0))e_{yij}(\dot{\mathbf{u}}^{(1)})dy \end{aligned} \quad (4.80)$$

Using the Reynolds transport theorem [137] together with the singularity of the $\mathbf{u}^{(1)}$ field, for the last integral in (4.80) we get:

$$\begin{aligned} & \int_Y (a_{ijkl}e_{xkl}(\mathbf{u}^{(0)}) - b_{ij}(T^{(0)} - T_0))e_{yij}(\dot{\mathbf{u}}^{(1)})dy = \\ & \frac{d}{dt} \int_Y (a_{ijkl}e_{xkl}(\mathbf{u}^{(0)}) - b_{ij}(T^{(0)} - T_0))e_{yij}(\mathbf{u}^{(1)})dy \\ & \quad - \int_Y (a_{ijkl}e_{xkl}(\dot{\mathbf{u}}^{(0)}) - b_{ij}\dot{T}^{(0)})e_{yij}(\mathbf{u}^{(1)})dy \end{aligned} \quad (4.81)$$

such that (4.80) becomes:

$$\begin{aligned} & \int_{CY} \left(a_{ijkl}(e_{xkl}(\mathbf{u}^{(0)}) + e_{ykl}(\mathbf{u}^{(1)})) - b_{ij}(T^{(0)} - T_0) \right) N_j [\dot{u}_i^{(1)}] ds_y - \frac{dd}{dt} L_c \mathcal{G}^{(1)} \\ & \quad - \frac{1}{2} \frac{d}{dt} \int_Y \left(a_{ijkl}(e_{xkl}(\mathbf{u}^{(0)}) + e_{ykl}(\mathbf{u}^{(1)})) - b_{ij}(T^{(0)} - T_0) \right) e_{yij}(\mathbf{u}^{(1)}) dy \\ & = \frac{1}{2} \frac{d}{dt} \int_Y (a_{ijkl}e_{xkl}(\mathbf{u}^{(0)}) - b_{ij}(T^{(0)} - T_0))e_{yij}(\mathbf{u}^{(1)})dy \\ & \quad - \int_Y (a_{ijkl}e_{xkl}(\dot{\mathbf{u}}^{(0)}) - b_{ij}\dot{T}^{(0)})e_{yij}(\mathbf{u}^{(1)})dy \end{aligned} \quad (4.82)$$

On the other hand, we can rewrite the equation (4.43) as:

$$\frac{\partial}{\partial y_j} \left(a_{ijkl}(e_{xkl}(\mathbf{u}^{(0)}) + e_{ykl}(\mathbf{u}^{(1)})) - b_{ij}(T^{(0)} - T_0) \right) = 0 \quad (4.83)$$

Multiplication by $u_i^{(1)}$ and integration on Y give:

$$\begin{aligned} & \int_Y \left(a_{ijkl}(e_{xkl}(\mathbf{u}^{(0)}) + e_{ykl}(\mathbf{u}^{(1)})) - b_{ij}(T^{(0)} - T_0) \right) e_{yij}(\mathbf{u}^{(1)}) dy = \\ & \int_{CY} \left(a_{ijkl}(e_{xkl}(\mathbf{u}^{(0)}) + e_{ykl}(\mathbf{u}^{(1)})) - b_{ij}(T^{(0)} - T_0) \right) N_j [u_i^{(1)}] ds_y \end{aligned} \quad (4.84)$$

This identity can be used in (4.82) to obtain the energy relation:

$$\begin{aligned} \int_{CY} \sigma_{ij}^{(0)} N_j \left[\dot{u}_i^{(1)} \right] ds_y - \frac{dd}{dt} L_c \mathcal{G}^{(1)} - \frac{1}{2} \frac{d}{dt} \int_{CY} \sigma_{ij}^{(0)} N_j \left[u_i^{(1)} \right] ds_y = \\ \frac{1}{2} \frac{d}{dt} \int_Y (a_{ijkl} e_{xkl}(\mathbf{u}^{(0)}) - b_{ij}(T^{(0)} - T_0)) e_{yij}(\mathbf{u}^{(1)}) dy \\ - \int_Y (a_{ijkl} e_{xkl}(\dot{\mathbf{u}}^{(0)}) - b_{ij} \dot{T}^{(0)}) e_{yij}(\mathbf{u}^{(1)}) dy \end{aligned} \quad (4.85)$$

Based on the particular form of the microscopic first-order correctors (4.52) and (4.63) and using the frictional contact and heating boundary conditions, it is shown in the Appendix C that we can obtain from (4.85) damage relation:

$$\frac{dd}{dt} \left(\frac{\mathcal{G}^{(1)}}{L_c} - \mathcal{Y} + \mathcal{Y}_f \right) = 0 \quad (4.86)$$

where the effective thermomechanical energy-release rate is

$$\begin{aligned} \mathcal{Y} = -\frac{1}{2} \frac{dC_{klpq}}{dd} e_{xpq}(\mathbf{u}^{(0)}) e_{xkl}(\mathbf{u}^{(0)}) \\ + \frac{1}{2} \left(\frac{d\vartheta_{kl}}{dd} + \alpha \frac{dC_{pqkl}}{dd} \delta_{pq} \right) (T^{(0)} - T_0) e_{xkl}(\mathbf{u}^{(0)}) + \frac{1}{2} \frac{dS^*}{dd} (T^{(0)} - T_0)^2 \end{aligned} \quad (4.87)$$

and the amount of energy dissipated by friction

$$\mathcal{Y}_f = I_{mnpq} e_{xmn}(\mathbf{u}^{(0)}) e_{xpq}(\mathbf{u}^{(0)}) + J_{mn} e_{xmn}(\mathbf{u}^{(0)}) (T^{(0)} - T_0) - P (T^{(0)} - T_0)^2 \quad (4.88)$$

Explicit expressions of the effective coefficients I_{mnpq} , J_{mn} and P are given in the Appendix C.

The damage relation (4.86) can be viewed as an identity between the energy dissipated during the propagation of microcracks and the corresponding damage dissipation at the macroscopic scale, calculated with the difference between the total energy release rate and the dissipation due to frictional sliding.

The relation between the dynamic and the quasi-static energy release [59, 129] is $\mathcal{G}^{d\varepsilon} = g_2(v_p) \mathcal{G}^\varepsilon$, where $\mathcal{G}^\varepsilon = \varepsilon \mathcal{G}^{(1)}$ is the quasi-static energy release rate, $v_p = \frac{l_c}{2} \frac{dd}{dt}$ is the crack-tip speed and $g_2(v_p)$ a universal function for mode II propagation. Retaining the approximation proposed in [8]:

$$g_2(v_p) \simeq \sqrt{1 - \frac{v_p}{c_R}} \quad (4.89)$$

we deduce

$$\mathcal{G}^{(1)} = \frac{L_c}{l_c} \frac{\mathcal{G}^{d\varepsilon}}{\sqrt{1 - \frac{l_c}{2c_R} \frac{dd}{dt}}} \quad (4.90)$$

If we adopt a Griffith type propagation criterion $\mathcal{G}^{d\varepsilon} = \mathcal{G}_c$, with \mathcal{G}_c the fracture energy, then (4.86) leads to the damage law:

$$\frac{dd}{dt} = \frac{2C_R}{\varepsilon} \left\langle 1 - \frac{\mathcal{G}_c^2}{\varepsilon^2(\mathcal{Y} - \mathcal{Y}_f)^2} \right\rangle \quad (4.91)$$

where $\langle . \rangle$ represent the positive part.

The experiments on the dynamic failure of some brittle materials reveal the necessity to consider velocity-dependent fracture energy. In the case of a linear approximation [42] : $\mathcal{G}_c(v_p) = \mathcal{G}_{c0}(1 + a.v_p)$ we obtain from (4.86) a more complex form of the damage law:

$$\frac{dd}{dt} = \left\langle \frac{2\Pi}{a^2\mathcal{G}_{c0}^2 l_c^2} - \frac{l_c}{a^2 C_R \mathcal{G}_{c0}^2} (\mathcal{Y}_d - \mathcal{Y}_f)^2 - \frac{2}{a l_c} \right\rangle \quad (4.92)$$

where

$$\Pi = \sqrt{\left(a\mathcal{G}_{c0}^2 l_c + \frac{l_c^3}{2C_R} (\mathcal{Y} - \mathcal{Y}_f)^2 \right)^2 - a^2\mathcal{G}_{c0}^2 l_c^2 \left(\mathcal{G}_{c0}^2 - l_c^2 (\mathcal{Y}_d - \mathcal{Y}_f)^2 \right)} \quad (4.93)$$

We remark that the microstructural length l_c is present in the equations (4.91) and (4.92) and will give rise to size effects related to damage evolution. Also, the energy-release rate terms depend on the macroscopic deformation and temperature assuring the thermoelastic and damage coupling. These effects will be illustrated by the response analysis considered in the last section.

At this point, using the developments in the Appendix C, we can deduce from (4.73) the macroscopic temperature equation in the form

$$(c + T^{(0)} S^*) \frac{\partial T^{(0)}}{\partial t} + T^{(0)} \beta_{pq} \frac{\partial e_{xpq}(\mathbf{u}^{(0)})}{\partial t} + \frac{\partial Q_j^{(0)}}{\partial x_j} = \mathcal{R}_d + \mathcal{R}_f \quad (4.94)$$

The first term in the right member of this equation \mathcal{R}_d represents a heat source related to damage evolution and is given by

$$\mathcal{R}_d = \frac{dd}{dt} (\mathcal{Y} - \mathcal{Y}_f) = \frac{dd}{dt} \left(\frac{1}{2l_c} \frac{2 + a.l_c \frac{dd}{dt}}{\sqrt{1 - \frac{l_c}{2C_R} \frac{dd}{dt}}} \mathcal{G}_{c0} \right) \quad (4.95)$$

We can observe that the first expression of \mathcal{R}_d is a typical damage dissipation formula with the energy-release rate $\mathcal{Y} - \mathcal{Y}_f$ involved in the previous damage laws. The heat source \mathcal{R}_d corresponds to the first term in the right member of the temperature equation (4.73) and is activated in the material points where damage evolves.

The second term accounts for the frictional heating on microcracks and reads:

$$\begin{aligned} \mathcal{R}_f = \frac{dd}{dt} & \left(I_{mnpq}^2 e_{xmn}(\mathbf{u}^{(0)}) e_{xpq}(\mathbf{u}^{(0)}) + J_{mn}^2 e_{xmn}(\mathbf{u}^{(0)}) (T^{(0)} - T_0) - P^2 (T^{(0)} - T_0)^2 \right) \\ & + \mathcal{Z}_{mnpq}^1 e_{xmn}(\mathbf{u}^{(0)}) \frac{\partial e_{xpq}(\mathbf{u}^{(0)})}{\partial t} + \mathcal{Z}_{pq}^2 \frac{\partial e_{xpq}(\mathbf{u}^{(0)})}{\partial t} (T^{(0)} - T_0) \\ & + \mathcal{Z}_{mn}^3 e_{xmn}(\mathbf{u}^{(0)}) \frac{\partial T^{(0)}}{\partial t} + \mathcal{Z}^4 (T^{(0)} - T_0) \frac{\partial T^{(0)}}{\partial t} \end{aligned} \quad (4.96)$$

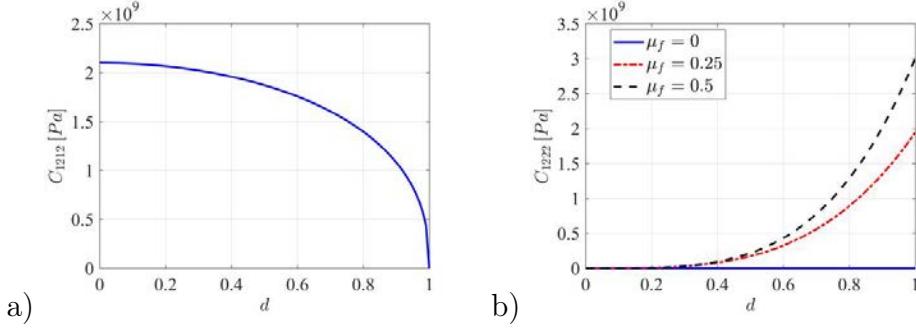


Figure 4.3: Effective elastic coefficients C_{1212} (a) and C_{1222} (b) vs damage variable d computed for the friction coefficients $\mu_f = 0, 0.25, 0.5$.

The details concerning the coefficients \mathcal{Z}_{mnpq}^1 , \mathcal{Z}_{mn}^2 , \mathcal{Z}_{mn}^3 , I_{mnpq}^2 , J_{mn}^2 and P^2 are given in the Appendix C. In the case of non-frictional sliding on microcracks, all of them are vanishing.

4.5 Local macroscopic response

The analysis of the local macroscopic response predicted by the new damage model is presented in this section. We first present the effective coefficients and their dependence on damage and friction coefficients, then we study the local macroscopic response. The coefficients are computed with unit-cell FE solutions for different microcrack lengths. For the study of the macroscopic response the solution of the damage law (4.92) coupled with the equation of temperature (4.94) in the adiabatic approximation is obtained for a given history of compression and shear macroscopic strains. Shear stresses are obtained from the constitutive law (4.75). Effects of the size of microstructure, shear strain rate, initial microcrack length, compression loading and friction coefficient will be discussed.

The generic material parameters used in the simulations for the PMMA polymer are summarized in Table 4.1. A velocity-dependent fracture energy $\mathcal{G}_c(v_p) = \mathcal{G}_{c0}(1 + a \cdot v_p)$ is assumed for the mode II propagation.

4.5.1 Homogenized coefficients

All the effective coefficients were computed with the FE solution of the corresponding cell problems using the FEM software COMSOL Multiphysics. Since they are functions of damage, such computations have been done for different values of $d \in [0, 1]$ and the results have been interpolated with polynomials.

E (GPa)	ν	ρ (kg m ⁻³)	c (Jm ⁻³ K ⁻¹)	α (K ⁻¹)	μ_f	\mathcal{G}_{c0} (Jm ⁻²)	a (s m ⁻¹)
5.6	0.33	1180	10 ⁶	10 ⁻⁴	0.5	2100	0.01

Table 4.1: Generic material parameters for PMMA used in the local macroscopic analysis.

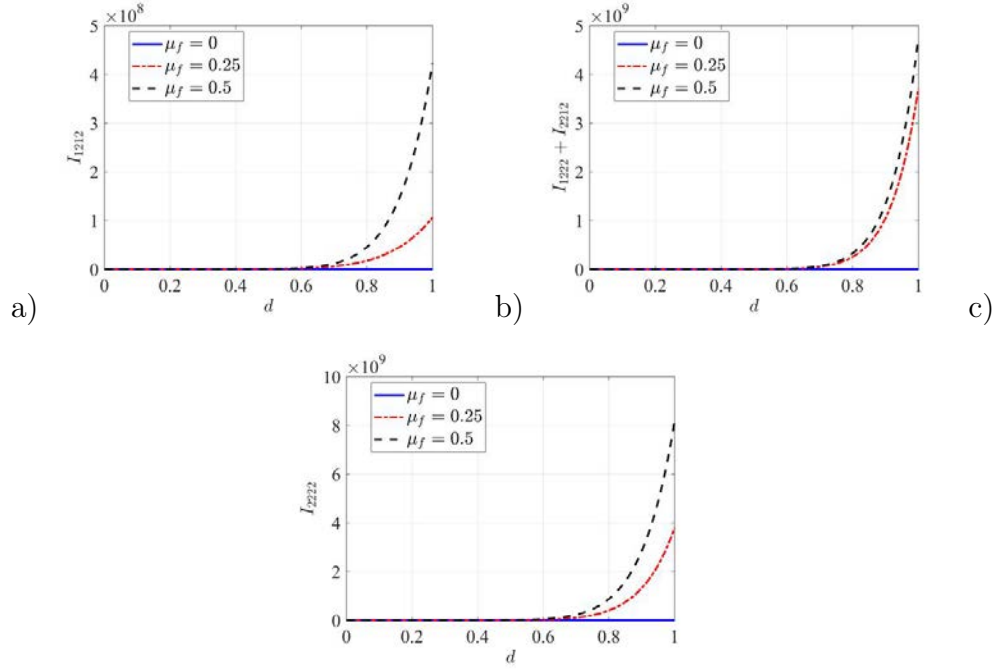


Figure 4.4: Homogenized coefficients I_{1212} (a), $I_{1222} + I_{2212}$ (b) and I_{2222} (c) vs damage variable d , for $\mu_f = 0, 0.25, 0.5$.

For the elastic coefficients C_{ijpq} , the problem (4.53-4.57) is solved numerically on the unit cell. Except C_{1222} and C_{1212} , the others components of the tensor C_{ijpq} are not dependent on the damage variable. If λ and μ are the Lamé coefficients, we obtain $C_{1111} = C_{2222} = \lambda + 2\mu$, $C_{1122} = C_{2211} = \lambda$ and $C_{1112} = C_{1211} = 0$.

In Figure 4.3, the coefficients C_{1212} and C_{1222} are represented as functions of the damage variable d for three values of the friction coefficient $\mu_f = 0, 0.25, 0.5$. Damage induced degradation is observed for C_{1212} without dependence on the friction coefficient. It represents the effect of the shear deformation of the unit cell on the macroscopic shear stress and the presence of microcracks makes easier the deformation of the cell, reducing the level of resulting shear stress. For a completely fractured cell, no shear stresses are generated since the two parts move freely. C_{1222} characterizes the influence of the compression deformation e_{x22} on the macroscopic shear stress. In the absence of friction, there is no such influence while, in the case of frictional sliding, the compression influences the frictional resistance giving rise shear stresses. This effect is amplified by the value of the friction coefficient μ_f and also by the size of the friction zone, controlled by the normalized microcrack length d . Both effects can be seen in Figure 4.3b.

The effective thermoelastic coefficients ϑ_{ij} and the thermal modulus S^* are given by the formulae (C.5) and, respectively, (C.1). The presence of microcracks with contact between their lips do not modify the initial values of the thermoelastic coefficients: $\vartheta_{ij} = b_{ij}$. The thermal contact conditions also preserves the initial value of the thermal modulus $S^* = 0$.

As concerns the thermal conduction coefficients, they are calculated by (C.6) using the solution of the problem (4.64 - 4.66). We remark that $\theta = 0$ is the solution of this cell problem. The effective thermal conduction coefficients are not influenced by the presence

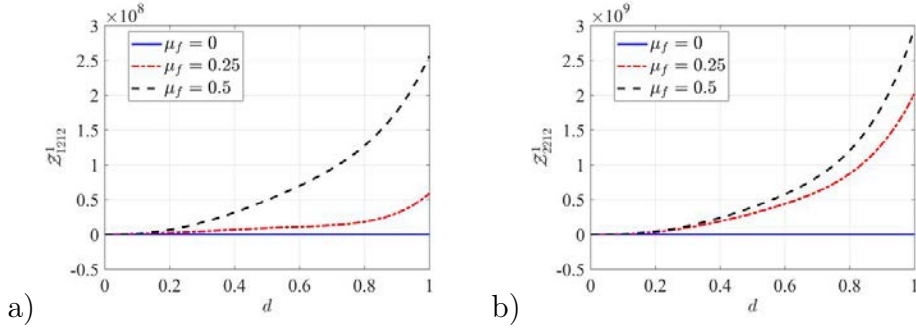


Figure 4.5: Coefficients Z_{1212}^1 (a), Z_{2212}^1 (b) vs damage variable d , for $\mu_f = 0, 0.25, 0.5$.

of microcracks with contact conditions: $k_{11}^{eff} = k_{22}^{eff} = k$ and $k_{12}^{eff} = 0$.

The components of the tensor I_{mnpq} are controlling the amount of energy dissipated by friction (4.88) involved in the expression of the energy-release rate. They are evaluated numerically using the procedure described in the Appendix C. For the considered microcrack orientation and the continuity of the normal displacement field we deduce that the only non-vanishing components I_{1212} , $I_{1222} + I_{2212}$ and I_{2222} . Figure 4.4 shows the effective coefficients I_{1212} , $I_{1222} + I_{2212}$, and I_{2222} as functions of the damage variable d for three values of μ_f . As they influence the amount of energy dissipated by friction, these coefficients are increasing with the friction coefficient and the size of the friction zone which is proportional to d . If $\mu_f = 0$ there is no dissipation and $I_{mnpq} = 0$. The other coefficients J_{mn} and P involved in the expression (4.88) of \mathcal{Y}_f are also vanishing. The thermal variations have no influence on the dissipated energy by frictional sliding.

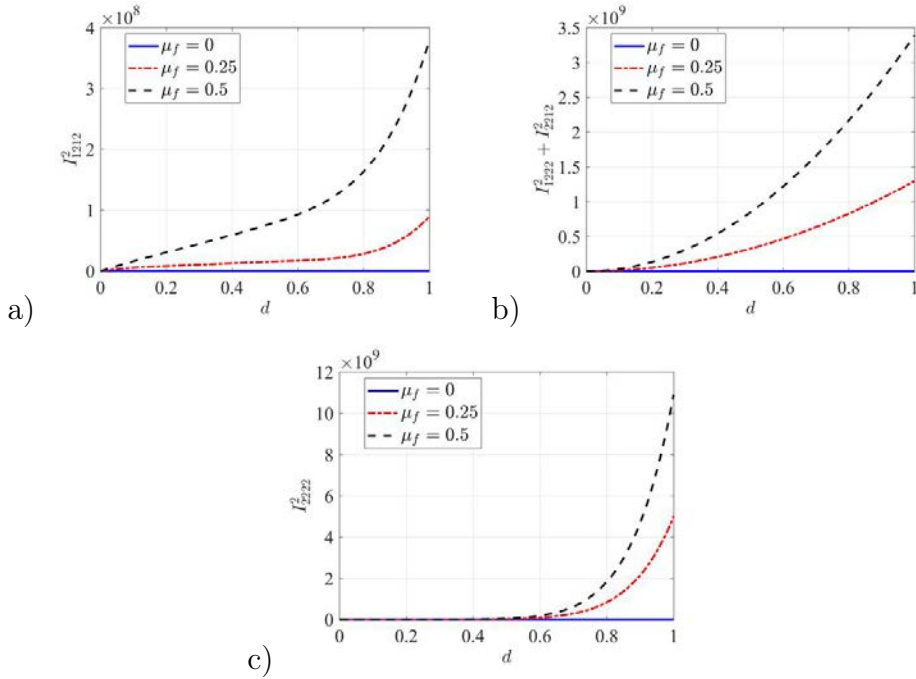


Figure 4.6: Components I_{1212}^2 (a), $I_{1222}^2 + I_{2212}^2$ (b), I_{2222}^2 (c) of I_{mnpq}^2 vs damage variable d , for $\mu_f = 0, 0.25, 0.5$.

Since only two strain components are used in the present analysis, the coefficients \mathcal{Z}_{1212}^1 and \mathcal{Z}_{2212}^1 of (4.96) are needed. They are represented in Figure 4.5 as functions of the damage variable d . These coefficients increase with the microcrack length and with the friction coefficient μ_f . Since they characterize the effect of the strains and strain-rate on the frictional heating, larger microcracks or higher values of μ_f give rise to more heating at the macroscopic scale. The other coefficients \mathcal{Z}_{mn}^2 , \mathcal{Z}_{mn}^3 and \mathcal{Z}^4 are equal to 0. As for the terms in \mathcal{Y}_f , thermal variations do no influence on the energy dissipated as heat during frictional sliding on microcracks.

As concerns I_{mnpq}^2 , the components I_{1212}^2 , $I_{1222}^2 + I_{2212}^2$ and I_{2222}^2 are represented in the Figure 4.6. They are also involved in the expression (4.96) of the frictional heat sources. All of them are increasing functions of d and μ_f for the same physical reasons, while J_{mn}^2 and P^2 are vanishing.

4.5.2 Macroscopic response

In order to analyze the macroscopic thermomechanical and damage response, a shear strain $e_{x12}(t) = \dot{e}_{x12} \times t$ with constant strain rate \dot{e}_{x12} and a constant compressive strain e_{x22} are assumed. Their numerical values are given in Table 4.2, together with those for the microstructural size l_c , initial damage d_0 and initial temperature T_0 . Unless specified, these generic values and the material parameters in Table 4.1 will be used in all the studies of the present section. The coupled system of the adiabatic temperature equation and the damage law is solved numerically and the macroscopic stresses are obtained with the computed damage and temperature solutions.

In Figure 4.7, we plot the stress Σ_{12} , the damage variable d and the temperature variation ΔT as function of the strain e_{x12} for different values of the size of microstructure l_c . As for the mode I microcracks [42], smaller microstructures are more resistant to damage initiation since smaller microcracks are more difficult to propagate. Since larger microscopic cells have more important stored kinetic energy near the crack lips, the corresponding stress response is more ductile, with delayed damage evolution because a smaller amount of energy remains available for damage.

For small l_c , the damage propagates rapidly with more dissipated energy converted to heat. This leads to a more important temperature rise, while for slow evolutions of damage, corresponding to large l_c , we have less dissipation heating and the temperature increase is less important. The frictional heating effect is also present before damage initiation, but its value is negligible. Its contribution is increasing during damage evolution since R_f depends on the damage rate.

Figure 4.8 shows the effect of the shear strain rate on damage, shear stress and temperature evolutions. A compression loading $e_{x22} = -1 \times 10^{-2}$ is considered and the initial

e_{x22}	\dot{e}_{x12} (s ⁻¹)	l_c (m)	d_0	T_0 (K)
-5×10^{-3}	-8000	5×10^{-4}	0.1	295.15

Table 4.2: Normal strain, shear strain rate, internal length and initial damage and temperature used in the study of the macroscopic response.

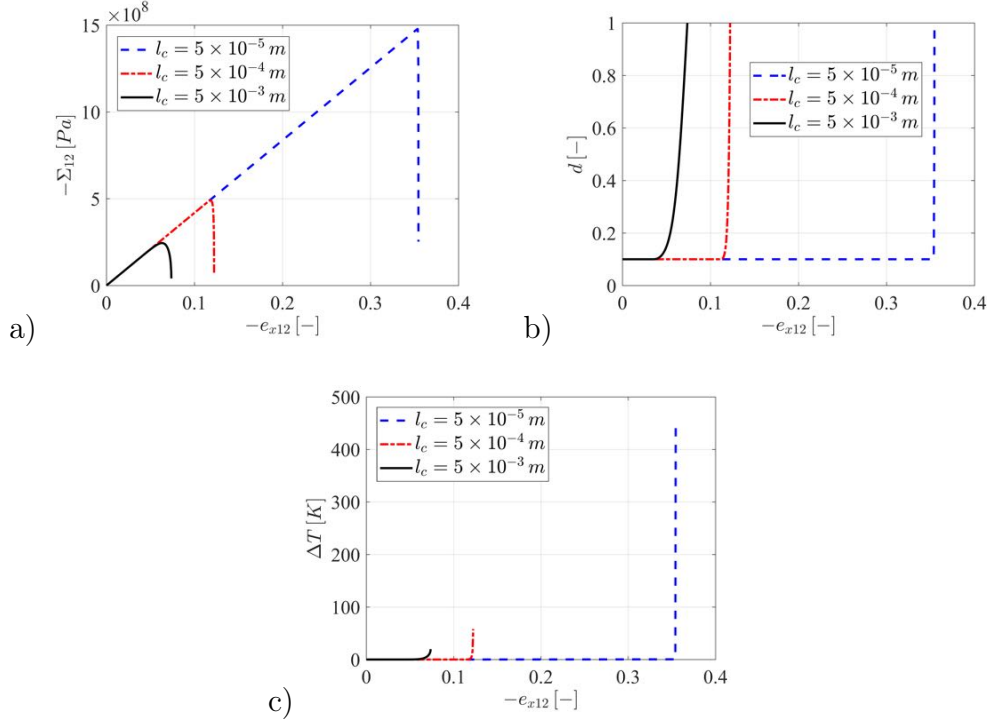


Figure 4.7: Effective stress Σ_{12} , damage variable d and temperature variation ΔT vs. the strain e_{x12} , for different values of the microstructural length: $l_c = 5 \times 10^{-5} m$, $l_c = 5 \times 10^{-4} m$, $l_c = 5 \times 10^{-3} m$.

damage is $d_0 = 0.2$. For these computations we consider $l_c = 1 \times 10^{-3} m$ as the size of the microstructure.

The strain-rate effect obtained for mode I microcracks [82, 42] is also present in this case. The increase of the loading rate induces more ductility in the macroscopic response, as a consequence of the inertial effects incorporated in the damage model. At high strain rates, a more important part of the supplied energy is stored as kinetic energy around microcrack tips, slowing the microcrack propagation. Compared to the case of opening microcracks [82, 42], where the kinetic energy may be more important, the strain-rate effect for closed and frictional microcracks is less pronounced.

Since the damage rate influences the amount of energy converted to heat, for higher loading rates the model predicts lower heat production during the propagation phase. This effects seems to be balanced by the duration of the heating process in the Figure 4.8c. When the temperature variations are not so important (less than ten degrees in the figure) it is the second effect that dominates. For more radical temperature evolutions, like in the Figure 4.7, it is damage rate influence that prevails.

We study now the effects of the initial damage on the macroscopic response. The stress, temperature variation and the damage were computed for three different values of d_0 and represented in Figure 4.9. Retarded damage initiation leading to higher strength is observed for smaller values of d_0 and the strength decreases for higher values of d_0 , as expected. This example is particularly interesting for the study of thermal effects. Larger initial crack lengths increase the frictional heating effect by augmenting the fric-

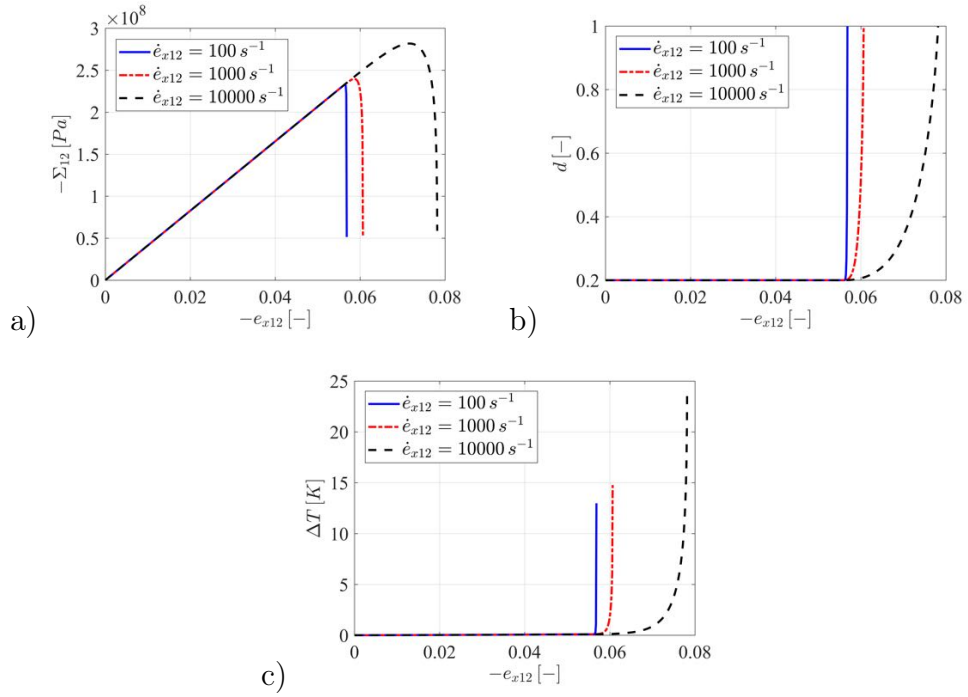


Figure 4.8: Effective stress Σ_{12} , damage variable d and temperature variation ΔT vs. the strain e_{x12} , for different values of strain rate: $\dot{e}_{x12} = -100 \text{ s}^{-1}$, $\dot{e}_{x12} = -1000 \text{ s}^{-1}$, $\dot{e}_{x12} = -10000 \text{ s}^{-1}$.

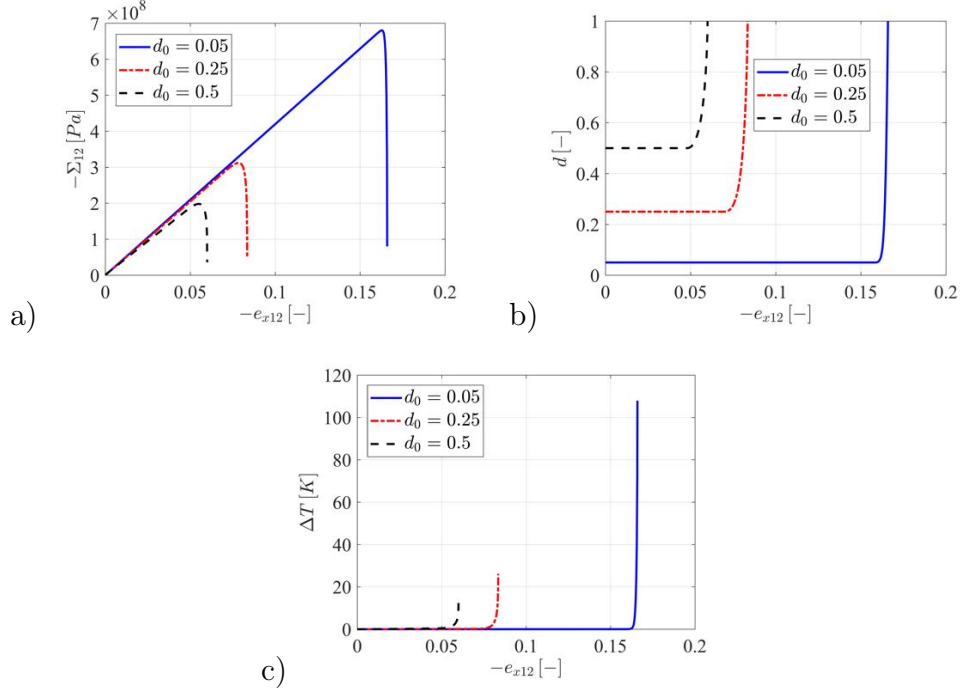


Figure 4.9: Effective stress Σ_{12} , damage variable d and temperature variation ΔT vs. the strain e_{x12} , for initial values of damage $d_0 = 0.05$, $d_0 = 0.25$, $d_0 = 0.5$.

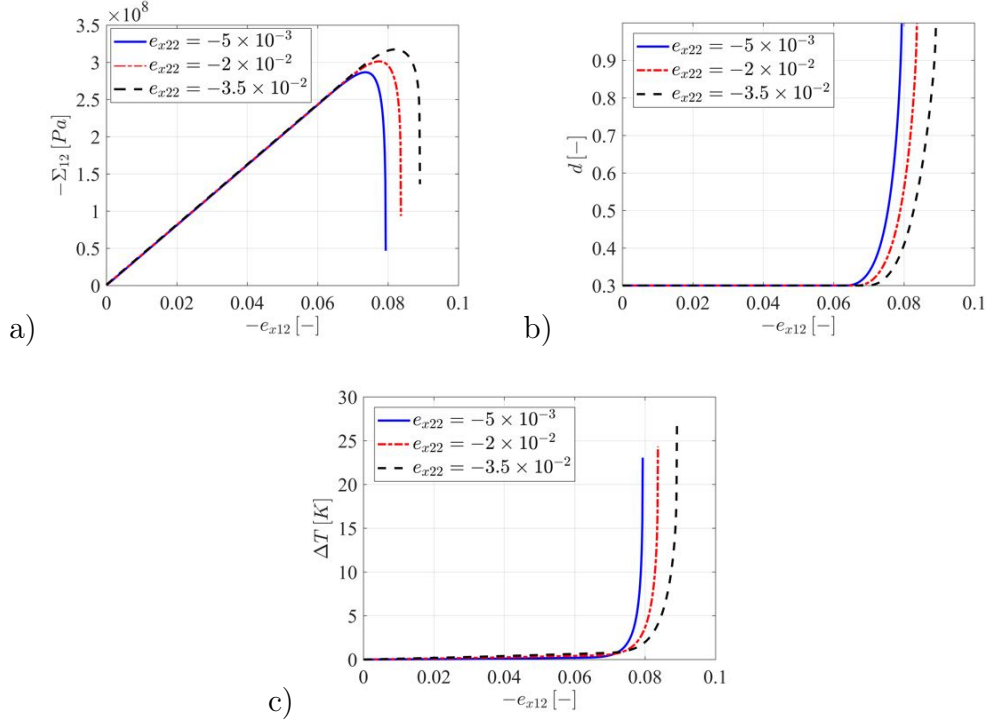


Figure 4.10: Effective stress Σ_{12} , damage variable d and temperature variation ΔT vs. the strain e_{x12} , for different compressive strains: $e_{x22} = -5 \times 10^{-3}$, $e_{x22} = -2 \times 10^{-2}$, $e_{x22} = -3.5 \times 10^{-2}$.

tion zone. Smaller initial lengths lead to high damage rates and corresponding crack propagation heating. The temperature behavior in Figure 4.9c shows that the second effect is dominant, since the temperature increase is substantially higher for smaller initial crack lengths.

Let us analyze now the effect of the compressive strain on the damage variable d , the macroscopic shear stress Σ_{12} and the temperature variation ΔT . Three values were considered for the compression loading : $e_{x22} = -5 \times 10^{-3}$, -2×10^{-2} , -3.5×10^{-2} . The shear strain rate used in this case is $\dot{e}_{x12} = -10000 \text{ s}^{-1}$ while $d_0 = 0.3$.

Figure 4.10 shows that the increase of the compressive strain retards the damage evolution due to the increased frictional resistance on microcracks. The corresponding frictional heating is also increased. Since the damage rates in the propagation phase are not radically different, the relatively small temperature increase could be explained as a frictional heating effect. Moreover, this effect is also present before damage initiation, as can be seen in the represented temperature evolution.

Consider now the influence of friction coefficient μ_f . In Figure 4.11, we plot the damage variable d , the stress Σ_{12} and the temperature variation as function of the strain e_{x12} , for different values of μ_f . The compressive strain is $e_{x22} = -3 \times 10^{-2}$ while the value of initial damage and microstructural size are correspondingly $d_0 = 0.25$, and $l_c = 10^{-3}$ m.

For large coefficients μ_f , the frictional resistance is increased on microcracks and this induces larger shear strengths and delayed damage evolutions. This effects can be seen in

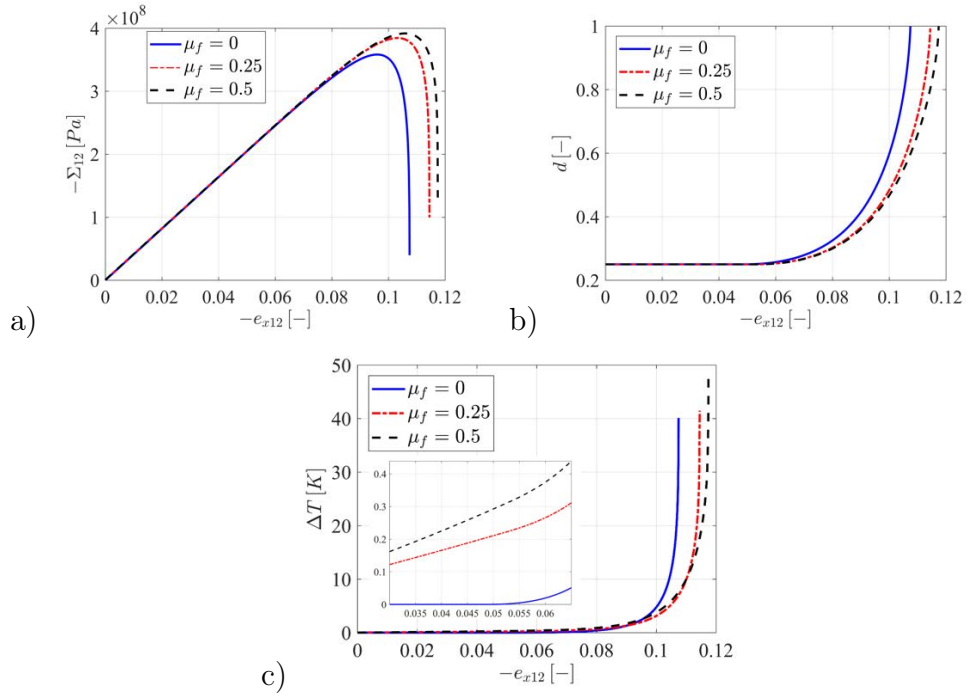


Figure 4.11: Effective stress Σ_{12} , damage variable d and temperature variation ΔT for different values of the friction coefficient μ_f .

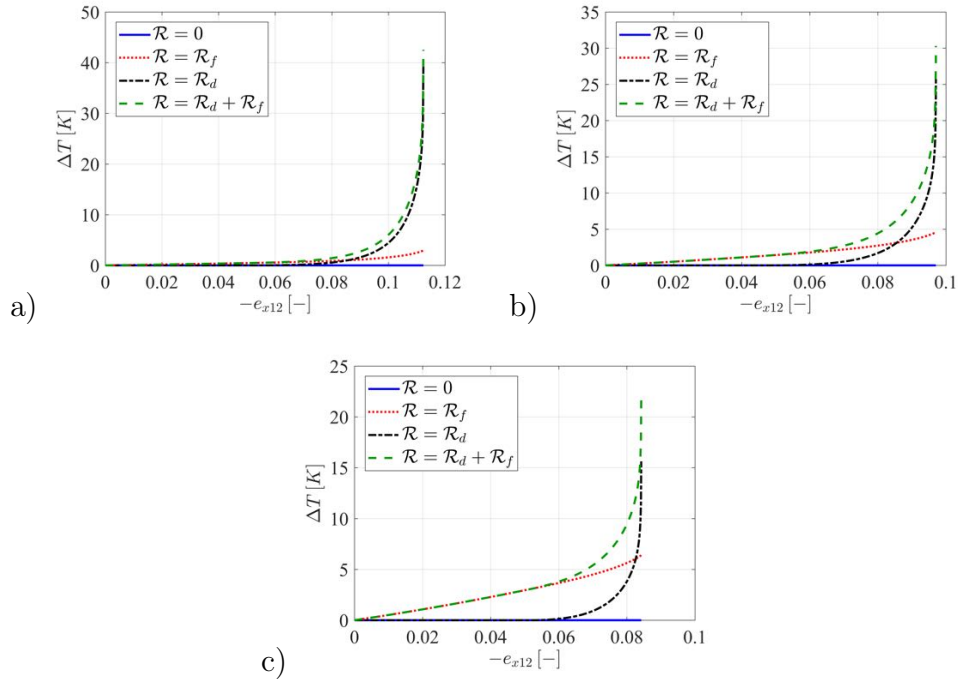


Figure 4.12: Temperature variations for different expressions of the heat source \mathcal{R} in the temperature equation (4.94), with \mathcal{R}_d and \mathcal{R}_f respectively the damage and frictional heating terms. Results are presented for a) $d_0 = 0.3$, b) $d_0 = 0.5$ and c) $d_0 = 0.7$.

Figure 4.11. As in the previous case, the temperature increase is slightly more important for large values of μ_f as a result of the frictional heating. Before damage initiation, a small increase of ΔT is present having the same frictional origin. Since the damage rates are close during the propagation phase, the comparison between the cases $\mu_f = 0$ and $\mu_f \neq 0$ reveals the effect of frictional heating on microcracks.

Finally, we analyze the effects of damage and frictional heating sources on the variation of the macroscopic temperature. For this, we consider in the equation of the temperature (4.94) different combinations of the source terms \mathcal{R}_d and \mathcal{R}_f . The resulting temperature variations are plotted in Figure 4.12, for a) $d_0 = 0.3$, b) $d_0 = 0.5$ and c) $d_0 = 0.7$.

When the two sources are absent ($\mathcal{R} = 0$), no temperature variations occur. In the case $\mathcal{R} = \mathcal{R}_f$, we remark the relatively linear increase of the temperature due to frictional contact on microcrack lips. The temperature rate is higher during propagation since the frictional zone is extending. The variation is amplified for larger values of d_0 . In the case $\mathcal{R} = \mathcal{R}_d$, the temperature increases abruptly due to crack-tip dissipation during the propagation regime and up to values that are superior to those of the frictional heating case. The superposition of the two sources ($\mathcal{R} = \mathcal{R}_d + \mathcal{R}_f$) confirms that damage induced heating becomes dominant in the propagation regime. For smaller values of d_0 this effect is even more pronounced.

4.6 Numerical simulations of heating in mode II failure under impact

We present in this section an example of application of the new model to simulate the mode II dynamic failure of a grooved PMMA panel under impact. The temperature evolution obtained in the FEM computations is compared to the experimental results presented in [19].

The details of the panel geometry and loading [19] are shown on Figure 4.13. The specimen has width $W = 127$ mm, height $2H = 292$ mm and thickness $T = 8.5$ mm. Both sides of the panel have a groove of height $H_g = 3.2$ mm and depth 2.5 mm. A starter notch of length $l = 25$ mm and width 1 mm is cut into one edge of the panel, inside the groove. The impact velocity $V_{imp} = 40$ m s⁻¹ is applied asymmetrically over a zone of $D = 38$ mm, as shown in Fig. 4.13. Under this loading, a shear crack is initiated at the notch tip and propagates in the groove.

The model parameters used in the simulations are reported in Table 4.3. As in the previous section, we consider crack-speed dependency of the critical fracture energy in the form $\mathcal{G}_c = \mathcal{G}_{c0}(1 + a \cdot v_p)$.

In order to reproduce numerically the dynamic shear fracture of the specimen and the corresponding temperature evolution, we implemented the thermoelastic damage model in ABAQUS Explicit software [1]. The numerical integration of the temperature equation

E (GPa)	ν	ρ (kg m ⁻³)	α (K ⁻¹)	c (J m ⁻³ K ⁻¹)	μ_f	l_c (m)	\mathcal{G}_{c0} (J m ⁻²)	a (s m ⁻¹)
5.5	0.36	1190	7×10^{-5}	1.725×10^6	0.5	3×10^{-4}	1900	5×10^{-3}

Table 4.3: Material parameters used in the FEM simulations.

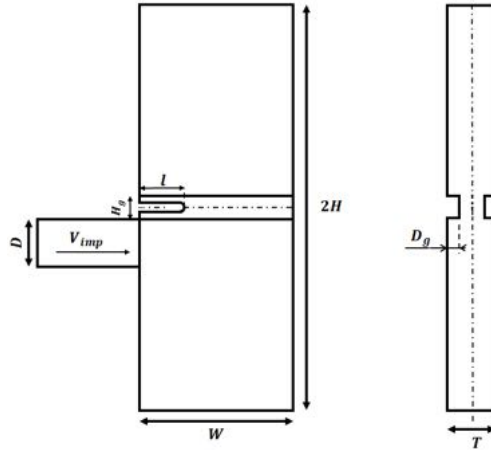


Figure 4.13: Geometry of the specimen and loading for mode II impact test.

and of the damage evolution law is implemented in a VUMAT user subroutine for dynamic explicit analysis. On a time step and for a strain increment, an Euler forward scheme is used to solve the damage equation (4.92) at each integration point of the FE mesh, with the temperature at the end of the previous step. Then, a similar time integration scheme is employed to solve the adiabatic temperature equation (4.94) using the computed damage variable. The new values of the damage and temperature are used to update the stress components at the end of the time step according to the constitutive relation (4.75). Only the in-plane components of the strain are considered for the calculation of the damage energy $\mathcal{Y} - \mathcal{Y}_f$.

A 3D numerical modeling of the impact test is adopted in order to take into account the effect of the groove in the initiation and the evolution of the shear failure. The structure is then meshed with four nodes tetrahedral linear elements C3D4 with one integration point. The mesh is refined in the groove where the path of crack is expected, using elements of size $5 \times 10^{-2} \text{ mm}$. Details of the mesh are shown on Figure 4.14. Element deletion is activated when the damage variable reaches a value of 0.99. Unilateral contact with friction is introduced between the new formed interior faces after deletion.

The use of the damage model allows us to reproduce both fracture initiation at the notch tip and fracture propagation in the groove. A relatively straight trajectory is

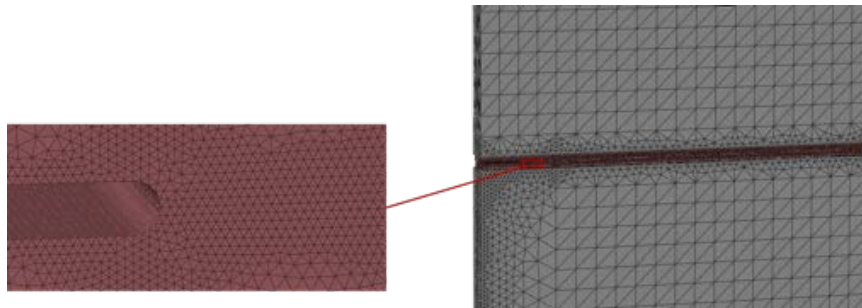


Figure 4.14: Details of the mesh used in the FE computations.

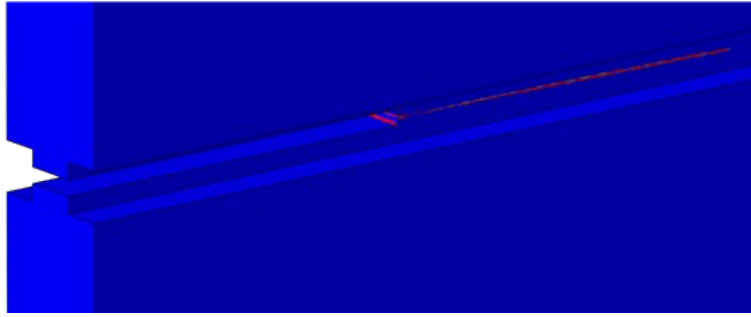


Figure 4.15: Damage band in the groove at $70 \mu s$.

observed for the evolution of the damage band as depicted on Figure 4.15. The thickness of the damage band is about 3 times the element size. As in the purely mechanical case considered in [8], where a similar impact test [109] was reproduced numerically, the front velocity is increasing up to values close to the Rayleigh wave speed.

We focus here on the analysis of the thermal evolution during failure. In the experiment performed by Bjerke and Lambros [19], a vertical array of infrared detectors has been placed in the groove, at 20 mm from the initial notch. These elements provide the temperature variations during the passage of the crack front. The computed temperature field around the damage band is represented in Figure 4.16. The area framed by the red rectangle is corresponding to the temperature detection points. The damage evolution in the elements is accompanied by a change in temperature.

In Figure 4.17a, we reproduce the measured temperature by Bjerke & Lambros [19] using the array of infrared detectors located at 20 mm from the initial notch tip. The maximal temperature variation is obtained by the thermal signal of detector element 8 after an increase of about 85 K , during a time interval between $55 \mu s$ and $65 \mu s$. From the numerical simulations, we obtained a relatively similar temperature increase of $85 - 90 \text{ K}$ in the integration point of element located in the middle of the damage band and at 20 mm of the notch tip, as shown on Figure 4.17b. The temperature increase in the simulations takes place in $10 \mu s$ which is close to that in the experiments.

Also measured in [19] are the temperatures in the flanking detectors 7 and 9. The size of these photovoltaic elements is of $8 \times 10^{-2} \text{ mm}$. In the numerical simulations, the size of the mesh elements is approximately $5 \times 10^{-2} \text{ mm}$. Despite this small difference, for the sake of comparison we represented in Figure 4.17b the temperatures computed in the

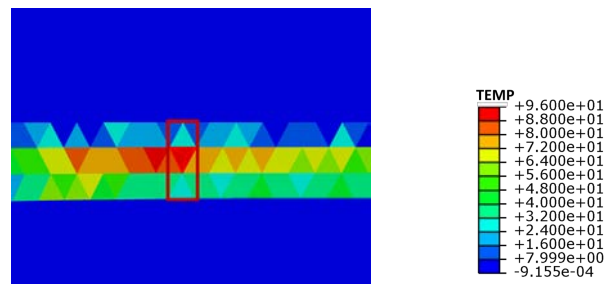


Figure 4.16: Temperature variation induced by damage at 20 mm of the initial notch tip.

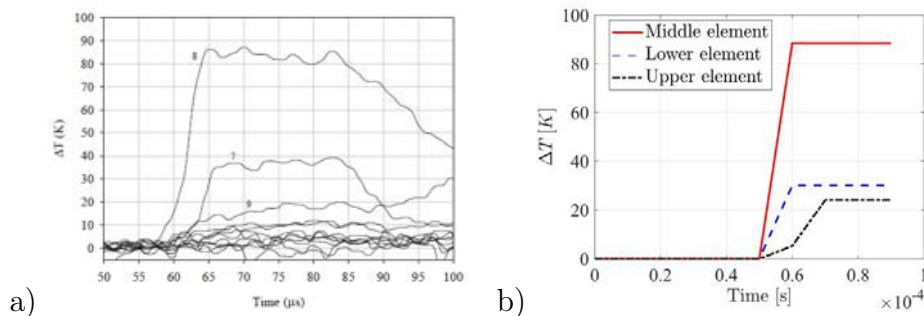


Figure 4.17: Temperature variation: measured values (a) from [19] and (b) computed values in 3 neighbor elements located in the region of IR detectors.

corresponding lower and upper elements as can be seen in Figure 4.16. We remark that the computed values are relatively close to those measured by the corresponding detectors, with a mean value of about 30 K and a few μ s delay with respect to the temperature of the middle element. We finally note that the deletion of the damaged elements do not allow for the representation of further decrease of the temperature after the passage of the damage front.

While further studies are necessary to better understand the prediction potential of the new thermo-mechanical damage model, the first example presented in this section illustrated its capacity of reproducing the temperature variations associated to the dynamic shear failure of brittle solids.

4.7 Conclusions

We developed a coupled thermomechanical damage model for dynamic shear failure in brittle materials. The new damage law has been obtained using an adapted asymptotic homogenization procedure from the microscopic Griffith-type propagation criterion in mode II. Besides the unilateral contact and friction conditions, heat sources at the tips and over the lips of microcracks have been assumed in order to account for damage and frictional heating effects. The upscaling procedure led to a macroscopic equation of temperature with distributed heat sources related to damage propagation and frictional sliding mechanisms. A strong coupling between the mechanical, thermal and damage fields has been obtained. The analysis of the local macroscopic response predicted by the new model revealed specific influences of the microstructural size, the strain rate, the compression loading, the initial microcrack length and the friction coefficient. Structural simulations have been performed to reproduce the dynamic shear failure of a grooved PMMA panel. The obtained numerical temperature fields of these first numerical tests were compared to the experimental results reported in [19] and relatively good agreement has been found.

General conclusions

In this thesis, we developed fully coupled thermo-mechanical dynamic damage models for solids with micro-cracks subjected to tensile and shear loadings using a two-scale approach based on asymptotic homogenization technique.

A model for opening microcracks is constructed in Chapter 2. This mode I damage model is developed assuming heat sources at the moving microcracks tips. The macroscopic thermoelastic constitutive equations are obtained using the homogenization procedure and the damage law is deduced through an energy analysis at the microstructural level and the asymptotic developments. The model involves strong couplings between the damage evolution law and the thermoelastic equations.

One of the salient ingredients of the model is the conversion of the energy dissipated during failure into heat at the tips of microcracks. At the macroscopic level, this corresponds to the presence of volume heat sources at damage fronts. The evolution of the damage also leads to degradation of the thermoelastic properties. The model predictions are sensitive to the size of microstructure and the strain rate. All these features have been revealed by the local analysis of the macroscopic macroscopic.

The thermoelastic damage model has been implemented in a commercial FEM code to reproduce numerically the thermal effects associated with crack propagation in PMMA specimen under impact loadings. Adiabatic and heat-conduction versions have been used in the simulations, their comparison revealing the validity of the adiabatic approximation. The numerical predictions for the thermal and mechanical fields were found to be in good agreement with the reported experimental results.

In Chapter 3 we develop a damage model for mode II propagation, with frictional contact between micro-cracks lips. A similar procedure based on asymptotic homogenization and energy analysis allows for the construction of the effective thermoelastic constitutive relations and the damage evolution law. The obtained homogenized coefficients depend on the damage variable and the friction coefficient. The damage law accounts for energy dissipation due to friction on the lips of microcracks. The analysis of the local response predicted by the model illustrates the delay effects related to the compressive loadings and the coefficient of friction. We also investigated influences of initial damage, microstructural size and strain rate on stress and damage evolutions.

The rapid shear failure of grooved PMMA plates under impact loadings is reproduced numerically with the new damage model implemented in a FEM software. The numerical simulations show damage front speeds approaching the Rayleigh waves velocity as measured in the experiments. The comparison between numerical and experimental crack evolutions prove that the model is able to reproduce the dynamic shear failure in brittle

materials.

In Chapter 4, we extended the frictional damage law in order to include thermoelastic couplings. Two dissipation mechanisms, related to friction and propagation of microcracks, are considered as sources of heating at the microscopic levels. The upscaling analysis provides a general damage law accounting for these complex effects and with multiple thermo-mechanical couplings.

The study of the local response predicted by the new dynamic damage model illustrated the effects of the coefficient of friction and the compression loading on the temperature and stress evolutions. The heating effects are influenced by compression loadings or the friction coefficients, even in the absence of damage propagation. The size of the microstructure and the strain rate have important influences on the thermo-mechanical response.

Through the approaches presented in this thesis we have provided methods of incorporation of the thermal effects in the multi-scale analysis of brittle failure of solid bodies. Different microscopic mechanisms, like friction and microcrack propagation in opening or shear modes have been considered as sources of heating during failure processes. The analysis of the local and structural macroscopic responses illustrated the relevant effects of the new approaches and the comparisons with experiments have proved the validity of the model predictions.

Among the research perspectives that may complete the present work we can mention:

- The study of damage in mixed mode by coupling mode I and mode II at the microscopic level.
- Consideration of randomly distributed microcracks with different orientations and the use of stochastic homogenization approaches, like the one developed by Gambin & Telega [65].
- The two scale thermomechanical damage models can be extended for non planar growth of micro-cracks. The approach developed in [61] can be used for this purpose.
- We obtained our models considering 2-D fracture problems, we could also consider 3D cases and obtain thermomechanical damage models by extending the developments in [38] to dynamics and thermo-mechanical coupling.
- Consideration of a microstructure with interacting microcracks [94] in order to study the effect of microcracks interaction and coalescence on thermoelastic damage in brittle materials.
- In order to improve the objectivity with respect to the FE meshes and in some cases avoid very costly structural computations, the models can be regularized by adding gradient terms.

Appendix A

Asymptotic expansion of the energy release-rate

We give here details about the asymptotic expansion of the energy release rate of Chapter 2.

By retaining the first two terms in the asymptotic developments (2.15-2.16) of displacements and temperature, we obtain the expression of the energy-release rate

$$\mathcal{G}^{d\varepsilon} = \frac{1}{\varepsilon}\mathcal{G}^{(-1)} + \mathcal{G}^{(0)} + \varepsilon\mathcal{G}^{(1)} + \varepsilon^2\mathcal{G}^{(2)} + \varepsilon^3\mathcal{G}^{(3)} \quad (\text{A.1})$$

where the terms of different orders are:

$$\begin{aligned} \mathcal{G}^{(-1)} = \lim_{r \rightarrow 0} \int_{\Gamma_{Y_r}} & \left(\frac{1}{2}(\lambda e_{yii}(\mathbf{u}^{(0)})e_{yjj}(\mathbf{u}^{(0)}) + 2\mu e_{yij}(\mathbf{u}^{(0)})e_{yij}(\mathbf{u}^{(0)}))n_1 \right. \\ & \left. - (\lambda e_{ykk}(\mathbf{u}^{(0)})\delta_{ij} + 2\mu e_{yij}(\mathbf{u}^{(0)}))n_j \frac{\partial u_i^{(0)}}{\partial y_1} \right) ds_y \end{aligned} \quad (\text{A.2})$$

$$\begin{aligned} \mathcal{G}^{(0)} = \lim_{r \rightarrow 0} \int_{\Gamma_{Y_r}} & (\lambda e_{yii}(\mathbf{u}^{(0)})(e_{xjj}(\mathbf{u}^{(0)}) + e_{yjj}(\mathbf{u}^{(1)})) \\ & + 2\mu e_{yij}(\mathbf{u}^{(0)})(e_{xij}(\mathbf{u}^{(0)}) + e_{yij}(\mathbf{u}^{(1)})) + (3\lambda + 2\mu)\alpha T_0 e_{ykk}(\mathbf{u}^{(0)}))n_1 \\ & - (\lambda(e_{xkk}(\mathbf{u}^{(0)}) + e_{ykk}(\mathbf{u}^{(1)}))\delta_{ij} + 2\mu(e_{xij}(\mathbf{u}^{(0)}) + e_{yij}(\mathbf{u}^{(1)})))n_j \frac{\partial u_i^{(0)}}{\partial y_1} \\ & - (\lambda e_{ykk}(\mathbf{u}^{(0)})\delta_{ij} + 2\mu e_{yij}(\mathbf{u}^{(0)}))n_j \left(\frac{\partial u_i^{(0)}}{\partial x_1} + \frac{\partial u_i^{(1)}}{\partial y_1} \right) ds_y \end{aligned} \quad (\text{A.3})$$

$$\begin{aligned}
\mathcal{G}^{(1)} = & \lim_{r \rightarrow 0} \int_{\Gamma_{Y_r}} \left(\frac{1}{2} (\lambda (2e_{yii}(\mathbf{u}^{(0)})e_{xjj}(\mathbf{u}^{(1)}) + (e_{xii}(\mathbf{u}^{(0)}) + e_{yii}(\mathbf{u}^{(1)}))^2) \right. \\
& + 2\mu (2e_{yij}(\mathbf{u}^{(0)})e_{xij}(\mathbf{u}^{(1)}) + (e_{xij}(\mathbf{u}^{(0)}) + e_{yij}(\mathbf{u}^{(1)}))(e_{xij}(\mathbf{u}^{(0)}) + e_{yij}(\mathbf{u}^{(1)}))) \\
& + (3\lambda + 2\mu)\alpha T_0 (e_{xkk}(\mathbf{u}^{(0)}) + e_{ykk}(\mathbf{u}^{(1)})) + cT^{(0)} + \frac{\rho}{8} \frac{\partial u_i^{(0)}}{\partial y_1} \frac{\partial u_i^{(0)}}{\partial y_1} \left(\frac{dd}{dt} \right)^2 n_1 \\
& - (\lambda e_{ykk}(\mathbf{u}^{(0)})\delta_{ij} + 2\mu e_{yij}(\mathbf{u}^{(0)})n_j \left(\frac{\partial u_i^{(1)}}{\partial x_1} + \frac{\partial u_i^{(2)}}{\partial y_1} \right) \\
& - (\lambda (e_{xkk}(\mathbf{u}^{(0)}) + e_{ykk}(\mathbf{u}^{(1)}))\delta_{ij} + 2\mu (e_{xij}(\mathbf{u}^{(0)}) + e_{yij}(\mathbf{u}^{(1)})))n_j \left(\frac{\partial u_i^{(0)}}{\partial x_1} + \frac{\partial u_i^{(1)}}{\partial y_1} \right) \\
& \left. - (\lambda e_{xkk}(\mathbf{u}^{(1)})\delta_{ij} + 2\mu e_{xij}(\mathbf{u}^{(1)}))n_j \frac{\partial u_i^{(0)}}{\partial y_1} \right) ds_y \quad (\text{A.4})
\end{aligned}$$

$$\mathcal{G}^{(2)} = \lim_{r \rightarrow 0} \int_{\Gamma_{Y_r}} (cT^{(1)})n_1 ds_y + L_c^2 \lim_{r \rightarrow 0} \int_{\Gamma_{Y_r}} \left(\frac{\rho}{4} \frac{\partial u_i^{(0)}}{\partial y_1} \left(\frac{\partial u_i^{(0)}}{\partial x_1} + \frac{\partial u_i^{(1)}}{\partial y_1} \right) \left(\frac{dd}{dt} \right)^2 n_1 \right) ds_y \quad (\text{A.5})$$

$$\mathcal{G}^{(3)} = L_c^2 \lim_{r \rightarrow 0} \int_{\Gamma_{Y_r}} \frac{\rho}{8} \left(\frac{dd}{dt} \right)^2 \left(2 \frac{\partial u_i^{(0)}}{\partial y_1} \frac{\partial u_i^{(1)}}{\partial x_1} + \left(\frac{\partial u_i^{(0)}}{\partial x_1} + \frac{\partial u_i^{(1)}}{\partial y_1} \right) \left(\frac{\partial u_i^{(0)}}{\partial x_1} + \frac{\partial u_i^{(1)}}{\partial y_1} \right) \right) ds_y \quad (\text{A.6})$$

For the velocity field the local relation $\frac{\partial u_i^\varepsilon}{\partial t} \simeq -\frac{d(l/2)}{dt} \frac{\partial u_i^\varepsilon}{\partial x_1} = -\frac{\varepsilon L_c}{2} \frac{dd}{dt} \frac{\partial u_i^\varepsilon}{\partial x_1}$ in the vicinity of the crack tips [59, 25] has been used.

Since $\mathbf{u}^{(0)}$ and $T^{(0)}$ are independent of the y variable, some of the terms in the above expressions are vanishing. And if we take into account the singularity of $\mathbf{u}^{(1)}(\mathbf{y})$ and $T^{(1)}(\mathbf{y})$ at the crack tips, we deduce that $\mathcal{G}^{(-1)} = \mathcal{G}^{(0)} = \mathcal{G}^{(2)} = 0$.

Finally, the only non-vanishing terms in the development of $\mathcal{G}^{d\varepsilon}$ are:

$$\mathcal{G}^{d\varepsilon} = \varepsilon \mathcal{G}^{(1)} + \varepsilon^3 \mathcal{G}^{(3)} \quad (\text{A.7})$$

where:

$$\begin{aligned}
\mathcal{G}^{(1)} = & \lim_{r \rightarrow 0} \int_{\Gamma_{Y_r}} \left(\frac{1}{2} (\lambda e_{yii}(\mathbf{u}^{(1)})e_{yjj}(\mathbf{u}^{(1)}) + 2\mu e_{yij}(\mathbf{u}^{(1)})e_{yij}(\mathbf{u}^{(1)}))n_1 \right. \\
& \left. - (\lambda e_{ykk}(\mathbf{u}^{(1)})\delta_{ij} + 2\mu e_{yij}(\mathbf{u}^{(1)})n_j \frac{\partial u_i^{(1)}}{\partial y_1}) ds_y \right) \quad (\text{A.8})
\end{aligned}$$

$$\mathcal{G}^{(3)} = L_c^2 \lim_{r \rightarrow 0} \int_{\Gamma_{Y_r}} \frac{\rho}{8} \left(\frac{dd}{dt} \right)^2 \frac{\partial u_i^{(1)}}{\partial y_1} \frac{\partial u_i^{(1)}}{\partial y_1} ds_y \quad (\text{A.9})$$

The kinetic energy only contributes to the term $\mathcal{G}^{(3)}$ of the above development of the dynamic energy release rate. The term of order ε can be obtained in (A.1) by considering higher order correctors for the thermomechanical fields.

Appendix B

Computation of the effective coefficients C_{ijkl} and I_{mnpq}

We provide here the details concerning the computation of the homogenized coefficients C_{ijkl} and I_{mnpq} appearing in the formulation of the macroscopic elasto-damage problem in Chapter 3. As explained in [140], a particular system of generators for the cell problem is necessary to respect the frictional contact conditions on the crack lips. The construction is specific to the present orientation of microcracks.

Following the method in [140], we choose a system of generators \mathbf{E}^{pq} in the form:

$$\mathbf{E}^{11} = \begin{pmatrix} -1/\gamma & 0 \\ 0 & 0 \end{pmatrix}; \quad \mathbf{E}^{12} = \begin{pmatrix} 0 & -1/\gamma \\ -1/\gamma & -1/2\gamma \end{pmatrix}; \quad \mathbf{E}^{22} = \begin{pmatrix} 0 & -1/\gamma \\ -1/\gamma & -1/\gamma \end{pmatrix} \quad (\text{B.1})$$

such that the macroscopic strains can be written as a linear combination of these elements:

$$e_{xij}(\mathbf{u}^{(0)}) = \varrho_{pq}(\mathbf{u}^{(0)}) E_{ij}^{pq} \quad (\text{B.2})$$

where $\varrho_{pq}(\mathbf{u}^{(0)})$ are linear combinations of the macroscopic strain components: $\varrho_{11}(\mathbf{u}^{(0)}) = -\gamma e_{x11}(\mathbf{u}^{(0)})$, $\varrho_{12}(\mathbf{u}^{(0)}) = \varrho_{21}(\mathbf{u}^{(0)}) = \gamma(e_{x22}(\mathbf{u}^{(0)}) - e_{x12}(\mathbf{u}^{(0)}))$ and $\varrho_{22}(\mathbf{u}^{(0)}) = \gamma(e_{x12}(\mathbf{u}^{(0)}) - 2e_{x22}(\mathbf{u}^{(0)}))$. In the summation terms of the relation (B.2) we take $\mathbf{E}^{21} = \mathbf{E}^{12}$. The applied macroscopic strains in the computations of the cell-problem solutions are adjusted with the constant $\gamma = 800$ in order to maintain the numerical contact conditions, imposed through a penalty method, and avoid penetrations of the crack lips due to high compressive loadings

If the vectors $\boldsymbol{\xi}^{pq}(\mathbf{y}, d)$ are particular solutions, corresponding to $e_{xij}(\mathbf{u}^{(0)}) = E_{ij}^{pq}$, of the cell problem:

$$\frac{\partial}{\partial y_i} (a_{ijkl} e_{ykl}(\boldsymbol{\xi}^{pq})) = 0 \quad \text{in } Y \quad (\text{B.3})$$

$$[a_{ijkl} e_{ykl}(\boldsymbol{\xi}^{pq}) N_j] = - [(a_{ijkl} E_{kl}^{pq}) N_j] \quad \text{on } CY^\pm \quad (\text{B.4})$$

$$N_i a_{ijkl} (e_{ykl}(\boldsymbol{\xi}^{pq}) + E_{kl}^{pq}) N_j < 0 \quad \text{on } CY^\pm \quad (\text{B.5})$$

$$|T_i a_{ijkl} (e_{ykl}(\boldsymbol{\xi}^{pq}) + E_{kl}^{pq}) N_j| = -\mu_f N_i a_{ijkl} (e_{ykl}(\boldsymbol{\xi}^{pq}) + E_{kl}^{pq}) N_j \quad \text{on } CY^\pm \quad (\text{B.6})$$

then the general solution $\mathbf{u}^{(1)}$ can be written as the linear combination:

$$\mathbf{u}^{(1)}(\mathbf{x}, \mathbf{y}, t) = \boldsymbol{\xi}^{pq}(\mathbf{y}, d(t)) \varrho_{pq}(\mathbf{x}, t) \quad (\text{B.7})$$

For the numerical solution, it is preferable to use the change of function from ξ_i^{pq} to v_i , with $\xi_i^{pq} = v_i^{pq} - E_{ij}^{pq} y_j$. With this change of variable, the periodicity conditions on the outer edges of the cell become:

$$(\mathbf{v}^{pq} - \mathbf{E}^{pq} \mathbf{y})^+ = (\mathbf{v}^{pq} - \mathbf{E}^{pq} \mathbf{y})^- \quad (\text{B.8})$$

where \mathbf{y} is the position vector and \pm defines the opposite edges of the unit cell. With this change, the problem (B.3-B.6) becomes :

$$\frac{\partial}{\partial y_i} (a_{ijkl} e_{ykl}(\mathbf{v}^{pq})) = 0 \quad \text{in } Y \quad (\text{B.9})$$

$$[a_{ijkl} e_{ykl}(\mathbf{v}^{pq}) N_j] = 0 \quad \text{on } CY^\pm \quad (\text{B.10})$$

$$N_i a_{ijkl} e_{ykl}(\mathbf{v}^{pq}) N_j < 0 \quad \text{on } CY^\pm \quad (\text{B.11})$$

$$|T_i a_{ijkl} e_{ykl}(\mathbf{v}^{pq}) N_j| = -\mu_f N_i a_{ijkl} e_{ykl}(\mathbf{v}^{pq}) N_j \quad \text{on } CY^\pm \quad (\text{B.12})$$

The condition of continuity of the normal displacements on the crack lips becomes:

$$[\mathbf{v}^{pq} \cdot \mathbf{N}] = 0 \quad \text{on } CY^\pm \quad (\text{B.13})$$

The particular solutions \mathbf{v} of this problem are determined for given values of the variable d . Numerical solutions of (B.9 - B.13) are depicted on Figure B.1

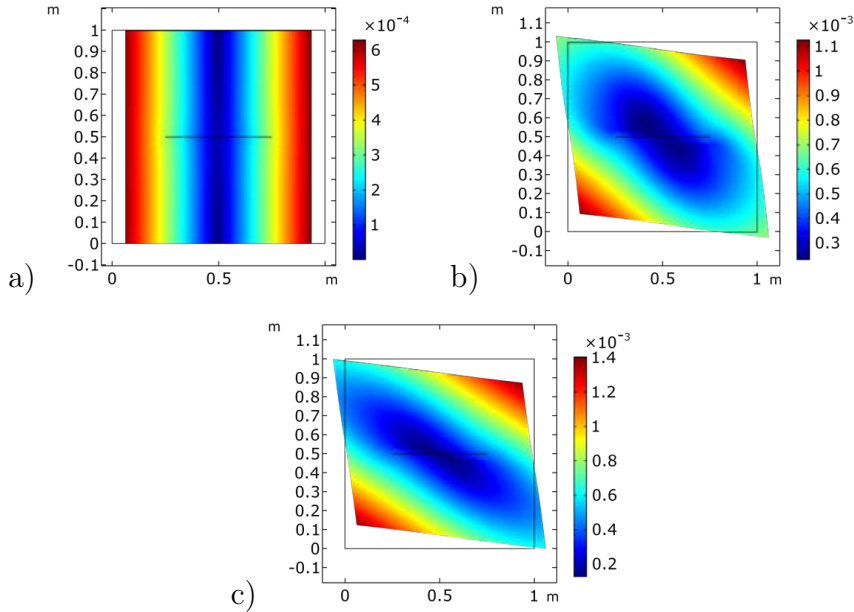


Figure B.1: Displacements \mathbf{v}^{11} (a), \mathbf{v}^{12} (b) and \mathbf{v}^{22} (c) obtained from FE unit cell computations.

Let us provide now details for the computation of the effective coefficients C_{ijmn} in (3.28). Replacing the relations (B.2) and (B.7) in (3.26), we get:

$$\Sigma_{ij}^{(0)} = \frac{1}{L_c^2} \int_Y a_{ijkl} (E_{kl}^{mn} + e_{ykl}(\boldsymbol{\xi}^{mn})) dy \varrho_{mn}(\mathbf{u}^{(0)}) \quad (\text{B.14})$$

which can be rewritten :

$$\Sigma_{ij}^{(0)} = C_{ijmn}^e \varrho_{mn}(\mathbf{u}^{(0)}) \quad (\text{B.15})$$

with the coefficients

$$C_{ijmn}^e = \frac{1}{L_c^2} \int_Y a_{ijkl} (E_{kl}^{mn} + e_{ykl}(\boldsymbol{\xi}^{mn})) dy \quad (\text{B.16})$$

Using the link between e_{xij} and ϱ_{pq} in (B.15) allows to rewrite the macroscopic stress in order to obtain the homogenized constitutive relation (3.28) with the effective coefficients

$$C_{ij11} = -\frac{1}{L_c^2} \int_Y \gamma a_{ijkl} (E_{kl}^{11} + e_{ykl}(\boldsymbol{\xi}^{11})) dy \quad (\text{B.17})$$

$$C_{ij12} = \frac{1}{L_c^2} \int_Y \frac{\gamma}{2} a_{ijkl} ((E_{kl}^{22} + e_{ykl}(\boldsymbol{\xi}^{22})) - 2(E_{kl}^{12} + e_{ykl}(\boldsymbol{\xi}^{12}))) dy \quad (\text{B.18})$$

$$C_{ij22} = \frac{1}{L_c^2} \int_Y 2\gamma a_{ijkl} ((E_{kl}^{12} + e_{ykl}(\boldsymbol{\xi}^{12})) - (E_{kl}^{22} + e_{ykl}(\boldsymbol{\xi}^{22}))) dy \quad (\text{B.19})$$

As concerns the energy relation (3.36), following the analysis in [140] one obtains it in terms of $\varrho_{pq}(\mathbf{u}^{(0)})$:

$$\left(\frac{\mathcal{G}^{(1)}}{L_c} + \left(\frac{1}{2} \frac{\partial C_{mnpq}^e}{\partial d} + I_{mnpq}^e \right) \varrho_{mn}(\mathbf{u}^{(0)}) \varrho_{pq}(\mathbf{u}^{(0)}) \right) \dot{d} = 0 \quad (\text{B.20})$$

where

$$\begin{aligned} I_{mnpq}^e &= \frac{1}{2L_c^2} \frac{d}{dd} \int_{CY} a_{ijkl} (E_{kl}^{mn} + e_{ykl}(\boldsymbol{\eta}^{mn})) N_j [\eta_i^{pq}] ds_y \\ &\quad - \frac{1}{L_c^2} \int_{CY} a_{ijkl} (E_{kl}^{mn} + e_{ykl}(\boldsymbol{\eta}^{mn})) N_j \left[\frac{d\eta_i^{pq}}{dd} \right] ds_y \end{aligned} \quad (\text{B.21})$$

And adopting the previous change of variables, we can rewrite the expression (B.21) as a function of v_i^{pq} :

$$I_{mnpq}^e = \frac{1}{2L_c^2} \frac{d}{dd} \int_{CY} a_{ijkl} e_{ykl}(\mathbf{v}^{mn}) N_j [v_i^{pq}] ds_y - \frac{1}{L_c^2} \int_{CY} a_{ijkl} e_{ykl}(\mathbf{v}^{mn}) N_j \left[\frac{dv_i^{pq}}{dd} \right] ds_y \quad (\text{B.22})$$

To express the coefficients I_{mnpq} as a function of I_{mnpq}^e , we calculate the expression of $I_{mnpq}^e \varrho_{mn}(\mathbf{u}^{(0)}) \varrho_{pq}(\mathbf{u}^{(0)})$ in the law (B.20), depending on the strains $e_{xmn}(\mathbf{u}^{(0)})$, to obtain the equivalent form (3.36).

The numerical evaluation of the integrals shows that the following terms can be neglected: $I_{1111}^e, I_{1112}^e, I_{1122}^e, I_{2211}^e, I_{1211}^e$. Using the expressions of the strains $\alpha_{11} = -\gamma e_{x11}$, $\alpha_{12} = \gamma(e_{x22} - e_{x12})$, $\alpha_{22} = \gamma(e_{x12} - 2e_{x22})$ one obtains:

$$\begin{aligned} I_{mnpq}^e \varrho_{mn}(\mathbf{u}^{(0)}) \varrho_{pq}(\mathbf{u}^{(0)}) &= \gamma^2 (-2I_{2222}^\alpha + 6I_{1222}^\alpha + 6I_{2212}^\alpha \\ &- 8I_{1212}^\alpha) e_{x12}(\mathbf{u}^{(0)}) e_{x22}(\mathbf{u}^{(0)}) + 4\gamma^2 (I_{2222}^\alpha - I_{1222}^\alpha - I_{2212}^\alpha + I_{1212}^\alpha) (e_{x22}(\mathbf{u}^{(0)}))^2 \\ &+ \gamma^2 (I_{2222}^\alpha - 2I_{1222}^\alpha - 2I_{2212}^\alpha + 4I_{1212}^\alpha) (e_{x12}(\mathbf{u}^{(0)}))^2 \end{aligned} \quad (\text{B.23})$$

From this last equation (B.23), we deduce the necessary coefficients for evaluating the term $\mathcal{Y}_f = I_{mnpq} e_{xmn}(\mathbf{u}^{(0)}) e_{xpq}(\mathbf{u}^{(0)})$ in the damage law as:

$$\begin{aligned} I_{1222} + I_{2212} &= \frac{\gamma^2}{2} (-2I_{2222}^\alpha + 6I_{1222}^\alpha + 6I_{2212}^\alpha - 8I_{1212}^\alpha) \\ I_{2222} &= 4\gamma^2 (I_{2222}^\alpha - I_{1222}^\alpha - I_{2212}^\alpha + I_{1212}^\alpha) \\ I_{1212} &= \frac{\gamma^2}{4} (I_{2222}^\alpha - 2I_{1222}^\alpha - 2I_{2212}^\alpha + 4I_{1212}^\alpha) \end{aligned} \quad (\text{B.24})$$

Appendix C

Thermoelastic effective coefficients and damage law

Thermomechanical effective coefficients

We provide here the details concerning the computation of the homogenized coefficients appearing in the formulation of the macroscopic elasto-damage problem in Chapter 4.

As concerns the expressions of the homogenized coefficients, we obtain a thermal modulus S^* given by coefficient:

$$S^* = \frac{1}{L_c^2} \int_Y b_{ij} e_{yij}(\phi) dy \quad (\text{C.1})$$

The effective elastic moduli C_{ijpq}^e are computed with the cell solutions as:

$$C_{ijpq}^e = \frac{1}{L_c^2} \int_Y a_{ijkl} (E_{kl}^{pq} + e_{ykl}(\xi^{pq})) dy \quad (\text{C.2})$$

and the homogenized mass density:

$$\rho^{eff} = \frac{1}{|Y|} \int_Y \rho dy \quad (\text{C.3})$$

For the effective thermo-elastic coupling coefficients we obtain:

$$\beta_{pq}^e = \frac{1}{L_c^2} \int_Y b_{ij} (E_{ij}^{pq} + e_{yij}(\xi^{pq})) dy \quad (\text{C.4})$$

$$\vartheta_{ij} = \frac{1}{L_c^2} \int_Y (b_{ij} - a_{ijkl} e_{ykl}(\phi)) dy \quad (\text{C.5})$$

The homogenized thermal conduction components are:

$$\begin{aligned} k_{11}^{eff} &= \frac{1}{|Y|} \int_Y k dy ; & k_{12}^{eff} &= \frac{1}{|Y|} \int_Y k \frac{\partial \theta}{\partial y_1} dy ; \\ k_{22}^{eff} &= \frac{1}{|Y|} \int_Y k \left(1 + \frac{\partial \theta}{\partial y_2} \right) dy \end{aligned} \quad (\text{C.6})$$

As explained in [140], a particular system of generators for the cell problem is necessary to respect the frictional contact conditions on the crack lips. The construction is specific to the present orientation of microcracks. The macroscopic strains $e_{xij}(\mathbf{u}^{(0)})$ are linear combinations of the elements of the system of macroscopic strains generators \mathbf{E}^{pq} :

$$e_{xij}(\mathbf{u}^{(0)}) = \varrho_{pq}(\mathbf{u}^{(0)})E_{ij}^{pq} \quad (\text{C.7})$$

where \mathbf{E}^{pq} has the form:

$$\mathbf{E}^{11} = \begin{pmatrix} -\frac{1}{\gamma} & 0 \\ 0 & 0 \end{pmatrix} ; \quad \mathbf{E}^{12} = \begin{pmatrix} 0 & -\frac{1}{\gamma} \\ -\frac{1}{\gamma} & -\frac{1}{2\gamma} \end{pmatrix} ; \quad \mathbf{E}^{22} = \begin{pmatrix} 0 & -\frac{1}{\gamma} \\ -\frac{1}{\gamma} & -\frac{1}{\gamma} \end{pmatrix} \quad (\text{C.8})$$

and $\varrho_{pq}(\mathbf{u}^{(0)})$ are defined as:

$$\begin{aligned} \varrho_{11}(\mathbf{u}^{(0)}) &= -\gamma e_{x11}(\mathbf{u}^{(0)}); & \varrho_{12}(\mathbf{u}^{(0)}) &= \gamma(e_{x22}(\mathbf{u}^{(0)}) - e_{x12}(\mathbf{u}^{(0)})); \\ \varrho_{22}(\mathbf{u}^{(0)}) &= \gamma(e_{x12}(\mathbf{u}^{(0)}) - 2e_{x22}(\mathbf{u}^{(0)})) \end{aligned} \quad (\text{C.9})$$

In (4.73) the coefficients β_{ij} are obtained as linear combination of β_{ij}^e using Equation (C.9):

$$\beta_{11} = -\gamma\beta_{11}^e; \quad \beta_{12} = \frac{\gamma}{2}(\beta_{22}^e - 2\beta_{12}^e); \quad \beta_{22} = 2\gamma(\beta_{12}^e - \beta_{22}^e) \quad (\text{C.10})$$

Using the equality $b_{ij} = \alpha a_{ijkl}\delta_{kl}$, we can write :

$$\beta_{pq}^e = \alpha C_{ijpq}^e \delta_{ij} \quad (\text{C.11})$$

This gives:

$$\begin{aligned} \beta_{11}^e &= \alpha(C_{1111}^e + C_{2211}^e); & \beta_{12}^e &= \alpha(C_{1112}^e + C_{2212}^e); \\ \beta_{22}^e &= \alpha(C_{1122}^e + C_{2222}^e) \end{aligned} \quad (\text{C.12})$$

Finally we obtain β_{ij} as linear combination of C_{ijpq}^e :

$$\begin{aligned} \beta_{11} &= -\gamma\alpha(C_{1111}^e + C_{2211}^e); \\ \beta_{12} &= \frac{\gamma}{2}\alpha(C_{1122}^e + C_{2222}^e - 2(C_{1112}^e + C_{2212}^e)); \\ \beta_{22} &= 2\gamma\alpha(C_{1112}^e + C_{2212}^e - C_{1122}^e - C_{2222}^e) \end{aligned} \quad (\text{C.13})$$

The coefficients C_{ijpq} in Equation (4.74) are linear combination of C_{ijpq}^e :

$$\begin{aligned} C_{ij11} &= -\gamma C_{ij11}^e; & C_{ij12} &= \frac{\gamma}{2}(C_{ij22}^e - 2C_{ij12}^e); \\ C_{ij22} &= 2\gamma(C_{ij12}^e - C_{ij22}^e) \end{aligned} \quad (\text{C.14})$$

Computation of the S^* and ϑ_{ij} required the solution ϕ of the cell problem (4.58-4.62). In order to simplify the numerical computation of this solution, we introduce a new function $\bar{\phi}$ as:

$$\phi = \bar{\phi} + \alpha \mathbf{y} \quad (\text{C.15})$$

Using this new function in combination with the relation $b_{ij} = a_{ijkl}\delta_{kl}$, we obtain a new cell problem:

$$\frac{\partial}{\partial y_j} (a_{ijkl} e_{ykl}(\bar{\phi})) = 0 \quad \text{in } Y \quad (\text{C.16})$$

On CY :

$$\left[a_{ijkl} e_{ykl}(\bar{\phi}) N_j \right] = 0 \quad (\text{C.17})$$

$$N_i a_{ijkl} e_{ykl}(\bar{\phi}) N_j < 0 \quad (\text{C.18})$$

$$\left[T_i a_{ijkl} e_{ykl}(\bar{\phi}) N_j \right] = -\mu_f N_i a_{ijkl} e_{ykl}(\bar{\phi}) N_j \quad (\text{C.19})$$

$$\left[\bar{\phi}_i N_i \right] = 0 \quad (\text{C.20})$$

To this new problem, we add the periodic boundary conditions $(\bar{\phi} + \alpha \mathbf{y})^+ = (\bar{\phi} + \alpha \mathbf{y})^-$ on the external faces of the cell.

The numerical solution obtained by solving the problem (C.16 - C.20) with *COMSOL MULTIPHYSICS* is presented on Figure C.1 for a value of damage variable $d = 0.5$ and $\mu_f = 0.5$.

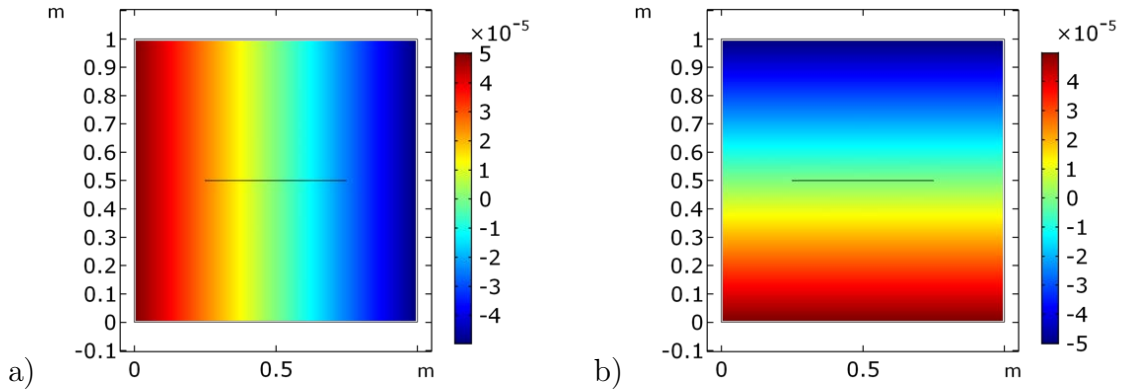


Figure C.1: Components $\bar{\phi}_1$ and $\bar{\phi}_2$ of the solution $\bar{\phi}$ computed with FEM

Figure C.1.a for $\bar{\phi}_1$ a symmetrical variation with respect to the axis $y_2 = 0.5$ while $\bar{\phi}_2$ exhibits symmetrical variation with respect to the axis $y_1 = 0.5$ as depicted on Figure C.1.b . Using $\alpha = 10^{-4} K^{-1}$ for the applied periodic boundary condition we obtain values of $\bar{\phi}_1$ and $\bar{\phi}_2$ between $-\frac{\alpha}{2}$ and $\frac{\alpha}{2}$ for the square shape unit cell.

Construction of the damage law

In this appendix we give details about the procedure used to obtain the damage law presented in Section 4.4. From the expression of $\mathbf{u}^{(1)}$ in (4.52), we deduce the following

relations:

$$\begin{aligned} \int_Y a_{ijkl} e_{yij}(\mathbf{u}^{(1)}) dy &= \int_Y a_{ijkl} e_{yij}(\boldsymbol{\xi}^{pq}) dy \varrho_{pq}(\mathbf{u}^{(0)}) \\ &+ \int_Y a_{ijkl} e_{yij}(\boldsymbol{\phi}) dy (T^{(0)} - T_0) \end{aligned} \quad (\text{C.21})$$

$$\begin{aligned} \int_Y b_{ij} e_{yij}(\mathbf{u}^{(1)}) dy &= \int_Y b_{ij} e_{yij}(\boldsymbol{\xi}^{pq}) dy \varrho_{pq}(\mathbf{u}^{(0)}) \\ &+ \int_Y b_{ij} e_{yij}(\boldsymbol{\phi}) dy (T^{(0)} - T_0) \end{aligned} \quad (\text{C.22})$$

And using the expressions of the effective coefficients (C.4), (C.2), (C.5) and (C.1), we deduce:

$$\int_Y a_{ijkl} e_{yij}(\boldsymbol{\xi}^{pq}) dy = L_c^2 C_{klpq}^e - a_{klij} E_{ij}^{pq} \quad (\text{C.23})$$

$$\int_Y b_{ij} e_{yij}(\boldsymbol{\xi}^{pq}) dy = \alpha \delta_{kl} (L_c^2 C_{klpq}^e - a_{klij} E_{ij}^{pq}) \quad (\text{C.24})$$

$$\int_Y a_{ijkl} e_{yij}(\boldsymbol{\phi}) dy = b_{kl} - L_c^2 \vartheta_{kl} \quad (\text{C.25})$$

$$\int_Y b_{ij} e_{yij}(\boldsymbol{\phi}) dy = L_c^2 S^* \quad (\text{C.26})$$

Replacing the equations (C.23-C.26) in (C.21-C.22) gives:

$$\begin{aligned} \int_Y a_{ijkl} e_{yij}(\mathbf{u}^{(1)}) dy &= (L_c^2 C_{klpq}^e - a_{klij} E_{ij}^{pq}) \varrho_{pq}(\mathbf{u}^{(0)}) \\ &+ (b_{kl} - L_c^2 \vartheta_{kl}) (T^{(0)} - T_0) \end{aligned} \quad (\text{C.27})$$

$$\begin{aligned} \int_Y b_{ij} e_{yij}(\mathbf{u}^{(1)}) dy &= \alpha \delta_{kl} (L_c^2 C_{klpq}^e - a_{klij} E_{ij}^{pq}) \varrho_{pq}(\mathbf{u}^{(0)}) \\ &+ L_c^2 S^* (T^{(0)} - T_0) \end{aligned} \quad (\text{C.28})$$

With the relations (C.27) and (C.28), we can calculate the first term in the right side of (4.85) to obtain:

$$\begin{aligned}
& \frac{1}{2} \frac{d}{dt} \int_Y (a_{ijkl} e_{xkl}(\mathbf{u}^{(0)}) - b_{ij}(T^{(0)} - T_0)) e_{yij}(\mathbf{u}^{(1)}) d_y = \\
& \quad \frac{1}{2} L_c^2 \frac{dC_{klpq}^g}{dd} \frac{dd}{dt} \varrho_{pq}(\mathbf{u}^{(0)}) \varrho_{mn}(\mathbf{u}^{(0)}) E_{kl}^{mn} \\
& \quad - \frac{1}{2} L_c^2 \frac{d\vartheta_{kl}}{dd} \frac{dd}{dt} (T^{(0)} - T_0) \varrho_{mn}(\mathbf{u}^{(0)}) E_{kl}^{mn} \\
& \quad - \frac{1}{2} L_c^2 \frac{dC_{klpq}^g}{dd} \frac{dd}{dt} (T^{(0)} - T_0) \alpha \delta_{kl} \varrho_{pq}(\mathbf{u}^{(0)}) \\
& \quad \quad - \frac{1}{2} L_c^2 \frac{dS^*}{dd} \frac{dd}{dt} (T^{(0)} - T_0)^2 \\
& + \frac{1}{2} (L_c^2 C_{klpq}^g - a_{klij} E_{ij}^{pq}) (\varrho_{pq}(\dot{\mathbf{u}}^{(0)}) \varrho_{mn}(\mathbf{u}^{(0)}) - \varrho_{pq}(\mathbf{u}^{(0)}) \varrho_{mn}(\dot{\mathbf{u}}^{(0)})) E_{kl}^{mn} \\
& \quad + \frac{1}{2} (b_{kl} - L_c^2 \vartheta_{kl}) ((T^{(0)} - T_0) \varrho_{mn}(\dot{\mathbf{u}}^{(0)}) + \varrho_{mn}(\mathbf{u}^{(0)}) \dot{T}^{(0)}) E_{kl}^{mn} \\
& \quad - \frac{1}{2} \alpha \delta_{kl} (L_c^2 C_{klpq}^g - a_{klij} E_{ij}^{pq}) ((T^{(0)} - T_0) \varrho_{pq}(\dot{\mathbf{u}}^{(0)}) + \varrho_{pq}(\mathbf{u}^{(0)}) \dot{T}^{(0)}) \\
& \quad \quad - L_c^2 S^* \dot{T}^{(0)} (T^{(0)} - T_0)
\end{aligned} \tag{C.29}$$

In the same way, we obtain for the second term in the right side of (4.85):

$$\begin{aligned}
& \int_Y (a_{ijkl} e_{xkl}(\dot{\mathbf{u}}^{(0)}) - b_{ij} \dot{T}^{(0)}) e_{yij}(\mathbf{u}^{(1)}) d_y = \\
& \quad (L_c^2 C_{klpq}^g - a_{klij} E_{ij}^{pq}) \varrho_{pq}(\mathbf{u}^{(0)}) \varrho_{mn}(\dot{\mathbf{u}}^{(0)}) E_{kl}^{mn} \\
& \quad + (b_{kl} - L_c^2 \vartheta_{kl}) (T^{(0)} - T_0) \varrho_{mn}(\dot{\mathbf{u}}^{(0)}) E_{kl}^{mn} \\
& \quad - \alpha \delta_{kl} (L_c^2 C_{klpq}^g - a_{klij} E_{ij}^{pq}) \varrho_{pq}(\mathbf{u}^{(0)}) \dot{T}^{(0)} - L_c^2 S^* \dot{T}^{(0)} (T^{(0)} - T_0)
\end{aligned} \tag{C.30}$$

Replacing (C.29-C.30) in (4.85) we obtain:

$$\begin{aligned}
& \frac{1}{L_c^2} \int_{CY} \sigma_{ij}^{(0)} N_j [\dot{u}_i^{(1)}] ds_y - \frac{1}{2L_c^2} \frac{d}{dt} \int_{CY} \sigma_{ij}^{(0)} N_j [u_i^{(1)}] ds_y - \frac{1}{L_c} \frac{dd}{dt} \mathcal{G}^{(1)} = \\
& \frac{dd}{dt} \left(\frac{1}{2} \frac{dC_{klpq}^g}{dd} \varrho_{pq}(\mathbf{u}^{(0)}) \varrho_{mn}(\mathbf{u}^{(0)}) E_{kl}^{mn} - \frac{1}{2} \frac{d\vartheta_{kl}}{dd} (T^{(0)} - T_0) \varrho_{mn}(\mathbf{u}^{(0)}) E_{kl}^{mn} \right. \\
& \quad \left. - \frac{1}{2} \frac{dC_{klpq}^g}{dd} (T^{(0)} - T_0) \alpha \delta_{kl} \varrho_{pq}(\mathbf{u}^{(0)}) - \frac{1}{2} \frac{dS^*}{dd} (T^{(0)} - T_0)^2 \right) \\
& + \frac{1}{2L_c^2} \int_{CY} a_{ijkl} E_{kl}^{mn} N_j [\xi_i^{pq}] ds_y (\varrho_{pq}(\dot{\mathbf{u}}^{(0)}) \varrho_{mn}(\mathbf{u}^{(0)}) - \varrho_{pq}(\mathbf{u}^{(0)}) \varrho_{mn}(\dot{\mathbf{u}}^{(0)})) \\
& + \frac{1}{2L_c^2} \int_{CY} a_{ijkl} E_{kl}^{mn} N_j [\phi_i] ds_y (\varrho_{mn}(\mathbf{u}^{(0)}) \dot{T}^{(0)} - (T^{(0)} - T_0) \varrho_{mn}(\dot{\mathbf{u}}^{(0)})) \\
& + \frac{1}{2L_c^2} \int_{CY} b_{ij} N_j [\zeta_i^{pq}] ds_y (\varrho_{pq}(\mathbf{u}^{(0)}) \dot{T}^{(0)} - (T^{(0)} - T_0) \varrho_{pq}(\dot{\mathbf{u}}^{(0)}))
\end{aligned} \tag{C.31}$$

Using the expressions of $\mathbf{u}^{(1)}$ and $\sigma_{ij}^{(0)}$ we have:

$$\begin{aligned}
 & \frac{1}{L_c^2} \int_{CY} \sigma_{ij}^{(0)} N_j [u_i^{(1)}] ds_y = \\
 & \frac{1}{L_c^2} \int_{CY} a_{ijkl} (E_{kl}^{mn} + e_{ykl}(\boldsymbol{\xi}^{mn})) N_j [\xi_i^{pq}] ds_y \varrho_{mn}(\mathbf{u}^{(0)}) \varrho_{pq}(\mathbf{u}^{(0)}) \\
 & + \frac{1}{L_c^2} \int_{CY} a_{ijkl} (E_{kl}^{mn} + e_{ykl}(\boldsymbol{\xi}^{mn})) N_j [\phi_i] ds_y \varrho_{mn}(\mathbf{u}^{(0)}) (T^{(0)} - T_0) \\
 & - \frac{1}{L_c^2} \int_{CY} (b_{ij} - a_{ijkl} e_{ykl}(\boldsymbol{\phi})) N_j [\xi_i^{pq}] ds_y \varrho_{pq}(\mathbf{u}^{(0)}) (T^{(0)} - T_0) \\
 & - \frac{1}{L_c^2} \int_{CY} (b_{ij} - a_{ijkl} e_{ykl}(\boldsymbol{\phi})) N_j [\phi_i] ds_y (T^{(0)} - T_0)^2
 \end{aligned} \tag{C.32}$$

With (C.32) we calculate the second term in the left side of (C.31) and obtain:

$$\begin{aligned}
 & \frac{1}{2L_c^2} \frac{d}{dt} \int_{CY} \sigma_{ij}^{(0)} N_j [u_i^{(1)}] ds_y = \left(\frac{1}{2} \frac{dZ_{mnpq}^{\varrho^1}}{dd} \varrho_{mn}(\mathbf{u}^{(0)}) \varrho_{pq}(\mathbf{u}^{(0)}) \right. \\
 & \left. + \frac{1}{2} \left(\frac{dZ_{mn}^{\varrho^2}}{dd} + \frac{dZ_{mn}^{\varrho^3}}{dd} \right) \varrho_{mn}(\mathbf{u}^{(0)}) (T^{(0)} - T_0) + \frac{1}{2} \frac{dZ^4}{dd} (T^{(0)} - T_0)^2 \right) \frac{dd}{dt} \\
 & + \frac{1}{2} Z_{mnpq}^{\varrho^1} (\varrho_{mn}(\dot{\mathbf{u}}^{(0)}) \varrho_{pq}(\mathbf{u}^{(0)}) + \varrho_{mn}(\mathbf{u}^{(0)}) \varrho_{pq}(\dot{\mathbf{u}}^{(0)})) \\
 & + \frac{1}{2} (Z_{mn}^{\varrho^2} + Z_{mn}^{\varrho^3}) (\varrho_{mn}(\dot{\mathbf{u}}^{(0)}) (T^{(0)} - T_0) + \varrho_{mn}(\mathbf{u}^{(0)}) \dot{T}^{(0)}) \\
 & + Z^4 \dot{T}^{(0)} (T^{(0)} - T_0)
 \end{aligned} \tag{C.33}$$

where

$$Z_{mnpq}^{\varrho^1} = \frac{1}{L_c^2} \int_{CY} a_{ijkl} (E_{kl}^{mn} + e_{ykl}(\boldsymbol{\xi}^{mn})) N_j [\xi_i^{pq}] ds_y \tag{C.34}$$

$$Z_{mn}^{\varrho^2} = \frac{1}{L_c^2} \int_{CY} a_{ijkl} (E_{kl}^{mn} + e_{ykl}(\boldsymbol{\xi}^{mn})) N_j [\phi_i] ds_y \tag{C.35}$$

$$Z_{mn}^{\varrho^3} = -\frac{1}{L_c^2} \int_{CY} (b_{ij} - a_{ijkl} e_{ykl}(\boldsymbol{\phi})) N_j [\xi_i^{mn}] ds_y \tag{C.36}$$

$$Z^4 = -\frac{1}{L_c^2} \int_{CY} (b_{ij} - a_{ijkl} e_{ykl}(\boldsymbol{\phi})) N_j [\phi_i] ds_y \tag{C.37}$$

When the time derivative of $\mathbf{u}^{(1)}$:

$$\begin{aligned}
 \dot{\mathbf{u}}^{(1)} &= \dot{\boldsymbol{\xi}}^{pq}(\mathbf{y}) \varrho_{pq}(\mathbf{u}^{(0)})(\mathbf{x}, t) + \boldsymbol{\xi}^{pq}(\mathbf{y}) \varrho_{pq}(\dot{\mathbf{u}}^{(0)})(\mathbf{x}, t) \\
 &+ \dot{\boldsymbol{\phi}}(\mathbf{y}) (T^{(0)}(\mathbf{x}, t) - T_0) + \boldsymbol{\phi}(\mathbf{y}) \dot{T}^{(0)}(\mathbf{x}, t)
 \end{aligned} \tag{C.38}$$

is used in the first integral in the left member of (C.31) one obtains:

$$\begin{aligned}
\frac{1}{L_c^2} \int_{CY} \sigma_{ij}^{(0)} N_j \left[\dot{u}_i^{(1)} \right] ds_y &= \left(I_{mnpq}^{\varrho 2} \varrho_{mn}(\mathbf{u}^{(0)}) \varrho_{pq}(\mathbf{u}^{(0)}) \right. \\
&+ J_{mn}^{\varrho 2} \varrho_{mn}(\mathbf{u}^{(0)}) (T^{(0)} - T_0) - P^2 (T^{(0)} - T_0)^2 \left. \right) \frac{dd}{dt} \\
&+ \mathcal{Z}_{mnpq}^{\varrho 1} \varrho_{mn}(\mathbf{u}^{(0)}) \varrho_{pq}(\dot{\mathbf{u}}^{(0)}) + \mathcal{Z}_{mn}^{\varrho 2} \varrho_{mn}(\mathbf{u}^{(0)}) \dot{T}^{(0)} \\
&+ \mathcal{Z}_{mn}^{\varrho 3} \varrho_{mn}(\dot{\mathbf{u}}^{(0)}) (T^{(0)} - T_0) + \mathcal{Z}^4 \dot{T}^{(0)} (T^{(0)} - T_0)
\end{aligned} \tag{C.39}$$

with

$$I_{mnpq}^{\varrho 2} = \frac{1}{L_c^2} \int_{CY} a_{ijkl} (E_{kl}^{mn} + e_{ykl}(\boldsymbol{\xi}^{mn})) N_j \left[\frac{d\xi_i^{pq}}{dd} \right] ds_y \tag{C.40}$$

$$\begin{aligned}
J_{mn}^{\varrho 2} &= \frac{1}{L_c^2} \int_{CY} a_{ijkl} (E_{kl}^{mn} + e_{ykl}(\boldsymbol{\xi}^{mn})) N_j \left[\frac{d\phi_i}{dd} \right] ds_y \\
&- \frac{1}{L_c^2} \int_{CY} (b_{ij} - a_{ijkl} e_{ykl}(\boldsymbol{\phi})) N_j \left[\frac{d\xi_i^{mn}}{dd} \right] ds_y
\end{aligned} \tag{C.41}$$

$$P^2 = \frac{1}{L_c^2} \int_{CY} (b_{ij} - a_{ijkl} e_{ykl}(\boldsymbol{\phi})) N_j \left[\frac{d\phi_i}{dd} \right] ds_y \tag{C.42}$$

Using the cell problems (4.53), (4.58) one can prove that the integral $\int_{CY} a_{ijkl} e_{ykl}(\boldsymbol{\xi}^{mn}) N_j [\xi_i^{pq}] ds_y$ is symmetrical in respect to the pairs mn and pq and we have

$$\int_{CY} a_{ijkl} e_{ykl}(\boldsymbol{\xi}^{mn}) N_j [\phi_i] ds_y = \int_{CY} a_{ijkl} e_{ykl}(\boldsymbol{\phi}) N_j [\xi_i^{pq}] ds_y$$

Combination with (C.33) and (C.39) and substitution in (C.31) allow us to obtain the damage relation:

$$\begin{aligned}
&\frac{dd}{dt} \left(\frac{\mathcal{G}^{(1)}}{L_c} + \frac{1}{2} \frac{dC_{klpq}^{\varrho}}{dd} \varrho_{pq}(\mathbf{u}^{(0)}) \varrho_{mn}(\mathbf{u}^{(0)}) E_{kl}^{mn} \right. \\
&\quad \left. - \frac{1}{2} \frac{d\vartheta_{kl}}{dd} (T^{(0)} - T_0) \varrho_{mn}(\mathbf{u}^{(0)}) E_{kl}^{mn} \right. \\
&- \frac{1}{2} \frac{dC_{klpq}^{\varrho}}{dd} (T^{(0)} - T_0) \alpha \delta_{kl} \varrho_{pq}(\mathbf{u}^{(0)}) - \frac{1}{2} \frac{dS^*}{dd} (T^{(0)} - T_0)^2 \\
&\quad \left. + I_{mnpq}^{\varrho} \varrho_{mn}(\mathbf{u}^{(0)}) \varrho_{pq}(\mathbf{u}^{(0)}) \right. \\
&\quad \left. + J_{mn}^{\varrho} \varrho_{mn}(\mathbf{u}^{(0)}) (T^{(0)} - T_0) - P^{\varrho} (T^{(0)} - T_0)^2 \right) = 0
\end{aligned} \tag{C.43}$$

with the effective coefficients

$$I_{mnpq}^e = \frac{1}{2L_c^2} \frac{d}{dd} \int_{CY} a_{ijkl} (E_{kl}^{mn} + e_{ykl}(\boldsymbol{\xi}^{mn})) N_j [\xi_i^{pq}] ds_y - \frac{1}{L_c^2} \int_{CY} a_{ijkl} (E_{kl}^{mn} + e_{ykl}(\boldsymbol{\xi}^{mn})) N_j \left[\frac{d\xi_i^{pq}}{dd} \right] ds_y \quad (\text{C.44})$$

$$J_{mn}^e = \frac{1}{2L_c^2} \frac{d}{dd} \int_{CY} a_{ijkl} (E_{kl}^{mn} + e_{ykl}(\boldsymbol{\xi}^{mn})) N_j [\phi_i] ds_y - \frac{1}{2L_c^2} \frac{d}{dd} \int_{CY} (b_{ij} - a_{ijkl} e_{ykl}(\boldsymbol{\phi})) N_j [\xi_i^{mn}] ds_y - \frac{1}{L_c^2} \int_{CY} a_{ijkl} (E_{kl}^{mn} + e_{ykl}(\boldsymbol{\xi}^{mn})) N_j \left[\frac{d\phi_i}{dd} \right] ds_y + \int_{CY} (b_{ij} - a_{ijkl} e_{ykl}(\boldsymbol{\phi})) N_j \left[\frac{d\xi_i^{mn}}{dd} \right] ds_y \quad (\text{C.45})$$

$$P = \frac{1}{2L_c^2} \frac{d}{dd} \int_{CY} (b_{ij} - a_{ijkl} e_{ykl}(\boldsymbol{\phi})) N_j [\phi_i] ds_y - \frac{1}{L_c^2} \int_{CY} (b_{ij} - a_{ijkl} e_{ykl}(\boldsymbol{\phi})) N_j \left[\frac{d\phi_i}{dd} \right] ds_y \quad (\text{C.46})$$

In the equation (4.88) the coefficients I_{mnpq} and J_{mn} are linear combinations of I_{mnpq}^e and, respectively, J_{mn}^e . For I_{mnpq} we get:

$$\begin{aligned} I_{1212} &= \frac{\gamma^2}{4} (I_{2222}^e - 2I_{1222}^e - 2I_{2212}^e + 4I_{1212}^e) \\ I_{2222} &= 4\gamma^2 (I_{2222}^e - I_{1222}^e - I_{2212}^e + I_{1212}^e) \\ I_{1222} + I_{2212} &= \gamma^2 (-2I_{2222}^e + 3I_{1222}^e + 3I_{2212}^e - 4I_{1212}^e) \end{aligned} \quad (\text{C.47})$$

while the others components I_{1111} , I_{1112} , I_{1122} , I_{2211} , I_{1211} are vanishing.

Similar combinations are obtained for I_{mnpq}^2 of equation (4.96).

$$\begin{aligned} I_{1212}^2 &= \frac{\gamma^2}{4} (I_{2222}^{e2} - 2I_{1222}^{e2} - 2I_{2212}^{e2} + 4I_{1212}^{e2}) \\ I_{2222}^2 &= 4\gamma^2 (I_{2222}^{e2} - I_{1222}^{e2} - I_{2212}^{e2} + I_{1212}^{e2}) \\ I_{1222}^2 + I_{2212}^2 &= \gamma^2 (-2I_{2222}^{e2} + 3I_{1222}^{e2} + 3I_{2212}^{e2} - 4I_{1212}^{e2}) \\ I_{1111}^2 &= I_{1112}^2 = I_{1122}^2 = I_{2211}^2 = I_{1211}^2 = 0 \end{aligned} \quad (\text{C.48})$$

Expressions of J_{mn} and J_{mn}^2 in the definition (4.88) of \mathcal{Y}_f and, respectively, (4.96) are:

$$J_{11} = -\gamma J_{11}^e; \quad J_{12} = \frac{\gamma}{2} (J_{22}^e - 2J_{12}^e); \quad J_{22} = 2\gamma (J_{12}^e - J_{22}^e) \quad (\text{C.49})$$

$$J_{11}^2 = -\gamma J_{11}^{e2}; \quad J_{12}^2 = \frac{\gamma}{2} (J_{22}^{e2} - 2J_{12}^{e2}); \quad J_{22}^2 = 2\gamma (J_{12}^{e2} - J_{22}^{e2}) \quad (\text{C.50})$$

Finally, the coefficients \mathcal{Z}_{mnpq}^1 , \mathcal{Z}_{mn}^2 and \mathcal{Z}_{mn}^3 in (4.96) are linear combinations of \mathcal{Z}_{mnpq}^{e1} , \mathcal{Z}_{mn}^{e2} and \mathcal{Z}_{mn}^{e3} correspondingly:

$$\begin{aligned}
\mathcal{Z}_{1212}^1 &= \frac{\gamma^2}{4} (\mathcal{Z}_{2222}^{e1} - 2\mathcal{Z}_{1222}^{e1} - 2\mathcal{Z}_{2212}^{e1} + 4\mathcal{Z}_{1212}^{e1}) \\
\mathcal{Z}_{2222}^1 &= 4\gamma^2 (\mathcal{Z}_{2222}^{e1} - \mathcal{Z}_{1222}^{e1} - \mathcal{Z}_{2212}^{e1} + \mathcal{Z}_{1212}^{e1}) \\
\mathcal{Z}_{2212}^1 &= \gamma^2 (-\mathcal{Z}_{2222}^{e1} + \mathcal{Z}_{1222}^{e1} + 2\mathcal{Z}_{2212}^{e1} - 2\mathcal{Z}_{1212}^{e1}) \\
\mathcal{Z}_{1222}^1 &= \gamma^2 (-\mathcal{Z}_{2222}^{e1} + 2\mathcal{Z}_{1222}^{e1} + \mathcal{Z}_{2212}^{e1} - 2\mathcal{Z}_{1212}^{e1}) \\
\mathcal{Z}_{1111}^1 &= \mathcal{Z}_{1112}^1 = \mathcal{Z}_{1122}^1 = \mathcal{Z}_{2211}^1 = \mathcal{Z}_{1211}^1 = 0.
\end{aligned} \tag{C.51}$$

$$\mathcal{Z}_{11}^2 = -\gamma \mathcal{Z}_{11}^{e2}; \quad \mathcal{Z}_{12}^2 = \frac{\gamma}{2} (\mathcal{Z}_{22}^{e2} - 2\mathcal{Z}_{12}^{e2}); \quad \mathcal{Z}_{22}^2 = 2\gamma (\mathcal{Z}_{12}^{e2} - \mathcal{Z}_{22}^{e2}) \tag{C.52}$$

$$\mathcal{Z}_{11}^3 = -\gamma \mathcal{Z}_{11}^{e3}; \quad \mathcal{Z}_{12}^3 = \frac{\gamma}{2} (\mathcal{Z}_{22}^{e3} - 2\mathcal{Z}_{12}^{e3}); \quad \mathcal{Z}_{22}^3 = 2\gamma (\mathcal{Z}_{12}^{e3} - \mathcal{Z}_{22}^{e3}) \tag{C.53}$$

Bibliography

- [1] ABAQUS 6.13, Analysis User's Manual. Dassault Systems Simulia Corporation, RI, USA (2013).
- [2] Andrieux S., Bamberger Y., Marigo J-J., Un modele de materiau microfissure pour les betons et les roches. *J. Méc. Theor. Appl.*, vol. 5, p.471-513 (1986).
- [3] Allix O., Feissel P., Thévenet, P., A delay damage mesomodel of laminates under dynamic loading: basic aspects and identification issues. *Comput. Struct.*, 81, 1177-1191 (2003).
- [4] Archer J.S., Lesser A.J., Shear band formation and mode II fracture of polymeric glasses. *J. Polym. Sci. B: Polymer Physics* 49, 103-114 (2010).
- [5] Ashby M.F., Hallam S.D., The failure of brittle solids containing small cracks under compressive stress states. *Acta Metall.* 34, 497-510 (1986).
- [6] Atiezo M.K., Dascalu C., Antiplane two-scale model for dynamic failure. *Int J. Fracture*, vol. 206, 195-214 (2017).
- [7] Atiezo M.K., Chen W., Dascalu C., Loading rate effects on dynamic failure of quasi-brittle solids: Simulations with a two-scale damage model. *Theor. Appl. Frac. Mech.*, 100, 269-280 (2019).
- [8] Atiezo, M. K., Gbetchi, K., Dascalu, C., Dynamic shear damage with frictional sliding on microcracks. *Eng. Fract. Mech.* to appear (2020).
- [9] Auriault J.-L., 2012. Wave propagation and transient heat transfer in thermoelastic composites. *Int. J. Heat Mass Transfer* 55, 5972-5978.
- [10] Bakhvalov N., Panasenko G., Homogenization: Averaging Processes in Periodic Media, Kluwer Academic Publishers Group, Dordrecht (1989).
- [11] Bazant Z.P., Caner F.C., Impact comminution of solids due to local kinetic energy of high shear strain rate: I- Continuum theory and turbulence analogy, II- Microplane model and verification. *J. Mech. Phys. Solids*, 64, 223-248 (2014).
- [12] Bazant Z.P., Size effect in blunt fracture : Concrete, rock, metal. *J. Eng. Mech., Am. Soc. Civil Eng.* 100 : 518-535, (1984).

- [13] Bazant Z.P., Scaling of quasi-brittle fracture : Asymptotic analysis. *Int J. Fracture* 83 : 19-40 (1997).
- [14] Berry J.P., Surface characteristics of fractured poly(methyl methacrylate). *Nature* 185 (4706), 91-92 (1960).
- [15] Benssousan A., Lions J., Papanicolaou G., *Asymptotic Analysis for Periodic Structures*. Kluwer Academic Publisher, Amsterdam (1978).
- [16] Bhatt H., Rosakis A., Sammis G., A micro-mechanics based constitutive model for brittle failure at high strain rates. *J. Appl.Mech.*, 79(3), 1016-28 (2011).
- [17] Bjerke T. W., Thermomechanical behavior of amorphous polymers during high-speed crack propagation. Army Research Lab Aberdeen, Proving Ground MD 21005-5066 (2002).
- [18] Bjerke T. W., Lambros J., Theoretical development and experimental validation of a thermally dissipative cohesive zone model for dynamic fracture of amorphous polymers. *J. Mech. Phys. Solids* 51, 1947-1970 (2003).
- [19] Bjerke T. W., Lambros J., Heating During Shearing and Opening Dominated Dynamic Fracture of Polymers. *Exp. Mech.* 42, 107-114 (2003).
- [20] Borden M.J., Verhoosel C.V., Scott M.A., Hughes, T.J.R., Landis, C.M., A phase-field description of dynamic brittle fracture. *Comp. Meth. Appl. Mech. Engng.* 217-220, 77-95 (2012).
- [21] Børvik T., Langseth M., Hopperstad O.S., Malo K.A., Perforation of 12mm thick steel plates by 20mm diameter projectiles with flat, hemispherical and conical noses, part II : numerical simulations. *International Journal of Impact Engineering*, 27, 37-64 (2002).
- [22] Børvik T., Langseth M., Hopperstad O.S., Malo K.A., Ballistic penetration of steel plates. *International Journal of Impact Engineering*, 22, 855-886 (1999).
- [23] Bougaut O., Rittel D., On crack-tip cooling during dynamic crack initiation. *Int. J. Solids Structures* 38, 2517-2532 (2001).
- [24] Bourdin B., Larsen C.J., Richardson C., A time-discrete model for dynamic fracture based on crack regularization. *Int. J. Fract.* 168, 133-143 (2011).
- [25] Bui H.D., Ehrlacher A., Nguyen Q.S., Propagation de fissure en thermoélasticité dynamique. *Journal de Mécanique*, 19, 697-723 (1980).
- [26] Bui H.D., Ehrlacher, A., Nguyen, Q.S., Thermomechanical couplings in fracture mechanics. In *Thermomechanical couplings in solids*, eds. H.D. Bui and Q.S. Nguyen, Elsevier Amsterdam, North Holland, 327-341 (1986).
- [27] Broberg KB, On crack paths. *Engineering Fracture Mechanics*, vol. 28, 5-6, 663 - 679 (1987).

-
- [28] Broberg K.B., The near-tip field at high crack velocities. *Int. J. Fract.* 39,1-13 (1989).
- [29] Broberg K.B., Intersonic mode II crack expansion. *Arch. Mech.* 47(5), 859-871 (1995).
- [30] Broberg K.B., *Cracks and fracture*, Academic Press, San Diego (1999).
- [31] Burridge R., Conn G., Freund L.B., The stability of a rapid mode II shear crack with finite cohesive traction. *J. Geophys. Res.* 85(B5), 2210-2222 (1979).
- [32] Carslaw H.S., Jaeger J.C, *Conduction of Heat in Solids*, Oxford University Press, England, (1959).
- [33] Camacho G.T., Ortiz M., Computational modelling of impact damage in brittle materials. *Int. J. Solids Struct.*, 33, 2899-2938 (1996).
- [34] Chu D., Li X., Liu Z., Study the dynamic crack path in brittle material under thermal shock loading by phase field modeling. *Int. J. Fract.* 208, 114-130 (2017).
- [35] Comsol Multiphysics, *User's Guide Version 5.2* (2015).
- [36] Dalmas D., Guerra C., Scheibert J., Bonamy D., Damage mechanisms in dynamic fracture of nominally brittle polymers. *Int. J. Fract.* 184, 93-111 (2013).
- [37] Dascalu C., Bilbie G., Agiasofitou E., Damage and size effect in elastic solids: a homogenization approach. *Int. J. Solids Struct.*, 45, 409-430 (2008).
- [38] Dascalu C., Dobrovat A., Tricarico M., On a 3D micromechanical damage model. *International Journal of Fracture* vol. 166, 153-162 (2010).
- [39] Dascalu C., François B., Keita O., A two-scale model for subcritical damage propagation. *Int. J. Solids Struct.* 47, 493-502 (2010).
- [40] Dascalu C., Dynamic localization of damage and microstructural length influence. *Int. J. Damage Mech.*, 28, 1190-1218 (2017).
- [41] Dascalu C., Multiscale modeling of rapid failure in brittle solids: branching instabilities. *Mech. Mater.*, 116, 77-89 (2018).
- [42] Dascalu C., Gbetchi K., Dynamic evolution of damage by microcracking with heat dissipation. *Int. J. Solids Struct.* 174-175, 128 - 144 (2019).
- [43] De Bellis, M.L., Della Vecchia, G., Ortiz, M., Pandolfi, A. (2017). A multiscale model of distributed fracture and permeability in solids in all-round compression. *J. Mech. Phys. Solids*, 104, 12-31 (2017).
- [44] Deü J.F., *Rupture des composites stratifiés sous chargement dynamique : apport des méso-modèles avec endommagement retardé*. Thèse de Doctorat, École Normale Supérieure de Cachan (1997).
- [45] Denoual C., Hild F., A damage model for the dynamic fragmentation of brittle solids. *Comput. Methods Appl. Mech. Eng.*, 183, 247-258 (2000).

- [46] Dienes J. K., Zuo Q. H., Kershner J. D., Impact initiation of explosives and propellants via statistical crack mechanics. *J. Mech. Phys. Solids* 54(6), 1237-1275 (2006).
- [47] Dobrovat A., Dascalu, C., Hall S., Computational modeling of damage based on micro-crack kinking. *Int. J. Multiscale Comput. Engng.*, vol. 13, 201-217 (2015).
- [48] Döll W., Optical interference measurements and fracture mechanics analysis of crack tip craze zones. *Adv. Polymer Science*, 52-53, 105-168 (1983).
- [49] Duarte C. A., Grilli N., Koslowski M., Effect of initial damage variability on hot-spot nucleation in energetic materials. *J. Appl. Phys.*, 124(2), 025104 (2018).
- [50] Dubé J.F., Pijaudier-Cabot G., La Borderie C., Rate dependent damage model for concrete in dynamics. *J. Engng. Mech.*, 122, 939-947 (1996).
- [51] Dubé J.F., Modélisation simplifiée et comportement visco-endommageable des structures en béton. Thèse de Doctorat, École Normale Supérieure de Cachan (1994).
- [52] Ene H.I., On linear thermoelasticity of composite materials. *Int. J. Engng. Sci.* 21, 443-448 (1983).
- [53] Eshelby J. D., The determination of the field of an ellipsoidal inclusion and related problems. *Proc. R. Soc. Lond A*, 241, pp. 376-396 (1957).
- [54] Estevez R., Basu S., van der Giessen E., Analysis of temperature effects near mode I cracks in glassy polymers. *Int J. Fract.* 132, 249-273 (2005).
- [55] Fialko Y., Temperature fields generated by the elastodynamic propagation of shear cracks in the Earth. *J. Geophys. Res.*, 109, B01303 (2004).
- [56] Fish J., *Practical Multiscaleing*, John Wiley & Sons (2013).
- [57] Francfort G.A., Homogenization and linear thermoelasticity. *SIAM J. Math. Anal.*, 14, 696-708 (1983).
- [58] Freund L.B., The mechanics of dynamic shear crack propagation. *J. Geophys. Res.* 84, 2199-2209 (1979).
- [59] Freund L.B., *Dynamic Fracture Mechanics*, Cambridge University Press (1990).
- [60] Forquin P., Hild F., A probabilistic damage model of the dynamic fragmentation process in brittle materials. *Adv. Appl. Mech.* 44, 1-72 (2010).
- [61] François B., Dascalu C., A two-scale time-dependent damage model based on non-planar growth of micro-cracks, *J. Mech. Phys. Solids* 58, 1928-1946 (2010).
- [62] Fuller K.N.G., Fox P.G., Field J.E., The temperature rise at the tip of a fast-moving crack in glassy polymers. *Proc. R. Soc. London A*341, 537-557 (1975).
- [63] Gatuingt F., Prédiction de la rupture des ouvrages en béton sollicités en dynamique rapide. Thèse de Doctorat, École Normale Supérieure de Cachan (1999).

-
- [64] Gambarotta L., Lagomarsino S., A microcrack damage model for brittle materials. *Int. J. Solids Struct.*, 30(2), 177-198 (1993).
- [65] Gambin B., Telega J.J. Effective properties of elastic solids with randomly distributed microcracks. *Mechanics Research Communication*, 27(6), 697-706 (2000).
- [66] Gbetchi K., Dascalu C., Two-scale thermomechanical damage model for dynamic shear failure in brittle solids, under review (2020).
- [67] Grilli N., Duarte C. A., Koslowski M., Dynamic fracture and hot-spot modeling in energetic composites. *J. Appl. Phys.*, 123(6), 065101 (2018).
- [68] Griffith A., The phenomena of rupture and flow in solids, *Phil. Trans. Roy. Soc., London CCXXI-A*, 163-198 (1920).
- [69] Halm D., Dragon A., An anisotropic model of damage and frictional sliding for brittle materials. *European Journal of Mechanics A Solids*, Volume: 17, 439-460 (1998).
- [70] Hill R., A self consistent mechanics of composite materials. *J. Mech. Phys. Solids*, 13, 213-222, (1965).
- [71] Hofacker M., Miehe C., Continuum phase field modeling of dynamic fracture: variational principles and staggered FE implementation. *Int. J. Fract.* 178, 113-129 (2012).
- [72] Hu G., Liu J., Graham-Brady L., Ramesh K.T., A 3D mechanistic model for brittle materials containing evolving flaw distributions under dynamic multiaxial loading. *J. Mech. Phys. Solids*, 78, 269-297 (2015).
- [73] Huang C., Subhash G., Vitton S.J., A dynamic damage growth model for uniaxial compressive response of rock aggregates. *Mech. Mater.*, 34, 267-277 (2002).
- [74] Horii H., Nemat-Nasser S., Brittle failure in compression: splitting, faulting and brittle-ductile transition. *Philos. Trans. Roy. Soc. London*, 319, 337-374 (1986).
- [75] Irwin G.R., Analysis of Stresses and Strains near the End of a crack Traversing a Plate. *Journal of applied Mechanics*, 24, 361-364 (1957).
- [76] Johnson G.R., and Cook H.W., Fracture characteristics of three metals subjected to various strains, strain rates, temperatures, and pressures. *Engineering Fracture Mechanics*, 21, 31-48 (1985).
- [77] Johnson G. R., and Cook W. H., A constitutive model and data for metals subjected to large strains high strain rates. In *Seventh International Symposium on Ballistics*. pages 541-547, The Hague, The Netherlands, April 19-21 (1983).
- [78] Kachanov L.M., Time of the rupture process under creep conditions. *Isv. Akad. Nauk SSA Otd. Tekh.* (1958).
- [79] Kachanov L.M., A microcrack model of rock inelasticity - Part I: frictional sliding on microcracks; Part II: propagation of microcracks. *Mech. Mater.* 1, 19-41 (1982).

- [80] Kalpakides V.K., Dascalu C., On the Thermomechanical Formulation of Configurational Forces in Continua, Proc. R. Soc. London, A 458, 1-17 (2002).
- [81] Kanninen M.F., Popelar C.H., Advanced Fracture Mechanics. Oxford University Press, Oxford (UK) (1985).
- [82] Keita O., Dascalu C., François B., A two-scale model for dynamic damage evolution. J. Mech. Phys. Solids., 64, 170-183 (2014).
- [83] Lachenbruch A H., Frictional heating, fluid pressure, and the resistance to fault motion. J. Geophys. Res., 85, 6097-6122 (1980).
- [84] Ladevèze P., Allix O., Deü J.F., and Lévêque D., A mesomodel for localisation and damage computation in laminates. Computer Methods in Applied Mechanics and Engineering, 183 (1-2), 105-122 (2000).
- [85] Lawn B.R., Marshall D.B., Nonlinear stress-strain curves for solids containing closed cracks with friction. J. Mech. Phys. Vol.46, No. 1, 85-113 (1998).
- [86] Li J., A micromechanics-based strain gradient damage model for fracture prediction of brittle materials – Part I: Homogenization methodology and constitutive relations. Int. J. Solids Structures 48 : 3336-3345 (2011).
- [87] Li J., Pham T., Abdelmoula R., Song F., Jiang C.P., A micromechanics-based strain gradient damage model for fracture prediction of brittle materials – Part II: Damage modeling and numerical simulations. Int. J. Solids Structures 48 : 3346-3358 (2011).
- [88] Li J., Song F., Jiang C. A non-local approach to crack process modeling in ceramic materials subjected to thermal shock. Engng. Frac. Mech. 133 : 85-98 (2015).
- [89] Li Z., Lambros J., Strain rate effects on the thermomechanical response of brittle polymers, International Journal of Solids and Structures, 38, 3549 - 3562, (2001).
- [90] Li T., Marigo JJ., Guilbaud D., Potapov S., Gradient damage modeling of brittle fracture in an explicit dynamics context. Int. J. Num. Meth. Engng. 108, 1381-1405 (2016).
- [91] Lee X., Ju J.W., Micromechanical Damage Model for Brittle solids - II: Compressive Loadings. J. Engrg. Mech., ASCE, 117, 1515-1536 (1991).
- [92] Lemaitre J., Desmorat R, Engineering damage mechanics: ductile, creep, fatigue and brittle failures. Berlin: Springer (2005)
- [93] Leguillon D., Sanchez-Palencia E., On the behaviour of a cracked elastic body with (or without) friction. J. Mech. Theor. Appl. 1, 195-209 (1982).
- [94] Markenscoff X., Dascalu C., Asymptotic homogenization analysis for damage amplification due to singular interaction of microcracks. J. Mech. Phys. Solids 60, 1478-1485 (2012).

-
- [95] Miehe C., Schanzel L.M., Ulmer H., Phase field modeling of fracture in multi-physics problems Part I- Balance of crack surface and failure criteria for brittle crack propagation in thermo-elastic solids. *Comp. Meth. Appl. Mech. Engng.*, 294, 449-485 (2015).
- [96] Mori T., Tanaka K., Average stress in the matrix and average elastic energy of materials with misfitting inclusions. *Acta. Metall.*, 21, pp. 571- 574 (1973).
- [97] Nemat-Nasser S., Deng H., Strain-rate effect on brittle failure in compression. *Acta Metall. Mater.* 42, 1013-1024 (1994).
- [98] Nemat-Nasser S., Obata M., A microcrack model of dilatancy in brittle material. *J. of Applied Mechanics*, 55, 24-35 (1988).
- [99] Nemat-Nasser, S., Hori, M., *Micromechanics: overall properties of heterogeneous materials*. Elsevier, Amsterdam (1999).
- [100] Paliwal B., Ramesh K. T., An interacting micro-Crack damage model for failure of brittle materials under compression. *J. Mech. Phys. Solids*, 56(3), 896-923 (2008).
- [101] Pandolfi A., Conti S. and Ortiz M., A recursive-faulting model of distributed damage in confined brittle materials, *J. Mech. Phys. Solids*, 54, 1972-2003 (2006).
- [102] Parnell W.J., Coupled thermoelasticity in a composite half-space. *J. Eng. Math.*, 56, 1-21 (2006).
- [103] Penta R., Gerisch A., The asymptotic homogenization elasticity tensor properties for composites with material discontinuities. *Continuum Mechanics and Thermodynamics*, volume 29., 187–206, (2017).
- [104] Perzyna P., Fundamental problems in viscoplasticity. In *Advances in applied mechanics*, 9, 243-377 (1966).
- [105] Pijaudier-Cabot G., Bazant Z., Non local damage theory, *J. Eng. Mech. (ASCE)*, 113, pp. 1512 - 1533 (1987).
- [106] Qi M., Shao J.F., Giraud A., Zhu, Q.Z., Colliat J.B. Damage and plastic friction in initially anisotropic quasi brittle materials, *Int. J. Plasticity*, 82, 260-282 (2016).
- [107] Qi M., Giraud A., Colliat J.B. Shao J.F., A numerical damage model for initially anisotropic materials. *Int. J. Solids Struct.* 100-101, 245-256 (2016).
- [108] Rabotnov Y.N., *Creep problems in structure members*. North Holland, Amsterdam (1969).
- [109] Ravi-Chandar K., Lu J., Yang B., Zhu Z., Failure mode transitions in polymers under high strain rate loading. *Int. J. Fracture*, 101, 33-72 (2000).
- [110] Ravi-Chandar K., Knauss WG., An experimental investigation into dynamic fracture: II. Microstructural aspects. *Int J. Fract.* 26, 65-80 (1984).

- [111] Ravi-Chandar K., Yang B., On the role of microcracks in the dynamic fracture of brittle materials. *J. Mech. Phys. Solids* 45, 535-563 (1997).
- [112] Ravi-Chandar K., *Dynamic fracture*. Boston. Elsevier (2004).
- [113] Ravichandran G., Subhash G., A micromechanical model for high strain rate behavior of ceramics., *Int. J. Solids Struct.*, 32, 2627-2646 (1995).
- [114] Rice J R., Heating, weakening and shear localization in earthquake rupture. *Phil. Trans. R. Soc., A* 375: 20160015 (2017).
- [115] Rittel D., Experimental investigation of transient thermoelastic effects in dynamic fracture. *Int. J. Solids Struct.*, 35, 2959-2973 (1998).
- [116] Rittel D., Thermomechanical aspects of dynamic crack initiation. *Int. J. Fracture.*, 99, 199-209 (1999).
- [117] Roozbeh R., Xinwei Z., Gianluca C., Adaptive multiscale homogenization of the lattice discrete particle model for the analysis of damage and fracture in concrete. *International Journal of Solids and Structures*, 125, 50–67, (2017).
- [118] Rosakis A. J., Samudrala O., Coker D., Cracks Faster Than the Shear Wave Speed. *Science*, 284, pp. 1337-1340 (1999).
- [119] Rosakis A. J., Samudrala O., Coker D., Intersonic shear crack growth along weak planes. *Mat. Res. Innovat.*, 3, pp. 236-243 (2000).
- [120] Rosakis A. J., Intersonic shear cracks and fault ruptures. *Advances in Physics*, vol. 51, 1189-1257 (2002).
- [121] Rosakis A.J., Xia K.W., Lykotrafitis G., Kanamori H., Dynamic shear rupture in frictional interfaces: speeds, directionality and modes. In: *Treatise in Geophysics*, vol. 4., pp. 153-192 (2007).
- [122] Sanchez-Palencia, E., *Non-homogeneous Media and Vibration Theory*. Lecture Notes in Physics, vol.127, Springer, Berlin (1980).
- [123] Shao Y., Zhang Y., Xu X., Zhou Z., Li W., Liu B., Effect of crack pattern on the residual strength of ceramics after quenching. *J. Am. Ceram. Soc.*, 94, 2804-2807 (2011).
- [124] Sharon E., Gross SP., Fineberg J., Energy dissipation in dynamic fracture. *Phys. Rev. Lett.* 76, 2117-2120 (1996).
- [125] Sharon E., Fineberg J., Confirming the continuum theory of dynamic brittle fracture for fast cracks. *Lett. Nature* 397, 333-335 (1999).
- [126] Schlüter A., Willenbücher A., Kuhn C., Müller R., Phase field approximation of dynamic brittle fracture. *Comp. Mech.* 54, 1141-1161 (2014).

-
- [127] Schlüter A., Kuhn C., Müller R., Gross D., An investigation of intersonic fracture using a phase field model. *Arch. Appl. Mech.* vol. 86, 321-333 (2016).
- [128] Schlüter A., Kuhn C., Müller R., Tomut M., Trautmann C., Weick H., Plate C., Phase field modelling of dynamic thermal fracture in the context of irradiation damage. *Continuum Mech. Thermodyn.* 29, 977-988 (2017).
- [129] Slepyan L.I., *Models and Phenomena in Fracture Mechanics*, Springer, Berlin (2002).
- [130] Sobhaniragh B., Batra R.C., Mansur W.J., Peters F.C., Thermal response of ceramic matrix nanocomposite cylindrical shells using Eshelby-Mori-Tanaka homogenization scheme. *Composites Part B: Engineering*, 118, 41 - 53 (2017).
- [131] Soumahoro Z., Étude du couplage thermomécanique dans la propagation dynamique de fissure, Ph.D. Thesis École Polytechnique (2005).
- [132] Soumahoro Z., Maigre H., Thermomechanical coupling and Dynamic Crack Propagation. *Universal Journal of Fracture Mechanics*, 4, pp. 70-85 (2016).
- [133] Spatschek, R., Brener, E., Karma, A., Phase field modeling of crack propagation, *Phil. Mag.*, 91, 75-95 (2011).
- [134] Suffis A., Lubrecht T.A.A., Combescure A., Damage model with delay effect: Analytical and numerical studies of the evolution of the characteristic damage length. *Int. J. Solids Struct.* 40, 3463-3476 (2003).
- [135] Sun N.S., Hsu T.R., Thermomechanical coupling effects on fractured solids. *Int. J. Fract.* 78, 67-87 (1996).
- [136] Telega J. J., Homogenization of fissured elastic solids in the presence of unilateral conditions and friction. *Comput. Mech.*, 6, 109-127 (1990).
- [137] Truesdell C.A., Toupin R.A., *The Classical Field Theories*. Handbuch der Physik Springer-Verlag, Berlin, Germany, Vols. III-1 (1960).
- [138] Weichert R., Schönert K., Heat generation at the tip of a moving crack. *J. Mech. Phys. Solids* 26, 151-161 (1978).
- [139] Wool R.P., *Polymer Interfaces: Structure and Strength*. Hanser Publishers, New York (1995).
- [140] Wrzesniak A., Dascalu C., Besuelle P., A two-scale time-dependent model of damage: Influence of micro-cracks friction: *European Journal of Mechanics A/Solids* vol. 49, 345-361 (2014).
- [141] Wu, X., Jiang C., Song F., Li J., Shao Y., Xu X., Yan P. Size effect of thermal shock crack patterns in ceramics and numerical predictions. *J. Europ. Ceram. Soc.* 35: 1263-1271 (2015).

- [142] Yevtushenko A.A., Kuciej M., Influence of the protective strip properties on distribution of the temperature at transient frictional heating. *International Journal of Heat and Mass Transfer*, 52, 376-384 (2009).
- [143] Yevtushenko A.A., Kuciej M., Yevtushenko O., Three-element model of frictional heating during braking with contact thermal resistance and time-dependent pressure. *International Journal of Thermal Sciences* 50, 1116 - 1124 (2011).
- [144] Yoffé E.H., The moving Griffith crack. *Philosophical Magazine Series 7*, 42:330, 739-750 (1951).
- [145] Zhu Q.Z., Shao J.F., A refined micromechanical damage-friction model with strength prediction for rock-like materials under compression. *Int. J. Solids Struct.* vol., 60, 75-83 (2015).
- [146] Zhao L.Y., Shao, J.F., Zhu, Q.Z., Analysis of localized cracking in quasi-brittle materials with a micro-mechanics based friction-damage approach, *J. Mech. Phys. Solids*, vol. 119, 163-187 (2018).
- [147] Zhu Q.Z., Zhao L.Y., Shao J.F., Analytical and numerical analysis of frictional damage in quasi brittle materials. *J. Mech. Phys. Solids*, vol. 92, 137-163 (2016).
- [148] Zinszner J.L, Erzar B., Forquin P., Strain rate sensitivity of the tensile strength of two silicon carbides : experimental evidence and micromechanical modelling. *Philosophical Transactions Royal Society A* 375 : 20160167 (2016).

Résumé étendu en français

Les études présentées dans ce document de thèse portent sur la modélisation de l'endommagement des matériaux fragiles sous chargements d'impacts avec la prise en compte du couplage thermo-mécanique.

En effet, les matériaux fragiles (polymères, roches, céramiques...) sont très utilisés pour de nombreuses applications d'ingénierie. Le polyméthacrylate de méthyle (PMMA) est un polymère très utilisé dans l'industrie aérospatiale (exemples: fenêtres d'avion, cockpits d'hélicoptère, ...) pour ses excellentes propriétés optiques et sa légèreté. Selon les différentes applications, ces composants industriels peuvent être soumis à des sollicitations d'impact mécanique entraînant leur rupture. La prédiction de l'endommagement des matériaux fragiles est donc cruciale pour une conception efficace des structures.

Les premières théories de la mécanique de la rupture ont été développées en considérant les phénomènes de propagation des fissures comme des processus indépendants de la température [68], [75]. Néanmoins, des travaux de recherches plus récentes [25], [18], [19], [115], [116], [62], [135], [123], [138] montrent l'importance du couplage thermo-mécanique dans la description de la rupture des matériaux. Une partie importante de l'énergie dissipée pendant l'évolution dynamique d'une fissure est convertie en chaleur, tandis que la variation de température peut influencer l'endommagement du matériau. De plus, les études expérimentales présentées dans [110], [111], [124], [125], [36] montrent que l'évolution des microfissures joue un rôle essentiel dans la rupture dynamique de matériaux tels que les polymères et les céramiques. Des analyses post mortem de la morphologie des surfaces de fissures ont révélé que l'initiation, la croissance et la coalescence des microfissures représentent les mécanismes dominants dans la rupture dynamique. Les instabilités de micro-branchement ont été proposées pour expliquer l'augmentation de l'énergie dissipée en pointe de fissure. Malgré les progrès importants de la mécanique de la rupture pour reproduire les effets dynamiques de la rupture ([59]), cette approche reste limitée dans la prédiction de l'initiation ou des configurations de rupture complexes. Le cas des instabilités dues aux branchements en est un exemple parmi d'autres. Les observations microscopiques rapportées lors d'une rupture rapide dans des matériaux fragiles suggèrent qu'un modèle approprié pourrait être obtenu en incorporant le mécanisme de micro-fissuration. Puisqu'il se déroule à des échelles plus petites que celle de la structure macroscopique, une approche multi-échelle avec des microfissures en propagation peut représenter un cadre de modélisation approprié.

De nombreux auteurs proposent des modèles d'endommagement basés sur la propagation de microfissures, on peut citer entre autres les contributions [97], [100], [113], [73], [72], [86], [87], [16]. Dans [37], [39], [47], [61], [140] les auteurs ont développé une

technique de modélisation de l'endommagement à plusieurs échelles basée sur la méthode d'homogénéisation asymptotique. Cette procédure a été employée pour modéliser l'endommagement dynamique en considérant des microfissures qui se propagent en mode d'ouverture dans [82], [41]. Le modèle d'endommagement dynamique est obtenu par homogénéisation à partir des hypothèses à l'échelle de la microstructure en évolution et prend en compte l'influence de la taille de microstructure sur la réponse macroscopique.

Dans cette thèse, nous étendons ce modèle multi-échelle d'endommagement afin de prendre en compte les couplages thermo-mécaniques lors de la rupture des matériaux fragiles. Nous développons d'abord un nouveau modèle d'endommagement dynamique en considérant un solide avec des microfissures qui évoluent en mode I et dont la dissipation aux pointes en mouvement est représentée par des sources de chaleur. Ensuite, nous utilisons une procédure similaire pour obtenir un modèle d'endommagement dynamique dans le cas de propagation en mode II avec frottement sur les lèvres des microfissures. Enfin, nous étendons ce dernier modèle au cadre thermo-mécanique, en considérant des sources de chaleur aux pointes en propagation et sur les lèvres frottantes des microfissures. On obtient ainsi un modèle d'endommagement couplé dynamique pour le mode de cisaillement. Les lois d'endommagement construites sont implémentées dans un code de calcul utilisant la méthode des éléments finis et des simulations numériques sont effectuées afin de prédire le comportement macroscopique des structures lors de la rupture sous sollicitations rapides.

Le manuscrit est organisé en quatre chapitres principaux. Dans le premier chapitre, nous donnons quelques notions préliminaires et exemples de modèles de rupture dynamique et d'endommagement, de couplage thermo-mécanique et de la méthode d'homogénéisation asymptotique. Ce chapitre introduit essentiellement les éléments de base nécessaires aux développements dans les chapitres suivants.

Dans le deuxième chapitre on présente le développement du modèle d'endommagement couplé correspondant à la propagation en mode I des microfissures. Nous effectuons d'abord l'analyse d'homogénéisation basée sur des développements asymptotiques pour obtenir le comportement effectif d'un solide thermoélastique microfissuré. Ensuite, la loi d'endommagement thermo-mécanique est obtenue par une analyse énergétique combinée à la procédure d'homogénéisation, avec la prise en compte de la dissipation de chaleur aux pointes en propagation. Nous effectuons ensuite une étude paramétrique de la réponse locale prédite par le nouveau modèle d'endommagement en mettant en évidence l'influence de la vitesse de chargement, de la taille de la microstructure et de la dissipation de chaleur. Ensuite, le nouveau modèle est utilisé pour reproduire numériquement les résultats expérimentaux de Rittel [115] montrant les variations de température dans des échantillons de PMMA lors des tests d'impact. Dans la dernière partie du chapitre, on étudie la validité de l'hypothèse d'évolution adiabatique souvent considérée pour les phénomènes de rupture rapide. Une comparaison entre les résultats obtenus avec l'hypothèse d'adiabaticité et ceux donnés par la solution de l'équation de température complète montre des prédictions numériques similaires.

Le troisième chapitre présente un modèle d'endommagement dynamique par cisaillement avec frottement. Le modèle est obtenu en utilisant une procédure de même type pour le changement d'échelle et sans tenir compte du couplage thermomécanique. Parmi les conditions aux limites, le contact unilatéral avec frottement est supposé sur les lèvres

des microfissures. Dans ce cas particulier d'évolution d'endommagement en mode II, des méthodes de résolution spécifiques présentées dans l'annexe B sont utilisées pour le calcul des coefficients effectifs. Une approche énergétique tenant compte des dissipations d'énergie due au frottement et à la propagation est utilisée pour obtenir la loi d'endommagement. L'analyse de la réponse macroscopique locale du modèle a permis de mettre en évidence l'influence de la vitesse de déformation, du chargement en compression et du coefficient de frottement sur l'évolution de l'endommagement. Des simulations macroscopiques ont été réalisées dans le but de reproduire numériquement les résultats expérimentaux de Ravi-Chandar et al. [109] sur la rupture en cisaillement sous chargements d'impact.

Le dernier chapitre étend la formulation du modèle d'endommagement dynamique en mode de cisaillement au cas du couplage thermo-mécanique. En plus des sources de chaleur en pointes des microfissures, on suppose également des sources linéiques dues à la dissipation par frottement entre les lèvres. Comme dans le cas de la propagation en mode I, l'homogénéisation conduit à une équation de température macroscopique contenant des sources de chaleur distribuées induites par les dissipations microscopiques. Le modèle d'endommagement obtenu tient compte des effets de taille de microstructure et montre une sensibilité à la vitesse de déformation. On étudie la réponse macroscopique locale thermo-mécanique en mettant l'accent sur les effets du coefficient de frottement, des chargements de cisaillement et de compression. On termine le chapitre par un premier exemple de simulation numérique d'un essai d'impact en mode II et l'analyse de l'évolution thermique associée à la rupture dynamique.

Modèle d'endommagement dynamique thermo-mécanique en mode I

L'évolution de la température dans un solide microfissuré est donnée par l'Equation (1). Cette équation a été obtenue par homogénéisation asymptotique pour un solide thermoélastique avec une distribution localement périodique de microfissures en propagation dynamique en mode I. Des conditions aux limites de bords libres de contraintes et d'isolation thermique sur les lèvres, ainsi que de sources de chaleur aux pointes de microfissures ont été considérées dans la modélisation. Le terme à droite dans (1) représente une densité volumique de sources de chaleur pendant l'évolution de l'endommagement.

$$(c + T^{(0)}S^*)\frac{\partial T^{(0)}}{\partial t} + T^{(0)}\beta_{ij}^{eff}\frac{\partial e_{xij}(\mathbf{u}^{(0)})}{\partial t} + \frac{\partial Q_i^{(0)}}{\partial x_i} = \frac{\mathcal{G}_{c0}C_R(2 + a.l_c\frac{dd}{dt})}{l_c(2C_R - l_c\frac{dd}{dt})}\frac{dd}{dt} \quad (1)$$

L'équation d'évolution de l'endommagement est également obtenue par homogénéisation, à partir de critères microscopiques de propagation, sous la forme

$$\frac{dd}{dt} = \frac{2C_R}{l_c} \left\langle 1 - \frac{\mathcal{G}_{c0}(1 + aC_R)}{l_c\mathcal{Y} + aC_R\mathcal{G}_{c0}} \right\rangle \quad (2)$$

Le taux de restitution d'énergie d'endommagement \mathcal{Y} est obtenu comme fonction des champs macroscopiques de température $T^{(0)}$, de déplacement $\mathbf{u}^{(0)}$ et d'endommagement

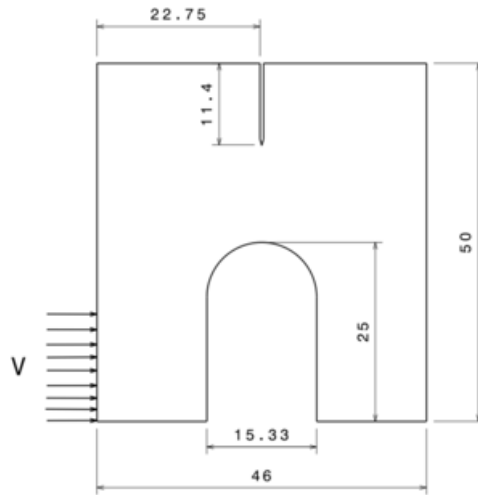


Figure 1: Géométrie de l'échantillon, avec des dimensions in mm . La vitesse d'impact V est appliquée sur une zone de $16.5 mm$.

d , ainsi que des dérivées des coefficients effectifs $S^*(d)$, $\beta_{ij}^{eff}(d)$, $C_{ijkl}^{eff}(d)$. C_R représente la vitesse des ondes de Rayleigh, \mathcal{G}_{c0} est l'énergie critique de rupture en quasi-statique et a est un paramètre du modèle. La taille de la microstructure est noté par l_c et le flux de chaleur macroscopique $Q^{(0)i}$ est obtenu comme fonction du gradient de la température $T^{(0)}$ par une loi de Fourier homogénéisée.

Les equations (1-2) couplées avec l'équation de mouvement homogénéisée forment un système couplé pour les inconnues macroscopiques $T^{(0)}$, $\mathbf{u}^{(0)}$ et d . Ce système peut être résolu numériquement en utilisant la méthode des éléments finis en espace et différences finies en temps. Un tel schéma a été implémenté dans le logiciel ABAQUS. Ainsi nous avons pu reproduire numériquement le test expérimental d'impact sur l'échantillon CCS [23], [115], [116].

La géométrie de l'échantillon en PMMA est illustrée dans la Figure 1. Les mesures expérimentales de [23], [115] et [116] ont été effectuées avec un thermocouple placé à $1 mm$ d'une fissure de fatigue créé en continuité de l'entaille initiale. Un chargement d'impact, d'une vitesse $V = 30 m.s^{-1}$, appliqué par l'intermédiaire d'une barre en acier de diamètre $16.5 mm$ permet d'initier une fissure à la pointe de l'entaille initiale qui se propage en mode mixte avec une dominance du mode I. En supposant des conditions adiabatiques pour l'évolution de la température, des calculs d'élasticité dynamique peuvent être effectués dans Abaqus Explicit avec la résolution complète des équations de température et d'endommagement dans la subroutine VUMAT.

L'évolution de la température à $1 mm$ de l'entaille initiale représentée sur la Figure ?? montre un refroidissement d'environ $30^\circ C$, tandis que pendant la propagation la température monte d'environ $30^\circ C$ par rapport à la température initiale. Les variations obtenues par simulations numériques avec le nouveau modèle sont relativement proches des valeurs expérimentales.

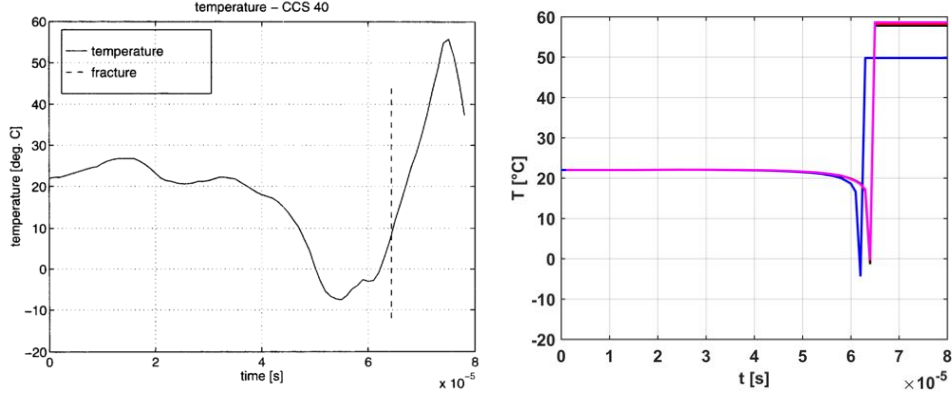


Figure 2: Variation de température à 1 mm de la pointe de l'entaille initiale: valeurs expérimentales (gauche) [115] et calculées (droite) dans 4 éléments voisins dans la région du thermocouple.

Modèle d'endommagement dynamique thermo-mécanique en mode II

Dans le cas d'une propagation en mode II des microfissures, dans des hypothèses similaires sur la microstructure, la procédure de changement d'échelle conduit à l'équation macroscopique de la température :

$$(c + T^{(0)} S^*) \frac{\partial T^{(0)}}{\partial t} + T^{(0)} \beta_{pq} \frac{\partial e_{xpq}(\mathbf{u}^{(0)})}{\partial t} + \frac{\partial Q_j^{(0)}}{\partial x_j} = \mathcal{R}_d + \mathcal{R}_f \quad (3)$$

Dans l'équation de la chaleur (3), le premier terme du membre de droite \mathcal{R}_d représente la source de chaleur due à l'évolution de l'endommagement dont l'expression est :

$$\mathcal{R}_d = \frac{dd}{dt} (\mathcal{Y} - \mathcal{Y}_f) = \frac{dd}{dt} \left(\frac{1}{2l_c} \frac{2 + a.l_c \frac{dd}{dt}}{\sqrt{1 - \frac{l_c}{2C_R} \frac{dd}{dt}}} \mathcal{G}_{c0} \right) \quad (4)$$

Le second terme \mathcal{R}_f représente une source volumique de chaleur produite par frottement sur les lèvres des microfissures. Son expression complexe en fonction des champs thermo-mécaniques et des coefficients effectifs, ainsi que les expressions du taux de restitution d'énergie volumique total \mathcal{Y} et de l'énergie dissipée par micro-frottement \mathcal{Y}_f sont données dans le dernier chapitre du manuscrit.

La loi d'évolution d'endommagement est obtenue par homogénéisation sous la forme :

$$\frac{dd}{dt} = \left\langle \frac{2\Pi}{a^2 \mathcal{G}_{c0}^2 l_c^2} - \frac{l_c}{a^2 C_R \mathcal{G}_{c0}^2} (\mathcal{Y}_d - \mathcal{Y}_f)^2 - \frac{2}{al_c} \right\rangle \quad (5)$$

avec

$$\Pi = \sqrt{\left(a \mathcal{G}_{c0}^2 l_c + \frac{l_c^3}{2C_R} (\mathcal{Y} - \mathcal{Y}_f)^2 \right)^2 - a^2 \mathcal{G}_{c0}^2 l_c^2 \left(\mathcal{G}_{c0}^2 - l_c^2 (\mathcal{Y}_d - \mathcal{Y}_f)^2 \right)} \quad (6)$$

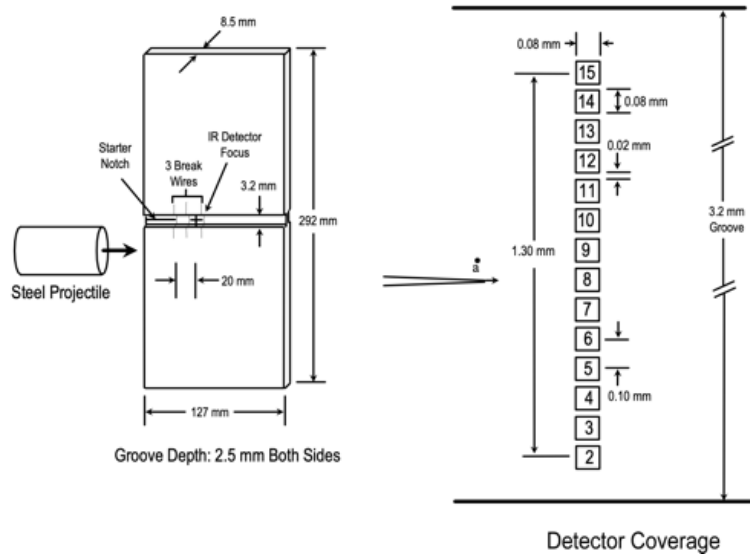


Figure 3: Echantillon avec rainure sous sollicitation d'impact non-symétrique et détecteurs IR pour mesure de température [17, 19].

On remarque que la loi d'endommagement dépend de la taille de la microstructure l_c et du frottement microscopique par l'intermédiaire de terme \mathcal{Y}_f . Quand le coefficient de frottement μ_f est nul on obtient $\mathcal{Y}_f = 0$ et la loi précédente donne l'évolution de l'endommagement en mode II non-frottant.

Une étude macroscopique locale nous a permis d'identifier les effets du coefficient de frottement, de la taille de microstructure, de la compression normale, de l'endommagement initial et de la vitesse de chargement en cisaillement sur la réponse en contrainte, endommagement et température du modèle. En particulier, l'analyse des effets des deux sources microscopiques d'échauffement montre que dans la phase d'évolution des microfissures la dissipation thermique due à la propagation devient vite dominante par rapport à la dissipation due au frottement.

Concernant les simulations au niveau de la macro-structure, le modèle d'endommagement en mode II a été implémenté dans ABAQUS, à l'aide d'une subroutine VUMAT, en vue de reproduire numériquement les résultats expérimentaux de [109] et [19]. Dans ces essais, une plaque rectangulaire en PMMA avec des rainures sur les deux faces comme représenté sur la Figure 3 est soumise à une sollicitation d'impact dans une zone décalée par rapport à l'entaille initiale. La rupture en mode II est initiée en appliquant ce chargement d'impact mécanique asymétrique.

Les simulations numériques montrent une bande d'endommagement initiée à la pointe de l'entaille et qui évolue en suivant une trajectoire relativement droite dans la rainure comme montré sur la Figure 4. Cette bande d'endommagement correspond à une fissure en mode de cisaillement observée expérimentalement dans [19] et [109].

Pour une vitesse d'impact $V = 60m/s$, la position du front de propagation en fonction de temps est représentée dans la Figure 5 pour les valeurs expérimentales [109] et numériques. Le modèle prédit une évolution de la rupture proche des valeurs mesurées dans les essais. La vitesse de la fissure augmente en $80 \mu s$ à une valeur proche de la vitesse

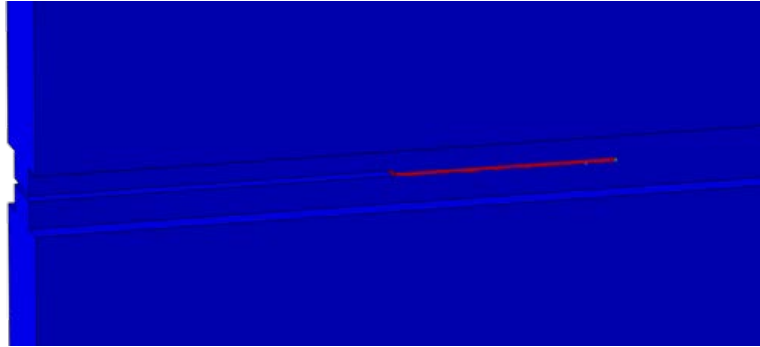


Figure 4: Bande d'endommagement à l'intérieur de la rainure.

d'ondes de Rayleigh dans le PMMA. Il s'agit d'un comportement typique de fissuration en mode II. Dans une propagation en mode I, les dissipations associées aux instabilités de micro-branchement conduisent à une vitesse limite bien inférieure à celle de Rayleigh.

La simulation de l'essai rapporté dans [19] a permis de reproduire l'évolution de la température pendant la rupture en mode II d'une plaque rainurée en PMMA (Figure 3). Dans [19] la variation de température à 20 mm de l'entaille initiale a été obtenue en utilisant des détecteurs infrarouge alignés verticalement. Cette évolution est montrée dans la Figure 6a. La variation de température maximale obtenue par le détecteur 8 est d'environ 85 K , pendant un intervalle de temps compris entre $55\ \mu\text{s}$ et $65\ \mu\text{s}$. Les résultats des simulations numériques sont représentés dans la Figure 6b. On a obtenu une augmentation de température relativement similaire de $85 - 90\text{ K}$ au point d'intégration de l'élément situé au milieu de la bande d'endommagement et à 20 mm de la pointe de l'entaille, correspondant au capteur 8. L'augmentation de température dans les simulations a lieu en $10\ \mu\text{s}$, ce qui est proche de celui des expériences. Les températures dans les éléments voisins, correspondant aux capteurs 7 et 9, sont également montrées dans la

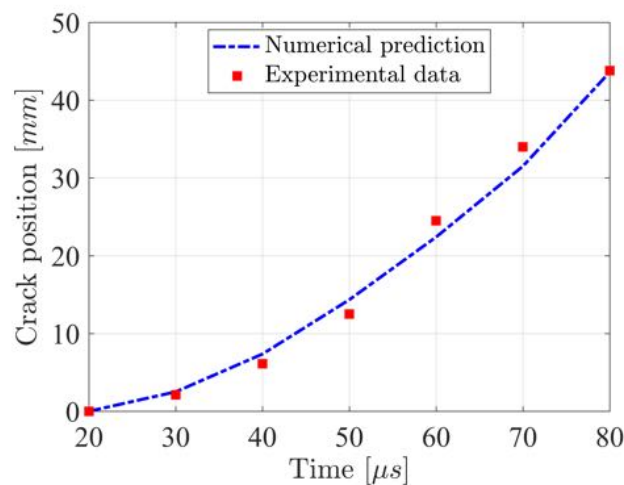


Figure 5: Position de la pointe de fissure en fonction du temps : valeurs expérimentales [109] et numériques.

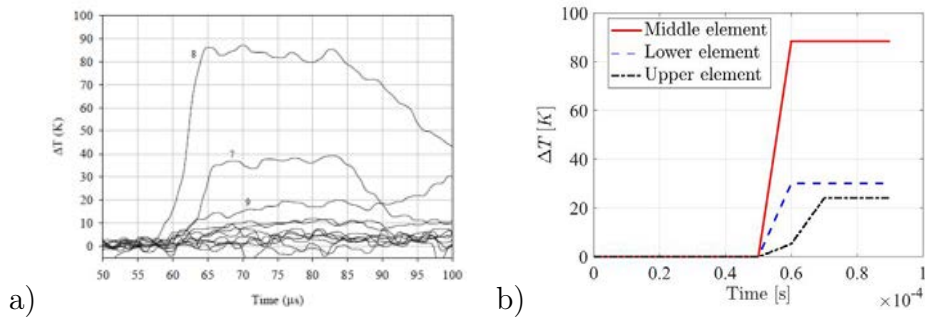


Figure 6: Variation de la température dans la région des détecteurs IR : (a) valeurs mesurées [19] et (b) valeurs numériques dans 3 éléments voisins correspondant aux trois détecteurs les plus proches de la fissure.

Figure 6b. On note des variations relativement proches des valeurs expérimentales.

Par rapport aux développements présentés dans ce document, plusieurs perspectives de recherche sont envisageables. Des extensions telles que l'étude de l'endommagement en mode mixte par couplage du mode I et du mode II au niveau microscopique, la modélisation des distributions aléatoires de microfissures utilisant des approches d'homogénéisation stochastique [65], des modèles d'endommagement thermomécanique en 3D [38], l'étude de l'interaction et de la coalescence des microfissures [94] ou la régularisation des modèles obtenus par des termes de type gradient pour une meilleure objectivité par rapport aux maillages EF sont possibles.